Department of Physics and Astronomy
University College London

Electronic Transport in Nano-scale Organic Semiconductors from Non-Adiabatic Molecular Dynamics

Author:
Samuele Giannini

Supervisor:
Prof. Jochen Blumberger

A dissertation submitted in fulfillment
of the requirements for the degree of
Doctor of Philosophy
of
University College London.

December 16, 2020

I, Samuele Giannini, confirm that the work presented in this thesis is my own. Where information has been derived from other sources, I confirm that this has been indicated in the work.

Abstract

New electronic devices fabricated from organic molecules have been greatly improved over the past two decades. Yet, understanding the electronic transport mechanism of free carriers and excitons (bound electron-hole pairs) in organic semiconductors (OSs) is still a pertinent challenge. The soft molecular nature of these materials gives rise to an intricate interplay between electronic and nuclear motion as well as unique solid-state physical properties. Standard (analytic) treatments describing electronic transport often rely on one of two extremes: a travelling wave propagating through the material or a particle hopping from one molecular unit to the next. These are often unsuitable to fully describe the complex dynamics, which falls in between these regimes. In this regard, non-adiabatic molecular dynamics simulations permit a direct view into the transport mechanism, thus providing new important insights.

In this thesis, I have further developed and improved in terms of efficiency and accuracy a fully atomistic non-adiabatic molecular dynamics algorithm, called fragment orbital-based surface hopping (FOB-SH). This allows the propagation of the coupled electron-nuclear motion in large nano-scale systems. After validating the accuracy of this methodology and discussing important physical requirements (i.e. energy conservation, detailed balance and internal consistency), I will present the application of FOB-SH to the calculation of room temperature charge mobility of a series of molecular organic crystals. I will discuss the agreement with experimental mobility values and the role of the disorder, induced by thermal fluctuations, on the delocalization of the states and the subsequent formation of a polaronic charge state. This polaronic charge propagates through the crystal by diffusive jumps over several lattice spacings at a time during which expands to more than twice its size. I will show that FOB-SH can recover the crossover from hopping to band-like transport depending on the strength of the electronic coupling and the temperature, thus successfully bridging the gap between these two extreme transport regimes. Finally, I will discuss a further extension of FOB-SH to the treatment of exciton transport in OSs. This opens up new exciting avenues for the application of FOB-SH to the study of electronic processes occurring in organic photovoltaic cells.

Impact Statement

Organic semiconductors (OSs) are emerging as a viable semiconductor technology for displays, electronic devices, renewable energies and many more profitable industries. The work presented in this thesis tackles important and long-debated topics in this field that may help optimizing and improving OSs for application relevant devices.

In particular, this work is concerned about important experimental observables such as charge mobility and exciton diffusion length. These fundamental transport properties of the material should be further pushed and increased to obtain more efficient OSs with a greater impact on the market and large-scale applications. So far this aim has been pursued mainly by means of experimental trial and error approaches. Here, using advanced computer simulations, new design rules and principles to achieve this goal will be presented and discussed.

This work also provides new insights into the underlying transport mechanisms in OS materials by directly solving the time dependent electronic Schrödinger equation coupled to nuclear motion in experimentally relevant nano-scale systems. The approach presented in this thesis helps, for example, to reconcile the evidence from various experimental techniques of a coexistence of localized and delocalized charge carriers in OSs. The apparent contradiction between a band-like temperature dependence of the mobility (usually characteristic of delocalized band states) and the presence of localized carriers is rationalized here in terms of the relative strength of important parameters, such as electronic couplings, local electron-phonon coupling and their thermal fluctuations.

Finally, this work lays down a general framework that can be extended beyond electronic transport processes to include, for example, electron-hole separation and possible charge recombination processes taking place at the donor-acceptor heterojunction interface of organic solar panels. Renewable energies like the latter are becoming very important in our modern society and they account nowadays for a third of the global power capacity. Scientific advance in this field is therefore paramount.

Acknowledgements

First and foremost, I would like to express my deepest gratitude to my supervisor Prof. Jochen Blumberger who has given me guidance, support and encouragement during these years. His great passion and attitude towards science and research have been an invaluable source of inspiration. I am sincerely grateful to him for giving me the necessary confidence in myself as well as the knowledge and computational means to carry out my own research. In Jochen Blumberger's group, I had the honour to work with some of the most brilliant researchers, but also amazing people who have now become special friends, that I have ever had the pleasure to encounter in all my life.

I would like to thank, from the bottom of my heart, Dr. Antoine Carof for collaborating with me on further developing the computational method presented in this thesis and, most importantly, for his constant guidance and stimulating discussions taking place even after he left the group at UCL. I am greatly indebted to Antoine for his help in terms of math derivations, understanding and consolidation of my own work. Others who deserve special thanks include Dr. Orestis Ziogos (which is our group mastermind of molecular mechanics and whose knowledge and suggestions have been of invaluable help for my projects), Matthew Ellis and Xiuyun Jiang (for sharing with me almost the entirety of my PhD, for their friendship and, especially Matt, for constantly providing me with coding advice and all other sorts of help), Dr Soumya Ghosh, Dr. Zdenek Futera and Dr. Hui Yang (with whom I had countless stimulating discussions on different computational methods besides the ones presented here and about code improvements), Dr. Wei-Tao Peng and Jan Elsner (for happily joining our new projects and for building on our work to continue exciting research on organic solar cells and other applications) and finally, I wish to really thank Dr. Lorenzo Cupellini and Prof. Benedetta Mennucci (for the long-standing collaboration since my time at the University of Pisa as a BSc. and MSc. student, and for very useful discussions as well as computer codes provided to complete the last chapter of this thesis).

I thank also all current and past group members for very many discussions and insights: Dr. Guido Falk von Rudorff, Dr. Patrick Gutlein, Peter Cooke, Christian Ahart, Dr. Xiaojing Wu, Dr. David Dell'Angelo, Oliver Gittus, Kevin Lively, Zak Zheng, Dr. Philipp Schienbein.

I would also like to express my gratitude to Prof. Alexander Shluger and Prof. Graeme M. Day for agreeing to be part of my PhD examination panel and for the constructive dis-

cussions and comments during my PhD viva. I thank also Prof. Franco Cacialli and Prof. Graham Worth for the insightful comments during my upgrade viva from Mphil to PhD. I thank very much Prof. Jenny Nelson and her group at Imperial College London for sharing their experience and profound knowledge with us.

I now wish, with all my heart, to express my affect and gratitude to Eleonora and my beloved family: my mother and father, Roberta and Giancarlo, my siblings, Daniel and Deborah and my grandmothers, Ivana and Liliana. They have never once failed to encourage me and give me strength even in the most difficult moments and stressful periods. I thank them for the unwavering support, kindness and for understanding the hard work and long hours that go into a doctorate. I particularly thank Eleonora for sharing with me our long adventure "far from home" and the great time we have spent together. I would like to dedicate to all of them this achievement and this thesis.

Last but not least, I would like to thank my superb crew of friends back home and my old colleagues and friends from my time in Pisa. Very luckily for myself, they are too many to individually write their names. Nonetheless, I truly thank them for always being there for me even after years and months apart and to always put a smile on my face with their messages, jokes and laughs.

I have been supported by the European Research Council (ERC) under the European Union, Horizon 2020 research and innovation programme (grant agreement no. 682539/ SOFTCHARGE). Via our membership of the UK's HEC Materials Chemistry Consortium, which is funded by EPSRC (EP/L000202, EP/R029431), this work used the ARCHER UK National Supercomputing Service (http://www.archer.ac.uk), as well as the UK Materials and Molecular Modeling (MMM) Hub, which is partially funded by EPSRC (EP/P020194), for computational resources. I also acknowledge the use of the UCL Grace High Performance Computing Facility.

List of Publications

The work discussed here has been published in the following papers:

1. Giannini, S., Carof, A., Ellis, M., Ziogos, G.O. and Blumberger, J. "From atomic orbitals to nano-scale charge transport with mixed quantum/classical non-adiabatic dynamics: method, implementation and application" in *Nano- and Nano-bio Systems in Complex Environments.* RSC Book, Ed. Dennis S. and Dongqing W., Ch. X, submitted (2020).

2. Giannini, S., Ziogos, G.O., Carof, A., Ellis, M. and Blumberger, J. "Flickering Polarons Extending Over Ten Nanometres Mediate Charge Transport in High-mobility Organic Crystals" *Adv. Theory Simul.* 3, 2000093 (2020) (Cover Article).

3. Carof, A., Giannini, S. and Blumberger, J. "How to calculate charge mobility in molecular materials from surface hopping non-adiabatic molecular dynamics beyond the hopping/band paradigm." *Phys. Chem. Chem. Phys.* 21, 26368–26386 (2019).

4. Giannini, S., Carof, A., Ellis, M., Yang, H., Ziogos, G.O., Ghosh, S. and Blumberger, J. "Quantum localization and delocalization of charge carriers in organic semiconducting crystals." *Nat. Comm.* 10, 3843 (2019).

5. Giannini, S., Carof, A. and Blumberger, J. "Crossover from Hopping to Band-Like Charge Transport in an Organic Semiconductor Model: Atomistic Nonadiabatic Molecular Dynamics Simulation." *J. Phys. Chem. Lett.* 9, 3116-3123 (2018).

6. Carof, A., Giannini, S. and Blumberger, J. "Detailed balance, internal consistency, and energy conservation in fragment orbital-based surface hopping." *J. Chem. Phys.* 147, 214113 (2017).

Contents

List of Figures

List of Tables

List of abbreviations

1D	One-Dimensional
2D	Two-Dimensional
ANT	Anthracene
AOM	Analytic Overlap Method
ARPES	Angle-Resolved Photoemission Spectroscopy
BOMD	Born-Oppenheimer Molecular dynamics
CCDC	Cambridge Crystallographic Data Centre
CDFT	Constraint DFT
CMS	Current Modulation Spectroscopy
COC	Center Of Charge
CT-MQC	Coupled-trajectory Mixed Quantum-Classical
DATT	dianthra[2,3-b:20,30-f]thieno[3,2-b]thiophene
DC	Decoherence Correction
DCICT	Decoherence Correction-Induced Spurious Charge Transfers
DCVSN5	Dicyanovinyl-capped S,N-heteropentacene
DFT	Density Functional Theory
DFTB	Density Functional Tight Binding
DOS	Density Of States
EDC	Energy-based Decohererence time
EFH	Elimination of Forbidden Hops
ELM	Ethylene Like Molecule
EPC	Electron-Phonon Couplings
ESR	Electron Spin Resonance
ET	Electron Transfer
FDC	Force-based Decoherence Correction
FED	Fragment Excitation Difference
FET	Field Effect Transistor
FOB-SH	Fragment Orbital-Based Surface Hopping
FODFT	Fragment Orbital Density Functional Theory
sFODFT	Scaled FODFT
FF	Force Field
FSSH	Fewest Switches Surface Hopping
GAFF	Generalized Amber Force Field
GGA	Generalized Gradient Approximation
HOMO	Highest Occupied Molecular Orbital
IDA	Instantaneous Decoherence after Attempted hop
IPR	Inverse Participation Ratio
LUMO	Lowest Unoccupied Molecular Orbital

MD	Molecular Dynamics
MF	Mean-Field dynamics
MFED	Multi-state FED
MIR	Mott-Ioffe-Regel limit
MQCD	Mixed Quantum-Classical Molecular Dynamics
MSD	Mean Squared Displacement
MTS	Multiple Time Step algorithm
NACE	Non-Adiabatic Coupling Element
NACV	Non-Adiabatic Coupling Vector
NAMD	Non-Adiabatic Molecular Dynamics
NAP	Naphthalene
OFET	Organic Field Effect Transistor
OLED	Organic Light Emitting Diode
OPV	Organic Photovoltaic
OSs	Organic Semiconductors
OT6	α-sexithiophene
PAS	Projected Active State population
PBC	Periodic Boundary Conditions
PDA	Point Dipole Approximation
PDDC	Pure Dephasing Decoherence Correction
PEN	Pentacene
PES	Potential Energy Surface
PER	Perylene
pMSB	1,4-bis(4-methylstyryl)benzene
PTCDI-H	perylenetetracarboxylic diimides
PYR	Pyrene
QCLE	Quantum Classical Liouville Equations
RK	Runge-Kutta algorithm
RMSE	Root Mean Square Error
RPMD	Ring-Polymer Molecular Dynamics
RTA	Relaxation Time Approximation
RUB	Rubrene
SC-FSSH	Self Consistent FSSH
SCLC	Space-Charge Limited Current
SCTC	Spurious Charge Transfer Correction
SC-FDC	Stochastic algorithm FDC
SH	Surface Hopping
TDDFT	Time Dependent Density Functional Theory
TDSE	Time Dependent Schrödinger Equation
TLT	Transient Localization Theory
TOF	Time-of-Flight
TrESP	Transition Electrostatic Potential charges

Chapter 1

Introduction

1.1 Organic semiconductors

Organic energy materials (carbon-based molecules) capable of conducting electrical current have nowadays many applications for solar power conversion, energy generation, electronics and displays. The development of electronic devices fabricated from organic molecules constitutes a vibrant and active field of research. These conducting materials are generally called organic semiconductors (OSs) and the name organic underlines the difference with respect to more conventional semiconductors based on inorganic materials such as silicon, germanium and gallium arsenide. OSs can be roughly classified into two main categories: relatively small single molecules (e.g. molecular crystals of anthracene) and polymeric semiconductors, very long molecules made of covalently bonded repeat units (e.g. heterocyclic polymers). Both these classes of OSs are commonly characterized by π-conjugated orbitals delocalized over the individual aromatic units. It is this electronic delocalization what makes organic molecules capable of conducting electrical current [1]. In addition, the extended π-conjugation places the energy difference between the highest occupied and the lowest unoccupied molecular orbital (HOMO-LUMO gap) in the visible range and gives conjugated molecules photoactive properties such as the ability to absorb or emit light. These electronic characteristics along with the low synthesis and device fabrication cost, chemical tunability via multiple functionalization routes, and their compatibility with other soft materials, have contributed to the wide spread use of OSs for electronics and optoelectronics devices [2, 3]. For example organic materials have nowadays been employed to make organic field effect transistors (OFETs) [4], organic photovoltaics (OPVs) [5, 6], and organic light emitting diodes (OLEDs) [7] as represented in Figure 1.1.

OFETs are one of the most common technologies used to induce and measure charge transport in OSs. In such devices, organic molecules are used as semiconducting substrate to sustain migration of free carriers (holes or electrons). Since the first publication on OFETs dating back to 1986 [8], device architecture optimization and the discovery of better semiconducting molecules, largely lead by experimentalists via trial and error approaches, have enabled several breakthroughs in term of OFETs conductivity [3, 4, 9]. These days, they

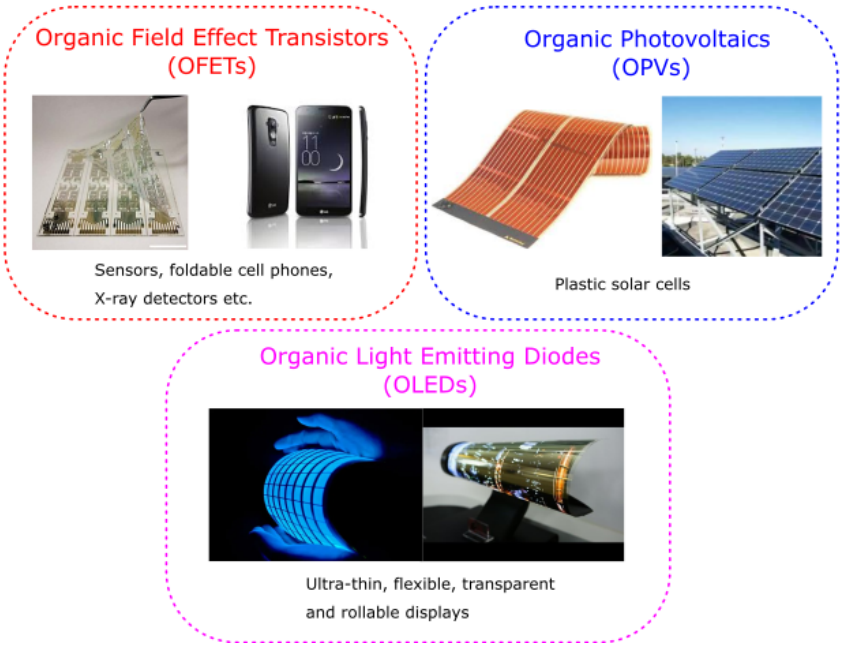

Figure 1.1: Illustration of the three main applications of organic semiconductors: organic field effect transistors (OFETs), organic photovoltaics (OPVs), organic light emitting diodes (OLEDs).

play an important role in organic electronics, e.g., as inverters and integrated circuits for logic operations. Despite these achievements, the rational design of OSs with high charge carrier mobility to permit a lower power consumption and a faster operation of organic circuits remains a central challenge [4].

The charge carrier mobility, μ ($cm^2\ V^{-1}\ s^{-1}$), which is related to the transport of free hole or electron carriers, is a fundamental metric for the performance of the OS material (and it will be a central quantity considered in this thesis). To contextualize the mobility of OSs in relation to more common inorganic semiconductors, to date the highest reproducible values for hole mobility of a well-known crystalline organic semiconductor, i.e. rubrene, lays in the range of 15-20 $cm^2\ V^{-1}\ s^{-1}$ at room temperature and, the same quantity, is usually an order of magnitude smaller for semiconducting polymers [2]. Despite the mobility of OSs is higher than that of thin films of amorphous silicon (around 1 $cm^2\ V^{-1}\ s^{-1}$), a fact that makes OSs technologically interesting, it is still few orders of magnitude smaller than that of top inorganic semiconductors (e.g. monocrystalline silicon, and gallium arsenide with mobilities of about 1,000 and 8,000 $cm^2\ V^{-1}\ s^{-1}$, respectively). One reason for the modest mobility of OSs is that design approaches are still hampered by our incomplete fundamental understanding of the elusive charge dynamics and transport mechanism in these materials.

There is still a considerable debate both experimentally [2, 10, 11] and theoretically [12–16] about the true nature of the charge carriers in OSs. The propagating charge seems to be neither a wave, like in most inorganic semiconductors, nor a particle, as in strongly disordered systems (e.g. solution-processed polymers), but rather a mixture of the two [17, 18]. Examples of this intriguing dichotomy between localized and delocalized charge carriers are the evidence from electron spin resonance (ESR) [19, 20] and optical charge modulation spectroscopy (CMS) [21–23] measurements that point to a finite extension for the carrier wavefunction, typically delocalized over a few molecular units in different OSs depending on the temperature and the degree of thermal disorder. As I will point out in the following, this intermediate regime poses a challenge to most of the traditional transport pictures and existing theories [12, 15] making the charge transport mechanism not yet fully understood. Addressing some of the underlying features of the charge transport mechanism in OSs will constitute one of the major results of this thesis (see Chapter 4 and Chapter 5).

Another ground-breaking innovation enabled by organic semiconductors, are organic photovoltaic (OPV) cells. They have a much lower cost than conventional silicon solar panels and a wider range of potential applications (due to their semi-transparency and flexibility) [24, 25]. After light harvesting and absorption processes, the three fundamental steps enabling a typical donor-acceptor solar cell to convert light into electricity are: the diffusion of bound-electron hole pairs (excitons diffusion) towards the donor-acceptor interface (heterojunction), the dissociation of excitons into free electrons in the acceptor material and a free holes in the donor material and finally their transport towards the electrodes generating current. Although this thesis will not be concerned with the exciton separation process, it will computationally explore the transport mechanism of free charges [1, 10] and excitons [26, 27] in OSs at the nano-scale level. One quantity of particular importance in photovoltaic materials is the exciton diffusion length (see Chapter 6). This is defined as the distance travelled by excitons before recombining to the ground state. A long diffusion length is a prerequisite for efficient organic solar cell, where excitons should travel towards the donor-acceptor interface in order to initiate the separation process.

The soft molecular composition of OSs due to the weak van der Waals intermolecular interactions has allowed their use as flexible OLED displays and other hugely profitable applications currently being launched on the market by several companies. Nevertheless, this

feature is also one of the major performance-limiting factors for both their charge transport and optoelectronic properties [2, 12]. A detailed understanding of the interplay between strong thermal nuclear motion and electronic transport is also elusive, as we will see in the following. Theory and computation are, therefore, expected to play a prominent role in providing design rules and physical insights that might help experimentalists to push charge mobilities and exciton diffusion lengths further which are paramount requisites for efficient organic electronics and photovoltaics materials.

1.2 Electronic transport and current challenges

A particularly important challenge in understanding electronic transport processes from a computational perspective is the fact that relevant transport parameters are on very similar energy scales, typically around 10-600 meV (in efficient OSs). This is due to the dynamical disorder caused by the molecular nature of the OSs and results in the inapplicability of perturbative approaches based on energy scale separation [2, 12, 15, 16, 28–30]. The most common parameters entering the Hamiltonian of the system are: the electronic couplings, V (normally about 10-200 meV), i.e. the interactions between the relevant electronic states localized on different molecular sites; and the electron-phonon couplings, i.e. the interactions of the charge carrier (or exciton) with nuclear degrees of freedom. The local part of the electron-phonon coupling is also called reorganization energy, λ, and it is usually about 100-600 meV, while the non-local electron-phonon coupling is related to the dynamical disorder of the system modulated by its fluctuations and it is about 10-100 meV [31]. Notably the aforementioned quantities are also in the same order of magnitude of the thermal energy ($k_BT \approx 25$ meV at room temperature), meaning that thermal motion plays a non-negligible role in the dynamics.

Importantly, the relative magnitudes of electronic coupling V and reorganization energy, λ, can be used to distinguish between the two limiting transport regimes of both charge and exciton transport (though the nomenclature and theories developed to describe these two processes are somewhat different) [1, 27]. I refer to Figure 1.2 for a visual illustration of the different regimes. On the one hand, when $V << \lambda$, the hopping or incoherent regime is applicable, namely the local electron-phonon coupling is strong enough for the wavefunction to be localized on one molecule at a time. Notably, in this regime golden-rule rates theories are well defined [16]. On the other hand, when $V >> \lambda$, the wavefunction is completely delocalized over the system and its eigenstates completely delocalized. In

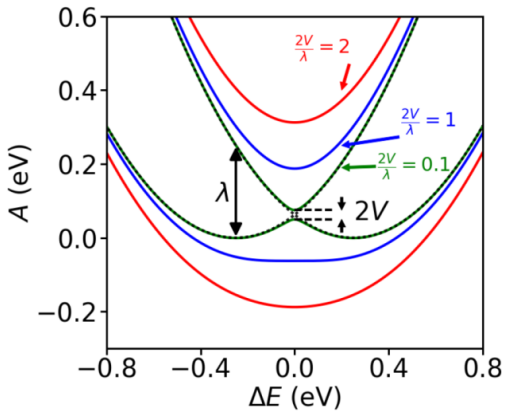

Figure 1.2: Adiabatic (coloured) and diabatic (black) free energy surfaces for electron transfer. The adiabatic surfaces, $A_{0,1}(\Delta E) = \frac{A_k(\Delta E)+A_l(\Delta E)}{2} \pm \frac{1}{2}\sqrt{\Delta E^2 + 4V^2}$, are plotted for three different values of the electronic coupling V for constant reorganization free energy λ of 250 meV. ΔE is the diabatic energy gap (or site energy difference) working as reaction coordinate for the electron transfer reaction. The diabatic free energy surface are written as two parabolas: $A_{k(l)}(\Delta E) = \frac{1}{4\lambda}(\Delta E \pm \lambda)^2$ valid for self-exchange reactions [32].

this regime Redfield theory [33] and band theory [15] have been respectively applied in the context of exciton and charge transport in various materials.

Another important factor to account for when studying electronic transport processes in nano-scale systems is the dimensionality of the problem. In fact, individual organic molecules forming the active layers of real OSs are often already quite large, and contain tens of atoms, if not more. Therefore any method such as density functional theory (DFT) which attempts to simulate a realistically large systems (at least a few thousand atoms, and possibly more to properly converge transport properties) will correspondingly be extremely slow [34]. As I will explain below, this observation along with the fact that standard theories are not always justified and applicable when it comes to technologically relevant high-mobility OSs, has triggered the need of developing new theories, such as the transient localization theory (see Section 1.3.3), and also alternative more powerful and efficient numerical propagation schemes that give insight into the actual electron-nuclear dynamics (see Section 1.4) [35–43], that may be then used to formulate more appropriate theories. The development/improvement of such a scheme will be a central topic of this work (see Chapter 2).

1.3 Standard and new theories for charge transport

I will summarize here some of the most important aspects of the so-called standard theories (i.e. hopping and band theories) and briefly discuss their regimes of validity as well as

the emergence of an alternative transport scenario for OSs. For the sake of brevity I will keep the discussion focussed only on the charge transport mechanism, which is an essential theme of this thesis. Nevertheless, I note that similar arguments would be applicable to the theories describing excitons and excitation energy transfer processes [1, 27].

1.3.1 Incoherent hopping mechanisms

One of the most common and still widely used approaches for the evaluation of the mobility is based on rates and related perturbative theories (the most well-known is the Marcus theory [44]). Some of the reasons for their fame are their simplicity and the possibility of a straightforward combination with kinetic Monte-Carlo schemes or Master equations approaches for the efficient solution of coupled kinetic equations and multiscale modelling [45, 46]. The common assumption of rate theories is the existence of a finite activation barrier $\Delta A^{\ddagger}$ for the electron transfer from an initial to a final states ($\Delta A^{\ddagger} = \lambda/4$ for self-exchange reactions), and that the charge must relax in the initial configuration before the transfer from one potential well to the other takes place. The violation of these condition makes the concept of rate constant undefined and inapplicable.

The common Marcus rate [44] reads:

$$k_{\mathrm{na}} = \frac{2\pi}{\hbar}|V|^2 \frac{1}{\sqrt{4\pi\lambda k_B T}} \exp\left(-\frac{\Delta A^{\ddagger}}{k_B T}\right) \tag{1.1}$$

where k_B is the Boltzmann constant and T the temperature. This equation assumes also that $V << \lambda$ (i.e. so-called non-adiabatic electron transfer (ET) regime) [32]. Other equivalent expressions exist for the intermediate and adiabatic ET, in which the latter assumption is relaxed and V becomes as large as $\approx \lambda/2$ [16, 32] (see Figure 1.2). A generalized semiclassical rate expression will be used in this work and it is presented in Appendix B.1.

I note at this point that using the harmonic approximation, if vibrations were treated quantum-mechanically, the zero-point energy would correspond to adding $\frac{1}{2}\hbar\omega$ (with ω a characteristic high-frequency mode) to the energy of the ground state. This further reduces the distance between the ground state minimum and the energy barrier. The zero point energy is typically in the order of $60-90$ meV for common organic crystals. Thus, it can be sometime larger than the energy barrier between the two energy minima (see Figure 1.1), making hopping rate undefined.

Notably, Troisi in Ref [47], only basing his analysis on experimental quantities and

elementary arguments, has shown that an incoherent hopping mechanisms is strictly valid and justified only when the room temperature mobility falls below 0.1 $cm^2\ V^{-1}\ s^{-1}$, thus ruling out Marcus and similar theories for describing high-mobility semiconductors.

1.3.2 Band transport and extended polaronic theories

In the band regime, $V >> \lambda$, the charge carrier delocalizes in a perfect molecular lattice to form a propagating Bloch wave with a well defined momentum k and energy dispersion $E(k)$ [12, 16]. This wave may be scattered by lattice vibrations or defects. In this picture the carriers diffuse quickly through the crystal and molecules do not have time to relax to accommodate the travelling charge. In OS solids where non-covalent interactions are present and thermal molecular motion is strong, e.g. at room temperature, there is a substantial electron scattering [12, 15]. Consequently, band transport theory breaks down due to the progressive loss of momentum conservation and because the mean-free-path of the travelling wave becomes smaller than intermolecular spacing a, i.e., below the Mott-Ioffe-Regel (MIR) limit.

Considering the semiclassical Drude expression as a starting point ($\mu = e\tau_s/m^*$, where τ_s is the time interval between two successive scattering events and m^* the effective mass of the carrier), Fratini et al. [15] evaluated the minimum mobility value at the MIR limit for a 1D OS lattice, under which band transport becomes undefined. In particular, by writing the effective mass $m^* = \hbar^2/2Va^2$ and imposing the equipartition principle to express the diffusion coefficient in terms of τ_s and m^*, Fratini et al. [15] wrote:

$$\mu_{\mathrm{MIR}} \approx \frac{ea^2}{\hbar}\sqrt{\frac{2V}{k_B T}}. \tag{1.2}$$

This means that taking $V \approx 150$ meV (i.e. within the range previously defined) at $T = 300$K and a lattice spacing of about 7 Å (as, e.g., in rubrene), gives a $\mu_{\mathrm{MIR}} \approx 27\ cm^2\ V^{-1}\ s^{-1}$. This value is already higher than the mobility of rubrene (about 15-20 $cm^2\ V^{-1}\ s^{-1}$), which is, to date, one of the highest mobility OS materials. At room temperature, therefore, band theory is unattainable for most OSs (though it may be still valid at lower temperature).

There are other successful approaches that reconcile the effects of electronic and nuclear motion in polaronic band theories [48]. In particular, these theories introduce the concept of "polarons", i.e. charge carriers and associated (phonon) deformations. Since the polaron is delocalized (and the system has translational symmetry), one can describe the

polaron states by a band and its propagation in a similar way as the propagation of a single carrier in a band. It is also possible to include both local and non-local electron-phonon couplings at the level of model Hamiltonians (Holstein-Peierl Hamiltonians) [13, 48–50].

These theories predict that, in response to an increase in electron-phonon couplings and scattering events, the charge carrier becomes increasingly more localized (higher effective m^*) as the temperature increases, leading to narrower bands at high temperature. The consequence of this effect is that the mobility decreases with increasing temperature following a power-law, $\mu \propto T^{-n}$ normally with $0.5 < n < 3$ (in agreement with experimental observations from time-of-flight (TOF) [10] and angle-resolved photoemission spectroscopy (ARPES) [51]). Thus, with polaronic theories, a band-like behaviour is recovered at low temperatures, while at high temperatures a more hopping-like behaviour is observed (because of the stronger lattice deformation). Already at room temperature though, polaronic theories suffer the same shortcomings as band theory, i.e., the mean-free-path becomes shorter than the lattice spacing and the mobility falls below the MIR limit [12].

1.3.3 An alternative scenario for organic semiconductors

The underlying assumption of both band and polaronic theories on the one hand, and hopping-like theories on the other, is that the states of the OS system "seen" by the travelling charge carrier are either delocalized states over the full OS solid (as in perfect crystal), or completely localized on a single site (as assumed by Marcus theory). However, as shown by Fratini et al. [15, 52] and anticipating what is found in Chapter 4 of this thesis, in OSs there is rather a coexistence between extended states and more localized states in different regions of the thermally accessible excitation spectrum. Delocalized states characterize the bulk of the spectrum, while localized states, which are formed as a results of thermal motion, are found in the tails. Thus, the charge carrier will be subject to a transient localization and delocalization scenario depending on whether it can thermally access localized or delocalized states. This view, that is in agreement with several experimental observations [19, 21–23, 53], has led Fratini and co-workers to develop a more "appropriate" theory to describe the charge transport in OSs, that is called transient localization theory (TLT) [15, 54–56].

This theory is based on the observation that OSs are disordered systems where the carrier can be transiently localized (i.e. it can assume a finite localization length) to some extent depending on its energy in the excitation spectrum and the degree of disorder induced by thermal vibrations [52]. On a longer timescale than a characteristic timescale τ,

the transiently localized charge carrier undergoes diffusive motion driven by the ripples of the molecular lattice. The model is thus able to reconcile the experimental observation of concomitant delocalized and localized transport signatures. The timescale τ is taken as the inverse of a characteristic vibrational mode frequency ω $(1/\tau)$ characterizing the timescale of the electronic coupling fluctuations (non-local electron-phonon couplings). Fratini et al. [15, 54–56] were able to formalize this picture by using the relaxation time approximation (RTA) and a suitably chosen disordered reference system from which the charge starts spreading. The transient localization theory assumes that the charge will diffuse, with diffusion coefficient $D_{\mathrm{RTA}} = L_\tau^2/2\tau$. Where the so-called transient localization length (L_τ^2) is the wavefunction spreading at time τ reached before the thermal disorder (in this case given by coupling fluctuations) sets back in.

The main result of TLT is that the mobility, obtained from the Einstein diffusion relation ($\mu_{\mathrm{TLT}} = eD_{\mathrm{RTA}}/k_BT$), is related to the transient localization length of the carrier wavefunction, L_τ^2, by

$$\mu_{\mathrm{TLT}} = \frac{eL_\tau^2}{2k_{\mathrm{B}}T\tau} \tag{1.3}$$

where e is the unit charge, k_{B} the Boltzmann constant and T the temperature. The transient localization length, L_τ^2, can be numerically found as described in the Appendix B.2. The theory predicts transient localization length and the mobility to decrease with increasing temperature due to stronger localization, result of increased thermal molecular disorder. It was successfully used to show that charge transport in the high mobility planes of typical single-crystalline OSs is enhanced if electronic couplings between the molecules within the plane are isotropic and are of specific sign combinations [15, 31, 54, 56, 57]. TLT has also recently been connected to the standard band transport description in the case of small disorder [58].

Yet, I note that TLT does not give information on how the charge carrier moves across the material in real time due to the assumptions of this theory with regards to the preconceived dynamics. Moreover, it is currently unclear how this theory is extended to the small polaron hopping regime where the mobility is no longer proportional to localization length [2]. Hence, although it is extremely useful to have analytic theories such as TLT, it is also important to develop numerical schemes that can track the actual dynamics of the wavefunction and seamlessly bridge the gap between different mechanistic regimes without restrictive model assumptions. With this purpose in mind, I will describe in the the next

section a set of mixed-quantum classical methods that have been developed and used to propagate coupled electron-nuclear motion in time.

1.4 Mixed quantum-classical methods

A complete understanding of electronic processes occurring in OSs and analytic models fully capable of capturing the physics of these processes is still missing. Arguably a direct propagation of the electron-nuclear dynamics is one of the most appealing approaches to study charge and exciton transport in OSs as it is, in principle, free of model assumptions and permits an "ab initio" view into transport mechanisms. As already mentioned though, the problem is that even using the most powerful supercomputers, it is not yet computationally feasible to perform full atomistic quantum dynamics of electronic processes occurring in systems formed by more than a dozen atoms, especially when these processes occur on a picoseconds or even longer time-scale. Molecular dynamics (MD) and the use of classical force fields (FF) have often been the methods of choice to perform large scale simulations [32, 59]. However, classical MD has two important limitations to be considered. The first is the assumption that the atomic motion can be described by classical mechanics (Newtonian equations of motion) and the second, which is possibly the most stringent in many cases, is that this motion takes place on a single potential energy surface (PES). The latter is also called Born-Oppenheimer (or adiabatic) approximation. There are a huge number of processes especially related to energy materials, including the ones that will be discussed in this thesis such as charge and energy transport, for which one or both these approximations are not valid [41, 60].

Mixed quantum-classical approaches (MQCD) have been developed to deal with these problems [35–41]. As the name suggests, the strategy is to select some degrees of freedom of the system to be treated quantum mechanically while keeping others at a classical level of description. Within such methods, normally all the nuclei in the system are treated classically and the electronic degrees of freedom are the ones dealt with quantum-mechanically by solving the time dependent Schrödinger equation (except when the physics of the problem requires to treat quantum mechanically some of the fast moving ions as well, like for example in proton transfer reactions [61]). In MQCD methods, the electron density of the system and therefore the electronic potential depends on the the position of the nuclei at a given time along the dynamics. Importantly, the nuclear motion, in turn, can be influenced by the potential change induced by the electronic motion (via quantum transitions

between PESs). Thus, the majority of MQCD methods can couple electron and nuclear motions treating both directions of the feedback, i.e. the classical subsystem influences the quantum subsystem, and also vice versa (see Figure 1.3). In this way MQCD goes beyond the standard Born-Oppenheimer approximation, that does not include the second direction of the response from the electronic degrees of freedom onto the nuclei. Nevertheless, the classical treatment of some or all nuclei of the systems in MQCD approaches remains an approximation compared to full quantum dynamics treatment (e.g. multiconfigurational time-dependent Hartree (MCTDH) [62] or the full ab-initio multiple spawning (FMS) [63]). Nevertheless, this approximation not only is necessary to study condensed phase systems but, as it will be clearer in the following, it is also very well justified by the physics of the problem in many cases [40, 41]. For example, when dealing with van der Waals bonded organic semiconductors the intermolecular nuclear vibrations are usually slow and low frequency, thus justifying their classical treatment (at least at room temperature).

In general, MQCD approaches are divided in two categories: mean-field (MF) dynamics (such as the Ehrenfest method) and surface hopping (SH) methods [35–37]. There are alternative methods which do not fit into neither of these two, such as the exact factorization approach published by Gross et al. [64], used to developed methods like the coupled-trajectory mixed quantum/classical (CT-MQC) approach [65, 66], or the quantum-classical Liouville method [67, 68] and Bohmian dynamics [69], just to mention a few. From the practical point of view, MQCD methods have received a huge amount of attention and have been applied in many different fields (mainly because of their simplicity and accuracy) [39, 70, 71]. Few, but significant, applications of both MF and surface hopping approaches regarding the investigation of charge and energy transport mechanisms (the main topics of this thesis) in molecular materials can be found [30, 72–77].

1.4.1 Mean-field Ehrenfest dynamics

In brief, when it comes to the feedback from the electronic (quantum) subsystem to the nuclei, the Ehrenfest approach evolves the nuclei on a mean-field potential energy surface which corresponds to a weighted average of the energy surfaces associated with each adiabatic electronic state of the system (see Figure 1.3). In practice, the weightings are given by the instantaneous quantum populations of the electronic states. There are important well-known shortcomings in this method, such as the lack of detailed balance [78, 79] (namely, the correct thermal Boltzmann population of the adiabatic states) and the failure in capturing

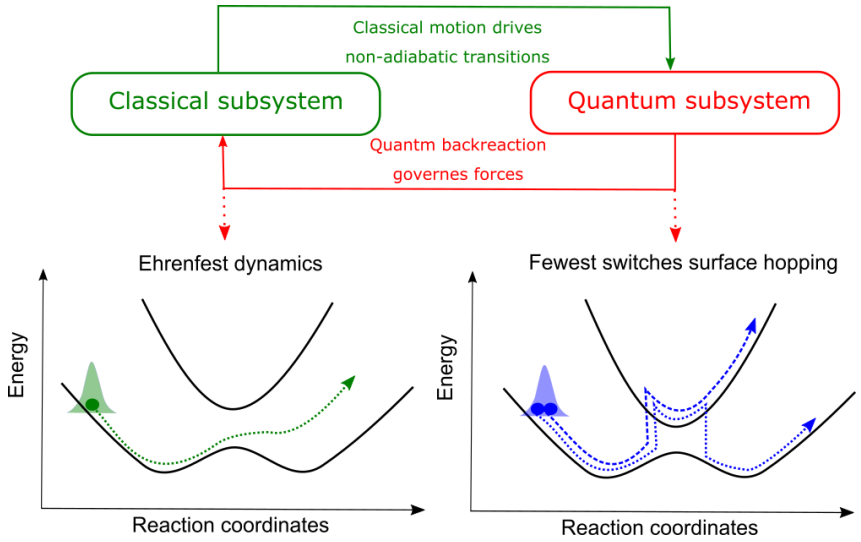

Figure 1.3: Illustration of two MQCD approaches: Ehrenfest method and fewest switches surface hopping (FSSH). In Ehrenfest the wavepacket moves on an average potential. In FSSH the wavepacket is represented by a swarm of classical trajectories that can switch potential energy surfaces.

the physical branching associated with diverging wave-packets on difference surfaces. As discussed below, this makes Ehrenfest method less accurate compared to surface hopping in many situations [35, 36, 80]. When considering charge transport in organic semiconductors, Wang and Beljonne, for example, have highlighted the superiority of surface hopping to account for charge localization and polaronic effects [72, 73]. In this thesis, I shall not discuss Ehrenfest method any further and I will focus the attention on the surface hopping approach. The latter will be the method of choice on which a novel fully atomistic and very efficient mixed quantum-classical method called fragment orbital-based surface hopping (FOB-SH) is based (see Chapter 2).

1.4.2 Fewest switches surface hopping

The (fewest switches) surface hopping (FSSH) algorithm was developed by John C. Tully [81]. With this algorithm, rather than constructing an average potential energy surface like in the Ehrenfest approach, the wavefunction of the system is constructed by considering all its possible quantum states. The nuclei evolve according to Newton's law on single PES and non-adiabatic effects, namely the feedback from the electrons on to the nuclei, are included by allowing instantaneous hops from one adiabatic surface to another (see Figure 1.3). These hops occur stochastically. In the common fewest switches version of surface hopping [81], the probability to hop is proportional to the variation of the relative populations of the electronic states obtained solving the time dependent Schrödinger

equation (TDSE) (see Section 2.1.5). Along a single surface hopping trajectory, the nuclei switch between potential energy surfaces multiple times in proximity of regions with high non-adiabatic coupling (i.e. the coupling between different electronic states of the system). I refer to Figure 1.3 for a graphical representation of this method.

The idea of a sudden state switch of a single trajectory can appear a severe approximation of the smooth quantum mechanical transition between two electronic PESs, but the Tully's algorithm relies on a swarm of trajectories to correctly describe the dynamics of the wavepacket. In this way, even if a single trajectory makes a sudden switch, the overall transition is represented by a gradual flow of trajectories changing electronic state and possibly branching in proximity of avoided state crossing regions, effectively reproducing the dynamics of a quantum wavepacket. Importantly, once a surface hop is assigned, energy conservation needs to be taken into account. If the classical kinetic energy is enough to afford the energy cost of the quantum transition, the nuclei switch simultaneously to the new PES. The nuclear positions are kept unchanged and the nuclear velocities are adjusted to conserve total energy (see Section 2.1.5 and Section 2.2.1). On the other hand, if the system does not have enough energy to "hop" to the new PES (i.e. rejected hop or frustrated hop) the dynamics continues to the current active PES. Practically, if a single trajectory can conserve energy, the entire swarm will fulfil this requirement. It is worth noting that, the energy conservation procedure and the presence of frustrated hops make surface hopping capable of approximately reproducing the Boltzmann distribution of the quantum states (i.e. the detailed balance), which is important for an accurate description of equilibrium and thermodynamic properties [79, 82] as well as for transport properties [83–86] (e.g., charge carrier mobility and wavefunction delocalization) as it will become more clear in Section 2.2 of this thesis. In contrast to this, as mentioned before, the mean field approximation lacks these important features [79, 80].

Last but not least, provided that the so-called decoherence correction (DC) is included, surface hopping probabilities obey approximately internal consistency [87], which means that the portion of trajectories on a given state at any time equals the corresponding quantum population obtained by the TDSE (see Section 2.2.2).

1.5 Scope and structure of this thesis

As seen in the Introduction, although there are several lines of evidence that weak van der Waals interactions between the molecules of OSs give rise to slow molecular motions that

impact charge carrier mobility and exciton diffusion [2, 12, 15, 88], it is currently debated and poorly understood how this (dynamical) disorder and thermal vibrations actually affect the underlying dynamics of free carriers and excitons. It is also unclear how to best explain the intermediate transport scenario that was seen as in "between" the well-established band and hopping limits and interpreted as a coexistence regime of localized and delocalized carriers by experiments [19, 21–23, 53].

The goal of this thesis is to shed light on the interplay between nuclear and electronic motion in OSs and to provide a better understanding about the influence of this complex dynamics on charge and exciton transport mechanisms. The aim is to go beyond common limiting approximations of analytic theories and also reduced dimensionality of first principle quantum schemes, in terms of model coarse-graining and number of degrees of freedom. This has been done by means of further developing, improving and applying a novel fully atomistic non-adiabatic molecular dynamics approach, called fragment orbital-based surface hopping (FOB-SH) [42], which allows to propagate the electron-nuclear motion in real time for large nano-scale systems.

In Chapter 2, I report the main working equations and give an overview of the FOB-SH method (with particular focus on the charge transport process) and I will discuss its advantages compared to other methods. I will present the implementation of important algorithms already available in the literature (e.g. the decoherence correction), as well as new ones conceived by myself, specifically tailored to tackle issues arising from the simulation of large systems with a high density of states (e.g. the trivial crossings problem and the spurious long-range wavefunction transfer). Important properties, that any surface hopping scheme should fulfil for a reliable and accurate dynamics, such as energy conservation, detailed balance and internal consistency as well as fundamental quantities such as mobility and wavefunction delocalization will be presented and discussed.

In Chapter 3, I will present the validation of the improved FOB-SH approach and discuss its accuracy when considering both thermodynamic equilibrium properties as well as transport properties for two different class of systems (i.e., atomistic OS models and real OS systems). After testing various parameters and algorithmic improvements for a broad range of transport regimes (going from localized to delocalized transport), I will devise in this Chapter the best FOB-SH set-up for accurate dynamics with regards to energy conservation, detailed balance and internal consistency. I will also discuss the correct way to

evaluate important electronic and transport properties such as electronic populations, mean squared displacement of the wavefunction and mobility from surface hopping dynamics.

Chapter 4 will be devoted to the study of charge carrier transport at room temperature in experimentally well-characterized organic semiconducting crystals. I will benchmark FOB-SH carrier mobilities against experiments and extract the full 2D mobility tensor for systems with more than a thousand molecules. I will also compare the computed FOB-SH mobilities with other theories, including the newly proposed transient localization theory. This Chapter will give new important insights about unique and fascinating phenomena intimately related to the molecular nature of OSs, such as the quantum localization and delocalization steps that charge carriers undergo during their dynamics in OSs. Design rules to further improve OS devices performance will be discussed as well.

In Chapter 5, I will tackle another long-debated topic in the charge transport realm, namely the temperature dependence of the charge mobility. The different trends that mobility exhibits with increasing or decreasing temperature are often taken as a signature to distinguish between hopping and band-like transport. I will analyse the dichotomy between these two regimes as a function of temperature and describe the crossover between the two from the perspective of the non-perturbative FOB-SH approach. I will also show the comparison between the mobility temperature dependence of FOB-SH and experiments and discuss some limitations of FOB-SH when simulating low temperature mobilities.

In Chapter 6, I will present an extension of the FOB-SH Hamiltonian and its implementation to treat Frenkel exciton diffusion in OSs. I will discuss and validate few approximate (yet efficient) ways for computing excitonic couplings against reliable electronic structure calculations. I will also present the comparison between calculated diffusion length with other computational schemes as well as experimental estimates. This work will constitute an additional step towards the development of an extended Hamiltonian to study exciton separation and recombination processes occurring in organic photovoltaic cells.

Finally, I will conclude the work in Chapter 7. In light of the results obtained, I will argue that FOB-SH shows promise for future investigations into charge transport and other electronic processes occurring in organic semiconductors. I will also outline ongoing projects and how I believe the method may be extended and used in future works to help advancing the field of optoelectronics.

Chapter 2

Non-adiabatic molecular dynamics in atomistic nano-scale systems

Explicit coupled electron-nuclear propagation schemes are expected to play a prominent role in describing of the complex interplay between nuclear and electron motion within the dense manifold of electronic states characterizing nano-scale organic materials, with important applications in molecular electronics, solar harvesting and power conversion. As seen in the Introduction, fascinating quantum localization and delocalization phenomena affect travelling particles and the processes of charge (electron and hole) transport, exciton (bound electron-hole pair) transport and exciton separation are the key to rationally design new materials and improve their properties.

To obtain insights into these processes at the atomic level, it is important to use methodologies that (i) can account for multiple electronic states and transitions between them, (ii) can describe the coupling and the interplay between electronic and nuclear degrees of freedom (i.e. electron-phonon couplings) and (iii) can give a real-time dependent picture of the dynamics. It is however very challenging to develop accurate methodologies that can meet all these criteria and that allow large scale simulations at the same time. To this end, I have improved and further developed a novel fully atomistic non-adiabatic molecular dynamics approach, called fragment orbital-based surface hopping (FOB-SH) previously devised in our group [42] and based on the original Tully's fewest switches surface hopping (FSSH). In this regard, the main FOB-SH equations previously implemented by Dr. Jacob Spencer and Dr. Antoine Carof [42, 82] are presented in Section 2.1. I have subsequently refined and made important improvements to this original algorithm as detailed in Section 2.2 and made substantial advances in the efficiency of the code (see, e.g., Section 2.1.7) in order to treat realistic systems [43, 84–86]. I also extended the FOB-SH formalism and code to treat exciton diffusion, which will be the main theme of Chapter 6. I will argue that FOB-SH is now a very good method to effectively meet objectives (i)-(iii). To keep the presentation not too cumbersome with regard to technical details, I shall refer to our recent publications [42, 43, 82–86, 89] for some more technical aspects and derivations.

2.1 Fragment orbital-based surface hopping (FOB-SH)

The FOB-SH code is tailored to propagate the wavefunction in condensed phase systems without assuming any prior transport model, thus bridging the regime where standard analytic models, i.e. hopping or band transport theories, are less justified or invalid. The FOB-SH methodology rests on a DFT parametrized tight-binding representation of the electronic Hamiltonian (updated on-the-fly along the molecular dynamics) to naturally incorporate local and non-local electron-phonon couplings and their fluctuations (see Section 2.1.2). This Hamiltonian constitutes the main difference compared to other FSSH approaches present in the literature [39, 41, 70, 71, 90]. The latter are usually based, on the one hand, on electronic structure methods performed at each step along the dynamics to retrieve energies and forces (e.g. by time dependent density functional theory (TDDFT) or post-Hartree-Fock methods) [39, 60, 90] and, on the other, on model Hamiltonians [30, 40, 73, 74, 81] that give a coarse grained representation of the system (as opposed to FOB-SH where the full atomistic representation of the system is used).

A cornerstone of the FOB-SH is an efficient computation of the electronic Hamiltonian and the forces acting on the atoms of the system, evaluated by using a combination of parametrized force fields and approximate electronic interactions between the different molecular sites (for the off-diagonal elements of the Hamiltonian) as discussed in Section 2.1.2 (for charge transport) and Section 6.1.1 (for exciton transport). This allows to simulate electronic transport in large and realistic nano-scale systems (up to few thousand molecules), thereby providing unprecedented insights into the actual dynamics and the time propagation of the wavefunction in these systems. A flowchart of the algorithm can be found in Figure 2.1.

2.1.1 Electronic propagation in a site basis representation

The FOB-SH approach for charge (exciton) transport relies on the notion of an excess charge carrier (exciton) moving in an effective, time-dependent potential due to the other electrons and the nuclei. The complicated many-body or multi-determinantal electron dynamics can be effectively described by a one-particle wavefunction for this excess charge (or a localized exciton as we will see in Chapter 6). The interactions with the effective potential are then included through parametrization of the electronic Hamiltonian.

Focussing for the moment on charge carrier transport, in organic π-conjugated molecular crystals, hole transport occurs in the highest valence band state and electron transport

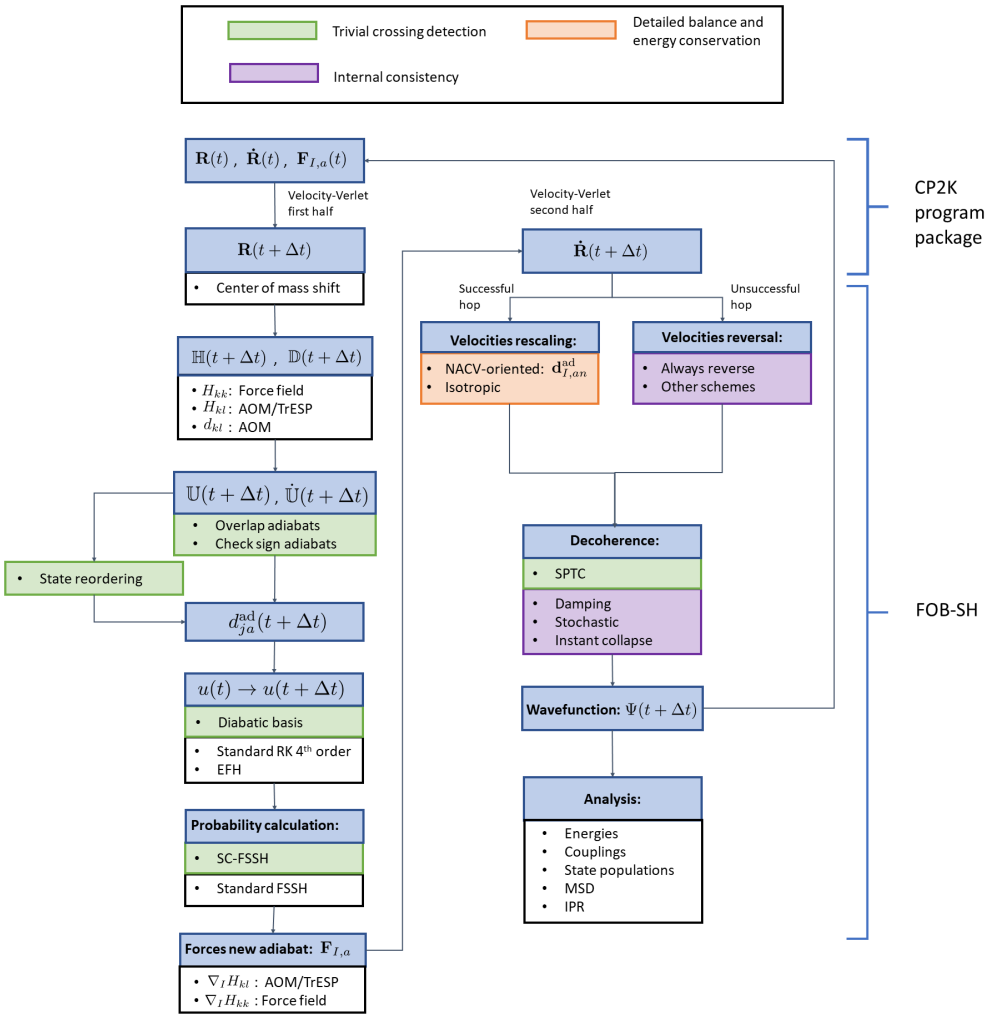

Figure 2.1: Scheme of the fragment orbital-based surface hopping (FOB-SH) algorithm. Different colors represent improvements of the algorithm necessary to fulfil: trivial crossings detection, detailed balance and energy conservation and internal consistency (see Section 2.2). The code is implemented in an in-house version of CP2K program package [91]. Symbols are defined according to equations in the text. RK: Runge-Kutta algorithm, EFH: Elimination of forbidden hops (for a discussion on this algorithm I refer to Ref. [83]), AOM: Analytic overlap method for charge transfer couplings (Section 2.1.4), TrESP: Transition electrostatic potential charges for exciton transfer couplings (Section 6.2), SC-FSSH: self-consistent surface hopping, FSSH: fewest switches surface hopping, NACV: non-adiabatic coupling vectors, SCTC: Spurious charge transfer correction, MSD: mean squared displacement (Eq. 2.33), IPR: inverse participation ratio (Eq. 2.38).

in the lowest conduction band state. Since the interaction between molecules in organic crystals is weak (typically in the order of $10-200$ meV) as opposed to conventional inorganic semiconductors, the electronic structure of typical OSs exhibits narrow bands across the entire Brillouin zone and a minimal band dispersion. Hence, the highest valence band or lowest conduction band states of these materials can approximated by a combination of the highest occupied (HOMOs) or lowest unoccupied molecular orbitals (LUMOs) of the isolated molecules, respectively, as observed in Ref. [12, 31, 56] as well. Therefore, a natural way of constructing the charge carrier wavefunction $\Psi(t)$ is to use a set of molecular orbitals as suitable basis ($\{\varphi_m\}$). Considering one orbital per molecular site already provides a very accurate description of the electronic band structure of the material [12, 31, 56]. Nevertheless, The accuracy of this tight-binding description will be further investigated in Chapter 4 for real OSs. I note that, more orbitals could be added in the case of (quasi-) degeneracy. The extension of this picture to excitons will be discussed in Chapter 6.

Depending on whether the excess hole or excess electron transport is taken into consideration, the charge carrier wavefunction $\Psi(t)$ can be expanded in the localized basis set formed by the HOMOs or LUMOs of each molecule of the system, respectively. $\Psi(t)$ takes the form:

$$\Psi(t) = \sum_{m=1}^{M} u'_m(t)\varphi_m(\mathbf{R}(t)) \tag{2.1}$$

where $\mathbf{R}$ is the $3N$ vector of nuclear positions and M is the number of fragment orbitals mediating the charge transfer at a given time t. This non-orthogonal set of orbitals is directly available by a single calculation of an isolated molecule prior the simulation in a parametrization step (see Section 2.1.4). As it will become clearer in Section 2.1.8, employing a charge localized state basis to represent the wavefunction and propagate the dynamics has few other advantages as well (e.g. a greater stability and accuracy for the integration of the time dependent Schrödinger equation). Since several transformations between different bases will be required in the FOB-SH formalism, I summarize the notation I use for the different representations in Table 2.1.

To facilitate the forthcoming propagation equations, Löwdin orthogonalization of the

Table 2.1: Notation used in the three different representations of the carrier wavefunction. NACE stands for non- adiabatic coupling elements and NACV for non-adiabatic coupling vectors. Note, the diabatic representation is not strictly diabatic in the sense that the NACE vanishes; hence, it should in fact be considered as quasi-diabatic.

Represen.	Indices	Basis functions	Expansion coefficients	Electronic Hamiltonian	NACE	NACV
Non-orthogonal diabatic	m,k,l	φ_l	u'_l	$H'_{kl} \equiv [\mathbb{H}']_{kl}$	$d'_{kl} \equiv [\mathbb{D}']_{kl}$	$\mathbf{d}'_{I,kl}$
Orthogonal diabatic	k,l	ϕ_l	u_l	$H_{kl} \equiv [\mathbb{H}]_{kl}$	$d_{kl} \equiv [\mathbb{D}]_{kl}$	$\mathbf{d}_{I,kl}$
Adiabatic	i,j,a,n	ψ_j	c_j	E_j	d^{ad}_{ij}	$\mathbf{d}^{\mathrm{ad}}_{I,ij}$

basis set $\{\varphi_m\}$ is applied to define the orthogonal localized basis set $\{\phi_l\}$,

$$\phi_l = \sum_{m=1}^{M} T_{ml}\varphi_m \tag{2.2}$$

where $T_{ml} = \left[\mathbb{S}^{-1/2}\right]_{ml}$, with $\mathbb{S}$ the overlap matrix of the fragment orbital basis set ($\bar{S}_{ml} = [\mathbb{S}]_{ml} = \langle\varphi_m|\varphi_l\rangle$). The excess charge wavefunction is now:

$$\Psi(t) = \sum_{l=1}^{M} u_l(t)\phi_l(\mathbf{R}(t)). \tag{2.3}$$

Inserting Eq. 2.3 into the time-dependent Schrödinger equation, one can write the electronic equation of motion as,

$$i\hbar\dot{u}_k(t) = \sum_{l=1}^{M} u_l(t)\left(H_{kl}(\mathbf{R}(t)) - i\hbar d_{kl}(\mathbf{R}(t))\right) \tag{2.4}$$

where $H_{kl} \equiv [\mathbb{H}]_{kl} = \langle\phi_k|H|\phi_l\rangle$, with H the electronic Hamiltonian and $d_{kl} \equiv [\mathbb{D}]_{kl} = \left\langle\phi_k|\frac{d\phi_l}{dt}\right\rangle$ are the non-adiabatic coupling elements (NACEs) of the localized orthogonal basis set. As those NACEs are generally close to zero (see Section 2.1.7), I label the orthogonal localized basis as diabatic basis (see Table 2.1). I will discuss in-depth the construction of the Hamiltonian in Section 2.1.2 and the calculation of the d_{kl} terms in Section 2.1.4.

From an algorithmic point of view, H_{kl} and d_{kl} terms can be calculated at t and then at $t+\Delta t$ when the nuclear positions have been updated by the first half of the velocity-Verlet algorithm (see Figure 2.1). The expansion coefficients of the charge carrier wavefunction in the diabatic basis, u_k, are propagated according to Eq. 2.4 from time t to $t+\Delta t$ in N steps of length δt using the fourth-order Runge-Kutta algorithm. At each electronic integration

time step m, the H_{kl} and d_{kl} elements are linearly interpolated between t and $t+\Delta t$, $H_{kl}(t+m\delta t) = H_{kl}(t) + [H_{kl}(t+\Delta t) - H_{kl}(t)](m\delta t/\Delta t)$ for $m = 1, ..., (\Delta t/\delta t)$, and similarly for d_{kl}.

2.1.2 Tight-binding Hamiltonian for charge transport

Considering the transport of charge carriers, as discussed in Section 2.1.1, the valence (or conduction) band of OSs can be described by a tight-binding representation. The Hamiltonian matrix elements in Eq. 2.4 are given by,

$$H = \sum_{k}^{M} \varepsilon_k |\phi_k\rangle\langle\phi_k| + \sum_{k}^{M}\sum_{l\neq k}^{M} H_{kl}|\phi_k\rangle\langle\phi_l| \tag{2.5}$$

where, $\phi_k = \phi_k(\mathbf{R}(t))$ is the orthogonalized HOMO (LUMO) of molecule k for hole (electron) transport, $\mathbf{R}(t)$ are the time-dependent nuclear coordinates, $\varepsilon_k = H_{kk}(\mathbf{R}(t))$ is the site energy, that is, the potential energy of the state with the hole (excess electron) located at site k and $H_{kl} = H_{kl}(\mathbf{R}(t))$ is the electronic coupling between ϕ_k and ϕ_l. All Hamiltonian matrix elements, i.e. site energies and couplings, depend on the nuclear coordinates which, in turn, depend on time, $\mathbf{R} = \mathbf{R}(t)$ as determined by the nuclear dynamics (i.e. the first direction of the feedback from nuclear to electronic motion as discussed in Section 1.4). Note also that an analogue expression for Hamiltonian will be given in Section 6.1.1 in the case of exciton transport.

As mentioned before, to carry out simulations on large systems and long time scales, a parametrized approach to determine the electronic Hamiltonian was designed in Ref. [42], thus avoiding explicit expensive electronic structure calculations. The diagonal elements $H_{kk} = \langle\phi_k|H|\phi_k\rangle$, that correspond to the energy of a charge localized on molecule k, are calculated *via* a classical force field where the molecule k is charged and all the other $M-1$ molecules are neutral. The off-diagonal elements $H_{kl} = \langle\phi_k|H|\phi_l\rangle$, that corresponds to the electronic coupling matrix elements or transfer integrals, are calculated using a recently developed analytic overlap method (AOM) [92]. I shall describe both the classical force field parametrization for the diagonal elements and the AOM method in the Section 2.1.3 and 2.1.4, respectively. It is worth to note the analogy between the calculation of the FOB-SH electronic Hamiltonian and the empirical valence bond approach of Warshel and co-workers [93], where electronic Hamiltonian is also built from classical force fields for the diagonal elements and different parametrization for the off-diagonal elements. As mentioned before, this tight-binding Hamiltonian is a key feature of FOB-SH method that

allows fast computation and I will validate its accuracy for several organic semiconducting systems in Section 4.1.3.

2.1.3 Site energies and force field parametrization

In the case of charge transport (hole or electron) each molecule of the simulated systems can exist in two charge states: neutral and charged. Throughout this thesis, the intra- and inter-molecular interaction terms for the neutral state are taken from the Generalized Amber Force Field (GAFF) [94] and the parametrization for the charge state of the investigated systems will follow the present protocol, unless stated otherwise. For the charged state, the equilibrium bond lengths of the molecule are displaced with respect to the neutral state so that the reorganization energy λ obtained from the force field is equal to the value obtained from DFT calculations,

$$\lambda = [E_C(\mathbf{R}_N) + E_N(\mathbf{R}_C)] - [E_C(\mathbf{R}_C) + E_N(\mathbf{R}_N)] \tag{2.6}$$

where $E_{C(N)}(\mathbf{R}_{N(C)})$ is the energy of the charged (neutral) molecule in the optimized neutral (charged) state and $E_{C(N)}(\mathbf{R}_{C(N)})$ is the energy of charged (neutral) molecule in the optimized charged (neutral) minimum. The geometry of charged and neutral molecules are optimized with the B3LYP functional and the 6-311g(d) basis set using the Gaussian program [95]. Hybrid functionals are known to give good equilibrium structures and better energies for bond stretching than GGA functionals, which is important for the calculation of reorganization energies [96, 97]. Taking anthracene as an example of a common organic semiconducting crystal [98], I obtain similar values for two of the most popular hybrid functionals, $\lambda = 142.1$ meV for B3LYP and 149.9 meV for PBE0, but a smaller value for the GGA functional BLYP, 102.4 meV, due to the well known deficiency of the latter functional to underestimate the energy for bond stretching. The results are usually robust with respect to the basis set choice. Only very small changes in λ are obtained as the basis set is increased: 138.1, 142.1 and 138.5 meV for the 6-31G(d), 6-311G(d) and 6-311G+(d,p) basis sets, respectively, using the B3LYP functional.

The force field equilibrium bond lengths of the charged state, $\mathbf{R}_{C,k}$, is adjusted by scaling the DFT displacements, $\Delta\mathbf{R}_k^{\mathrm{DFT}}$, namely: $\mathbf{R}_{C,k} = \mathbf{R}_{N,k} + \beta\Delta\mathbf{R}_k^{\mathrm{DFT}}$, until force field and DFT reorganization energies (Eq. 2.6) match. When the scaling constant β is close to unity this means that the displacements in the force field and in DFT are almost identical.

All other intra- and inter-molecular parameters were chosen to be the same as for the neutral state. In Section 4.1.1, I report the parametrized force field for different organic molecules that will be considered in this work.

The site energies H_{kk} of the Hamiltonian (first term on the RHS of Eq. 2.5) and their nuclear gradients $\nabla_I H_{kk}$ are obtained by assigning molecule k the force field parameters for the charged state and all other molecules $l \neq k$ the parameters for the neutral state.

2.1.4 Fast analytic overlap method for charge transfer couplings

The off-diagonal elements $H_{kl} = \langle \phi_k | H | \phi_l \rangle$, that correspond to the electronic coupling matrix elements, are calculated using the recently developed analytic overlap method (AOM) [92]. The AOM relies on two assumptions: (i) a linear relationship between off-diagonal H_{kl} and the overlap $\bar{S}_{kl}$ (overlap between the projected (non-orthogonal) fragment orbitals into Slater-type functions, $\bar{S}_{kl} = \langle \varphi_k | \varphi_l \rangle$) and (ii) an analytical expression to calculate $\bar{S}_{kl}$ (see below). The AOM coupling is written as:

$$H_{kl} = C\bar{S}_{kl} \tag{2.7}$$

C is a fitting parameter and can be obtained by correlating the overlap $\bar{S}_{kl}$ against DFT calculations, e.g. scaled fragment orbital density functional theory (sFODFT) [99–101] as done in Refs. [85, 89, 92], or wavefunction based methods [102, 103]. AOM allows the calculation of H_{kl} for a cost several orders of magnitude lower than explicit electronic structure calculations [92].

In the first step of the parametrization of AOM couplings, the (non-orthogonal) molecular frontier orbital, φ_k (Table 2.1), is obtained by DFT calculation on an isolated molecule (HOMO is used for hole transfer and LUMO for electron transfer). This orbital is then projected on a minimum Slater basis of p orbitals with optimized Slater decay coefficients as proposed in Ref. [92]. Since $\pi-$conjugated systems are the main focus of this work (and they have hybridization sp^2), the p^j orbitals of each atom, with $j = x, y, z$, are projected onto a locally defined ($p_{\sigma 1}$, $p_{\sigma 2}$, p_π) atomic basis set. The $p_{\pi,i}$ direction is determined by the nearest neighbours of the i atom on which it is centred. In the case of sp^2 carbons, this means three connected atoms. These three neighbours determine a plane and the normal vector of this plane is chosen to be the $p_{\pi,i}$ direction. When heteroatoms participate in the delocalised π systems, the plane is determined by the two neighbouring atoms and the het-

eroatom itself instead. Importantly, when AOM is combined with FOB-SH, the orientation of these orbitals is updated after each nuclear time step (following the intramolecular motion) so that $p_{\pi,i}$ remains orthogonal to its plane. Hence, the atomic orbitals comprising the molecular orbital follow the motion of the atoms and are expanded as:

$$\varphi_k = \sum_{i \in k}^{atoms} c_{p\pi,i} p_{\pi,i} \tag{2.8}$$

where i runs over all $\pi-$conjugated atoms in molecule k and $p_{\pi,i}$ is the Slater type orbital p on atom i, $c_{p\pi,i}$ is the corresponding (normalized) expansion coefficient obtained by projection of the DFT molecular frontier orbital (completeness of projection should be close to 1 to have an accurate orbital representation). In the current AOM version the projection coefficient are calculated once, for the minimum energy structure of molecule k in vacuum and, in contrast to the orientation of $p_{\pi,i}$, they do not change along dynamics. In this minimum Slater basis the overlap between the (non-orthogonal) HOMO (LUMO) orbitals (φ_k, φ_l) of two monomers forming a dimer, $\bar{S}_{kl}$, is calculated analytically and is very fast due to the small number of basis functions involved:

$$\bar{S}_{kl} = \langle \varphi_k | \varphi_l \rangle = \sum_{i}^{atoms} \sum_{j}^{atoms} c_{p\pi,i} c_{p\pi,j} \langle p_{\pi,i} | p_{\pi,j} \rangle. \tag{2.9}$$

The overlap $\langle p_{\pi,i} | p_{\pi,j} \rangle$ can be calculated extremely efficiently using the analytic formulas provided by Mulliken [104]. I refer to the original publication [92] for an even more detailed description of the AOM method.

The second step in the AOM procedure involves the calculation of electronic couplings to use as a reference for the parametrization of C on a set of molecular dimer geometries (taken in this work from MD). Since AOM couplings are parametrized for several snapshots along a MD trajectory, the parametrization of C actually takes into consideration different configurations that the interacting pairs of molecules assume during the dynamics. In this thesis, I obtained the reference couplings from scaled FODFT calculations [99–103] (I will discuss the electronic structure in more detail in Section 3.1.2 when considering the parametrization of anthracene crystal). In brief, the FODFT calculations are carried out with the CPMD program package [105] using the PBE exchange correlation functional. Core electrons are described by Troullier-Martins pseudo potentials and the valence electron states are expanded in plane waves with a reciprocal space plane wave cutoff of 90

Ry (see Section 3.1.2). The accuracy of FODFT couplings was benchmarked before on the HAB11 [102] and HAB7- databases [103] for electronic couplings for hole and electron transfer in π-conjugated organic dimers. While the mean relative unsigned error with respect to high-level ab-initio reference values was found to be reasonably small (37.6% [102] and 27.9% [103]), the values were slightly but uniformly underestimated. Hence, it was recommended in the previous studies to scale the FODFT couplings for hole and electron transfer systems by a factor of 1.348 and 1.325 to obtain best estimates. I report a comparison between the scaled FODFT (sFODFT) couplings for a set of organic crystals that will be studied in this work and literature values found with other computational methods in Table A.1.

Importantly, good linear correlation between $\bar{S}_{kl}$ from Eq. 2.7 and H_{kl} from sFODFT was found for several different organic molecules and HAB7- databases [92, 103] allowing the fitting of a simple linear function as in Eq. 2.7 , $|H_{kl}| = C|\bar{S}_{kl}|$, and C is a constant of proportion. AOM couplings were also tested against approximate coupled cluster (SCS-CC2)/Generalized Mulliken Hush calculations [103]. It was found that errors are less than 29%, translating in an error in the non-adiabatic electron transfer rate of a factor of 1.7. When I applied AOM to relevant organic crystals studied in this thesis (e.g., as reported in Chapter 4), the fits of the scaling factor C was done either by minimization of residuals of $\log(H_{kl})$ to weight the error of couplings over all orders of magnitude uniformly (giving $C = C_{\log}$), or by minimization of residuals of H_{kl} to weight more strongly the error of the largest couplings (giving $C = C_{\text{lin}}$). I report these fitting results in Appendix A.1. For the systems analysed in this work both methods give very similar results with mean relative unsigned errors (considering all coupling pairs) of 36 % ($C_{\log}$) and 44 % (C_{lin}) for AOM couplings with respect to sFODFT couplings. This error is not insignificant though it translates into only a relatively small error in the non-adiabatic electron transfer rates of about a factor 1.8 and 2.0, respectively. Hence, AOM offers a good compromise between accuracy and efficiency (note that billions of electronic coupling matrix elements need to be computed for a single mobility calculation, as I will present Chapter 4, thereby the need of an ultrafast parametrized method).

When using AOM within FOB-SH, each MD time step the HOMO (LUMO) on each molecule is updated and H_{kl} between molecular pairs is estimated from $\bar{S}_{kl}$ via the above linear relationship. Possible shortcomings of AOM arise from the fact that, although atomic

orbitals comprising the HOMO (LUMO) follow the motion of the atoms during the dynamics, the expansion coefficients in Eq. 2.9 are otherwise frozen. However, some checks [92] indicated that this is a very good approximation, especially for rigid molecules, where orbitals are stable against intermolecular vibrations. To improve reconstruction of the orbitals along the dynamics, for example for flexible molecules, AOM could be supplemented with more sophisticated interpolation schemes (e.g. machine-learning techniques), nowadays used to develop a new generation of force fields.

AOM allows also an efficient calculation of the nuclear derivatives $\nabla_I H_{kl} = C\nabla_I \bar{S}_{kl}$ and the orthogonal NACE d_{kl} in Eq. 2.4. These quantities are obtained from finite differences of the overlap Eq. 2.9 with respect to nuclear displacements and time increments, respectively [42]. In particular, the latter orthogonal NACEs d_{kl} in Eq. 2.4 can be related to the non-orthogonal NACEs ($d'_{kl} \equiv [\mathbb{D}']_{kl} = \langle \varphi_k | \dot{\varphi}_l \rangle$) by,

$$d_{kl} = \left[\mathbb{T}^\dagger \mathbb{D}' \mathbb{T}\right]_{kl} + \left[\mathbb{T}^\dagger \mathbb{S} \dot{\mathbb{T}}\right]_{kl} . \tag{2.10}$$

Both $\mathbb{D}'$ and $\dot{\mathbb{T}}$ are obtained from finite difference between t and $t + \Delta t$ (note that $\mathbb{T} = \mathbb{S}^{-1/2}$, where $[\mathbb{S}]_{kl} \equiv \bar{S}_{kl} = \langle \varphi_k | \varphi_l \rangle$). For a more technical details regarding the actual finite difference implementation I refer to Ref. [42]. If Eq. 2.10 allows to calculate the d_{kl} terms and to integrate exactly Eq. 2.4, I will point out in Section 2.1.7 that neglecting them gives essentially the same dynamic but for much smaller simulation cost.

2.1.5 Non-adiabatic transitions

When the electronic propagation is completed from t to $t + \Delta t$, the nuclear velocities need to be consistently evaluated according to the new electronic potential energy and related forces. As mentioned in Section 1.4.2, the core of any method based on FSSH is the choice of the active adiabatic potential energy surface E_a on which the nuclei evolve and the inclusion of the feedback from the electronic dynamics onto the nuclear motion (see also Figure 1.3).

The energy of the active PES a is calculated as $E_a = \left[\mathbb{H}^{\text{ad}}\right]_{aa}$, with $\mathbb{H}^{\text{ad}} = \mathbb{U}^\dagger \mathbb{H} \mathbb{U}$ and $\mathbb{U}$ the unitary transformation matrix that diagonalizes $\mathbb{H}$ in the diabatic representation to $\mathbb{H}^{\text{ad}}$ in the adiabatic representation (eigenvectors basis).

In Tully's approach [81], the active surface is decided in two steps: (i) a new state is chosen *via* a stochastic process and (ii) the energy conservation requirement is applied to determine whether the change of active state is energetically possible. The stochastic

process (i) is based on the hopping probabilities calculated at each time step t between the active surface, a, and all the other states j:

$$g_{ja} = \max\left[0, -\frac{2\mathrm{Re}(c_j^* c_a d_{ja}^{\mathrm{ad}})}{|c_a|^2}\Delta t\right] \tag{2.11}$$

where $d_{ja}^{\mathrm{ad}} = \left\langle \psi_j | \frac{d\psi_a}{dt} \right\rangle = \left\langle \psi_j | \dot{\psi}_a \right\rangle$ are the NACEs in the adiabatic basis (see Table 2.1). The higher the NACE values, the more probable the non-adiabatic transition from the active PES to a new one. One can write any adiabatic state j of the system, ψ_j, in terms of the localized basis (see Table 2.1) as

$$\psi_j = \sum_{k=1}^{M} U_{kj}\phi_k. \tag{2.12}$$

In this way the adiabatic NACEs are calculated (in FOB-SH) from the NACEs in the diabatic basis ($d_{kl} \equiv [\mathbb{D}]_{kl} = \left\langle \phi_k | \dot{\phi}_l \right\rangle$) via,

$$d_{ja}^{\mathrm{ad}} = \left[\mathbb{U}^\dagger \mathbb{D} \mathbb{U}\right]_{ja} + \left[\mathbb{U}\dot{\mathbb{U}}\right]_{ja} . \tag{2.13}$$

The adiabatic coefficients c_j are the expansion coefficients of the electronic wavefunction in the adiabatic basis, $\{\psi_j\}$ (see Table 2.1),

$$\Psi(t) = \sum_{j=1}^{M} c_j(t)\psi_j(\mathbf{R}(t)). \tag{2.14}$$

The probability to remain on state a is simply $g_{aa} = 1 - \sum_{j\neq a} g_{ja}$. After the calculation of the probability g_{ja}, a random number is drawn to decide whether a hop can be attempted to a new state n. If so, the following condition should hold to ensure energy conservation,

$$E_{\mathrm{tot}}(\mathbf{R}) = T_a(\mathbf{R}) + E_a(\mathbf{R}) = T_n(\mathbf{R}) + E_n(\mathbf{R}) \tag{2.15}$$

where E_a and E_n are the potential energies and T_a and T_n are the nuclear kinetic energies before and after the hop. When a hop is attempted from state a to n, all quantities E_a, T_a and E_n are already known. To ensure Eq. 2.15 is satisfied, the nuclear kinetic energy (i.e. the nuclear velocities) must be adapted. Based on the theoretical work of Pechukas [106] and Herman [107], Tully prescribes to adjust the velocity component in the direction of the non-adiabatic coupling vectors (NACVs) $\mathbf{d}_{I,an}^{\mathrm{ad}} = \langle \psi_a | \nabla_I \psi_n \rangle$ [81] (see Section 2.2.1). I note in passing that, the NACEs and NACVs are related by the chain rule $d_{an}^{\mathrm{ad}} = \dot{\mathbf{R}}_I \cdot \mathbf{d}_{I,an}^{\mathrm{ad}}$. If

there is not enough kinetic energy along the NACVs to satisfy Eq. 2.15, the hop is rejected, the active state remains state a and the velocity components along the NACVs direction are reversed [61]. To apply the NACV-oriented adjustment in the FOB-SH framework, an exact expression for the NACVs in terms of available nuclear gradients in the diabatic basis was derived by Carof in Ref. [82] and will be discussed in Section 2.2.1.

2.1.6 Forces and nuclear equation of motion

I now turn to the propagation of the nuclei along the MD according to the Velocity-Verlet algorithm as shown in Figure 2.1 and to the force calculation. In the FSSH algorithm, the nuclei evolve on one adiabatic energy surfaces E_a chosen as described in the previous Section. The nuclear force acting on nucleus I, of the active state a, is $\mathbf{F}_{I,a} = -\nabla_I E_a$ and is obtained from the Hellmann-Feynman theorem

$$\begin{aligned} \mathbf{F}_{I,a} &= -\langle \psi_a | \nabla_I H | \psi_a \rangle = -\left[\mathbb{U}^\dagger (\nabla_I \mathbb{H}) \mathbb{U}\right]_{aa} \\ &= -\sum_{k,l} \left[\mathbb{U}^\dagger\right]_{ak} [\nabla_I \mathbb{H}]_{kl} [\mathbb{U}]_{la} \\ &= -\sum_k |U_{ka}|^2 [\nabla_I \mathbb{H}]_{kk} - \sum_{k \neq l} U_{ka} U_{la} [\nabla_I \mathbb{H}]_{kl} \end{aligned} \tag{2.16}$$

where $[\nabla_I \mathbb{H}]_{kl} = \nabla_I \langle \phi_k | H | \phi_l \rangle$. I refer to our previous papers [42, 82] for the derivation of Eq. 2.16. Importantly, the nuclear forces on a given adiabatic state a obtained in Eq. 2.16 consist of a linear combination of the diagonal forces ($\nabla_I H_{kk}$), and off-diagonal forces ($\nabla_I H_{kl}$) on the diabatic states. The weighting $U_{ka}U_{la}$ is proportional to the projection of the active adiabatic state on the diabatic states and therefore it incorporates the effect of wavefunction delocalization on the adiabatic forces.

Notably, even a finite difference calculation of the off-diagonal gradients requires an order of $N_{\text{atom}}M^2$ calculations of H_{kl} elements that would make explicit electronic structure calculations unaffordable. I discussed the use of a fast analytic overlap method (AOM) for the evaluation electronic coupling elements (off-diagonal matrix elements) and related gradient calculations in Section 2.1.4 in case of charge transport simulations. In addition, a multiple time step scheme for an even more efficient calculation of the off-diagonal gradients when simulating large organic semiconducting systems will be presented in Section 2.1.7.

On a similar note, in Section 6.2, I will discuss an alternative and equally efficient strategy, still based on analytic expressions, to calculate excitonic couplings and related

gradients in case of exciton transport simulations based on transition electrostatic potential charges (TrESP).

2.1.7 Efficient optimizations for large systems

The calculation of the nuclear forces $\mathbf{F}_{I,i}$ on a given adiabatic state i and nucleus I via Eq. 2.16, needs the gradients of both diagonal elements ($\nabla_I H_{kl}$ with $k = l$) and off-diagonal elements of the Hamiltonian ($\nabla_I H_{kl}$ with $k \neq l$). The latter, in the case of charge transport, are found by finite differences of the orbital overlap that comes from AOM, namely $\nabla_I H_{kl} = C\nabla_I \bar{S}_{kl}$ [42]. As the number of atoms in the system increases and the off-diagonal elements to evaluate becomes larger, the calculation of the off-diagonal gradients of the Hamiltonian becomes the time-limiting step.

I have developed a multiple time step algorithm (MTS) to reduce the computational cost and allow large scale simulations. In practice, all the gradients $\nabla_I H_{kl}$, with $k \neq l$, are updated only every N MD time steps and kept unchanged between two updates. N must be chosen small enough to reproduce the time oscillations of the off-diagonal gradients well. Since the electronic couplings in OSs (which are the systems of interest of this thesis) generally fluctuate with an oscillation period of ≈ 1 ps [57], one can expect the gradients of the couplings to oscillate on the same time scale. It is worth mentioning that similar MTS approaches are often used in MD codes to efficiently speed-up different parts of the computation [91]. I assessed the quality of this algorithm in Appendix A.3 and in Ref. [86]. Unfortunately, the same approach cannot be applied to the diagonal gradients without biasing the whole dynamics, as the site energies fluctuate in the order of the aromatic carbon stretching frequencies ($\approx 20-30$ fs).

In addition to the aforementioned optimization, it can be noted that the non-adiabatic coupling elements (d_{kl}) in the localized orthogonal orbital basis (Eq. 2.10), that would need to be evaluated together with the Hamiltonian at each nuclear time step, can be neglected in the propagation equation to a very good approximation. This is somewhat expected as, in practice, d_{kl} in the orthogonal basis (see Table 2.1) is always small (typically below 0.04 meV/$\hbar$ for the investigated OSs) and smooth along the entire dynamics since the localized orthogonal basis $\{\phi_k(t)\}$ is, in fact, quasi-diabatic. I note that in a truly diabatic basis, d_{kl} would be zero by definition. In addition, the second term on the RHS of Eq. 2.4 including d_{kl} is, on average, only 0.5% of the first term including electronic couplings for the OSs investigated here. Hence, for most practical purposes the term including d_{kl} can be

safely neglected. Importantly, avoiding the calculation of d_{kl} means bypassing a matrix-matrix-matrix multiplication at each nuclear time steps (Eq. 2.10) and it permits a speed-up of almost a factor of 1.5 compared to the usual interpolation scheme when the OS system size reaches more than a thousand molecules [86]. This efficient optimization combined with the MTS algorithm allows us to almost double the system size at the same computational cost without sacrificing accuracy of transport properties, such as charge mobility and wavefunction delocalization. I refer to Appendix A.3 for a validation of these algorithmic optimizations.

2.1.8 Stable electronic propagation in the diabatic basis

On a final technical note, I highlight that in contrast with standard FSSH approaches [39, 60, 90] in which both the electronic and the nuclear equation of motions are solved in the adiabatic basis (due to the fact that energy and forces are common output of electronic structure calculations), in FOB-SH only the nuclear propagation is carried out in the adiabatic basis while the electronic propagation is solved in the diabatic site basis (Section 2.1.1). As aforementioned, solving the electronic Schrödinger equation in the diabatic representation has some advantages. Most notable is the fact that, at avoided crossings, the adiabatic NACE, d_{ja}^{ad}, can be strongly peaked (because of the strong mixing of the adiabatic PESs). Thus, they could be easily missed because of the finite nuclear time step unless the latter is chosen very small. This could lead to serious artefacts called trivial crossings as I will point out in the Section 2.2.4. By contrast, the NACEs between the diabatic states, d_{kl}, remain small and negligible at avoided crossings (see Section 2.1.7) ensuring a more stable and accurate propagation [108, 109].

This practical advantage has led to the development of "local diabatization" in quantum chemical applications of FSSH [108, 109]. At each nuclear time step, the adiabatic states obtained from quantum chemistry are transformed to a diabatic basis in which the electronic wavefunction is propagated, followed by transformation back to the adiabatic basis. The first transformation is not needed in FOB-SH approach as the Hamiltonian is directly constructed in a diabatic basis. Nevertheless, an additional issue comes from the fact that, although the electronic propagation is accurately done in the diabatic basis taking advantage from the smoothness of the NACEs, the probability to hop (Eq. 2.11) is still calculated in the adiabatic basis where NACEs peak in avoided crossing regions, in some cases causing trivial crossings to be missed and other important consequences that I will discuss

in detail in Section 2.2.4.

2.2 Shortcomings and improvements of original surface hopping

As mentioned in Section 1.4.2, FSSH in its original formulation has a number of more or less known shortcomings. A plethora of variants appeared in the literature [38, 39, 70, 110], to address the most common issues, such as the correct rescaling of the velocities after a successful hop to reach detailed balance and the decoherence correction (DC) to attain internal consistency [87, 111–117] (see Section 2.2.2). Yet several open questions remain, especially in relation to electronic transport simulations. What is the impact of the different DC schemes on the equilibrium distribution of states? How important is the DC to calculate the electronic mobility using FSSH simulations? I will discuss different decoherence approaches in 2.2.3 and I will answer these questions later in Section 3.2 and Section 3.3, where I will provide a detailed account on the role of the decoherence in modelling electronic transport dynamics.

Other less known shortcomings of FSSH are mainly related to the simulation of large condensed phase systems with a high density of states [40, 72, 118–120], e.g. the presence of trivial crossings causing unphysical long-range wavefunction transfers hampering the correct dynamics as I will explain in detail in Section 2.2.4. Only very recently, I have discovered in Ref. [84] that along with these trivial crossing events, an additional source of spurious long-range charge transfers comes from the common DC schemes applied to FSSH. Wang and coworkers [121] independently reported at the same time the same issue in their simulations. I will discuss the problem in Section 2.2.5 and I will demonstrate that, if not removed, the decoherence induced spurious long-range charge transfer (DCICT) will render any mobility calculation and the dynamics erroneous.

The last shortcoming characterizing all semiclassical approaches, like FSSH, is the fact that nuclear quantum effects that are particularly important at low temperatures, such as zero-point energy and tunnelling, are missing. I will not discuss this problem in too much depth in this thesis, since soft organic semiconducting materials are generally characterized by slow and low-frequency vibrations, that can be to some extend approximated by classical dynamics at least at room temperature [15] (see also Chapter 4). Nevertheless, I refer the interested reader to our recent publication about a possible way of including nuclear

quantum effects in FOB-SH simulations of hole transfer by combining it with ring-polymer molecular dynamics (RPMD) (see Ref. [122] and reference therein). This new implementation will hopefully allow an in-depth analysis about the role of zero-point energy as well as tunnelling when computing charge carrier mobilities and/or exciton diffusion lengths in molecular semiconductors.

2.2.1 Energy conservation after a successful hop

As prescribed by Tully [81, 123] and explained in Section 2.1.5, whenever a surface hop occurs the velocities must be adjusted in the direction of the non-adiabatic coupling vectors (NACVs), $\mathbf{d}^{\text{ad}}_{I,an} = \langle \psi_a | \nabla_I \psi_n \rangle = \frac{1}{E_n - E_a} \langle \psi_a | \nabla_I H | \psi_n \rangle$, between the adiabatic electronic states in order to conserve energy in Eq. 2.15. This adjustment is performed by modifying the velocities on the new state as $\dot{\mathbf{R}}_{I,n} = \dot{\mathbf{R}}_{I,a} + \gamma \frac{\mathbf{d}^{\text{ad}}_{I,na}}{M_I}$ (with M mass of Ith nucleus). γ is found by inserting this expression in Eq. 2.15 and solving the related quadratic expression as described in detail in Ref. [82].

Employing the diabatic to adiabatic transformation matrix $\mathbb{U}$, Carof et al. in Ref. [82] express the adiabatic NACV (in a diabatic basis) on atom I between any two adiabatic states i and j (this could be active state, a, and new state, n, as before) as:

$$\mathbf{d}^{\text{ad}}_{I,ij} = \frac{1}{E_j - E_i} [\mathbb{U}^\dagger (\nabla_I H) \mathbb{U}]_{ij} + [\mathbb{U}^\dagger \mathbb{D}_I \mathbb{U}]_{ij} \tag{2.17}$$

where E_j and E_i are adiabatic energies. Notably, the last term in Eq. 2.17 is numerically small and can be ignored (so-called "Fast NACV" approximation). Therefore, NACVs can be rigorously computed in terms of nuclear gradients of the (non-orthogonal) diabatic states $\{\varphi_m\}$ (Eq. 2.16).

As I will show in Section 3.2.1, this adjustment in the velocities massively improves energy conservation and also detailed balance [82], compared to an isotropic rescaling, where the velocities are all rescaled by the same value κ, $\dot{\mathbf{R}}_{I,n} = \kappa \dot{\mathbf{R}}_{I,a}$. using

$$\kappa = \sqrt{1 - \frac{E_n - E_a}{T_a}} \tag{2.18}$$

where the notation follows the one in Eq. 2.15. Velocities adjustment along the direction of the NACVs allows also to obtain very accurate results for the surface population, namely the number of trajectories on a certain state (see Section 3.2).

2.2.2 Adiabatic populations and internal consistency

Tully's hopping probability (Eq. 2.11) was designed to ensure, for a two-states model system, that –within the fewest number of switches– the population of an adiabatic potential energy surface is equal to the amplitude of that adiabatic wavefunction. However, the energy conservation criteria leads to rejecting some hops along the dynamics (so-called frustrated hops). Without any correction, the electronic wavefunction will over-populate excited states that are high in energy and therefore unreachable for the classical nuclei (see Figure 2.2).

In addition to the presence of frustrated hops, that are necessary to maintain detailed balance and energy conservation, a more fundamental problem affecting SH is the overcoherent propagation of the off-diagonal elements of the density matrix (i.e., the coherence terms $c_i^* c_j$) along the classical trajectory. [87] In reality, after leaving an avoided crossing where the adiabatic states mix, the full electronic-nuclear wavefunction splits in two sub-wavepackets $\chi_i(\mathbf{R})$ and $\chi_j(\mathbf{R})$ which evolve on different adiabatic surfaces E_i and E_j. Immediately after the crossing, the center and/or the phase of each wavepacket may diverge in phase space, decreasing the wavefunction coherence between the surfaces i and j, $\int \mathrm{d}R \chi_i^*(R)\chi_j(R)$. This effect is not taken into account in standard FSSH, where the coherence term $(c_i^* c_j)$ remains finite (see Figure 2.2).

This yields the so-called SH internal inconsistency, i.e. a divergence between $\Psi(t)$ and $\psi_a(t)$. Importantly, due to this internal inconsistency, two different adiabatic populations coexist in the SH algorithm, the quantum amplitude averaged over many trajectories (adiabatic wavefunction population),

$$P_i^{\mathrm{ad-wf}}(t) = \frac{1}{N_{\mathrm{traj}}} \sum_{n=1}^{\mathrm{traj}} |c_{in}(t)|^2, \tag{2.19}$$

and the surface population,

$$P_i^{\mathrm{ad-surf}}(t) = \frac{1}{N_{\mathrm{traj}}} \sum_{n=1}^{\mathrm{traj}} \delta_{i,a_n(t)} \ , \tag{2.20}$$

where $a_n(t)$ is the index of the active state at time t of the trajectory n, and $\delta_{i,a_n(t)} = 1$ if the state i is the active state a on which the nuclear dynamics is running at time t. The internal inconsistency of FSSH leads to a divergence of these two adiabatic populations. In Section 2.2.3, I will discuss different remedies (e.g., electronic decoherence correction (DC) schemes) to attenuate the inconsistency of FSSH and the importance of restoring

the consistency between adiabatic wavefunction and surface populations. In Chapter 3, I will examine the huge negative impact that a lack of internal consistency can have on both (thermodynamic) equilibrium and transport properties of the material.

2.2.3 Decoherence corrections

The lack of a inherent decoherence mechanism is a long-standing issue of FSSH, already mentioned in Tully's original paper [81] and often advocated in the literature when studying excited state dynamics and relaxation processes [124]. The missing decoherence ruins the dynamics of the system leading to the failures of FSSH for some important processes. For example, Rossky and co-workers [124] found that, in absence of decoherence, decay rates from excited states to ground state are too fast yielding incorrect excited state dynamics. Landry and Subotnik [110, 125] have later shown that the decay in the charge transfer rate between two molecules obtained with FSSH does not follow the behaviour predicted by Marcus theory.

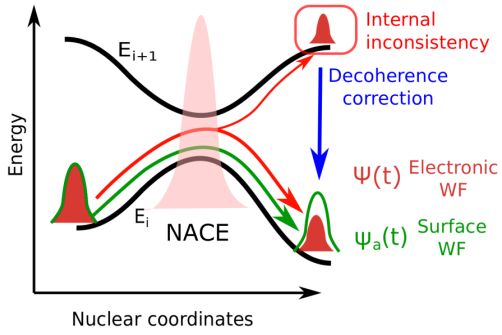

Figure 2.2: Decoherence problem illustration. The lack of decoherence biases the electronic wavefunction $\Psi(t)$ that becomes inconsistent with the active state wavefunction $\psi_a(t)$ after passing through an avoided crossing.

Since the pioneering work of Rossky and collaborators [111], numerous correction schemes have been suggested in the literature to tackle the decoherence problem (decoherence corrections (DCs)). The most common can be divided in three main categories: (i) collapsing approaches, in which the electronic wavefunction is reset to the active state $\Psi(t) = \psi_a(t)$ when a given criterion is fulfilled. Criteria suggested in the literature rely on collapsing events after each attempted or successful hop, after each successful hop [117] or when the adiabatic NACEs fall below a threshold [112]. (ii) Exponential damping approaches, in which all non-active adiabatic coefficients c_i are damped at each time step

$$c_i \rightarrow c_i \exp(-\Delta t/\tau_{ia}) \tag{2.21}$$

while the active state coefficient is scaled to ensure norm conservation [87]. τ_{ia} is the decoherence time [87, 113, 114]. (iii) Stochastic damping approaches that rely on random numbers to determine whether the wavefuntion is collapsed [115, 125, 126]. In the latter, each component of the wave-vector containing the expansion coefficients c_i with $i \neq a$ (a is the active state index), is reset to zero whenever the collapsing probability is larger than a given random number ($\eta \in [0,1]$) drawn at each time step). The relative population is transferred to the active state in order to conserve the norm. Within this method, the probability of a collapsing event can be expressed as $\gamma_i^{collapse} = \Delta t / \tau_{ia}$ in which Δt is the MD time step. A longer decoherence time τ_{ia} results in a lower probability to collapse $\gamma_i^{collapse}$. It is worth mentioning the existence of other decoherence approaches which do not fit in none of these groups and some of them are reviewed in Refs. [39, 40, 60]

As far as I know, no exact expression was derived in literature to calculate the decoherence time τ_{ia} in the context of mixed-quantum classical approaches. However different formulations were proposed based either on physically grounded justifications [113, 114] or derived using approximations for the evolution of frozen nuclear wavepackets [111, 124, 127]. More recently, using controlled assumptions, a decoherence time has been derived from quantum classical Liouville equations (QCLE) formalisms [128]. The most common expression relies on the absence of decoherence when the potential energy surfaces are close to each other or when nuclei are fixed. The energy-based decohererence time (EDC) proposed by Persico and Granucci [87] has the aforementioned characteristics and is widely used in literature,

$$\tau_{ia} = \frac{\hbar}{|E_i - E_a|} \left(C_0 + \frac{E_0}{T_a} \right). \tag{2.22}$$

Here T_a is the nuclear kinetic energy and C_0 and E_0 are parameters to determine [87]. I note that the system size implicitly enters into Eq. 2.22 through the nuclear kinetic energy T_a (an extensive quantity). Therefore, when studying large condensed phase systems, like the ones presented in this thesis, I suggest to normalize the nuclear kinetic energy by the number of degrees of freedom involved in the FSSH algorithm $T_a \rightarrow T_a / N_{\text{dof}}$. By taking only the first term of Eq. 2.22, one obtains

$$\tau_{ia} = \frac{\hbar}{|E_i - E_a|}, \tag{2.23}$$

i.e. the fastest decoherence time possible (due to Heisenberg uncertainty principle) and free

of any *ad-hoc* parameters.

Other expressions for the decoherence time, derived for condensed phase systems and frozen Gaussians travelling on different potential energy surfaces, involve nuclear forces rather than the energy. For instance Rossky and co-workers [111, 124] derived:

$$\tau_{ia} = \left(\sum_{I=1}^{N} \frac{|\mathbf{F}_i^I(t) - \mathbf{F}_a^I(t)|}{2\hbar\sqrt{a_I}} \right)^{-1}, \tag{2.24}$$

where the sum goes over the N nuclei of the system, $\mathbf{F}_i^I(t)$ and $\mathbf{F}_a^I(t)$ are the instantaneous forces on decoherent and active state respectively and a_I is a parameter dependent on the frozen Gaussians width, which has a simple expression in the high temperature limit, $a_I = 6M_I k_B T/\hbar^2$, where M_I is the mass of the Ith nucleus.

Finally, Subotnik and co-workers developed an extension of FSSH, the augmented-FSSH (A-FSSH), directly from QCLE to incorporate the decoherence mechanism more rigorously. New dynamical variables are propagated along the nuclear and electronic degrees of freedom to calculate an instantaneous decoherence time [116, 125]. Yet propagation with this method is more expensive than FSSH and might not be suitable to study large systems with several hundred molecules.

2.2.4 Trivial crossings and state tracking

The presence of trivial (or unavoided) crossing becomes a substantial limitation in performing FSSH simulations in condensed phase systems. A trivial crossing event occurs when two energy surfaces cross with zero couplings between them leading to an actual reordering of the state indices (as shown in Figure 2.3). Physically, such crossings occur when the adiabats are not interacting, i.e. when the adiabatic wavefunctions are localized at distant regions in space. If the state reordering is not taken care of, the dynamics is continued on the wrong surface. Major consequences of such situations are: discontinuity in the nuclear forces, deteriorating energy conservation, unwanted bias in the population of excited electronic states, causing degradation of detailed balance and most seriously in the context of charge and energy transport, spurious long-range charge transfer events (see Figure 2.3).

The problem is greatly amplified in systems with many adiabatic states in a narrow band of energy (e.g. in OSs), where adiabatic energy surfaces can frequently cross each other. In practice, the FSSH algorithm is implemented with a finite time step during which two adiabatic potential energy surfaces can cross. If this swap is not detected the FSSH

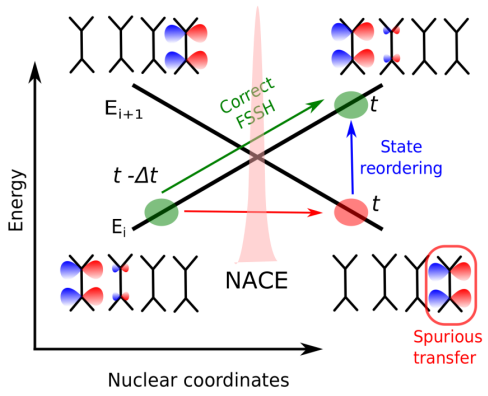

Figure 2.3: Trivial crossing problem illustration. Representation of a two states crossing region in which there is a change in state ordering causing spurious long-range charge/energy transfer between molecules far away in space. The localization of the active state is represented by a blue function at time $t - \Delta t$ and t. The correct wavefunction evolution is reported within green circles and can be achieved with the implemented corrections mentioned in the text. Whereas the wrong behaviour in absence of these corrective algorithms is represented within the red circle.

propagation continues on the wrong surface. Moreover, the distinction between a trivial crossing and an avoided crossing with a very small energy gap (weakly avoided crossings) is unclear with a finite time step. This inherent issue of the FSSH algorithm was often overlooked, as it only arises for systems with dense adiabatic states as is the case for charge and exciton transport in condensed phase materials.

Recently, different solutions emerged in the literature to tackle the missed trivial crossings. Most of them resort to a state tracking algorithm [72, 118–120, 123]. At each MD time step, a map is drawn between the index of the adiabatic states at time $t - \Delta t$ and at time t. To build that map, Thiel and co-workers have relied on energy criteria and maximum of overlap between adiabats at time $t - \Delta t$ and time t [123], whereas Tretiak and co-workers have used the more sophisticated min-cost algorithm [118, 129]. Another innovative approach, suggested by Wang and Beljonne, is their flexible surface hopping method (FSH), where the size of the "active" region of the OS that carries the charge evolves at each MD time step [72]. Such an approach permits to maintain the number of adiabatic states relatively small (provided that the charge carrier remains localized in space) and to diminish the number of trivial crossings, but also requires new criteria and rules to decide at each MD time step which part of the OS should be included in the active region.

An alternative route is trying to improve the calculation of the hopping probability to capture such trivial crossings. For example, a norm-preserving interpolation of the adiabats between the time $t - \Delta t$ and time t can provide a better estimation of the NACV d_{ij}^{ad} [130].

Subotnik and co-workers generalized the norm-preserving interpolation to multiple states crossing using the logarithm of the overlap matrix (Eq. 2.27) [126]. Wang and Prezhdo proposed few years ago an alternative straightforward improvement of the probability to hop [131]. They introduced a simple self-consistency test to the calculation of the hopping probability from the current state to the energetically closest state (and called the algorithm self-consistent fewest switches surface hopping (SC-FSSH)). Trivial unavoided crossings are detected as a significant discrepancy between the summation of probabilities to hop from the current state to all other states according to the FSSH prescription, and the value of the effective change in population of the current state evaluated at the same time interval. In particular, they invoked the exact sum rule (considering all possible probabilities g_{ia} with $i \neq a$),

$$\sum_{i \neq a} g_{ia} = -\frac{\mathrm{d}|c_a|^2/\mathrm{d}t}{|c_a|^2}\mathrm{d}t, \tag{2.25}$$

to correct the probability to hop to the state the closest in energy,

$$g_{ja} = -\frac{\mathrm{d}|c_a|^2/\mathrm{d}t}{|c_a|^2}\mathrm{d}t - \sum_{i \neq a,j} g_{ia}. \tag{2.26}$$

I implemented this simple correction in our previous work in Ref. [82]. This algorithm was found to be quite effective in improving detailed balance, energy drift and allowing for a larger time-step in a small 2-state ELM dimer system. However for larger system with a higher density of states, where more than two states may cross with each other, SC-FSSH alone could not completely solve the trivial crossing problem [84].

Therefore, when study large systems a combination of the mapping approach and the self-consistent correction (Eq. 2.26) for surface hopping was adopted and implemented in FOB-SH. In particular, a map $\mathscr{M}$ between the adiabatic states j at time t and adiabatic states i at time $t - \Delta t$ with a maximum overlap criteria is built. First, the overlap O_{ij} is calculated as,

$$O_{ij} = \left\langle \psi_i(t - \Delta t) | \psi_j(t) \right\rangle . \tag{2.27}$$

For each state $j = l$, the state i_l with the maximum overlap, $|O_{i_l l}| = \max_i |O_{il}|$ is identified. If $|O_{i_l l}| > 1 - \varepsilon$ (ε is a constant set to 0.1), the state l at time t is mapped with state i_l at time $t - \Delta t$, $\mathscr{M}(l) = i_l$. After that step, all remaining states $j = k$ at time t that could not be mapped to states at $t - \Delta t$ (since $|O_{i_k}| < 1 - \varepsilon$ for all unmapped states i) are arranged by index (i.e. by increasing adiabatic energy) and mapped onto one another. As the function

map $\mathscr{M}$ is a bijection between states at t and states at $t-\Delta t$, the reverse map $\mathscr{M}^{-1}$ (that associates states at $t-\Delta t$ with states at t) is easily found. One can track the index of the active state at t, knowing its value at $t-\Delta t$, $a_t = \mathscr{M}^{-1}(a_{t-\Delta t})$. This step permits to change the index of the active state without an actual surface hopping.

This algorithm maps all the states at t with the states at $t-\Delta t$, not only the active state, as required by the calculation of the NACEs (Eq. 2.13). After the mapping, the phase of the eigenvectors is made consistent along the trajectory by checking the sign of the overlap matrix element $O_{i,\mathscr{M}(i)}$ and by reversing the sign of ψ_i if $O_{i,\mathscr{M}(i)} < 0$ (as I underlined in Figure 2.1 with the comment "check sign"). The correct hopping probability (Eq. 2.11), that requires the adiabatic NACEs (Eq. 2.13) and in particular the second term $\left[\mathbb{U}^\dagger\dot{\mathbb{U}}\right]_{ja}$ is finally determined. As suggested by Hammes-Schiffer and Tully [61], we can take advantage of the anti-symmetry of this term. After mapping, this term now is,

$$\begin{aligned}
[\mathbb{U}^\dagger\dot{\mathbb{U}}](t)_{ja} &= \frac{1}{2}\left([\mathbb{U}^\dagger\dot{\mathbb{U}}](t)_{ja} - [\mathbb{U}^\dagger\dot{\mathbb{U}}](t)_{aj}\right) \\
&= \frac{1}{2\Delta t}\left([\mathbb{U}^\dagger(t)\mathbb{U}(t)]_{ja} - [\mathbb{U}^\dagger(t)\mathbb{U}(t-\Delta t)]_{j,\mathscr{M}(a)}\right) \\
&- \frac{1}{2\Delta t}\left([\mathbb{U}^\dagger(t)\mathbb{U}(t)]_{aj} - [\mathbb{U}^\dagger(t)\mathbb{U}(t-\Delta t)]_{a,\mathscr{M}(j)}\right) \\
&= \frac{1}{2\Delta t}\left(-[\mathbb{U}^\dagger(t)\mathbb{U}(t-\Delta t)]_{j,\mathscr{M}(a)} + [\mathbb{U}^\dagger(t)\mathbb{U}(t-\Delta t)]_{a,\mathscr{M}(j)}\right) .
\end{aligned} \tag{2.28}$$

Finally, I apply the self-consistent correction (SC-FSSH) to improve the probability to hop (as in Eq. 2.26) towards the closest state in energy, i.e. the one likely to be affected by numerical inaccuracies due to finite time steps. I will discuss the overall efficiency of this approach to remove the trivial crossings in Section 3.3.2.

2.2.5 Decoherence correction-induced spurious long-range charge transfer

In small systems with only a few electronic states surface hops between localized but spatially distant electronic states are unlikely due to the small NACEs (entering the probability Eq. 2.11). In large systems with a high density of electronic states the probability for a single transition is still small, but since many of these transitions are attempted, they are more likely to take place (because of the stochasticity of the surface hopping algorithm). If such unlikely transitions occur, the active adiabatic electronic state is reassigned from an adiabatic wavefunction localized in one region of space, say $\psi'_a(t-\Delta t)$, to another adiabatic wavefunction localized in a different region of space, $\psi_a(t)$. While such transitions are not an artefact of the SH algorithm *per se*, the problem is that the decoherence cor-

rection (Eq. 2.21 or instantaneous decoherence approaches) tends to quickly collapse the charge carrier wave function (Eq. 2.2) from $\Psi' \approx \psi'_a$ to $\Psi \approx \psi_a$. This results in unphysical long-range charge transfer and yields charge mobilities that increase with system size.

I recently pointed out this problem in Ref. [84] and labelled such events decoherence correction-induced spurious charge transfers (DCICTs). These spurious transfers arise because the different DC schemes act on the adiabatic (i.e. non-local) representation. Note that, since the mean squared displacement (MSD) depends on the square of the distance (see Section 2.3.2), this will have a strong impact on the diffusion coefficient and on the mobility (see Section 3.3.2).

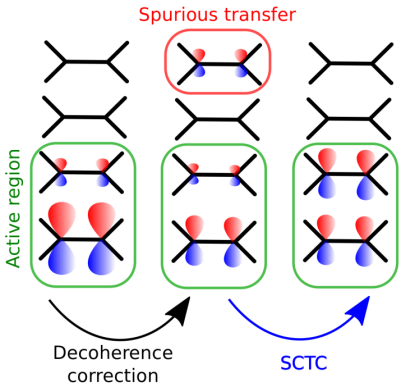

Figure 2.4: Decoherence correction-induced spurious charge transfer (DCICT). An algorithm called spurious charge transfer correction (SCTC) algorithm was developed to solve the DCICTs as described in the text.

Wang and collaborators [121] that, independently from my work in Ref. [84], found the same issue, proposed to switch-off the DC when the surface population is below a certain threshold and showed that the spurious transfer is indeed alleviated [121]. However, this formulation can reduce the internal consistency of surface hopping as some decoherence events are actually removed. By contrast, I developed in Ref. [84] a three-step strategy to remove the DCICTs as illustrated in Figure 2.4: (i) at each time step, an "active" region that encloses 99.5% of the electronic density $|\Psi(t)|^2$ is determined, (ii) the DC is applied and (iii) any change of diabatic population $\Delta|u_l|^2$ outside the active region is reset to zero, while the diabatic populations inside the active region are scaled accordingly to preserve the norm. Consequently, the wavefunction $\Psi(t)$ propagates physically (i.e. according to the TDSE, Eq. 2.4) towards the adiabatic wavefunction on the new surface, and not near-instantaneously (i.e. unphysically) via the DC.

This strategy was called spurious charge transfer correction (SCTC). In practice, it

amounts to a local DC within the active region, while outside the active region the diabatic populations remain unchanged. All DCICTs are removed while DC is still applied at each time step. Note that the propagation of the wave function according to Eq. 2.4 remains unaffected by the presence of the active region.

2.3 Electronic properties

2.3.1 Electronic populations

The calculation of electronic properties (such as charge mobility) from FOB-SH simulations is one of the major objective of this thesis. Electronic-based properties are however ambiguous in standard FSSH, as different definitions can be found for the electronic population. Landry and Subotnik have provided a detailed account of the existing definitions in Ref. [132] and they have highlighted that these populations can produce divergent properties. In the most common approach ("Method 1" in Ref. [132] or "surface method") electronic properties are calculated using the active adiabatic state $\psi_a(t)$. To avoid confusion with Eq. 2.20 (which is the adiabatic surface population), I prefer to call this population projected active state population (PAS). The electronic population on site k is

$$P_k^{\mathrm{PAS}} = |\langle \phi_k(t) | \psi_a(t) \rangle|^2 = |U_{ka}|^2(t) \,. \tag{2.29}$$

Note that the same kind of population can be written for any adiabatic state with $i \neq a$, namely $P_k^{(i)} = |U_{ki}|^2(t)$ (as it will be done in Section 2.3.3 when considering the inverse participation ratio of the adiabatic states).

Other authors use the intrinsic FSSH wavefunction $\Psi(t)$ ("Method 2" in Ref. [132] or "wavefunction population") to obtain electronic properties and the local population on site k is [84, 133, 134]

$$P_k^{\mathrm{wf}} = |\langle \phi_k(t) | \Psi(t) \rangle|^2 = |u_k|^2(t) \,. \tag{2.30}$$

This population definition relies on the propagated electronic wavefunction $\Psi(t)$ that, in general, does not observe detailed balance in absence of DC. I will demonstrate in Section 3.3 that this definition fulfils detailed balance as well as Method 1 when DC is included. Projected active state Method 1 has the advantage to give the correct detailed balance distribution (electronic states distribution follows approximately Boltzmann population in FSSH). However, this method is also more sensitive to trivial crossings, as any

missed trivial crossing will instantaneously modify $\psi_a(t)$. On the contrary $\Psi(t)$, in Method 2, would not be directly impacted by a missed trivial crossing, although in the long term there will be a bias in the dynamics. With a DC, the different definitions coincide on average, except in proximity of a crossing region, where the surface Method 1 cannot capture the delocalization of the wavefunction over two or more adiabatic surfaces (see Section 3.3.3). Therefore, in this work I will always adopt Method 2, P_k^{wf} (supplemented with a DC) to define the mobility and wavefunction delocalization. Nevertheless, for completeness, I will compare the two Methods (1 and 2) in Section 3.3.3.

2.3.2 Diffusion coefficient and charge mobility

The charge carrier wavefunction as a function of time, $\Psi(t)$, can be obtained by solving Eq. 2.4. This gives access to key dynamical properties, e.g. the (2^{nd} rank) mobility tensor (Eq. 2.31), the extent of localization or delocalization of the charge carrier as a function of time and the mechanism by which the charge carrier moves within the material. A particularly common expression for the charge mobility is given by the Einstein-Smoluchowski relation,

$$\mu_{\alpha\beta} = \frac{eD_{\alpha\beta}}{k_{\text{B}}T} \tag{2.31}$$

where $\alpha(\beta)$ represent the Cartesian x,y,z coordinates. e is the elementary charge, k_{B} the Boltzmann constant and T the temperature. This relation provides an important connection between the general concept of charge carrier mobility as the velocity response of a charge carrier to an external electric field, $\mu_{\alpha\beta} = \frac{\langle v\rangle_\alpha}{E_\beta}$ (where $\langle v\rangle_\alpha$ denotes the α component of the time-averaged velocity of the carrier and E_β a component of the electric field vector $\mathbf{E}$), and the classical kinetic theory based on a statistical treatment of the random walk of the carrier through the medium [135]. Eq. 2.31 coincides with the general definition of carrier mobility when the transport occurs in the diffusion regime and in the limit of zero electric field (see Section 4.2.1 for a further discussion on the dependence of the mobility on the field strength).

The diffusion tensor components, $D_{\alpha\beta}$, can be obtained in the long time limit as the time derivative of the mean squared displacement along the nine Cartesian components ($\text{MSD}_{\alpha\beta}$),

$$D_{\alpha\beta} = \frac{1}{2}\lim_{t\to\infty}\frac{\text{dMSD}_{\alpha\beta}(t)}{\text{d}t} \tag{2.32}$$

where the MSD is chosen as the expectation value of the operator $[(\alpha-\alpha_{0,n})(\beta-\beta_{0,n})]$,

$$\begin{aligned}\mathrm{MSD}_{\alpha\beta}(t) &= \frac{1}{N_{\mathrm{traj}}}\sum_{n=1}^{N_{\mathrm{traj}}}\langle\Psi_n(t)|(\alpha-\alpha_{0,n})(\beta-\beta_{0,n})|\Psi_n(t)\rangle \\ &\approx \frac{1}{N_{\mathrm{traj}}}\sum_{n=1}^{N_{\mathrm{traj}}}\sum_{k=1}^{M}|u_{k,n}|^2(t)(\alpha_{k,n}-\alpha_{0,n})(\beta_{k,n}-\beta_{0,n}).\end{aligned} \tag{2.33}$$

In Eq. 2.33, $\Psi_n(t)$ is the time-dependent charge carrier wavefunction in FOB-SH trajectory n, $\alpha(\beta)$ are the Cartesian coordinates, $\alpha_{0,n}(\beta_{0,n})$ are the initial positions of the center of charge in trajectory n, $\alpha_{0,n}=\langle\Psi_n(0)|\alpha|\Psi_n(0)\rangle$, and the square displacements are averaged over N_{traj} FOB-SH trajectories. In the second equation the coordinates of the charge are replaced by the center of mass of molecule k in trajectory n, $\alpha_{k,n}$, and $\alpha_{0,n}=\sum_{k=1}^{M}|u_{k,n}|^2(0)\alpha_{k,n}(0)$, where $|u_{k,n}|^2(t)$ is the time dependent charge population of site k in trajectory n as obtained by solving Eq. 2.4. Note that in case of 1D system oriented along a specific direction the MSD will be different from zero only along the studied direction, and the tensor will be therefore simplified.

I note at this point that while for a classical particle the MSD is well defined as, e.g. in Ref. [59], different definitions of MSD have been used in the literature for the calculation of charge mobility from explicit wavefunction propagation in addition to Eq. 2.33 (see also Ref. [83] for a discussion). In particular, one could first determine the expectation value of the "position" of the quantum particle, $\langle\alpha-\alpha_{0,n}\rangle=\langle\Psi_n(t)|(\alpha-\alpha_{0,n})|\Psi_n(t)\rangle$, and then use it with the classical definition [42, 59] to obtain the displacement of the center of charge (COC) of the wavefunction as

$$\mathrm{MSD}^{\mathrm{coc}}_{\alpha\beta}(t)=\frac{1}{N_{\mathrm{traj}}}\sum_{n=1}^{N_{\mathrm{traj}}}\left(\langle\Psi_n(t)|(\alpha-\alpha_{0,n})|\Psi_n(t)\rangle\langle\Psi_n(t)|(\beta-\beta_{0,n})|\Psi_n(t)\rangle\right). \tag{2.34}$$

On the other hand, one could define the spread of the wavefunction (see Ref. [74]). This is given by:

$$\mathrm{MSD}^{\mathrm{var}}_{\alpha\beta}(t)=\frac{1}{N_{\mathrm{traj}}}\sum_{n=1}^{N_{\mathrm{traj}}}\langle\Psi_n(t)|(\alpha-\langle\alpha\rangle)(\beta-\langle\beta\rangle)|\Psi_n(t)\rangle. \tag{2.35}$$

In general, Eq. 2.33 is always recommended because it accounts for both types of diffusion, center of charge motion (Eq. 2.34) and spreading of the charge distribution (Eq. 2.35). In fact, it is possible to related the three definitions, Eqs. 2.33-2.35, as:

$$\mathrm{MSD}_{\alpha\beta}(t)=\mathrm{MSD}^{\mathrm{coc}}_{\alpha\beta}(t)+\mathrm{MSD}^{\mathrm{var}}_{\alpha\beta}(t). \tag{2.36}$$

Hence, the mobilities can be interpreted in terms of these two contributions as well,

$$\mu_{\alpha\beta}(t) = \mu^{\mathrm{coc}}_{\alpha\beta}(t) + \mu^{\mathrm{var}}_{\alpha\beta}(t) \tag{2.37}$$

I will show in Section 3.3.1 that $\mu_{\alpha\beta}(t) \approx \mu^{\mathrm{coc}}_{\alpha\beta}(t)$, to a very good approximation since the average size of the polaron remains virtually unchanged after initial relaxation ($\mathrm{MSD}^{\mathrm{var}}_{\alpha\beta}(t) \approx const$).

2.3.3 Inverse participation ratio

The inverse participation ratio (IPR) is a common measure to describe the delocalization of the charge carrier wavefunction $\Psi(t)$,

$$\mathrm{IPR}(t) = \frac{1}{N_{traj}} \sum_{n=1}^{N_{traj}} \frac{1}{\sum_{k=1}^{M} |u_{k,n}|^4(t)} \tag{2.38}$$

where $|u_{k,n}|^2$ is the time dependent wavefunction population from Eq. 2.4. The numerical value of the IPR is about equal to the number of molecules the wavefunction is delocalized over. With a simple calculation indeed one can show that a wavefunction (of a single trajectory) fully localized on a single molecule gives an IPR of 1, while a wavefunction homogeneously delocalized over M molecules gives an IPR of M.

A similar definition is used to describe the delocalization of the adiabatic states or eigenstates of the Hamiltonian Eq. 2.5, $\psi_i(t)$,

$$\mathrm{IPR}_i(t) = \frac{1}{N_{traj}} \sum_{n=1}^{N_{traj}} \frac{1}{\sum_{k=1}^{M} |U_{ki,n}|^4(t)}, \tag{2.39}$$

where $U_{ki,n}$ are the components of the eigenvector i of the Hamiltonian Eq. 2.5 in trajectory n.

Chapter 3

Validation of FOB-SH for condensed phase systems

In this Chapter*, I discuss and critically asses the fundamental extensions of the original Tully's FSSH method implemented in FOB-SH and already described in Chapter 2. In particular, here I focus on the impact that the correction for missing electronic decoherence (DC), the detection of trivial crossings and removal of decoherence correction-induced spurious charge transfer, have on important physical properties (i.e. energy conservation, thermal Boltzmann population of the adiabatic states (detailed balance), internal consistency and mean squared displacement of the charge and mobility). These algorithms will be vital to the study of realistic nano-scale organic semiconductors that will be presented in the remaining Chapters of this thesis. As I will clarify here, if any one of these corrections is not included, the time evolution of the wavefunction is biased and transport properties such as charge mobility (see Section 2.3.2) and inverse participation ratio (see Section 2.3.3) diverge with system size. Yet if they are included, convergence with system size, detailed balance and good internal consistency are achieved.

This Chapter is organized as follows, in Section 3.1 I provide the details (and parametrization) of the molecular systems that I will use in this work. I stress that, unless pointed out otherwise, the set-up established in this Section, in term of parametrization protocol and employed algorithms, will be used throughout the whole thesis for similar OSs as well (see e.g. Chapter 4 and Chapter 6). In Section 3.2 and Section 3.3, I investigate the effect of the aforementioned improvements on both thermodynamic equilibrium and transport properties, respectively. Then, I draw some conclusions and outline some recommendations for the best "set-up" or "flavour" of FOB-SH simulations for reliable calculations of electronic properties in molecular materials in Section 3.4.

*The basis of this chapter has been published in Carof, A., Giannini, S. and Blumberger, J. "Detailed balance, internal consistency, and energy conservation in fragment orbital-based surface hopping." *J. Chem. Phys.* 147, 214113 (2017) and in Carof, A., Giannini, S. and Blumberger, J. "How to calculate charge mobility in molecular materials from surface hopping non-adiabatic molecular dynamics –beyond the hopping/band paradigm." *Phys. Chem. Chem. Phys.* 21, 26368-26386 (2019). The following figures and corresponding calculations have been performed by Dr. Antoine Carof: Figure 3.2(B), Figure 3.4 and Figure 3.5(A-C).

3.1 Numerical details and investigated systems

I have generally considered two classes of molecular systems through the whole thesis. On the one hand, I studied atomistic models of organic semiconductors, which have the same geometry as real ethylene molecules, but whose parameters are chosen to resemble realistic materials and, on the other hand, real application relevant organic semiconducting crystals. The former model systems are formed by a chain of ethylene-like molecules (ELMs), as shown in Figure 3.1(A). The name "ethylene-like" stresses that only the nuclear geometries correspond to a real ethylene molecule, while the charge transport parameters (namely the reorganization energy λ and the AOM scaling value C) are chosen freely to explore a wide range of physical behaviours and situations. This constitutes the main advantage of considering these kind of atomistic models, since they allow to explore many different physical cases by keeping the structural model unchanged. On the other hand, real OS crystal structures are taken from the Cambridge Crystallographic Data Centre (CCDC) and they form the semiconducting layer of real devices used in organic electronics. These organic crystals have generally been experimentally well characterized and their transport properties, i.e. charge mobilities and/or exciton diffusion lengths are available in the literature (an example is the anthracene system in Figure 3.1(B), and other OSs in Figure 4.1 and Figure 6.1).

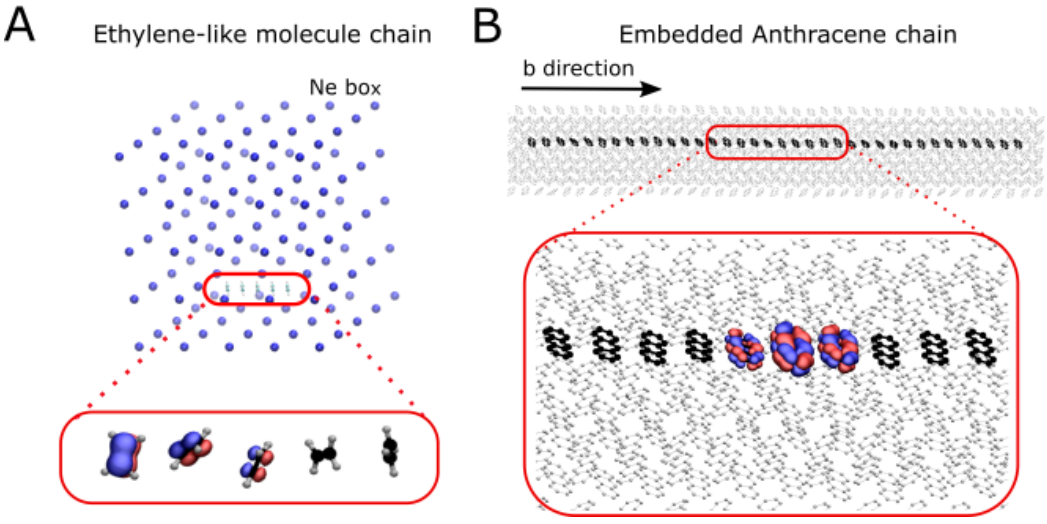

Figure 3.1: Two classes of atomistic systems investigated in this thesis. Namely (A) an organic semiconductor model in the form of a chain of ethylene-like molecules (ELM) embedded in a Neon bath, and (B) real OSs, in this case anthracene crystal, where the crystallographic *b* direction has been activated to the transport.

3.1.1 Chains of ethylene-like molecules as OS model

To assess detailed balance and other equilibrium properties of FOB-SH, I used one-dimensional chains of two (dimer) or more ethylene-like molecules (ELMs), as shown in Figure 3.1(A) in order to investigate the aforementioned properties as a function of electronic coupling strength. Within a chain, the ELMs are spaced by 4 Å and a weak center of mass restraint potential (force constant of 11 $\mathrm{kcal\,mol^{-1}\,\AA^{-2}}$) is applied to keep the chain straight. Because the NVE ensemble is used in all the FOB-SH simulations to avoid any dynamical bias introduced by the thermostat, the chain is embedded in a bath of Neon atoms that mimics the role of a thermostat and reduces the fluctuations of the temperature (especially for the short chains with few degrees of freedom). In particular, I believe that two criteria should be fulfilled to decide which thermostat to choose in the calculation of electronic mobility in OSs: (i) possibly avoiding any bias due to artificial thermostat added in the simulation (e.g. by introducing friction constant) and (ii) ensuring temperature conservation and reducing its fluctuations. The first criteria imposes the use of NVE ensemble for the calculation of electronic mobility, as any other ensemble (such as NVT) would require an artificial bias (e.g. Nosé-Hoover thermostat). To fulfil the second criteria, a large number of degrees of freedom are needed to reduce the temperature fluctuations (that scales in the order of $N^{-1/2}$). Thus, the choice of using a heat bath of Neon. The simulation boxes in Section 3.2 are cubic with size $a = 60$ Å and contain one chain of ELMs and 124 Neon atoms.

Periodic boundary conditions (PBC) are applied in all directions of the simulation box. I point out here that the electronic propagation occurring within the chain of ELMs is not periodic: when the charge reaches the edges of the chain, it is scattered backward and it does not continue at the other end of the chain. In particular, in the present model, hole transfer is mediated by a set of (orthogonalized) HOMO orbitals of the ethylene molecules, ϕ_k, $k = 1..M$, that are used to construct the electronic Hamiltonian $\mathbb{H}$ (Eq. 2.5). The molecules at each end of the chain do not interact with each other (i.e. no cyclic boundary interaction is applied to the tight-binding Hamiltonian in Eq. 2.5). In addition, as I will explain in more detail in Section 4.1.1, when considering real systems, electrostatic interactions in the form of fixed point charges do not significantly alter the energetics of this system because only one ELM carries a net charge and the other ELMs and Ne are charge neutral. Hence, for convenience, electrostatic interactions were switched off in all simulations. This avoids

possible problems related to charge-image interactions in PBC. Note that longer chains of ELMs will be used in Chapter 5 to explore the temperature dependence of the mobility as a function of different coupling strengths.

Digonalization of the Hamiltonian $\mathbb{H}$ gives the M adiabatic electronic states. For a detailed explanation of how the orbitals $\phi_i(\mathbf{R}(t))$, are reconstructed along the trajectory I refer to Section 2.1.4 and to Ref. [42]. The diagonal elements H_{kk} are calculated with a force field energy function whose parameters for neutral and positively charged ELMs are chosen as explained in Section 2.1.3 and done in previous works [42, 82]. For the charged ELM, the equilibrium distance of the C=C bond is displaced (1.387 Å) with respect to the one in the neutral state (1.324 Å) corresponding to a reorganization energy for hole transfer between two ELMs of $\lambda = 200$ meV, unless otherwise stated. These reorganization energies are typical for organic semiconductors and an order of magnitude smaller than e.g. for redox processes in aqueous solution [136–138] or oxide materials [139]. Intra-molecular interactions for the neutral ELM are taken from the Generalized Amber Force Field (GAFF) [94]. The intermolecular interactions among the ELMs and between ELMs and Ne atoms are modelled by Lennard-Jones terms with parameters taken again from the GAFF database for neutral and charged ELMs and from Ref. 140 for Ne and applying the Lorentz-Berthelot mixing rules.

For the results presented in Section 3.2, initial configurations are built with the investigated chain in its energy-minimized geometry and the Neon atoms positioned on a regular grid. The system is equilibrated with a 1 ns NVT run at 298 K using a Nosé-Hoover thermostat [141, 142] and using a force field energy function where the first molecules of the chain is charged (see also Section 2.1.2). From the last configuration of the NVT run, 100 ps Born-Oppenheimer molecular dynamics (BOMD) trajectories are started for the adiabatic electronic ground state. This is done for each of the six AOM scaling values C that determines the strength of electronic coupling according to $H_{kl} = C\bar{S}_{kl}$. For the dimers in Section 3.2, unless otherwise stated, I chose $C =$ 14, 82, 272, 381, 816 and 1360 meV that corresponds to an average coupling values $V = \sqrt{\langle |H_{kl}|^2 \rangle}$ of about 2, 10, 34, 51, 130 and 220 meV. I removed the first 20 ps where the system equilibrates and used the last 180 ps of the BO trajectories on the different states to calculate free energy differences for consecutive adiabatic electronic states, depending on the size of the system

$$\Delta A_{i,i-1}(C) = -k_{\mathrm{B}}T \ln \langle \exp[-(E_i - E_{i-1})/k_{\mathrm{B}}T\,] \rangle_{E_{i-1}} \tag{3.1}$$

where i represents the given state, for each scaling value C. The corresponding numerically "exact" excited state populations are determined according to the Boltzmann population of each state i:

$$P_i^{\mathrm{B}}(C) = \frac{e^{-\beta \Delta A_{i,0}}}{\sum_{i=0}^{M-1} e^{-\beta \Delta A_{i,0}}} \,. \tag{3.2}$$

I extracted Boltzmann-weighted configurations (nuclear coordinates and velocities) from such BOMD runs as starting configurations for the FOB-SH runs, to ensure the correct distribution of excited state populations at the start of the run (at $t = 0$) and a well-sampled phase space. The electronic wavefunction is initialized in the corresponding adiabatic state i ($\Psi(0) = \psi_i$) to ensure perfect internal consistency at $t = 0$. For each set of parameters (velocities adjustment, C value, decoherence correction (DC)), I generated 1000 independent FOB-SH trajectories starting from the initial configuration evenly sampled from the corresponding BOMD trajectories. Each trajectory is run for 10 ps in the NVE ensemble.

The nuclear dynamics in FOB-SH is propagated with the velocity-Verlet algorithm with forces calculated according to Eq. 2.16 and with an MD time step $\Delta t = 0.1$ fs. The wavefunction of the excess charge carrier $\Psi(t)$ was propagated by integrating Eq. 2.4 using the Runge-Kutta algorithm of 4th order and an electronic time step $\delta t = \Delta t/5 = 0.02$ fs. An interpolation scheme is used to calculate the Hamiltonian matrix elements at each electronic time step [42]. Error bars were determined by block averaging over the 1000 trajectories with a block size of 200 independent runs.

3.1.2 Chains of embedded anthracene molecules

To investigate mobility and IPR of a real system (see Section 3.3 below), hole transfer was modelled in a chain of "electronically active" anthracene molecules, embedded in a larger crystal comprised of electronically inactive anthracene molecules, see Figure 3.1(B). As for the ELMs model system described before, the selected active molecules form the basis for the electronic Hamiltonian (Eq 2.5), i.e. the HOMOs of these sites contribute to the expansion of the carrier wavefunction in Eq. 2.1. I refer to Section 4.1.3 for a discussion on the accuracy of this assumption.

The transport of the hole wavefunction was modelled in different chains of length: 12, 24, 36 and 48 molecules. The simulation boxes are monoclinic, with angles $\alpha = 90.0^\circ$, $\beta = 124.7^\circ$ and $\gamma = 90.0^\circ$ and with size $a = 8.562$ Å and $c = 11.184$ Å. The box length in the b direction was adapted to ensure that the distance between the chain and the edges of the box is above 8 Å (i.e. from 97.3 Å for the smallest system to 316.2 Å for the largest).

Periodic boundary conditions are applied in all directions of the crystal, but, similarly to the chains of ELMs, the electronic dynamics occurs along non-periodic chains. To check the convergence of mobility with respect to the length of the chains, different number of molecules forming the chain are investigated.

The M diagonal elements, H_{kk}, of the Hamiltonian are, again, estimated using M classical force field energy functions. In the kth energy functions, anthracene molecule k is positively charged while all the others are neutral. Intra-molecular interactions for the neutral anthracene molecule are taken from the Generalized Amber Force Field (GAFF) [94]. These intramolecular parameters are used also for the charged anthracene, except for the carbon-carbon bond length which was chosen instead to reproduce the reorganization energy λ as described in Section 2.1.3. The geometry of charged and neutral molecules were optimized with B3LYP functional [143] and 6-311g(d) basis set. The intermolecular interactions between anthracene molecules are also taken from the GAFF database. As in each classical force field all but one molecule are neutral and the anthracene has zero dipole moment, electrostatic interactions were not included just like for the ELMs.

The off-diagonal elements of the electronic Hamiltonian H_{kl} are calculated using AOM [92]. First, as explained in Section 2.1.4, the HOMO of anthracene (which is non-degenerate) is projected onto an atomic Slater basis consisting of one atomic p orbital per carbon atom. The calculation of the HOMO and its projection was done using CPMD software [105] using the PBE exchange correlation functional [144]. The dimers are centered in the simulation box at 4 Å away from the box edges. After that, the electronic coupling H_{kl} is calculated using the sFODFT method [102] for different dimers extracted from the crystal structure and along a classical MD trajectory, while the HOMO-HOMO overlap $\bar{S}_{kl} = \langle \varphi_k | \varphi_l \rangle$ is calculated using the AOM for the same dimers. A linear regression is applied between $|H_{kl}|$ and $|\bar{S}_{kl}|$ to determine the AOM scaling value $C = 3.1$ eV (see Appendix A.1). Note that the same protocol will be used for the parametrization of other organic crystals in Chapter 4. In the latter Chapter, I will comment more in detail about the accuracy of the electronic coupling calculations, the importance of their relative signs and the reliability of the tight-binding representation of the FOB-SH Hamiltonian.

Each FOB-SH simulation involves 1000 independent trajectories initialized from 100 different initial conditions (10 trajectories repeated with a different random seed for each initial condition). Starting from the crystal structure, the system is equilibrated 500 ps in the

NVT ensemble using a Nosé-Hoover thermostat [141, 142]. Then a MD run of length 500 ps is carried out in the NVE ensemble from which 100 configurations are chosen at equidistant intervals. These are used as initial configurations for subsequent FOB-SH runs. The initial wavefunction is fully localized on the first molecule of the chain, $\Psi(t=0)=\phi_1(0)$ and the initial active state is randomly drawn from all adiabatic states with a probability $\langle\psi_i(0)|\phi_1(0)\rangle^2$. Each trajectory is run for 2 ps in the NVE ensemble. This ensemble is used to avoid any artificial thermostat that may bias the calculation of the electronic mobility. The large number of degrees of freedom due to the "inactive" part (inactive for electronic propagation, as depicted in Figure 3.1) of the anthracene crystal plays the role of a thermostat and ensures small temperature fluctuations. The nuclear dynamics is propagated, as in the ELM system, using the velocity-Verlet algorithm and different MD time steps are tested to check for convergence ($\Delta t = 0.025, 0.05, 0.1$ and 0.5 ps). The electronic wavefunction is propagated using the Runge-Kutta algorithm of 4th order and electronic time step $\delta t = \Delta t/5$. The same algorithm and electronic step will be use through the whole thesis.

3.2 Detailed balance, energy conservation and internal consistency

Before investigating charge transport properties, I focus in this Section on the influence that different velocities adjustment algorithms and various DC schemes, have on key equilibrium properties (energy conservation and detailed balance) and internal consistency. I exclude, here, the analysis of trivial crossings or decoherence correction-induced long-range spurious charge transfers (DCICTs), as these issues arise only when considering large systems and transport properties (see Section 3.3 for a detailed discussion).

3.2.1 Effect of velocities adjustment

The investigation is started by comparing the two main different criteria used in the literature to determine whether a hop is energetically allowed: isotropic rescaling of the full velocity vector (Eq. 2.18) and adjustment of the component parallel to the NACV (Eq. 2.17) to conserve total energy. FOB-SH simulations were carried out for these two prescriptions, with all other simulation details given in Section 3.1.1 (however, note that here the scaling factor C was set to 0.03, 0.02, 0.01, 0.008, 0.003, 5×10^{-4} and 5×10^{-5}, and reorganization energy was set to 100 meV). Figure 3.2(B) shows the excited state populations obtained as a function of electronic coupling, together with the exact populations obtained from

the free energy calculation described in Section 3.1.1. The latter decreases by four orders of magnitudes when the electronic coupling (and thus the gap between the surfaces) is increased from 0.2 to 100 meV (see Figure 3.2(A)).

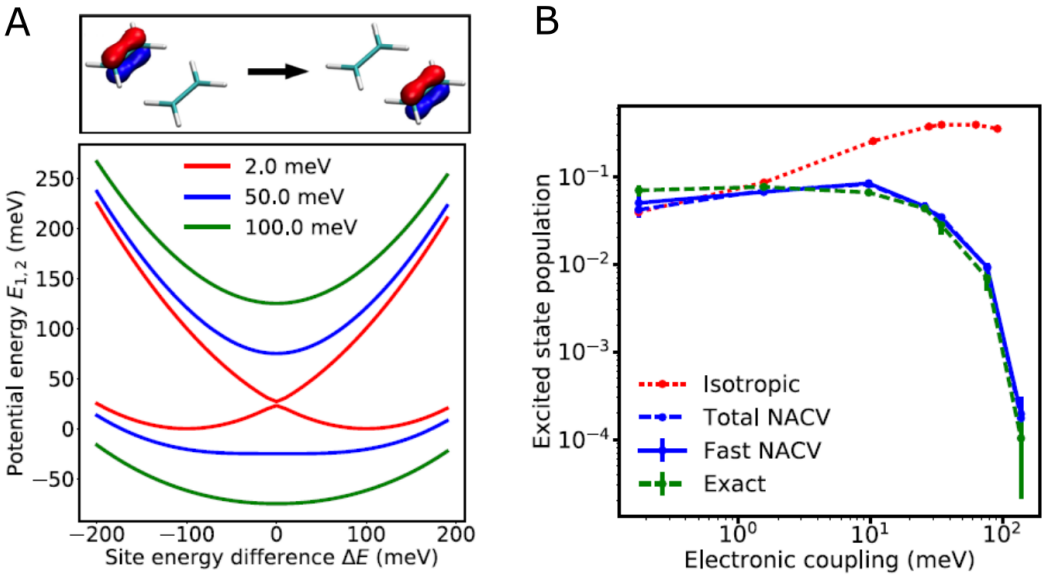

Figure 3.2: Effect of velocity adjustment on the ELM dimer. (A) Representation of the model system investigated and adiabatic energy surfaces against site energy difference. Three electronic coupling values are indicated with different colours, $\lambda = 100$ meV in this case. (B) Influence of the rescaling prescription used to ensure energy conservation on excited state population for different diabatic electronic couplings. "Isotropic" results use the isotropic rescaling with the factor given in Eq. 2.18. "Fast NACV" and "Total NACV" refer to rescaling along the direction of the NACV, Eq. 2.17. In the former case, the second term in the RHS of Eq. 2.17 is neglected. Error bars are shown for the default option (Fast NACV) and represent standard deviations over five independent blocks of 200 trajectories. Error bars for the numerically exact population indicate standard deviation over three blocks of 20 ps.

The energy criterion based on the NACV reproduces the exact populations very well in all coupling regimes both when the second term in the RHS of Eq. 2.17 is neglected ("Fast NACV") in solid blue lines and also when the full expression is considered, dashed blue lines. The deviation is typically within the error bars of these simulations. Turning to isotropic rescaling, we can see that the excited state populations are well reproduced only for a small coupling value of up to 2 meV. For larger coupling values, the populations increase rather than decrease, strongly overestimating the exact results. This unphysical behaviour can be rationalized as follows. In the isotropic rescaling method, a hop is successful if the kinetic energy of the quantum subsystem is larger than the adiabatic energy gap between the states. Estimating the average kinetic energy for the 2 ELMs as $T_a \approx 12 \times 3 \times k_B T/2 = 450$ meV, it was found this to be larger than the average adiabatic energy gaps at the crossing

regions, $2H_{12} = 0.4 - 200$ meV, for the range of coupling values investigated. Hence, virtually all attempted hops will be energy-allowed, even for the systems with large energy gaps. Whereas, the rescaling of the velocities along the component parallel to the NACV represents a much more stringent and rigorous criteria and is a key feature of the original Tully method [81]. This feature was shown essential to compare the FSSH results with quantum calculation [145]. The results presented here complement the previous literature analysis and demonstrates that adjusting the velocities along the NACV is also required to increase the number of frustrated hops, thereby allowing to achieve detailed balance.

3.2.2 Effect of decoherence correction

Despite the lack of decoherence is a well-known issue of FSSH, the role of the DC on detailed balance has been only partially considered in the literature [146]. To investigate to what extent DC influences the thermal population of each state, I have carried out FOB-SH simulations using a dimer of ELMs in a bath of Neon atoms employing several commonly used DC algorithms: instantaneous DC after each attempted hop (IDA) [117], energy-based decoherence correction (EDC, Eq. 2.22) [87], pure dephasing decoherence correction (PDDC, Eq. 2.23), force-based decoherence correction [111, 115, 124] using a damping algorithm (FDC, Eq. 2.24) and a stochastic algorithm (SC-FDC), and finally the absence of a correction scheme (NO DC). Simulations are initialized as described in the previous Sections. Figure 3.3(A) shows the energy drift averaged over 1000 FOB-SH NVE runs as functions of electronic coupling. We can observe a monotonic decrease of the energy drift from 10^{-5} Ha/ps/QM atom to 10^{-7} Ha/ps/QM atom. This behaviour can be explained by observing that, for increasing electronic couplings, the number of successful hops diminishes while the potential energy surface softens, thus improving total energy conservation. The notable fact is that the energy drift is independent of the DC scheme used. This can be expected as the DC only affects the electronic wavefunction, not directly the nuclear degrees of freedom whose total energy is conserved along the simulation.

A similar conclusion holds for the detailed balance. In Figure 3.3(B), I show the electronic population of the excited state (Eq. 2.19), averaged over the 1000 trajectories and over time, against the time average electronic couplings. The exact result (Eq. 3.2) obtained from BOMD simulations as described in Section 3.1.1 is also indicated. Since the work of Tully and collaborators [78, 79], the ability of the "vanilla" FSSH (i.e. without DC) to reach detailed balance is well-known. As seen in Section 3.2.1, Carof et. al recently reinforced

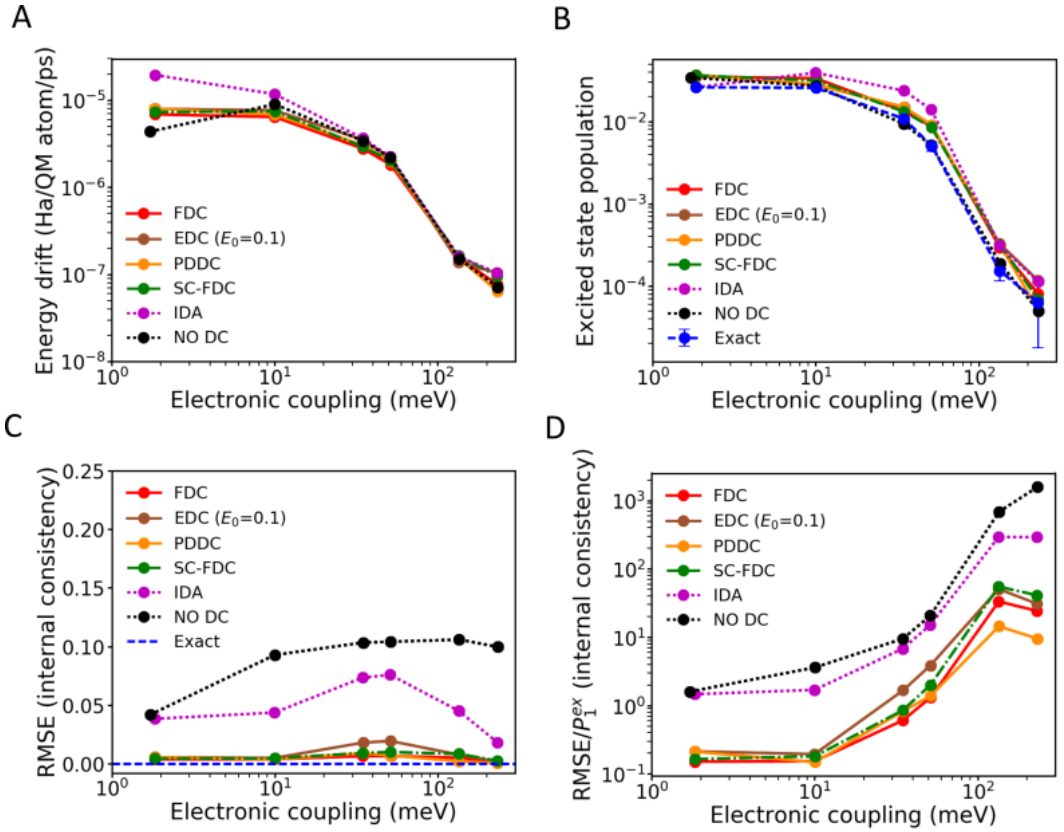

Figure 3.3: Equilibrium properties of the ELM dimer at $T = 300$ K. The conserved energy drift (A), excited state population (B) and internal consistency (C,D) are shown as a function of the diabatic electronic coupling strength between the two ELMs. Different electronic decoherence corrections (DC) are compared: damping of adiabatic electronic populations with force-based (FDC, Eq. 2.24), stochastic force-based (SC-FDC), energy-based (EDC, Eq. 2.22), and pure dephasing decoherence times (PDDC, Eq. 2.23), instant collapse (IDA) and no DC. Numerically "exact" populations (P_1^B, Eq. 3.2) in (B) are obtained as described in Section 3.1.1 The internal consistency in (C) is measured in terms of the root-mean-square error (RMSE, Eq. 3.3), and divided by the excited state population P_1^B in (D).

the point that the NACV-oriented adjustment of velocities after a hop is paramount for this agreement to hold and I refer to our work in Ref. [82] for a discussion on this. Remarkably, I find here that the bias introduced by the DC in the electronic dynamics is almost negligible in term of equilibrium distribution. This can be readily explained in the case of EDC, PDDC and FDC, for which the decoherence time is small (i.e. fast decoherence) far from the crossing region and it is large (i.e. slow decoherence) within the crossing region. For this reason, such corrections have only a minor effect in the proximity of an avoided crossing, which is where the probability for hops sharply increases and the thermal equilibration between the electronic states occurs. Thus, DC only affects the dynamics away from the crossing region, where, in any case, the surfaces are quite well separated in energy and the number of hops

is small. Therefore, damping-based schemes maintain the correct flux between states and do not ruin the detailed balance.

It is important to notice that such an argument does not apply to instantaneous DC algorithms, that do not depend on any decoherence time and require by definition to be in the crossing region for the algorithm to be applied (i.e. there must be either an attempted or a successful hop in order to collapse the wavefunction) [117]. This explains why, for the latter algorithms we can observe larger deviations both for energy drift and excited state population, even though the DC is still small due to the small number of collapsing events with respect to the total number of steps in the dynamics. I can conclude by saying that all the DC schemes investigated here can approximately reach detailed balance, meaning that the bias introduced in the electronic dynamics does not affect the flux between adiabatic states.

While the different DC algorithms give virtually identical results for energy drift and detailed balance, they give very different results for internal consistency. The internal consistency criteria can be measured by calculating the time-averaged root mean square error between the surface population and the quantum amplitude of the excited state i, $P_i^{\mathrm{ad-surf}}(t)$ (Eq. 2.20) and $P_i^{\mathrm{ad-wf}}(t)$ (Eq. 2.19), respectively,

$$\mathrm{RMSE}_i = \left(\frac{1}{T} \int_0^T \mathrm{d}t \left(P_i^{\mathrm{ad-surf}}(t) - P_i^{\mathrm{ad-wf}}(t) \right)^2 \right)^{1/2}, \tag{3.3}$$

where the populations are averaged over trajectories. In case of perfect internal consistency, $\mathrm{RMSE}_i = 0$ for all i. Figure 3.3 (C) shows the RMSE obtained for the usual range of coupling values and Figure 3.3 (D) shows the RMSE normalised with respect to the exact excited state population, $\mathrm{RMSE}_i / P_i^{\mathrm{ad-surf}}$. We can observe that RMSEs follow the same trend for all the DC methods (an increase from low couplings to medium-sized coupling values (maximum around 50 meV) and a slight decrease thereafter. The damping methods show very good internal consistency, with FDC and PDDC giving best performance for all coupling strengths, and significantly improving over wavefunction collapse and no DC (Figure 3.3 (C)). Hence, the particular choice of damping time seems rather unimportant for good average internal consistency, i.e. in the long time limit (Eq. 3.3).

However, Figure 3.3(D) reveals that the internal consistency, normalized with respect to the excited state population P_i^{B}, deteriorates with increasing coupling strength. The quantum populations of excited states are generally overestimated in this regime. In our previous

paper [82], it was shown that for couplings $V > k_B T/2$, adiabatic NACEs still transfer electronic population from the ground state to the excited state, while attempted hops become increasingly energy-forbidden. Therefore, the wavefunction population on the excited state is overestimated compared to the surface population. While for no DC and collapse the error is substantial to the extent that there is no longer any consistency between quantum and surface amplitudes in the high coupling regime, the damping methods significantly improve on this situation, albeit not perfectly. For a large coupling value of 100 meV, the excited state surface population is about 10^{-4} (Figure 3.3(B)), while the quantum populations are about 10^{-3} giving $\mathrm{RMSE}_1/P_1^{\mathrm{B}} \approx 10$. This deviation is expected not to be relevant in many practical situations for OSs with a higher density of states and smaller energy gaps between the adiabatic states (see Section 3.3.3).

Nevertheless, I note in passing that to further reduce the internal inconsistency in the high coupling region (and a large gap between the states), I explored and implemented an alternative electronic propagation scheme (called elimination of classically forbidden hops - EFH) in Ref. [83]. In this approach, the electronic population transfer between adiabatic states is removed in case of classically forbidden transitions for the nuclei (namely, those hops that do not fulfil the energy conservation criteria). I will not discuss the EFH in this thesis because, despite this alternative algorithm massively improves internal consistency at high coupling, the agreement with the detailed balance deteriorates due to the bias introduced in the electronic dynamics by removing population transfer between the states. Thus, I concluded that this algorithm was not suited to study transport properties in large systems, in which, in any case, the internal consistency can be largely corrected with the introduction of a more common DC scheme (see Section 3.3.3).

3.3 Charge transport properties

I now focus on building and describing the best FOB-SH set-up to calculate the mobility and delocalization of a charge carrier in organic semiconductors. I will use this set-up through the course of the whole thesis, unless stated otherwise. To this end, I make use of the system described in Section 3.1.2, a hole diffusing in a chain of anthracene molecules embedded in a larger crystal. Several parameters and set-ups need to be assessed: the role of the state tracking algorithm and/or the spurious transfer correction (SCTC), the convergence with respect to the size of the system, the impact of the DC scheme and the definition of the electronic population.

3.3.1 Mean squared displacement definitions

I first clarify how to determine the charge mobility from the diffusion coefficient in Eq. 2.32. The latter depends in turn on the mean squared displacement (MSD). As I have indicated in Section 2.3.2, different definitions of the MSD have been used in the literature [72, 74, 84, 134]. To asses these various definitions, FOB-SH simulations for a chain of 48 anthracene molecules were run for 2 ps and using what will be defined as the best set-up in the following Sections, namely state tracking and spurious transfer correction switched-on, the DC scheme actived and the diabatic population P^{wf} (Eq. 2.30) used to calculate the MSD. Figure 3.4(A) shows the three MSD definitions against time. $\mathrm{MSD}^{\mathrm{coc}}$ (Eq. 2.34) and MSD (Eq. 2.33) quickly rise simultaneously until 200 fs, then they diverge slightly and end up in a linear regime with the same slope, clearly visible after 0.5 ps. On the contrary, $\mathrm{MSD}^{\mathrm{var}}$ (Eq. 2.35) increases more slowly and reaches a plateau regime after 1 ps. In fact, as shown by different authors using simulation tools [72, 77, 84, 85, 121] and by experiments [20–22], in OSs the electronic wavefunction is delocalized over few molecules and the charge spreading remains approximately constant in time (see also Chapter 4 and Chapter 5 for an in-depth discussion on this point).

As described in Section 2.3.2, the mobility is related *via* the diffusion coefficient (Eq. 2.32) to the slope of the MSD at long times. In Figure 3.4(A), the best linear fit is indicated by a black dashed lines for all three MSD definitions. I conclude that to determine the mobility, both $\mathrm{MSD}^{\mathrm{coc}}$ and MSD will give the same value for the diffusion constant, whereas $\mathrm{MSD}^{\mathrm{var}}$ will give a zero value for this coefficient and so for the mobility.

Beside mobility, it is also interesting to measure the delocalization of the wavefunction. The inverse participation ratio (IPR) was evaluated according to Eq. 2.38. In particular, $\mathrm{IPR}_n(t)$ measures the number of sites over which the wavefunction is delocalized at time t for a trajectory n. This quantity can be averaged over time and over trajectories to obtain the equilibrium converged value. In Figure 3.4(B) I show the evolution of IPR against time. At $t = 0$, the wavefunction is initially localized on the first molecule of the chain and $\mathrm{IPR}(t = 0) = 1$. The IPR increases rapidly during the first few hundreds of femtoseconds before reaching a plateau at around 1 ps. The initial transient increase corresponds to the wavefunction spreading until the equilibrium polaron width is reached (see Chapter 4 for a more detailed discussion on this property). In fact, this behaviour of the IPR resembles closely the time evolution of $\mathrm{MSD}^{\mathrm{var}}$.

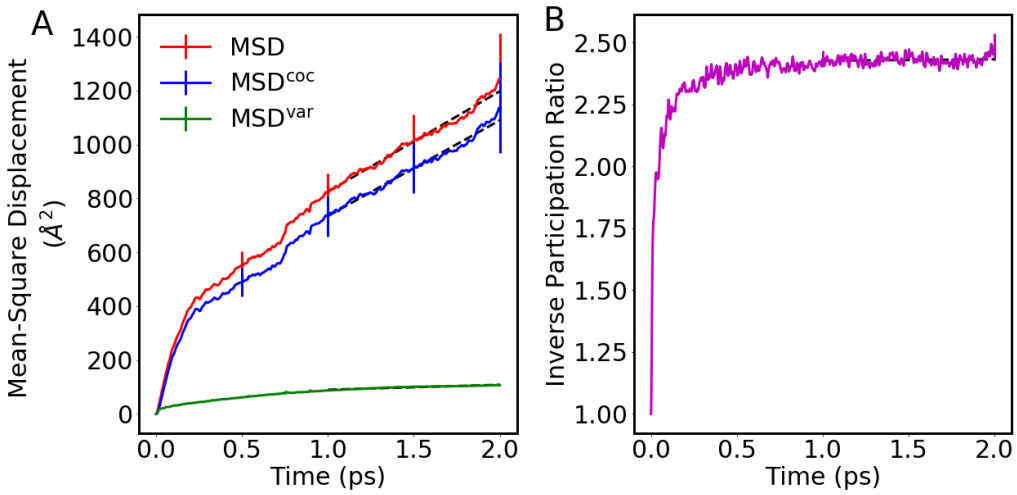

Figure 3.4: (A) Mean squared displacement (MSD) and (B) inverse participation ratio (IPR, Eq. 2.38) for hole transport in anthracene, from FOB-SH simulations. In (A) the MSD (Eq. 2.33) is broken down in the MSD for the centre of charge, MSD^{coc}(Eq. 2.34), and the MSD due to changes in the spread or variance of the wavefunction, MSD^{var} (Eq. 2.35). FOB-SH simulations were carried out for an embedded chain of 48 anthracene molecules, applying a MD time step of 0.1 fs. Error bars are obtained by block-averaging over five independent blocks of 200 trajectories each.

3.3.2 Trivial crossings and spurious charge transfers

I now investigate the need of the state tracking algorithm and decoherence correction-induced spurious charge transfer correction (SCTC) described respectively in Sections 2.2.4 and 2.2.5 in order to obtain convergence for the MSD and the mobility as a function of chain length.

Figure 3.5 shows the MSDs for different chain lengths and the wavefunction population of sites k, (P_k^{wf}, Eq. 2.30) for representative FOB-SH trajectory for three different set-ups: (A) state tracking and SCTC both active, (B) state tracking and no SCTC and (C) no state tracking and no SCTC. If both state tracking and SCTC are swichted-on, the MSDs are identical for the different chain lengths (except for the chain with 12 molecules where the MSD is slightly below the MSD of longer chains as the diffusive charge starts to feel the non-periodic boundary and to bounce back at the end of the chain). The smooth evolution of the polaronic charge carrier is illustrated for one representative trajectory in Figure 3.5(D), where no spurious charge transfer event is present. When the SCTC is switched-off (panel (B)), MSDs as function of chain lengths start to diverge after few femtoseconds, indicating that frequent decoherence correction-induced spurious transfer events bias the charge dynamics. It is worth noticing that spurious charge transfers induce a much larger displace-

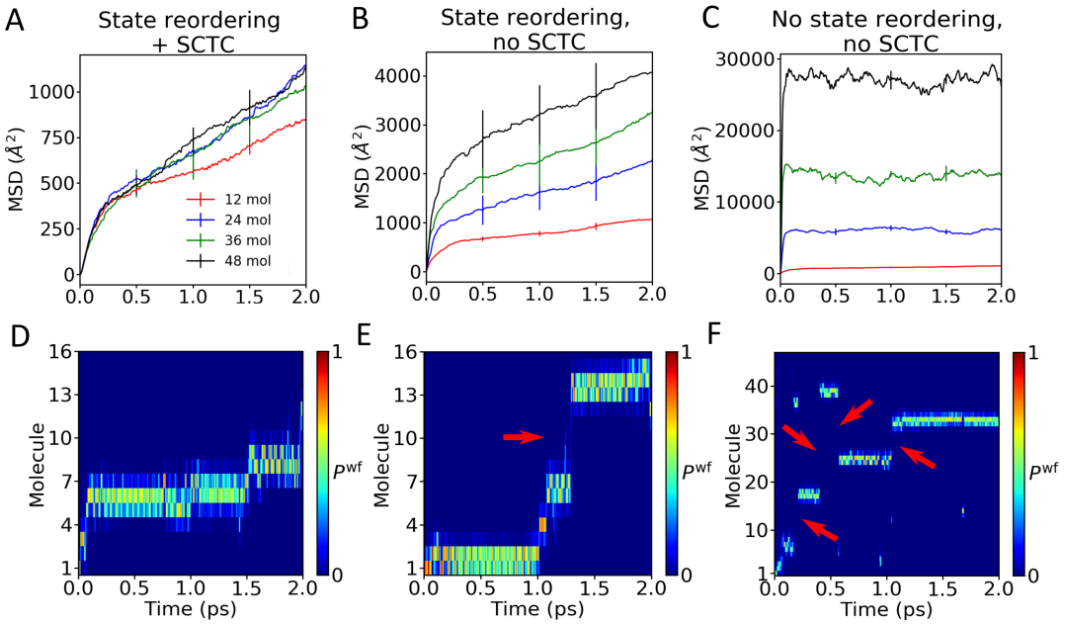

Figure 3.5: Importance of state reordering and spurious charge transfer correction in FOB-SH simulations of hole transport along an embedded chain of anthracene molecules. (A, B, C) MSD (Eq. 2.33) for hole transport with chain length as indicated (12, 24, 36 and 48 molecules). (D, E, F) Time evolution of the hole carrier wavefunction population (P_k^{wf}, Eq. 2.30) along a representative FOB-SH trajectory. The MSD and the wavefunction population are compared for three different set-ups : (A, D) adiabatic electronic states are reordered using the state tracking algorithm (see Section 2.2.4) and the decoherence correction-induced spurious charge transfer correction is active (SCTC, see Section 2.2.5); (B, E) state reordering is active, SCTC is switched off; (C, F) state ordering and SCTC are switched off. Note, the MSD is independent of system size only in (A). For all set-ups, DC keeps the charge localized over about 2 molecules. Long-range spurious transfer events are highlighted with red arrows in (E) and (F), note that charge transport in (C) is completely biased by unphysical jumps of the charge. The MD time step is 0.1 fs and the DC is damping with pure dephasing decoherence time. Error bars represent standard deviation over five independent blocks of 200 trajectories each.

ment of the charge, as in a few time steps the charge can completely change its localization. A spurious transfer is shown in panel (E) for a representative FOB-SH trajectory without SCTC, where the charge carrier unphysically "jumps" from molecule 7 to molecule 13 in a few femtoseconds. I also note that the order of magnitudes spanned by these MSDs and the presence of a linear regime may be deceptive, but the divergence with system size underlines the unphysical aspect of the charge displacement. In Figure 3.5(C), I show the MSDs for different chain lengths when both SCTC and state tracking are switched-off. In a few femtoseconds, the MSDs reach a plateau that depends on the size of the system (i.e. the larger the system the larger the plateau value). Such dynamics for the charge corresponds to an unphysically fast diffusion in which the numerous missed trivial crossings yield an almost stochastic motion of the charge along the chain. This is well exemplified in Figure 3.5(F)

for a FOB-SH trajectory without SCTC and state reordering. Missing index updates cause numerous jumps of the charge carrier at long distance (tens of molecule). Only the use of a state-tracking algorithm to detect the trivial crossings and the SCTC to eliminate the decoherence correction-induced spurious charge transfers leads to a physical MSD independent of the system size.

3.3.3 The importance of a decoherence correction for transport

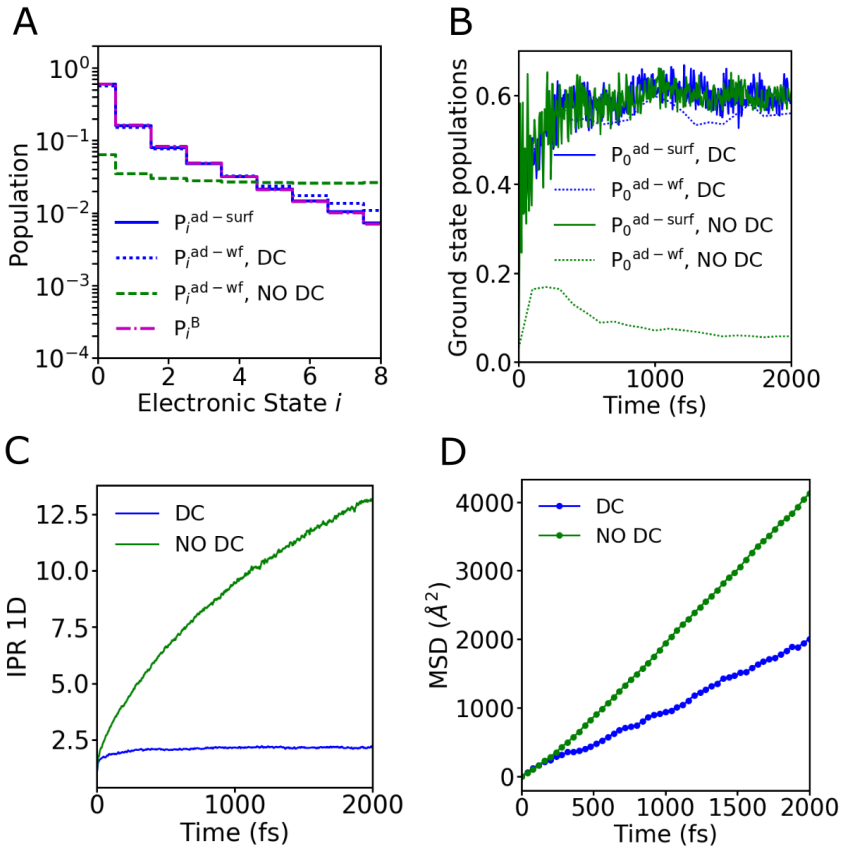

Figure 3.6: Importance of decoherence correction for accurate simulations. Illustrative FOB-SH hole transport trajectories have been carried out for anthracene crystal (ANT). (A) Electronic eigenstate ($P_i^{\mathrm{ad-wf}}$, Eq. 2.19) and surface ($P_i^{\mathrm{ad-surf}}$, Eq. 2.20) population with DC (data in blue) and without DC (green dashed). In the latter case the electronic eigenstates (also denoted adiabatic states) are almost equally populated, i.e. the electronic temperature tends to infinity. (B) Ground state population vs time with DC (blue) and without DC (green). Note that, without decocherence, despite the surface population reaches the correct equilibrium distribution after 300 fs, the ground state population remains severely underestimated. (C) Convergence of IPR with and without DC (blue and green lines). The IPR diverges without DC because of the near equal population of all electronic eigenstates (panel (B)). (D) MSD of the charge carrier (Eq. 2.33), with and without DC along the crystallographic *b* direction (blue and green lines). Without DC the slope of the MSD and mobility are strongly overestimated.

Here I highlight the paramount importance of including DC when studying transport properties in condensed phase systems. I show results for hole transport in anthracene when

the DC is switched off (green lines in Figure 3.6). The reference Boltzmann population (dash-dotted magenta line) is obtained similarly to what explained in Section 3.1.1 for the ELM chain. In this case however, I run 1000 independent equilibrium BOMD trajectories of length 1 ps in the electronic ground state E_0 to sample the exponential average in the free energy expression, Eq. 3.1. First we can see that, when the DC is active (in this case the PDDC time, Eq.2.23, was used), both the adiabatic wavefunction population ($P_i^{\mathrm{ad-wf}}$), Eq. 2.19, dashed blue lines and the surface population ($P_i^{\mathrm{ad-surf}}$), Eq. 2.20, solid blue lines, agree very well with each other and also with the reference Boltzmann population (down to populations of 10^{-2}), with some minor deviations for higher lying states. These are maybe be due to the residual small internal inconsistency associated with frustrated hops. Yet, since the small deviations only occur for states with low population this small discrepancy should have no significant effect on these results. As a further note, the population of excited states within the narrow band that is formed by the frontier orbitals of these molecules is significant for this system suggesting that thermal excitations of the charge carrier cannot be neglected (this point will be extensively discussed in Chapter 4). This aspect underlines the importance of including non-adiabatic transitions for transport processes.

On the other hand, when the DC is switched-off, I note that there is no longer internal consistency (Figure 3.6(A) and (B)), quite the opposite: the quantum population (dashed green line) is almost the same for all electronic states, i.e., the temperature of the electronic subsystem becomes infinite, the infamous problem of the original Ehrenfest and SH methods [38]. As a consequence, the polaron size (IPR) and the mobility are strongly overestimated because most of the higher lying electronic states that are now occupied are more delocalized than the lower lying states (Figure 3.6(C)). Even more seriously, the IPR and the MSD (and so the charge mobility) do not converge with system size and are therefore overestimated. For all these reasons it is of utmost importance to apply DC, otherwise the energy level population and the charge transport dynamics becomes unphysical.

3.3.4 Impact of decoherence on electronic populations

I now discuss the choice of the diabatic population definition (see Section 2.3.1 for details about the definitions), in relation to the effect of the DC on the mobility and system size convergence. Using the best set-up described in the previous Sections (state tracking, SCTC and 0.1 fs for the MD time step), FOB-SH simulations were run for different chain lengths (12, 24, 36 and 48) either without DC or using the pure-dephasing decoherence correc-

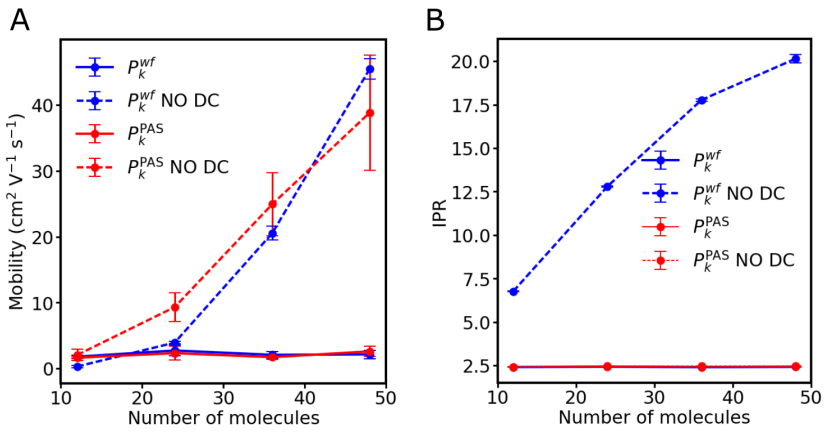

Figure 3.7: Importance of decoherence correction for convergence of (A) charge mobility and (B) IPR with system size. Results are shown of different choices for the diabatic populations used to calculate the charge mobility μ and the inverse participation ratio (IPR): wavefunction (P^{wf}, Eq. 2.30) with DC and without DC (solid and dashed blue lines, respectively) and projected active state population (P^{PAS}, Eq. 2.29) with DC and without DC (solid and dashed red lines, respectively). The data were obtained from FOB-SH simulations of hole transport along an embedded chain of anthracene molecules with a MD time step of 0.1 fs. Error bars are obtained by block-averaging over five independent blocks of 200 trajectories each.

tion schemes (PDDC, Eq. 2.23). For each FOB-SH run, the mobility and IPR for the two different diabatic population definitions P^{wf} and P^{PAS} were calculated (see Section 2.3.1). The results are reported in Figure 3.7 against number of molecules forming the chain. In the original FSSH implementation [81], no DC and P^{PAS} are used to calculate different properties, this set-up corresponds to the dashed red lines in Figure 3.7(A) and (B). We can immediately see that the mobility does not converge with increasing system size. In that case, when the the electronic wavefunction $\Psi(t)$ delocalizes equally over all the available adiabatic states, the corresponding adiabatic populations appearing in the denominator of the hopping probability (Eq. 2.11) are the same for all states (see also Figure 3.6(A)), so hops can be attempted between states localized in completely different positions. The larger the chain, the farther apart the charge can jump after such unphysical (but allowed by FSSH) hops. Thus the mobility for the two different diabatic population definitions increases with the number of molecules. Conversely, the IPR for P^{PAS} (dashed red line) is independent on the system size, showing that the delocalization of the eigenfunction of the active state (ψ_a) is size independent as well. On the contrary, the IPR for P^{wf} (dashed blue line) increases with the chain length, mirroring the delocalization of the electronic wavefunction on the adiabatic states. These results prove that without DC, the mobility cannot converge with different system size whatever the diabatic population definition.

Mobility and IPR obtained with a DC (PDDC time) are shown with solid lines in Figure 3.7(A) and (B) respectively. In contrast with the results obtained without DC, the mobility is well converged with respect to chain length. Adding a DC permits to localize (in adiabatic and diabatic space) the electronic wavefunction $\Psi(t)$, to eliminate the undesired hops present without DC and to converge with system size. The DC also ensures the internal consistency of the method, explaining why the two population definitions behave similarly. The IPR results are similar to the ones for the mobility: convergence for the different system sizes and similar values for all population definitions. In general, I recommend to use the wavefunction population (P^{wf}, Eq. 2.30) as it is generally less affected by potentially undetected trivial crossings. Based on these results, I conclude that a DC is mandatory for calculation of mobility and IPR.

3.4 Conclusion

In this Chapter, I have explored and discussed several possible improvements applicable to any surface hopping code when calculating equilibrium and dynamical properties, i.e. velocity adjustments, decoherence correction (DC) with various decoherence times, spurious charge transfer correction (SCTC), trivial crossings detection and state tracking algorithm. I also discussed the correct way to retrieve important observables from FSSH simulations such as electronic population and charge carrier mobility. I summarize in Table 3.1, the impact that each of these improvements has on the properties of interest for this work.

Table 3.1: Importance of various improvements for accurate properties.

Improvements	Energy conservation	Detailed balance	Internal consistency	Mobility	IPR
Velocity rescaling	✓✓	✓✓	-	✓✓	✓✓
Velocity reversal	-	-	✓	-	-
Decoherence correction	-	-	✓✓	✓✓	✓✓
Spurious charge transfer correction	-	-	-	✓✓	✓
Trivial crossings detection	✓	✓	-	✓✓	✓

✓✓, the correction is very important for a given property. ✓, the correction is reasonably important for a given property. − the correction has no effect on a given property. All the corrections above are implemented in FOB-SH.

Using an organic semiconductor model formed by a dimer of ethylene-like molecules

(ELMs), I have first looked at velocity rescaling after successful hops, equilibrium population of electronic states (i.e. detailed balance), internal consistency and total energy conservation over three orders of magnitude of electronic couplings to cover a broad range of regimes relevant for organic semiconductors (see, e.g., Chapter 4 for simulations of existing OSs). I have shown that good energy conservation and detailed balance is obtained regardless of the decoherence time and algorithm used. In fact, generally speaking, the decoherence biases the dynamics only away from the crossing region and it does not significantly modify the flux between adiabatic states. On the other hand, when comparing the effect of different DCs in restoring the consistency between surface and wavefunction populations, I have shown that the damping-based algorithms with fast decoherence times produce far better results than instantaneous collapsing events and maximize internal consistency across several orders of coupling strengths.

Then, focussing on charge transport in a real organic crystal (i.e. anthracene), I have discussed the influence of the different correction algorithms on two fundamental properties related to the actual efficiency of organic semiconductors: the electronic mobility and the inverse participation ratio (the latter measures the size of the charge carrier). State-tracking algorithm has proven mandatory in case of large number of states to detect the trivial crossings and to map the adiabatic states between two different MD time steps, thus improving the electronic and nuclear dynamics and avoiding spurious long-range charge transfers. Without a state-tracking procedure, the mean squared displacement (MSD) does not reach a diffusive linear regime, prohibiting mobility calculation. In addition, to ensure a convergence of the electronic mobility with the size of the system and the number of excited states, I have shown that a combination of DC scheme and decoherence-induced spurious charge transfer correction (SCTC) is required. Besides these paramount improvements to the surface hopping algorithm, different definitions used in the literature for the MSD and for the electronic population definition have been compared. I have shown that two commonly used definition for the mean squared displacement (MSD, Eq. 2.33, and MSD^{coc}, Eq. 2.34) give the same diffusion coefficient and the same mobility, whereas the third one (MSD^{var}, Eq. 2.35), which is related to the spreading of the wavefunction, rather then to the diffusion of the charge carrier, yields always a zero slope as the polaron reaches a finite equilibrium size and does not grow indefinitely. Regarding the choice of the electronic population to use in FSSH, I have compared the two electronic populations suggested in

the literature (P^{wf}, Eq. 2.30, and P^{PAS}, Eq. 2.29) and shown that these definitions coincide when a DC is active. Nevertheless, the use of P^{wf} is recommended for transport property calculations as it is in general less affected by trivial crossings.

In conclusion, a well-founded set-up to run fewest switches surface hopping simulation of charge transport that converges electronic mobilities for different time steps and system sizes and that achieves detailed balance and good internal consistency, have been established. The actual physics of charge/exciton transport dynamics will be considered in the following Chapters of this thesis.

Chapter 4

Room temperature mobilities in molecular semiconducting crystals

In this Chapter*, which is the central result of my work, I present the application of FOB-SH to the calculation of room temperature charge mobilities of a series of experimentally well-known molecular crystals.

I will show that FOB-SH –when supplemented with the algorithmic improvements considered in Chapter 3– is able to give near-quantitative agreement with experimental room temperature mobilities over three orders of magnitude successfully bridging the regime where hopping and band models are not well-justified or invalid (Section 4.2). I will carefully discuss the role of the disorder, induced by local and non-local electron-phonon couplings fluctuations, on the delocalization of the states and the subsequent formation of a polaronic charge state (extended over several molecules in the most conductive crystals) and its motion within the crystal (Section 4.3 and Section 4.4). Importantly, I will show that thermal intra-band excitations from modestly delocalized band edge states (up to 5 nm or 10-20 molecules) to highly delocalized tail states (up to 10 nm or 40-60 molecules in the most conductive materials) give rise to short, $\approx$ 10 fs-long bursts of the charge carrier wavefunction that drives the spatial displacement of the polaron, resulting in carrier diffusion and mobility. I refer to these wavefunction displacements as "diffusive jumps" and I will show that they are at the heart of the transport mechanism in OSs. I will discuss the implications of this work for the search of new efficient organic semiconducting materials and I will establish some design principles that will hopefully help to advance the field of organic electronics.

*The basis of this Chapter has been published in Giannini, S. et al. Quantum localization and delocalization of charge carriers in organic semiconducting crystals. *Nat. Comm.* 10, 3843 (2019) and in Giannini, S. et al. Flickering Polarons Extending over Ten Nanometres Mediate Charge Transport in High Mobility Organic Crystals. *Adv. Theory Simul.* 3, 2000093 (2020). The Kohn-Sham DFT calculations in Figure 4.4 have been performed by Dr. Orestis G. Ziogos as well as the AOM scaling factor parametrization of pyrene and DATT crystals. Matthew Ellis developed the python code for the wavefunction visualization and movie making, which I have extensively used to plot wavefunction delocalization and its time dependent dynamics.

4.1 Objectives and investigated molecular crystals

As discussed in the Introduction, OSs differ from inorganic semiconductors in two important aspects: they are made of small or polymeric molecules that are held together by weak van der Waals interactions rather than covalent bonds. Hence, thermal motions of the molecules around their lattice positions is very pronounced already at room temperature and leads to large fluctuations of electronic coupling, also termed off-diagonal electron-phonon coupling that impacts negatively the charge mobility (see also Chapter 5). Secondly, the static dielectric constant of OSs is typically very small and, as a consequence, the reorganization energy λ or local electron-phonon coupling is small, too (0.2 eV or less). These two material properties place charge transport in OSs in a regime that challenges traditional transport descriptions [12, 15, 16, 135, 147, 148]. It is in these conditions that a numerical scheme to explicitly solve the time dependent evolution of the wavefunction, like FOB-SH, can prove extremely useful and give insights into the actual wavefunction dynamics bridging the gap between different mechanistic regimes and permitting to go beyond existing analytic theories. FOB-SH results could serve in turn as a benchmark for existing and new theories for describing the transport in OSs.

The OSs investigated in this work are 1,4-bis(4-methylstyryl)benzene (pMSB-h^+) [149], pyrene (PYR-e^-), naphthalene (NAP-h^+) [150], anthracene (ANT-h^+) [151], perylene (PER-e^-) [152], rubrene (RUB-h^+) [153], dianthra[2,3-b:20,30-f]thieno[3,2-b]thiophene (DATT-h^+) [154] and pentacene (PEN-h^+) [155] (polymorph I and $d(001)$-spacing of 14.1 Å according to the classification in Ref. [156]) (see Figure 4.1 and Table 4.1 for the crystal structures). The appendix -h^+ and -e^- is used to distinguish between hole and electron transfer systems. I chose these systems as they have been well characterized experimentally and in order to represent low, medium and highly conductive OSs (e.g. pMSB, PER and RUB, respectively) with their experimental mobilities spanning three orders of magnitude, thus providing an ideal benchmark for the performance of the FOB-SH method in various transport regimes. In particular, for NAP, ANT and PER reliable experimental time of flight (TOF) bulk mobilities can be found in Ref. [98, 157, 158]. The experimental conditions of this technique match particularly closely the FOB-SH simulation conditions (see Section 4.2.1 for a discussion on this point). pMSB, DATT, PEN and RUB mobilities have been measured via fabrication of organic field effect transistors and other techniques [149, 154, 159, 160] such as space-charge limited current (SCLC)

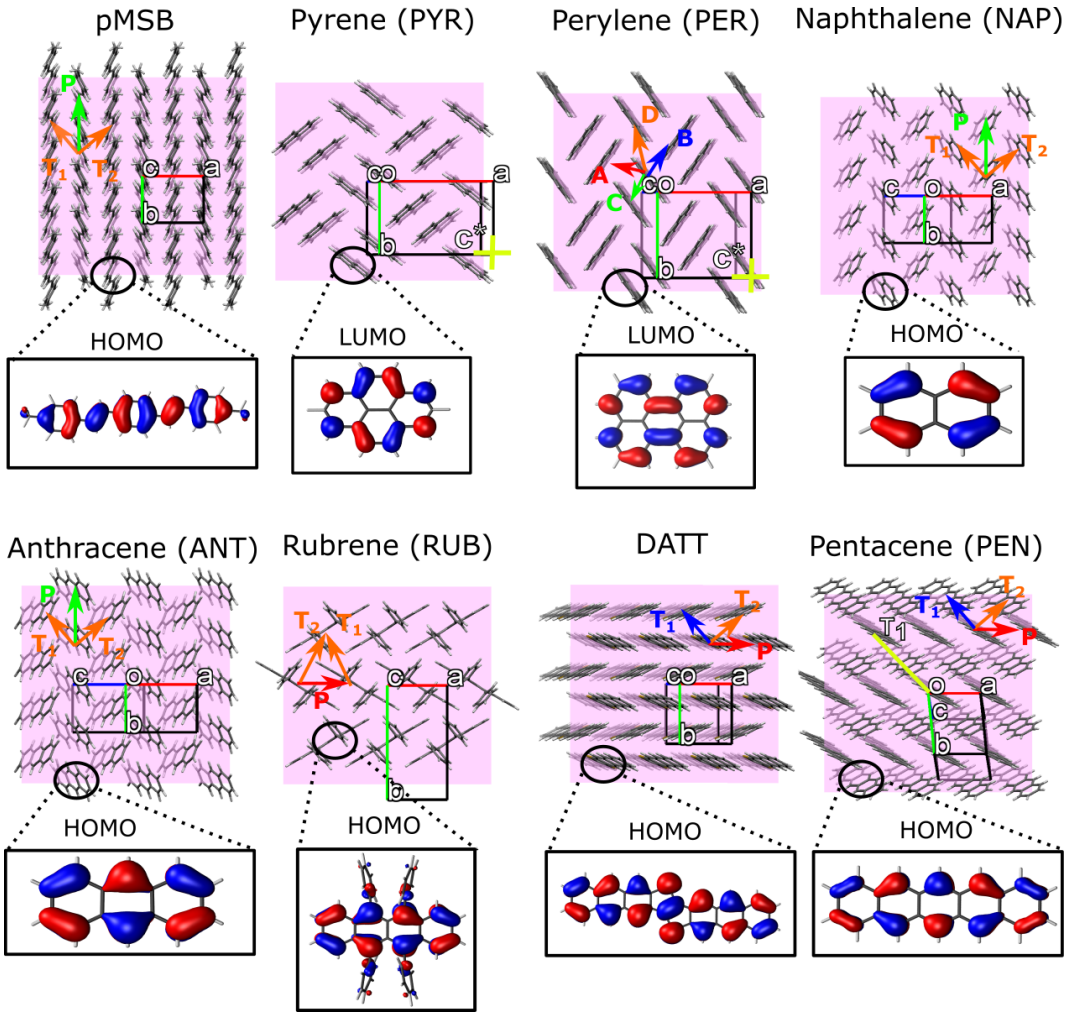

Figure 4.1: Molecular herringbone layer packing for all investigated OSs. The unit cell axes *a*, *b*, *c* are shown in red, green and blue, the herringbone layer is in the *a*-*b* plane, other specific directions discussed in the text are shown in yellow. The main coupling directions (values reported in Table 4.3) are indicated by arrows. Same colors are used when symmetry elements are present along T_1 and T_2 directions. The DFT highest occupied molecular orbital (HOMO) and lowest unoccupied molecular orbital (LUMO) of single molecules are depicted as isosurfaces for OSs where hole transfer and electron transfer is studied, respectively.

and Hall-effect [11, 161]. RUB and PEN are certainly the most widely studied crystals. While there is a large consensus about the intrinsic mobility (above 15 $cm^2\ V^{-1}\ s^{-1}$) of RUB [29, 159, 160], the same quantity is less reproducible in PEN (presumably due to the presence of different polymorphs [162, 163] and the technical difficulties in handling this crystal which is easily crackable [164]). Interestingly, Marumoto et al. in Ref. [19] have been able to measure the spatial extend of the carrier wavefunction in PEN that can be compared with FOB-SH calculated IPR (see Section 4.2.2 below).

As common to many organic crystals (with the notable exception of fullerene), the

molecules pack into crystal structures where a clear high-mobility $a-b$ plane can be identified (i.e. the plane featuring the largest π-stacking interactions). Indeed the electronic couplings and also the mobility perpendicular to this plane (c^* direction) are usually smaller by one to two orders of magnitude [45, 56, 85] (see Section 4.2.2). In the following, I will use the FOB-SH methodology to uncover the nature and transport mechanism of charge carriers in the aforementioned eight single crystalline OSs, I will present both the transport in embedded 1D chains of molecules (similarly to what was done in Section 3.1.2 for anthracene) and I will go one step further by analysing the transport and mobility in the 2D high conductive planes of these OSs.

4.1.1 Simulation details

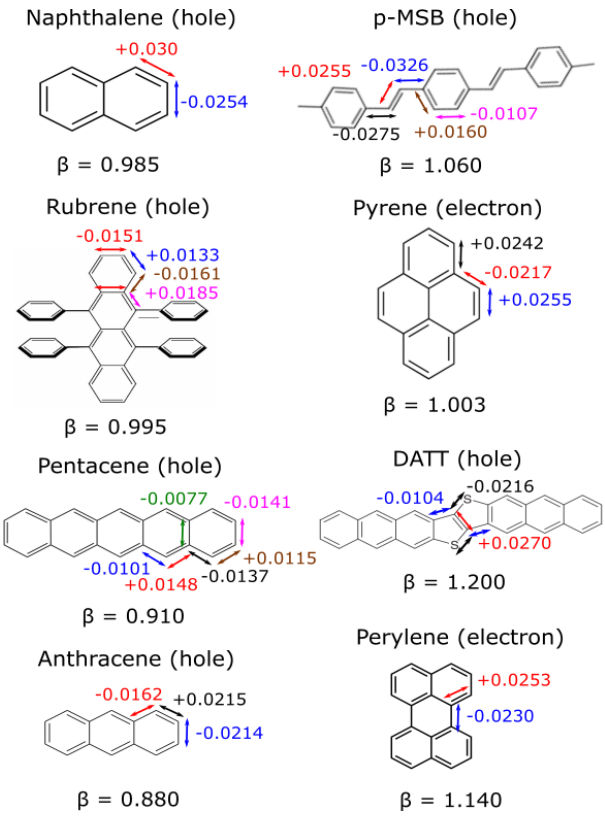

Figure 4.2: Force field parametrization charged states. Changes in bond length upon change from neutral to charged state, as obtained from DFT calculations. Displaced bond distances in Å are reported with different colours according to the displaced bonds. The + and − signs indicate an increase and decrease in bond length going from the neutral to the charged system, respectively. The displacements are used to parametrize the force field for the molecules in their charged state. For clarity, displacements symmetric to the ones indicated are not shown. Scaling factor β for force field parametrization of reorganization energy, as described in Section 2.1.3, is also reported for each system.

The force field parameters for calculation of the site energies of the Hamiltonian Eq. 2.5, ε_k, are parametrized to reproduce the intramolecular reorganization energy from DFT calculations (Eq. 2.6) as reported in Table 4.1 and explained in Section 2.1.3. I note in passing that reorganization energy is assumed to be equal to the intramolecular (or "inner-sphere") contribution. The intermolecular (or "outer-sphere") contribution is typically very small in apolar OSs [100, 165] studied here and is neglected. For the parametrization I

followed the same protocol established in Section 2.1.3 and validated for the calculation of transport properties in an embedded chain of anthracene in Section 3.1.2. Reorganization energies and the other force field parameters used are reported in Table 4.1 and Figure 4.2, respectively.

Notably, electrostatic interactions have been left out of the intermolecular interaction model, as already done for anthracene chains in Chapter 3, for few reasons. Firstly, for the systems investigated here, electrostatic interactions in the form of fixed point charges do not significantly alter the energetics of the charge localized states because only the charged molecule carries a net charge while the other molecules are charge neutral and apolar. In addition, it is well known that site energy fluctuations and hence reorganization free energies are overestimated for fixed point-charge models [99, 136, 137]. Therefore, one should include electronic polarization as well to counteract this overestimation, thereby adding an additional layer of complexity and computational cost (as induced polarizability usually means performing self-consistent iterations). Hence, for the purpose of computational efficiency, electrostatic interactions were switched off. I expect that this is no longer a good approximation for crystals formed of polar or hydrogen bonded molecules. In this case the full electrostatics including electronic polarization of the molecules should be included.

The protocol for the calculations of the reference electronic couplings via sFODFT was, again, described in Section 2.1.4 (and for anthracene in Section 3.1.2). In brief, several crystal pairs are extracted from an MD trajectory for each system and sFODFT calculations performed on each of these pairs. These values are used to extract the AOM scaling factor C, $H_{kl} = C\bar{S}_{kl}$ in Eq. 2.7, to be used within FOB-SH simulations. Reference sFODFT electronic couplings, AOM electronic couplings and C values are summarized in Table 4.3 for all systems investigated. The reliability of the tight-binding Hamiltonian constructed in this way will be tested and discussed in Section 4.1.3.

For each OS, I built a series of supercells of increasing size from the experimental crystallographic unit cell (Table 4.1). The dimensions of some of the largest supercells constructed are summarized in Table 4.2 for both embedded 1D chains and full 2D planes. These supercells were equilibrated in periodic boundary conditions for the neutral state for at least 250 ps in the NVT ensemble to a target temperature of 300 K using a Nosé-Hoover thermostat, followed by at least 250 ps equilibration in the NVE ensemble (similarly to what was done in Section 3.1.2). From the NVE trajectory an uncorrelated set of positions

Table 4.1: Unit cell parameters (Å) and reorganization energies (meV) for the OSs investigated in this work

System	a	b	c	α	β	γ	λ (meV)
RUB-h$^+$	7.184	14.433	26.898	90.00	90.00	90.00	152
PEN-h$^+$	6.275	7.714	14.442	76.75	88.01	84.52	98
DATT-h$^+$	6.259	7.569	20.826	90.00	92.78	90.00	88
ANT-h$^+$	8.562	6.038	11.184	90.00	124.70	90.00	142
NAP-h$^+$	8.098	5.953	8.652	90.00	124.40	90.00	187
PER-e$^-$	11.277	10.826	10.263	90.00	100.55	90.00	177
PYR-e$^-$	13.649	9.256	8.470	90.00	100.28	90.00	222
pMSB-h$^+$	7.362	5.883	38.950	90.00	90.00	90.00	255

and velocities were chosen as starting configurations for FOB-SH simulations. Molecules along a 1D chain (of length given in Table 4.2) or within a rectangular region of the $a-b$ high mobility plane were treated as electronically active, i.e., as molecular sites or fragments for construction of the electronic Hamiltonian (Eq. 2.5), with their frontier orbital (HOMO or LUMO) contributing to the expansion of the carrier wavefunction (Eq. 2.3). All other molecules of the supercell were treated electronically inactive. The initial carrier wavefunction is chosen to be localized on a single active molecule m, $\Psi(0) = \phi_m$ and propagated in time according to the FOB-SH algorithm in the NVE ensemble. All FOB-SH simulations applied a decoherence correction (DC), state-tracking for detection of trivial crossings, a projection algorithm for removal of decoherence correction-induced artificial long-range charge transfer (SCTC) and adjustment of the velocities in the direction of the non-adiabatic coupling vector in case of a successful surface hop as found in Chapter 3. The nuclear time step, Δt, ranged from 0.01 fs to 0.1 fs depending on the size of the systems. For each system and each simulation presented here at least 300 FOB-SH trajectories of length 1 ps were run (owing to the lower computational cost, from 600 to 1000 trajectories could be run when simulating 1D chains). The components of the diffusion tensor Eq. 2.33 were block averaged over 3 or 5 blocks depending on the number of trajectories (with an equal number of trajectories for each block) for calculation of error bars.

Here I note that for all crystals except pentacene the Cartesian coordinates (x,y) of the supercell were chosen parallel to the crystallographic directions (a,b) that define the high mobility plane (this was possible since they form either orthorhombic (pMSB, PEN) or monoclinic crystals (NAP, PER, PYR, ANT, DATT)). In this representation the off-diagonal components of the diffusion tensor characterizing the 2D high conducting plane are zero

Table 4.2: Supercell details for the investigated systems.

System	Geom.	Z	Dir.[a]	Super cell[b]	Tot. atoms[c]	Active molecules[d]
RUB	Orthorombic	4	a	44x2x2	49280	30
			$a-b$	30x17x1	142800	900
PEN	Triclinic	2	T_1	31x31x1	69192	61
			$a-b$	20x30x1	43200	800
DATT	Monoclinic	2	a	90x3x1	25920	88
			$a-b$	14x14x2	37632	216[e]
PER	Monoclinic	4	c^*	2x2x22	11264	20
			a	17x2x2	8704	20
			$a-b$	15x15x2	57600	564
PYR	Monoclinic	4	c^*	2x2x28	11648	25
ANT	Monoclinic	2	a	28x4x2	10752	30
			b	4x28x2	10752	24
			$a-b$	18x28x2	48384	378
NAP	Monoclinic	2	b	4x24x4	13824	20
			$a-b$	15x18x2	19440	284
pMSB	Orthorombic	2	b	4x25x1	18400	13
			$a-b$	14x14x1	36064	170

[a] Super cell direction along which mobilities and IPR as reported in Figures 4.5 and 4.7 are calculated. [b] Largest supercell size used in this work. [c] Total number of atoms in some of the largest supercells used. [d] Number of electronically active molecules required for converged FOB-SH mobilities and IPR as reported in Figures 4.5 and 4.7. When considering c^* direction the IPR is evaluated along the single chain. Note that larger electronically active regions than the ones reported here have been used for convergence tests for MD time step, Figure 4.6. [e] This size is only used for IPR calculation for which this value is converged, not for mobility calculation.

due to symmetry (note that the full 3D tensor is fully diagonal in the Cartesian reference framework only for orthorhombic systems but not for monoclinic ones). For pentacene (triclinic) the diffusion tensor was diagonalized when calculating mobility within the 2D plane. The number of active molecules required for convergence of charge mobility and the largest number of active molecules considered for each OS are summarized in Table 4.2. All simulations were carried out with our in-house implementation of FOB-SH in the CP2K simulation package [91].

4.1.2 Importance of the sign of the coupling matrix elements H_{kl}

Coupling (or off-diagonal) matrix elements, H_{kl}, are obtained for molecular dimers forming the crystal using the AOM [92] as described already in Section 2.1.4 and Section 3.1.2. As

explained before, this method is based on the observation that for conjugated molecules the coupling depends linearly on the orbital overlap, to a good approximation, $H_{kl} = C\bar{S}_{kl}$ where C is a constant determined from DFT calculations and $\bar{S}_{kl}$ is the overlap between HOMO (LUMO) orbitals on molecules k and l projected on a minimum Slater basis (see Section 2.1.4). Considering the actual coupling-overlap sign relationship (and not just the respective absolute values as done in Section 3.1.2), sFODFT gives $C < 0$ for these systems (see below).

For 1D systems (e.g. 1D embedded chains like anthracene in Section 3.1.2) with 2 nearest neighbour couplings per site, the eigenvalues and eigenvectors of the tight-binding Hamiltonian (Eq. 2.5) found with these couplings are invariant with respect to a change of sign of any nearest neighbour off-diagonal element H_{kl}. Therefore the sign of H_{kl} and the constant of proportion, C, between overlap, $\bar{S}_{kl}$, and coupling matrix element in the AOM [92] can be chosen arbitrarily at the beginning of the non-adiabatic dynamics simulation ($t = 0$). Indeed, for this simple situation (i.e. Hückel model) a well-known analytic expression for the eigenvalue spectrum exists depending only on the magnitude of electronic coupling, $|H_{kl}|$, not on the sign. This is no longer generally true for 2D and 3D systems, particularly not for the 2D simulations within the herringbone layer of the systems in Figure 4.1 with at least three unique couplings per site and translational symmetry [56].

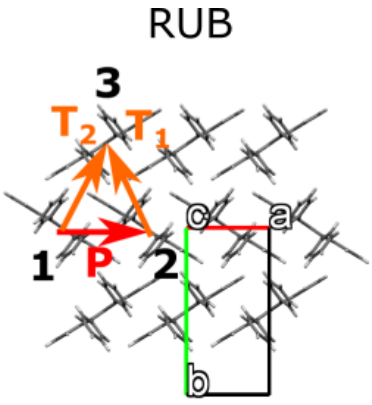

Figure 4.3: Herringbone layer ($a-b$) plane of rubrene, in which three coupled nearest neighbours are indicated and 1,2,3.

Considering e.g. rubrene (Figure 4.3), the phase or sign of the HOMO orbitals ϕ_l on the two molecules part of the unit cell of rubrene, $l = 1$ and 3, can be chosen arbitrarily at the beginning of the non-adiabatic dynamics simulation ($t = 0$) as they can be considered merely as basis functions for expansion of the carrier wavefunction, $\Psi(t)$, according to

Eq. 2.2. Hence the sign of the coupling between, P and T_2 can be freely chosen via a suitable choice of the sign of the orbitals on each of the two molecules 1 and 3. Importantly, this choice then fixes the sign of the coupling along T_1 because the unit cell is replicated along a and molecule 2 gets the same orbital as molecule 1. If one wanted to change the sign of T_1, one would also need to change the sign on molecule T_2 as well. Therefore, the eigenvalues and eigenvectors of the Hamiltonian remain invariant upon simultaneous change of sign of two couplings T_1 and T_2 (i.e. sign combination (+,-,-) for the pairs P, T_1 and T_2 respectively, is equivalent to the one (+,+,+)), but they no longer remain invariant if the sign of all three couplings are simultaneously changed (i.e. sign combination (-,-,-) will produce an inverted eigenvalues spectrum with respect to (+,+,+)). An inconsistent sign of any one of the three couplings has a major effect on the eigenvalues and eigenvectors affecting the symmetry of the electronic density of states (DOS), the extent and degree of anisotropy of the delocalization of the eigenstates (see Section 4.1.3), and ultimately the charge carrier dynamics and mobility, see also Refs. [56–58]. I also emphasize that it is important to maintain the sign of the orbitals between two MD time steps, otherwise the carrier dynamics (Eq. 2.4) becomes erroneous.

What remains to be investigated is the sign consistency between the site energies, ε_k, and the coupling matrix elements H_{kl} in the Hamiltonian (Eq. 2.5). For FOB-SH simulation of excess electron transport, the site energies, ε_k, that I obtain from the force field, correspond to electronic energy levels of the excess electron and the electronic coupling between them should have the same sign as the one obtained from electronic structure calculations. As mentioned before, it turns out that in electronic structure calculations, e.g. constraint DFT (CDFT) or sFODFT, the sign relation between H_{kl} and the overlap S_{kl} between the charge transfer states (charge transfer determinants in CDFT and simply frontier orbitals in sFODFT) is antisymmetric for the systems investigated, see Table 4.3. Therefore in the AOM estimate of the sFODFT electronic couplings for excess electron transport, the constant of proportion $C < 0$. At finite temperature, the occupation of each eigenstate i of the electronic Hamiltonian (also denoted conduction band state in the following) is proportional to $\exp[-E_{i,\mathrm{e}}/(k_\mathrm{B}T)]$, where $E_{i,\mathrm{e}}$ is the corresponding electronic eigenvalue, k_B the Boltzmann constant and T the temperature.

For FOB-SH simulation of hole transport, the site energies are obtained from the force field correspond to hole energy levels, not electronic energy levels. This is evident if one

Table 4.3: Computed electronic couplings and orbital overlaps for crystal structures and along MD trajectories at room temperature

			sFODFT (crystal)[a]		AOM[b] (crystal)		AOM[b] (MD)		
		Dist. (Å)	H_{kl} (meV)	S_{kl}	H_{kl} (meV)	$\bar{S}_{kl}$	$\langle H_{kl}\rangle^c$ (meV)	σ^d (meV)	C^e
RUB-h$^+$	P	7.18	113.4	-0.0186	92.3	-0.0441	73.7	23.4	-2.1
	T_2	8.03	-21.0	0.0039	-21.9	0.0105	-17.8	6.2	-2.1
	T_1	8.03	-21.0	0.0039	-21.9	0.0105	-17.8	6.2	-2.1
PEN-h$^+$	P	6.28	48.7	-0.0068	34.5	-0.0140	25.7	14.1	-2.5
	T_2	5.2	-69.3	0.0108	-66.0	0.0268	-61.1	27.1	-2.5
	T_1	4.73	116.1	-0.0193	116.7	-0.0474	110.7	24.1	-2.5
PER-e$^-$	A	6.1	59.6	-0.0181	53.1	-0.0166	41.7	18.2	-3.2
	B	6.47	-27.2	0.0114	-39.4	0.0123	-33.1	21.7	-3.2
	C	8.1	51.9	-0.0132	57.7	-0.0180	54.0	13.8	-3.2
	D	3.88	46.8	-0.0020	38.9	-0.0122	62.1	85.3	-3.2
PER-e$^-$[f]	c^*	10.26	8.3	-0.00160	7.0	-0.00219	-8.3	6.4	-3.2
PYR-e$^-$[f]	c^*	8.47	26.7	-0.07882	18.7	-0.0049	16.2	11.9	-3.8
DATT-h$^+$	P	6.26	94.9	-0.0137	74.8	-0.0122	69.1	24.1	-6.1
ANT-h$^+$	P	6.04	-57.0	0.0090	-57.5	0.0186	-50.5	30.2	-3.1
	T_2	5.24	-25.2	0.0038	-30.7	0.0099	-27.3	45.3	-3.1
	T_1	5.24	-25.2	0.0038	-30.7	0.0099	-27.3	45.3	-3.1
NAP-h$^+$	P	5.95	-46.2	0.0076	-35.7	0.0170	-30.1	17.6	-2.1
	T_2	5.03	10.8	-0.0027	16.2	-0.0077	21.0	24.6	-2.1
	T_1	5.03	10.8	-0.0027	16.2	-0.0077	21.0	24.6	-2.1
pMSB-h$^+$	P	5.88	-21.5	0.0034	-15.6	0.0068	-11.6	5.5	-2.3
	T_2	4.71	41.7	-0.0061	30.1	-0.0131	33.5	16.7	-2.3
	T_1	4.71	41.7	-0.0061	30.1	-0.0131	33.5	16.7	-2.3

[a] sFODFT couplings have been calculated as detailed in the text. [b] $H_{kl} = C\bar{S}_{kl}$ and the scaling factor C parametrized as explained in Section 2.1.4. [c] $\langle \dots \rangle$ indicates averaging over 100 2ps-long MD trajectories. [d] $\sigma = \sqrt{\langle (H_{kl} - \langle H_{kl}\rangle)^2\rangle}$. Note that $V^2 = \langle |H_{kl}|^2\rangle = \langle H_{kl}\rangle^2 + \sigma^2$. [e] For hole transport systems, $C = -C_{\log}$ is generally used for plane simulations as done in Ref. [86] and explained in Section 2.1.4, whereas $C = -C_{\text{lin}}$ is generally used for chains simulations to further improve the accuracy of AOM couplings along the high mobility direction (the corresponding coupling values $V = \sqrt{\langle |H_{kl}|^2\rangle}$ related to $C = -C_{\text{lin}}$ are reported in Ref. [85] and omitted from this table for clarity). [f] Only 1D chains have been considered along c^* direction perpendicular to the herringbone layer.

bears in mind that the site energy $\varepsilon_k(\mathbf{R})$ is minimum when site k is in the minimum energy geometry of the charged state (+1) and all other sites $l \neq k$ in the minimum energy geometry of the neutral state (if it was an electronic energy level the energy of this state would be maximum). Therefore the couplings between these states should be the coupling between hole

states, not electronic states. Hence, the sign of the electronic couplings obtained from DFT electronic structure and AOM calculations needs to be inverted for FOB-SH simulation of hole transport, which I do by inverting the sign $C \rightarrow -C$ (see also Ref. [166] for an independent discussion on this point). The occupation of the hole eigenstate i is thus proportional to $\exp[-E_{i,\mathrm{h}}/(k_{\mathrm{B}}T)]$, where $E_{i,\mathrm{h}}$ is the ith hole eigenvalue. In the simulations on hole transport the hole Hamiltonians were constructed in this way and inverting the sign of H_{kl} obtained from electronic structure calculations by changing the sign of C from negative to positive values [85, 86]. This allows to use the standard hopping procedure and forces expression presented in Section 2.1.5 and Section 2.1.6, respectively (see Ref. [166]). For comparison to DFT band structure calculations (see Section 4.1.3) one needs to go back from hole to electronic energy levels by reversing the sign of the hole energy levels, $E_{i,\mathrm{e}} = -E_{i,\mathrm{h}}$. This was done for the hole transport systems in Figure 4.4 further below. The occupation of the electronic level i by the hole is then proportional to $\exp[E_{i,\mathrm{e}}/(k_{\mathrm{B}}T)]$.

4.1.3 Benchmarking the tight-binding Hamiltonian and DOS

Before calculating mobility and wavefunction delocalization, I assess the quality of the electronic Hamiltonian in Eq. 2.5 by comparing the density of its eigenstates against the density of states (DOS) obtained from Kohn-Sham DFT band structure calculations and looking at the effect of the disorder on the states delocalization as a function of energy. The DOS is usually defined as:

$$\mathrm{DOS}(E) = \sum_i \delta(E - E_i) \tag{4.1}$$

with $\{E_i\}$ the set of eigenvalues of the electronic Hamiltonian. I constructed a static (i.e. time-independent) electronic Hamiltonian of the form of Eq. 2.5 for the high-mobility plane of the OSs, comprised of 5,000 sites and using the atomic coordinates from the experimental crystal structure. All the molecules in the plane are equivalent due to symmetry, hence all the site energies, ε_k, can be set to zero. In PEN the two molecules in the unit cell are not equivalent but the site energy is expected to be very similar. In pMSB, NAP, ANT, PEN and RUB each molecule is surrounded by 6 closest neighbours and there are only 3 sizeable couplings, H_{kl}, that we include along the P, T_1 and T_2 directions, denoted in the following H_P, H_{T1} and H_{T2} (see Figure 4.1). All other couplings are set to zero. In PER the herringbone layer is more complicated and 4 sizeable couplings are included. Couplings were calculated with sFODFT [99, 102] and AOM [92] (AOM is then use to recompute the Hamiltonian along FOB-SH dynamics). In particular, sFODFT calculations were carried

out as already described in Section 3.1.2 with the CPMD program package [105] using the PBE exchange correlation functional [167, 168]. The sign consistency of the couplings between molecules was ensured by imposing consistent phase relationships between orbitals that are coupled in a given pair.

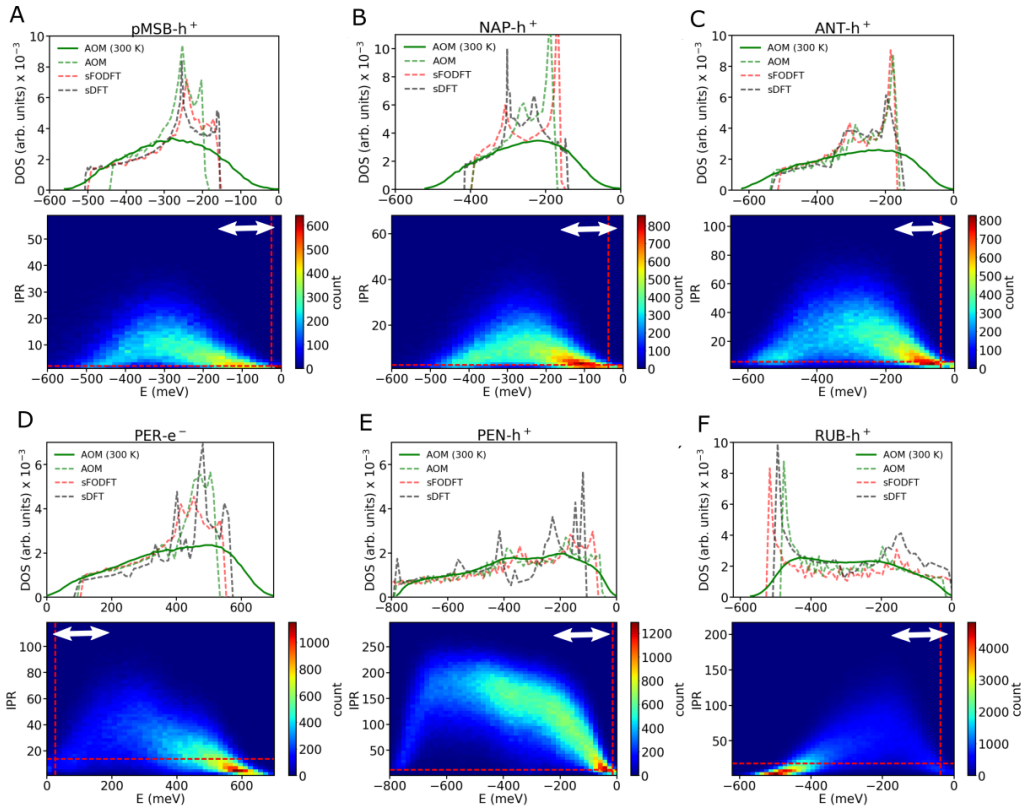

Figure 4.4: Normalized density of states (DOS) of HOMO and LUMO bands for hole and electron transfer systems, respectively. DOS for sDFT (dashed black), sFODFT (dashed red) and AOM (dashed green) are calculated for the static crystal structure as described in the text, by using only the coupling interactions represented in Figure 4.1 for each of the OSs analysed in this work. DOS for AOM (300 K), indicated with solid green lines, are computed from Hamiltonians extracted from a representative FOB-SH trajectory and including the effect of thermal disorder. The latter DOS are smoother than the DOS of the static (frozen) Hamiltonian, due to the fluctuations of electronic couplings and site energies. Bottom panels display 2D histograms correlating the delocalization of the band states, quantified by the inverse participation ratio IPR (Eq. 2.39), and their energies. Dashed red lines are used to indicate time averages of the band active state energy E_a and the active state delocalization IPR_a, with a being the active state index. Double white arrows indicate the thermally accessible (valence or conduction) band tail regions for the excess hole or electron.

Reference periodic Kohn-Sham DFT band structure calculations were carried out on the crystallographic unit cells with k-point sampling. Orbitals were expanded in plane-waves using the PBE exchange correlation functional [167, 168] and ultrasoft Rappe-Rabe-Kaxiras-Joannopoulos pseudopotentials [169] with a wavefunction cutoff of 40 Ry. The Blöchl tetrahedra method [170] was employed for reciprocal space sampling using k-point

meshes of $8 \times 8 \times 1$ for ANT and PER, $10 \times 10 \times 1$ for RUB, $12 \times 12 \times 1$ for PEN, and $15 \times 15 \times 1$ for NAP and pMSB. A slab vacuum larger than 1 nm was used for all DFT simulations. All plane-wave DFT calculations were carried out using the Quantum Espresso code [171]. The DFT eigenvalues for hole and electron transfer systems were scaled by a factor of 1.348 and 1.325 (referred to as sDFT in Figure 4.4), respectively, to remain consistent with the scaling of electronic coupling values in sFODFT as recommended in a previous ab-inito benchmark study [102, 103] .

The DOS profiles are shown in Figure 4.4. The agreement between the electronic Hamiltonian (Eq. 2.5) with AOM/sFODFT couplings (data in dashed green/red lines) and sDFT band structure calculations (data in dashed black lines) is generally good, most of the peaks are reproduced, even though with some differences in height and deviations in positions of typically a few 10 meV. The bandwidth also compares very favourably with the reference sDFT data with typical errors of less than 50 meV. I note in passing that the bandwidth is related to electronic couplings by $W_{\text{band}} = a\sqrt{H_P^2 + H_{T1}^2 + H_{T2}^2}$ [15], where a is a system dependent prefactor, $a > 4$ ($W_{\text{band}} = 4H_{kl}$ for a chain of molecules with only nearest neighbour couplings H_{kl}). The computed DOS also validates the sign of the couplings in sFODFT and AOM calculations reported in Table 4.3. Generally, if one of the signs (that is symmetry related with the other) is inverted, the DOS significantly differs from the one obtained from sDFT [57]. Related to this, we can notice a clear asymmetry in the DOS for the systems considered here. All hole transport materials except RUB exhibit large peaks at the top of the valence band whereas RUB exhibits a prominent peak at the bottom of the valence band. As shown by Fratini et al. [56] this is a particular feature of the electronic Hamiltonian that characterizes transport in the 2D planes of the hole transfer materials studied: when the product of the three electronic couplings H_P, H_{T1}, H_{T2} is positive, as e.g. in RUB, the DOS peaks at the bottom edge of the valence band and vice versa if the product is negative (pMSB, NAP, ANT and PEN). The opposite is valid for electron transfer systems (e.g. PER).

The Hamiltonian investigated so far is for $T = 0$, all eigenstates are delocalized. To investigate the effect of finite temperature on DOS and eigenstate localization I have carried out 1 ps FOB-SH molecular dynamics at 300 K and averaged over 500 configurations (data in solid green lines). During the FOB-SH run both the site energies and coupling matrix elements of the Hamiltonian (Eq. 2.5) fluctuate in time, hence both diagonal and off-diagonal

thermal disorder are included. As expected, the DOS (data in solid green lines) are now much broader (up to 3 times for some systems) and the sharp band edges have changed into smooth tails, while the aforementioned asymmetry in the DOS is still clearly visible.

Importantly, the thermal disorder in the electronic Hamiltonian leads to localization of all eigenstates. This dynamical localization is short lived (transient localization) and survives only up to the timescale of the molecular vibrations (see Section 1.3.3). This constitutes a fundamental difference from the static chemical or structural disorder, which instead can cause full localization of the carriers via a quantum process known as Anderson localization [172]. Here I analyse the degree of localization in some detail as it profoundly impacts the charge mobility of these materials (see, e.g., Section 4.3.1). Specifically, I resolve the DOS in terms of the inverse participation ratio of the states at a given energy (Eq. 2.39) resulting in the IPR-resolved DOS shown in Figure 4.4 (bottom panels). For all hole conducting materials except RUB, the top of the valence band is exclusively formed by a dense manifold of relatively localized states (average $\langle \mathrm{IPR}_a \rangle$ = 2 for pMSB to 20 for PEN at $E = -1.5\ k_\mathrm{B}T$, $T = 300$ K, horizontal dashed red lines), while the most delocalized states can be found in the middle of the valence band at $E \approx -300$ meV and are thus thermally inaccessible (IPR ≈ 30 for pMSB and 200 for PEN). Strikingly, in RUB the pattern of eigenstate localization is inverted. Thermally accessible states with a relatively high degree of delocalization can be found at the top of the valence band ($\langle \mathrm{IPR}_a \rangle$ = 15 at $E = -1.5\ k_\mathrm{B}T$, $T = 300$ K) and a dense manifold of localized states at the bottom of the valence band. The same trend was previously observed by Fratini et al. [56] who showed that this is again a particular feature of the Hamiltonian (Eq. 2.5) for 2D transport with three couplings H_P, H_{T1}, H_{T2}: if the product is positive, as e.g. in RUB, eigenstates tend to be more delocalized at the top than at the bottom of the valence band and vice versa for a negative sign combination. The opposite is true for electron transfer systems as well. This observation provides a rational for the high hole mobility in rubrene compared to the other materials studied since the charge can access more delocalized states at the same thermal energy cost, as I will discuss in the following Sections.

4.2 Charge mobility and wavefunction delocalization

After addressing some of the details concerning experimental measurements of charge mobility, I present in this section mobility results (in embedded 1D chains and 2D high mobility planes) and the charge transport mechanism in organic semiconductors obtained using

FOB-SH. I will also compare these numerical results with alternative analytic theories and discuss some design rules and principles to achieve higher mobilities in OSs.

4.2.1 Experimental mobility measurements

Charge carrier mobility measurements are of great importance to gain insights about the influence of morphology and chemical structure of a given material on charge transport properties and the efficiency of a particular semiconductor. In particular, the conductivity of the material is generally determined by charge mobility (as well as the density of mobile carriers [16]).

Different experimental techniques, for example time time of flight (TOF) [10], Hall-effect and field effect transistor (FET) [11, 173], space-charge limited current (SCLC) [161] and so on, exist to measure the mobility of a material (in this thesis an OS). However, these measurements not always yield the same value for the mobility as they probe different physical processes and they are, in some cases, affected by the actual morphology of the sample, the presence of structural defects and the device structure at the interface between different layers of the device (e.g. at the interface between the conductive layer and the substrate in FET). Nevertheless, in some cases, reliable and reproducible mobility values across different groups and experimental set-ups have been reported [4, 17, 29] (important reliability factors that needs to be considered when reporting mobility measurements have been described in Ref. [174]).

Among these different measurements, the ones that most closely resemble the FOB-SH set-up are the TOF measurements. These measurements monitor the time it takes for charge carriers to travel through a given semiconducting sample. The sample is placed between two non-injecting electrodes, which are used to apply a small electric field. Both electrodes are semi-transparent to allow photogeneration of charges by absorption of short laser light pulses. Upon generation, the charge carrier travels through the medium from one electrode to the other. The monitored current reveals the transit time of the carriers allowing calculation of the mobility in the sample. Depending on the side chosen for photogeneration, hole or electron mobilities may be measured. Importantly the number of generated charges must be small enough ($10^{14} - 10^{17}$ cm^{-3}) not to distort the external electric field, which must be also very small ($10^{3} - 10^{5}$ V cm^{-1}) [98]. Thus, the TOF mobilities give access to bulk properties achieved at low charge carrier concentration and electric field. This is precisely what is modelled in FOB-SH, where a single excess carrier is simulated (dilute carrier ap-

proximation) and mobilities are calculated in the limit of zero external electric field. I note that the effect of electric field on carrier mobility in a simple 1D chain of chemically identical molecules was previously investigated in Ref. [16]. It was found that for a typical set of parameters for OSs, 50 meV coupling and 150 meV reorganization energy, the mobility remains independent on the applied external field up to field strengths of about 10^6 V cm^{-1}. This is at least an order of magnitude higher than typical field strengths in time-of-flight (TOF) measurements. Non-linear transport behaviour may occur at higher field strengths, in which case the (field-dependent) diffusion coefficient in Eq. 2.31 could be obtained from the velocity-drift autocorrelation function or from the derivative of the drift velocity with respect to the electric field strength [16].

In the course of this thesis, I will extensively make use of the TOF mobility measurements performed by Karl's group on OSs like ANT, NAP, PER [10, 98, 175, 176] as a reference for FOB-SH. These TOF measurements are some of the most careful measurements ever performed on OS materials as it was very recently recognised in Ref. [4]. The exceptional results achieved by Karl et. al come from the extreme purification and care taken during sample fabrication in order to access ultra-high purity and low structural defect content and they constitute an ideal benchmark for any new theoretical and computational model.

4.2.2 FOB-SH mobilities vs experiments

I started the investigation by calculating mobility along 1D chains of the embedded systems in Figure 4.1 in order to asses the quality of FOB-SH mobilities compared to experimental data for a broad range of OS samples. To this end I run 1000 FOB-SH trajectories for each system to obtain the mean squared displacement (MSD) of $\Psi(t)$ (Eq. 2.33) as a function of time. After a short initial relaxation period I observe a linear increase of the MSD with time, implying that the Einstein diffusion approximation is valid (MSD for 1D chains are given in Ref [85]). The charge mobilities obtained from the Einstein relation are shown in Figure 4.5(A) (data in blue). They are in excellent agreement with experiment or within the experimental error bar where uncertain, with typical deviations of less than a factor of two for mobilities spanning 3 orders of magnitude. I find that charge mobility correlates very well with both: average polaron size, as defined by the inverse participation ratio (IPR) in the highly conductive plane, in Eq. 2.38 (Figure 4.5(B)), and the order parameter $\xi = 2V/\lambda$ (Figure 4.5(C)) determining the existence and height of the free energy barrier for charge

transfer between nearest neighbours, as illustrated in Figure 4.5(D). As discussed below, traditional hopping and band models fail to provide a uniformly good description of charge transport in the OSs investigated.

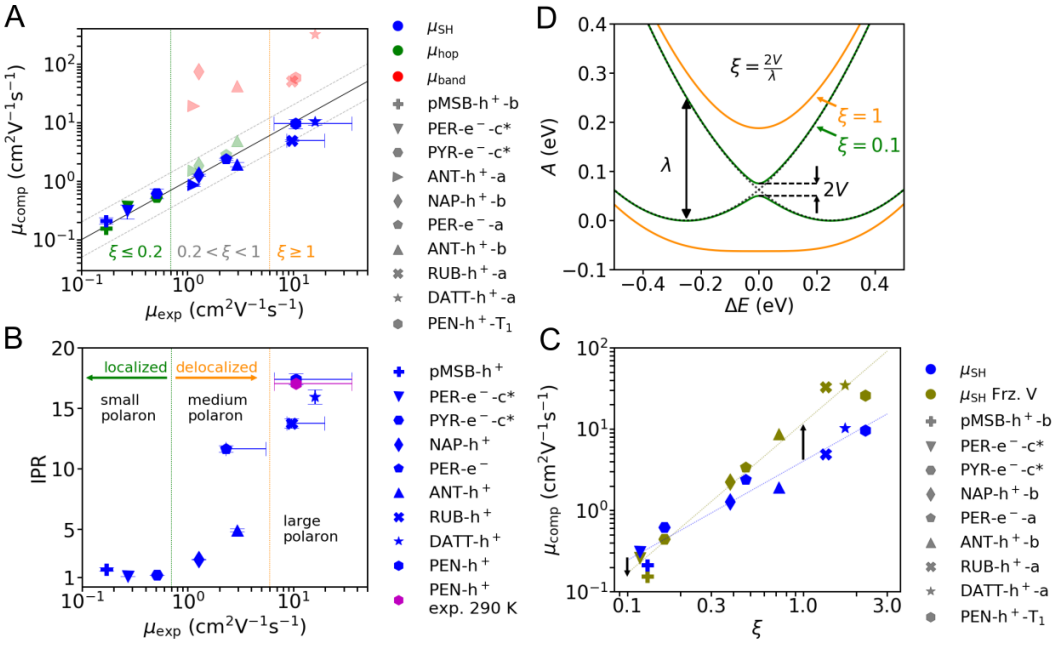

Figure 4.5: Charge mobility along 1D chains and IPR in the high-mobility plane for of all investigated OSs. (A) Computed versus experimental charge mobilities for the OS materials shown in Figure 4.1; pMSB-h$^+$-b denotes hole transport along the *b* crystallographic direction, and a similar notation is used for the other systems. Charge mobilities from FOB-SH (data in blue) are obtained by averaging the MSD of the charge carrier wavefunction $\Psi(t)$ over 1000 trajectories and inserting the corresponding diffusion coefficients in the Einstein relation (see Section 2.3.2). Statistical error bars indicate the standard deviations over five independent blocks of 200 trajectories. Experimental error bars for RUB, PEN and PER are based on the measurements cited in Table 4.4. Predictions from band theory calculations are taken from the literature (data in red, see Ref [177–179]). Charge mobilities from a small polaron hopping model (data in green) are obtained by solving a chemical Master equation for nearest neighbour hopping in the specified direction using semi-classical ET rates (see Appendix B.1). As a guide to the eye, perfect agreement is indicated by a thick solid line and deviations in mobility by a factor of 2 by thin dotted lines. (B) Correlation between time-averaged IPR and measured mobilities. The experimental estimate for the size of the hole polaron in pentacene was taken from Ref. [19]. Error bars were obtained by block averaging the equilibrated region of the IPR. (C) Influence of the thermal fluctuations of electronic coupling (off-diagonal electron-phonon coupling) on charge mobility. Data in olive are obtained from FOB-SH with electronic coupling between the molecules frozen to the thermal average. Data in blue are taken from panel (A) and shown for comparison. Note the significant increase in charge mobility for systems forming large polarons. (D) Diabatic (black dashed) and adiabatic free energy profiles (solid) for electron transfer between a donor and an acceptor, defining reorganization free energy, λ, average electronic coupling, V, and the parameter ξ determining existence and height of the barrier.

FOB-SH mobilities up to ≈ 1 cm^2 V^{-1} s^{-1} including the one for pMSB ($\xi < 0.2$), are well reproduced by a chemical Master equation for small polaron hopping between nearest neighbours with hopping rates from electron transfer (ET) theory (data in dark green

in Figure 4.5(A)), despite that for pMSB that the actual mechanism is more intricate than simple nearest neighbour hopping as I will discuss in detail in Section 4.3.1. The algorithm that I developed to solve the chemical Master equation with Marcus-like ET rates is described in Appendix B.1. For OSs with larger mobilities, $\approx$ 1-5 cm^2 V^{-1} s^{-1} ($0.2 < \xi < 1$), the free energy barrier is small, causing the polaron to delocalize over 2-5 molecules according to FOB-SH simulations. Hence, in this regime the small polaron hopping model assuming nearest neighbour hops of a fully localized charge carrier is no longer a good physical model of the charge transport process. Nonetheless, if one solves the chemical Master equation with nearest neighbour hopping rates from ET theory, the resultant mobilities are in good agreement with FOB-SH and experimental values (data in shaded green). This agreement appears to be coincidental as the small polaron hopping mechanism bears no resemblance with the actual mechanism obtained from FOB-SH (see Section 4.3.1 for a detailed explanation of the actual transport mechanisms). Indeed, it is well known that a small polaron hopping model may give the same order of magnitude in mobility or current as a larger polaron model [180] - agreement with the experimental mobility gives no sufficient information on the mechanism.

At even higher mobilities, $\gtrapprox$ 5 cm^2 V^{-1} s^{-1} ($\xi \geq 1$), the free energy barrier disappears completely and polarons are delocalized over several to many molecules, as observed above for pentacene. It is worth noticing at this point that there is an excellent agreement between polaron size calculated from FOB-SH, which gives an IPR (Eq. 2.38) of about 17-18 molecules in the 2D herringbone layer plane of pentacene, and estimates based on experimental electron spin resonance data, which gives a polaron size of 17 molecules at 290 K [19]. In this high-mobility regime band theory [177–179] does not give an adequate description either: experimental mobilities are overestimated due to strong thermal motions violating basic assumptions of this theory (data in shaded red; only for still higher mobilities this theory becomes valid). By contrast, FOB-SH describes all regimes relevant to OSs accurately and seamlessly bridges the gap between small polaron hopping and band transport.

Introducing what will be a more in-depth discussion in Section 4.4, I would like to briefly mention here that an important objective in the discovery process of efficient OSs is the understanding of the aspects limiting polaron delocalization and ultimately charge mobility. According to Troisi and co-workers the major limiting factor are the thermal

fluctuations of electronic coupling between the molecules leading to localization of the electronic eigenstates and hence to reduction in mobility [12, 54, 56, 74]. Indeed several attempts have already been made experimentally to reduce off-diagonal disorder, with some success [53, 181]. To estimate the maximum possible boost in charge mobility that one could achieve via complete removal of off-diagonal electron-phonon coupling, I carried out FOB-SH simulations with electronic couplings frozen to their mean values (Figure 4.5(C), data in olive). While in the small polaron hopping regime ($\xi < 0.2$) the mobility slightly decreases, as one would expect from non-adiabatic ET theory (see also Section 4.4.1 for a more detailed discussion), in the medium and large polaron regime ($\xi > 0.2$) the mobility increases significantly, by up to a factor of 7 for rubrene. Yet, the charge carrier is still polaronic due to the thermal fluctuations of the site energies (diagonal electron-phonon coupling). If the latter are frozen as well, the polaron fully delocalizes and the band transport regime is reached. I will come back to the impact that the thermal disorder has on the transport properties on OSs in more detail in Section 4.4.

4.2.3 Mobility anisotropy in 2D high-mobility planes of OSs

Owing to the algorithmic optimizations described in Section 2.1.7 to reduce the computational cost without sacrificing accuracy of FOB-SH dynamics, namely an effective multiple time step algorithm (MTS) and a more efficient propagation of the electronic Schrödinger equation Eq. 2.4, I was able to converge the full 2D mobility tensor for the high conductivity plane of some of the organic crystals in Figure 4.1.

The mean squared displacement (MSD) for the centre of charge of $\Psi(t)$ in the *a*-*b* high-mobility plane of PER-e^- and RUB-h^+ is shown in Figure 4.6(A) and (B), where again the appendix "e^-" and "h^+" indicates as before electron and hole transport, respectively (the MSD of the other systems is given in Ref. [86]). At short times the MSD tends to increase rapidly until after a few 100 fs the increase is linear in time within the error bars of these simulations. The initial dynamics is due to the relaxation of the fully localized charge carrier, which is a mixture of excited band states, to states close to the valence or conduction band edge (see Figure 4.4). During this quantum relaxation process the charge carrier "equilibrates" to form a polaron within the *a*-*b* plane accompanied by a non-linear increase in the MSD. A similar relaxation dynamics was found by Schnedermann et al. [182] by using optical transient absorption spectroscopy in the context of exciton and charge transport in a thin pentacene film. As I will describe in Section 4.3 the polaron is a highly dynamical

species constantly changing shape and extension. A representative snapshot is depicted in Figure 4.7(lower panels) where the carrier delocalization is larger than 10 molecules in the most conductive materials. I verified that the average polaron size and shape is insensitive to the choice of the initial carrier wavefunction while the time for relaxation to this state may, of course, vary. This is because FOB-SH maintains detailed balance in the long-time limit to a good approximation [82, 83] ensuring that after initial relaxation, the equilibrium (Boltzmann) populations of electronic band states are reached, independently on the initial starting point. It should be noted that the finite size of the polaron is due to the thermal diagonal and off-diagonal disorder in the electronic Hamiltonian Eq. (2.5). Without the disorder the carrier wavefunction would be a delocalized band state.

As shown in Figure 4.6(C), system sizes of almost 1000 electronically active molecules within the *a*-*b* plane are necessary to converge charge mobility for the most conductive materials, while the polaron size defined by the inverse participation ratio (IPR), Eq. (2.38), converges significantly faster, Figure 4.6 (D).

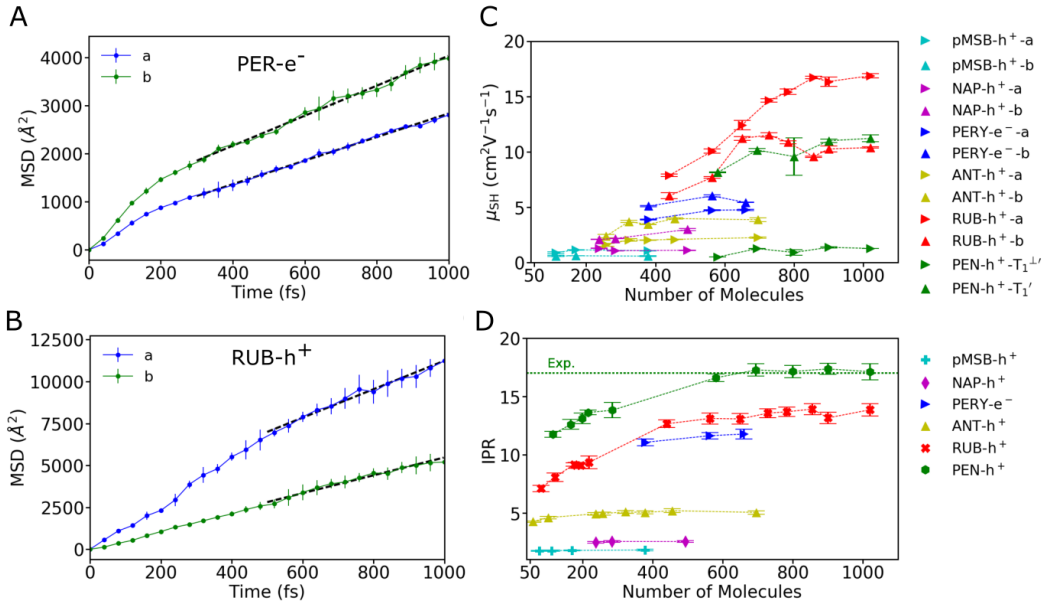

Figure 4.6: Charge carrier diffusion in organic single crystals from FOB-SH simulations and convergence with system size. The mean squared displacement (MSD) of the charge carrier wavefunction is shown for perylene (A) and rubrene (B) along the *a* (blue) and *b* (green) crystallographic directions. The diffusion coefficient is obtained from linear fits to the MSD after initial relaxation, as indicated by dashed black lines. The convergence of charge mobility and IPR with respect to the number of electronically active molecules is shown in (C) and (D), respectively. Mobilities are reported along the two eigendirections within the plane, coinciding with the *a* and *b* crystallographic directions for all systems except pentacene. For the latter the eigen-directions T_1' and $T_1'^{\perp}$ are close to the crystallographic directions T_1 and $T_1^{\perp}$. The experimental polaron size for pentacene, as obtained from electron spin paramagnetic resonance, is depicted in green dashed lines [19].

The computed charge mobilities for the *a*-*b* planes are shown in polar representation in Figure 4.7 (top panels). As one might expect, the mobility in a given direction correlates well with the delocalization of the polaron in that direction as both depend primarily on the strength of electronic coupling between the molecules. Overall, I observe again as in the previous Section good to near quantitative agreement between FOB-SH (data in blue) and experimental mobilities (data in black) for both magnitude and anisotropy within the plane, especially when comparing to Karl et al.'s time of flight (TOF) data for NAP, ANT and PER (panels (B), (C) and (D), relative error averaged over *a* and *b* direction is 24%, 31% and 30%).

Unfortunately, to the best of my knowledge, TOF data are not available for pMSB, RUB and PEN. Here comparison must be made to field-effect-transistor (FET) data, which are more characteristic of surface mobilities and may depend on the nature of the gate insulator (see Section 4.2.1). With these caveats in mind, I find good agreement between the computed highest in-plane mobility for RUB, 16 $cm^2\ V^{-1}\ s^{-1}$ along the *a*-direction, and the most reproducible experimental FET measurements, in the range 10-20 $cm^2\ V^{-1}\ s^{-1}$ [11, 159, 160]. The anisotropy is also reasonably well captured albeit somewhat underestimated. The computed mobility along the *b*-direction is 10 $cm^2\ V^{-1}\ s^{-1}$ compared to 4-8 $cm^2\ V^{-1}\ s^{-1}$ from experiment [11, 159, 160]. At first sight, this may be somewhat surprising because rubrene forms a slipped pi-stacked structure with electronic couplings along the *b*-direction (T_1 and T_2) about factor of 4 smaller than along the *a*-direction (*P* pair). However, the thermal fluctuations of the electronic couplings T_1 and T_2 are also a factor of 3 smaller than for *P* (see Table 4.3). In addition, the lattice spacing is larger along *b* and, since the mobility is proportional to the square of the lattice spacing [186], all this might partly offsets the smaller mean couplings leading to comparable mobilities in *a* and *b* directions.

In pMSB, NAP and ANT the electronic couplings are smaller than half the reorganization energy (see Table 4.3), hence as seen before finite barrier for site-to-site hopping of a fully localized polaron exists and ET rates may be defined. The mobility obtained by solving such a hopping model is shown in Figure 4.7 (green lines), see Appendix B.1 for detail on the Master equation solved. It gives relatively accurate results for the OSs with the lowest mobilities, pMSB and NAP, but significantly overestimates the mobility for ANT. However, it is clear from the FOB-SH simulation that even in the system with the lowest mobility (i.e. pMSB) the charge carrier does not simply transfer via site-to-site hopping as

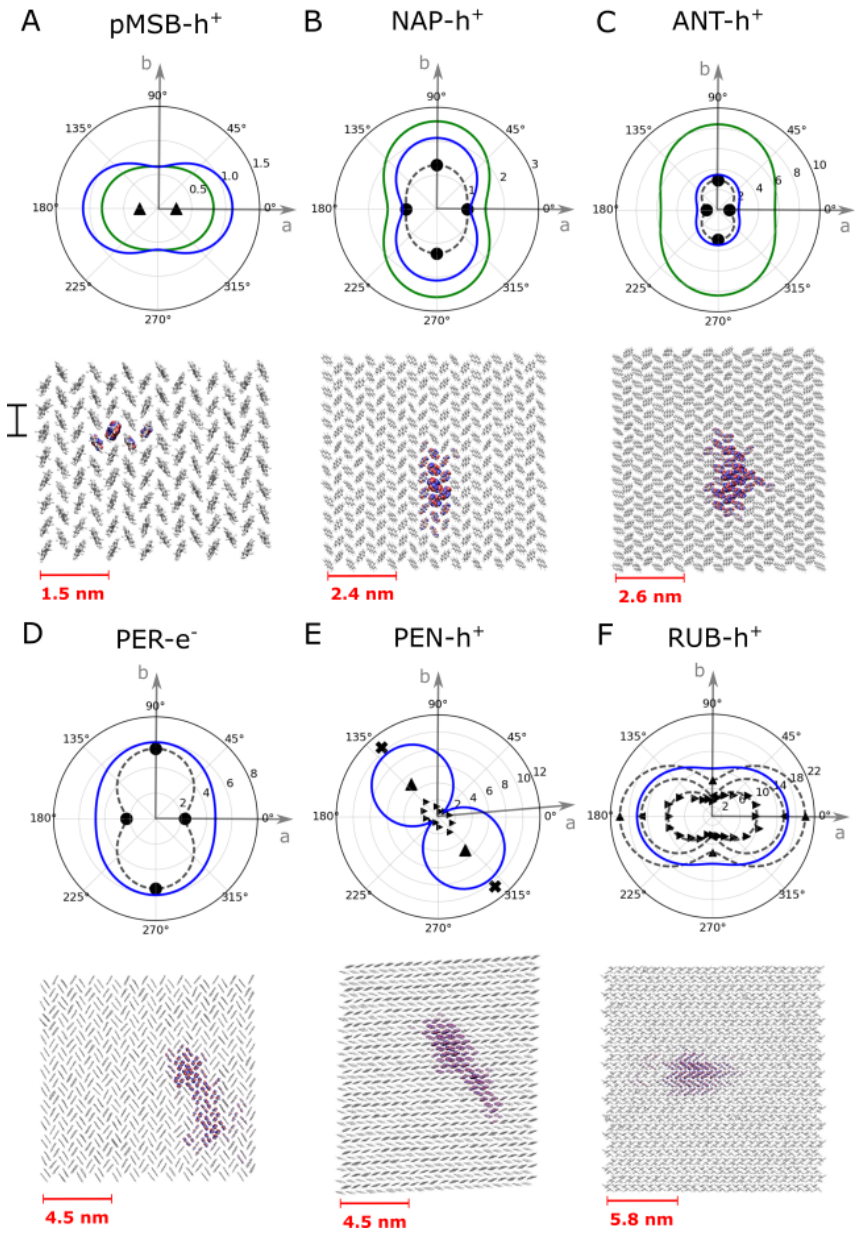

Figure 4.7: Polar representation of mobility anisotropy and snapshots of the charge carrier wavefunctions (polarons). Charge mobilities from FOB-SH (blue) and from a site-to-site hopping model using electron transfer rates (green) are compared to experimental mobilities (black). For NAP [157, 175], ANT [98] and PER [158, 176], time-of-flight (TOF) data along a and b directions are indicated by black circles. For pMSB, the field-effect transistor (FET) mobility is taken from Ref. [183]. For RUB, FET mobilities are taken from Ref. [159] , Ref. [184] and Ref. [160]. For PEN, FET mobilities are taken from Ref. [164] and Ref. [185] and SCLC mobilities from Ref. [161]. Where possible, the experimental in-plane mobility tensors are reconstructed and shown in dashed black lines. In Refs. [161, 164, 183, 185] the experimental mobility direction was not reported and was assumed to align with the computed high mobility direction. Isosurfaces of the magnitude of the wavefunction, $|\Psi(t)| = 1.5 \times 10^{-3}$, are coloured according to the phase θ, $\Psi(t) = |\Psi(t)| \exp(i\theta)$: $-\pi/4 \leq \theta \leq 3\pi/4$ in blue and $3\pi/4 < \theta < 7\pi/4$ in red.

in donor-acceptor electron transfer reactions. Moreover, as pointed out before [56], since the hopping rates depend on the magnitude of the couplings, the effect of the sign relationship between the different couplings on the symmetry of DOS is not accounted for in this approach (see Section 4.1.3). At the other extreme, standard band theory calculations tend to strongly overestimate mobility in all systems, as previously discussed.

4.2.4 Comparison 1D vs 2D mobilities

It is important to note that all mobilities reported from FOB-SH simulations for the full 2D planes in Figure 4.7 are larger than the mobilities in Figure 4.5(A) for 1D models along the same crystallographic direction, typically by a factor of 2-3 (see Table 4.4 for a summary).

Table 4.4: Comparison between FOB-SH mobilities and IPR obtained from simulation of the full 2D planes and from reduced 1D models along the specified directions within the 2D planes, and experimental results (μ (exp)). All values for mobility are in $cm^2\ V^{-1}\ s^{-1}$.

	Dir.	μ (1D)	μ (2D)	μ (exp)	IPR (1D)	IPR (2D)
pMSB	*a*	-	1.1± 0.02	0.17[a,b]	-	1.7± 0.05
	b	0.21± 0.03	0.61± 0.01		1.1± 0.01	
NAP	*a*	-	1.0± 0.01	0.9[c]	-	2.5± 0.07
	b	1.3± 0.05	2.1± 0.01	1.3[d]	1.6± 0.02	
ANT	*a*	0.86± 0.05	2.0± 0.02	1.1[e]	2.0± 0.02	5.0± 0.13
	b	1.9± 0.17	3.5± 0.02	2.9[e]	2.2± 0.03	
PER	*a*	2.4± 0.09	4.7± 0.03	2.3[f]	1.7± 0.02	11.6± 0.28
	b	-	6.0± 0.11	5.5[g]	-	
RUB	*a*	4.9± 0.18	16± 0.43	9.6,[h] 15.4,[i] 20[j]	3.2± 0.03	13.7± 0.04
	b	-	10± 0.26	3.7,[h] 4.4,[i] 7.8[j]	-	
PEN	$T_1^{\perp\prime}$	-	0.92± 0.24[o]	5[a,k,l], 5.6[a,m] 10.5[a,n]	-	17.1± 0.54[p]
	T_1'	9.6± 1.8	9.6± 1.7[o]		6.8± 0.11	

[a] Transport direction unknown. [b] Ref. [183]. [c] Ref. [157]. [d] Ref. [175]. [e] Ref. [98]. [f] Ref. [176]. [g] Ref. [158]. [h] Ref. [159]. [i] Ref. [184]. [j] Ref. [160]. [k] Ref. [185]. [l] Polymorph I, see text for discussion. [m] Ref. [187]. [n] Ref. [161]. [o] Mobilities along the eigendirections of the 2D mobility tensor, T_1' and $T_1^{\perp\prime}$. [p] Ref. [19] estimates 17 molecules from ESR spectroscopy.

This result is in line with the finding of Fratini et al. who concluded that 2D systems with isotropic couplings exhibit higher mobilities than anisotropic systems and noting that 1D models are perfectly anisotropic [56]. As previously discussed in Section 4.1.2 and Section 4.1.3, in contrast to 1D systems, 2D mobilities are influenced by the fact that the states delocalization is not symmetrical with respect to the band center and the relevant accessible states for hole transport are in the high energy tail of the DOS and vice versa for

electron transport. This asymmetry is a consequence of the coupling-sign relationship that influences the degree of localization of the thermally accessible states and, thus, charge delocalization and dynamics. From a more intuitive (and less formal) perspective, the charge carrier wavefunction can delocalize in a 2D plane more effectively than in a 1D chain because of the larger number of nearest neighbours. Therefore, when possible bottlenecks are present (e.g. neighbouring molecules in a pose with unfavourable couplings), the charge carrier may bypass them in other directions [45]. Nevertheless, rapid evaluations of mobilities from 1D models can already provide good estimates of the intrinsic mobilities of the system at hand [85, 166].

4.2.5 Comparison with transient localization theory

The results presented in the previous Sections obtained from explicit time propagation of the electron-nuclear dynamics can be used to test more recent theoretical models of charge transport in OSs, e.g., the transient localization theory (TLT) proposed by Fratini and Ciuchi [15, 31, 54, 56, 57] (see Section 1.3.3). I have calculated μ_{TLT} (Eq. 1.3) from L_τ^2 using the electronic Hamiltonians sampled along present FOB-SH trajectories and setting the site energies to zero (see Appendix B.2 for details).

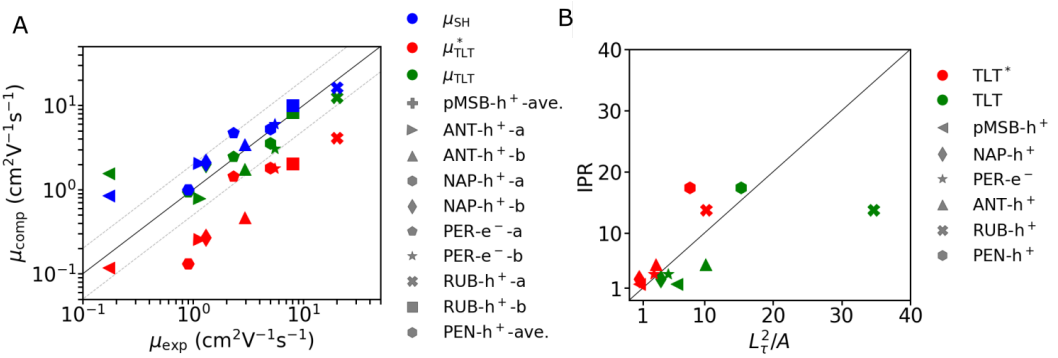

Figure 4.8: Comparison between 2D FOB-SH mobilities and transient localization theory. (A) Charge mobilities obtained from TLT vs experiment. The squared transient localization length L_τ^2 is calculated as described in Ref. [57] using electronic Hamiltonians from present FOB-SH trajectories, firstly, without modification of the onsite energies and their thermal fluctuations (data in red) and, in addition, after removal of onsite energy fluctuations by setting all diagonal matrix elements to zero (data in green). FOB-SH mobilities in blue are for 2D plane simulations as in Figure 4.7 and shown for comparison. (B) Correlation between IPR and L_τ^2/A, where A is the area per molecule within the herringbone layer.

Mobilities from TLT are reported in Figure 4.8 and compared to mobilities from FOB-SH and experiment. I note that the TLT mobilities correlates very well with FOB-SH and experiments but only if the diagonal disorder is excluded in the calculation of the localiza-

tion length (green symbols). When diagonal disorder is included to ensure a like-for-like comparison with FOB-SH, TLT mobilities tend to underestimate FOB-SH and experimental mobilities (red symbols). The deviation tends to become larger, in some cases up to an order of magnitude, for the OSs with the lowest mobilities. This is expected because TLT, at least in its present form, does not extend to the low mobility/strong localization regime. Another interesting point is that the average IPR (with which I quantify the extension of the polaron in a statistical manner) generally correlates well with the localization length. This was pointed out by Fratini et al. [56] and further investigated for real systems in this thesis (see Figure 4.8(B)). However, it is important to mention that the IPR *per-se* does not give dynamical information while the localization length is directly related to charge mobility by Eq. 1.3.

4.2.6 Possible sources of error in FOB-SH results

In this Section I briefly review the main sources of error in semi-quantitative predictions of polaron diffusion from FOB-SH simulations (note that analogue arguments apply to exciton diffusion results and will be discussed in Chapter 6). These numerical simulations require and combine two main different components: the time evolution of the coupled electronic-nuclear equation of motion according to the surface hopping algorithm and the re-construction of the (DFT-parametrized) Hamiltonian at each time step along the MD dynamics.

With regards to the possible errors coming from the dynamics part, I stress that crucial criteria such as energy conservation, detailed balance of the states and internal consistency have been addressed extensively in Chapter 3, and (to some extent) ensured by applying important algorithmic improvements. As the system size increases, the density of states becomes higher along with the number of potentially missed trivial crossings or unlikely hops (see Section 2.2.4 and 2.2.5, respectively). This stresses the effectiveness, e.g,. of the state tracking algorithm and one has to compromise between the simulation cost and its accuracy (e.g., by reducing the nuclear time step). Nevertheless, I note in passing that the good convergence of mobility and IPR with system size (Figure 4.6(C) and 4.6(D)) as well as with time step (see Ref. [86]) implies that spurious long-range transfers due, for example, to trivial crossings have been largely eliminated from the simulations presented here.

With regards to the Hamiltonian re-construction, all the parameters entering the FOB-SH Hamiltonian, such as the reorganization energies and the couplings are, in this work,

parametrized against DFT calculations. As any other parametrized approach, these values can only be as good as the reference data and they are not exempt from (small) errors. I refer to Section 2.1.3 and Section 2.1.4 for a detailed account of the accuracy of site energies and electronic couplings and their limitations. I remark, though, that the good agreement in shape and bandwidth of the DOS of the FOB-SH Hamiltonians compared with KS-DFT (Figure 4.4) attests to the reliability of the Hamiltonians used in this thesis. A challenge (rather than a shortcoming) is the inclusion of electronic polarization effects in the calculation of the site energies, in particular when the crystal is formed of polar or hydrogen-bonded molecules (which is not the case in the current systems studied). I refer to Section 4.1.1 for a discussion on this point.

Other possible sources of error on mobility estimates as the temperature changes are discussed in detail in Section 5.3.3. In particular, I will point out that nuclear quantum effects are expected to become increasingly important at low temperature [122, 177], whereas thermal expansion/contraction would need to be considered when the temperature varies.

4.3 Charge carrier transport mechanism

The initial dynamics of the hole carrier wavefunction $\Psi(t)$ and the polaron size (defined by the IPR) over the first 100 fs are shown in Figure 4.9 for two representative OSs ($T = 300$ K): panels (A)-(E) for the low mobility OS pMSB and panels (G)-(L) for the reasonably high mobility OS pentacene. Starting from an electronic wavefunction that is initially localized on a single pMSB molecule (Figure 4.9(B)), we can observe frequent hops of the electron hole, each involving rapid delocalization of the hole carrier wavefunction over a few molecules (Figure 4.9(C) and (E)) and re-localization on a single molecule that is one or a few molecular spacings (0.3-0.5 nm) apart (Figure 4.9(F)). The average IPR in the herringbone plane is equal to 1.7 and the root-mean-square fluctuation σ_{IPR} equals 0.9 (see Table 4.5). The observed hole hopping mechanism is not unexpected for this OS because the thermal average of electronic coupling between the molecules, $V = \langle |H_{kl}|^2 \rangle^{1/2}$, is significantly smaller than reorganization energy, $\xi = 2V/\lambda = 0.1$ (see Table 4.3). However, the mechanism differs from the Marcus picture often used to model small polaron hopping in OSs [16], in that several molecules bridging initial donor and final acceptor may come simultaneously into energetic resonance resulting in hole transfer to a molecule beyond the nearest neighbour in a single hopping event. This is more reminiscent of the flickering resonance mechanism recently proposed by Skourtis and Beratan for hole transport in

DNA [188], though it should not be confused with it as in the present case the dynamics is the result of explicitly solving the time-dependent electronic Schrödinger equation coupled to nuclear motion and not the outcome of an analytic model.

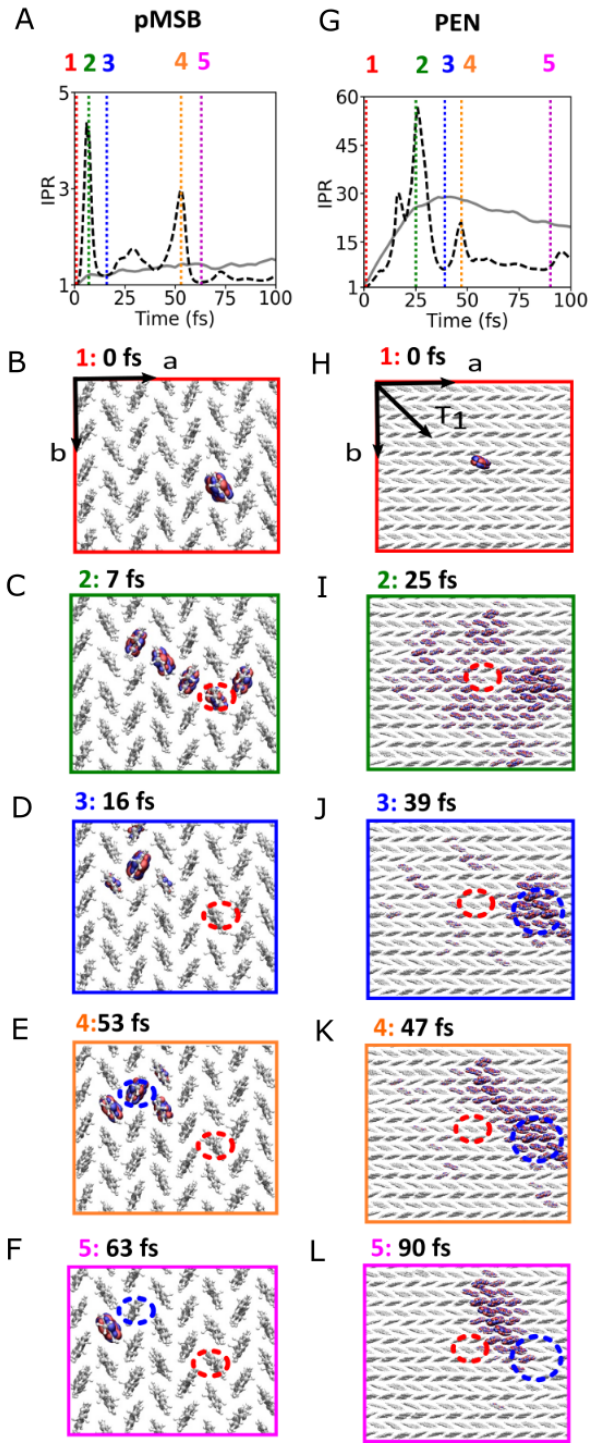

Figure 4.9: Time evolution of the charge carrier wavefunction in the first 100 fs[a]. The number of molecules over which the polaron is delocalized, defined by the inverse participation ratio (IPR) (Eq. 2.38) is shown in (A) and (G) for pMSB and pentacene, respectively, against time. Black dashed lines are used to indicate representative single FOB-SH trajectories and gray solid lines are averages over 300 trajectories. In (B)-(F) and (H)-(L) snapshots of the hole carrier wavefunction $\Psi(t)$ (Eq. 2.3) in the respective herringbone layers are shown starting from a fully localized wavefunction at time t=0. The snapshots are taken from the same single trajectories in (A) and (G) at the times indicated by vertical dotted lines with different colors. Isosurfaces of the magnitude of the wavefunction, $|\Psi(t)|=2\times10^{-3}$, are shown and coloured according to the phase θ, $\Psi(t)=|\Psi(t)|\exp(i\theta)$: $-\pi/4\leq\theta\leq3\pi/4$ in blue and $3\pi/4<\theta<7\pi/4$ in red. Only a zoomed-in region of the simulated herringbone layer is shown and the molecules perpendicular to the herringbone layer are removed to enhance visibility.

[a]The charge transport animations for the full representative FOB-SH trajectories are provided at https://www.dropbox.com/sh/a9jtv83sand4er9/AACWW2M0MefPIg9Sm3TOZ7Wya?dl=0 and/or as supplementary material at https://onlinelibrary.wiley.com/doi/full/10.1002/adts.202000093

The situation is strikingly different for pentacene. The initially localized electronic wavefunction $\Psi(t)$ (Figure 4.9(H)) rapidly spreads over several molecules (Figure 4.9(I))

to form a polaron that is preferentially delocalized along the T_1 direction where π-orbital overlap and hence electronic coupling between neighbouring molecules is the largest (Figure 4.9(J)). On average, the polaron, in agreement with estimates based on experimental electron spin resonance data at 290 K [19], is delocalized over 17 molecules ($\sigma_{\mathrm{IPR}} = 10.3$). Delocalization occurs because electronic coupling is now on the same order of magnitude as reorganization energy, $\xi = 2.2$, which brings several molecules simultaneously into energetic resonance at any point in time. Yet, disorder in the site energies and electronic couplings prevent the wavefunction from further delocalization. As I will explain in more detail in Section 4.3.1, in FOB-SH this effect is born out by the wavefunction $\Psi(t)$ projecting on the ground or low energy hole eigenstates (valence band states), i.e., states close to the valence band edge which are delocalized over no more than a dozen molecules (see Figure 4.4). The motion of the polaron within the herringbone layer of pentacene is particularly intriguing. Neighbouring clusters of molecules frequently come into energetic resonance with the polaron causing $\Psi(t)$ to expand to about twice its size for short durations of time (Figure 4.9(K)). At this point $\Psi(t)$ projects on higher-lying hole eigenstates (i.e., states closer to the middle of the valence band), which are more extensively delocalized, typically over 20-50 molecules. Some of these sudden bursts of the wavefunction are successful, meaning $\Psi(t)$ returns to a low-lying hole eigenstate that is localized on a neighbouring cluster of molecules (Figure 4.9(L)). The remarkable correlation between these so-called "diffusive jumps" and the delocalization of the electron adiabatic states that are thermally accessed by the charge carrier during its dynamics will be carefully investigated and discussed in Section 4.3.1.

The dynamics at longer times, up to a few picoseconds, is shown in Figure 4.10 for both materials. I found that the average duration of a "resonance", defined here by the time it takes for the IPR to exceed and subsequently return below $\langle \mathrm{IPR} \rangle + \sigma_{\mathrm{IPR}}$ is 7 and 12 fs for pMSB and pentacene, respectively, see Figure 4.10(A) and Figure 4.10(B), which is close to the characteristic oscillation time of intramolecular vibrations and site energy fluctuations. The average time between two resonances is about an order of magnitude larger, 52 fs for pMSB and 114 fs for pentacene. Similar values are obtained for the other compounds, see Table 4.5. These resonances give rise to spatial displacements as described qualitatively above and shown in Figure 4.10 by way of projecting $\Psi(t)$ on the crystallographic directions b and T_1 of pMSB (Figure 4.10(C)) and pentacene (Figure 4.10(D)), respectively. Yet,

Table 4.5: Characterization of polaron size (IPR) and its thermal fluctuations.[a]

crystal	$\langle \text{IPR} \rangle^b$	σ^c_{IPR} (IPR)	t^d_{r} (fs)	τ^e_{r} (fs)	τ^f (fs rad^{-1})
DATT-h$^+$	15.9	10.8	15	133	159
RUB-h$^+$	13.7	8.2	9	71	333
PEN-h$^+$	17.4	10.3	12	114	202
ANT-h$^+$	4.9	2.6	9	73	398
NAP-h$^+$	2.5	1.4	8	58	114
PER-e$^-$	11.6	6.5	10	81	199
PER-e$^-$-c^*	1.1	0.1	12	277	-
PYR-e$^-$-c^*	1.2	0.3	9	164	-
pMSB-h$^+$	1.7	0.9	7	52	159

[a] All values are averaged over 600 FOB-SH trajectories of approximate length 1 ps. The first 200 fs of dynamics were discarded. [b] Average of IPR. [c] Root-mean-square fluctuations of IPR. [d] Average duration of a resonance. The duration of a resonance is defined by the time it takes for the IPR to exceed and subsequently return below $\langle \text{IPR} \rangle + \sigma_{\text{IPR}}$. [e] Average time between two resonances. [f] Characteristic oscillation time of electronic coupling, corresponding to the peak of highest intensity at ω_0 in the power spectrum of electronic coupling fluctuations from a MD trajectory (5 ps long), $\tau = \omega_0^{-1}$, where ω_0 is the angular frequency.

significant displacements along these directions occur at somewhat longer times than the time between two resonances, more characteristic of the oscillation time of the electronic coupling fluctuations, $\tau = 159$ and 202 fs rad^{-1} for pMSB and pentacene, respectively, see Figure 4.10(C) and Figure 4.10(D). Hence, as one would expect, only a fraction of the diffusive jumps (estimated to be about 0.2-0.5) leads to a successful displacement. Notably, the wavefunction displacements in pentacene are over several lattice spacings at a time, 3-5 nm, that is about an order of magnitude larger than the (mostly nearest-neighbour) displacements in pMSB. This difference gives rise to a $\approx$ 50-fold higher charge mobility in pentacene relative to pMSB as seen in Section 4.2.2.

4.3.1 Investigation of the diffusive jumps motion

In Section 4.3, watching the real-time trajectories generated by FOB-SH, I found that the charge carrier wavefunction $\Psi(t)$ may be best described as a flickering polaron continuously changing its shape and extensions though with preference to delocalize in the direction with the highest coupling. Remarkably, I frequently observe events where the polaron expands to about 2-3 times its average size, followed by relocalization at a position about a polaron diameter apart from the original position (Figure 4.9). I now would like to answer the question what is actually causing the diffusive jumps and wavefunction displacement in the investigated organic crystals? Therefore, here I analyse the origin of the resonances and

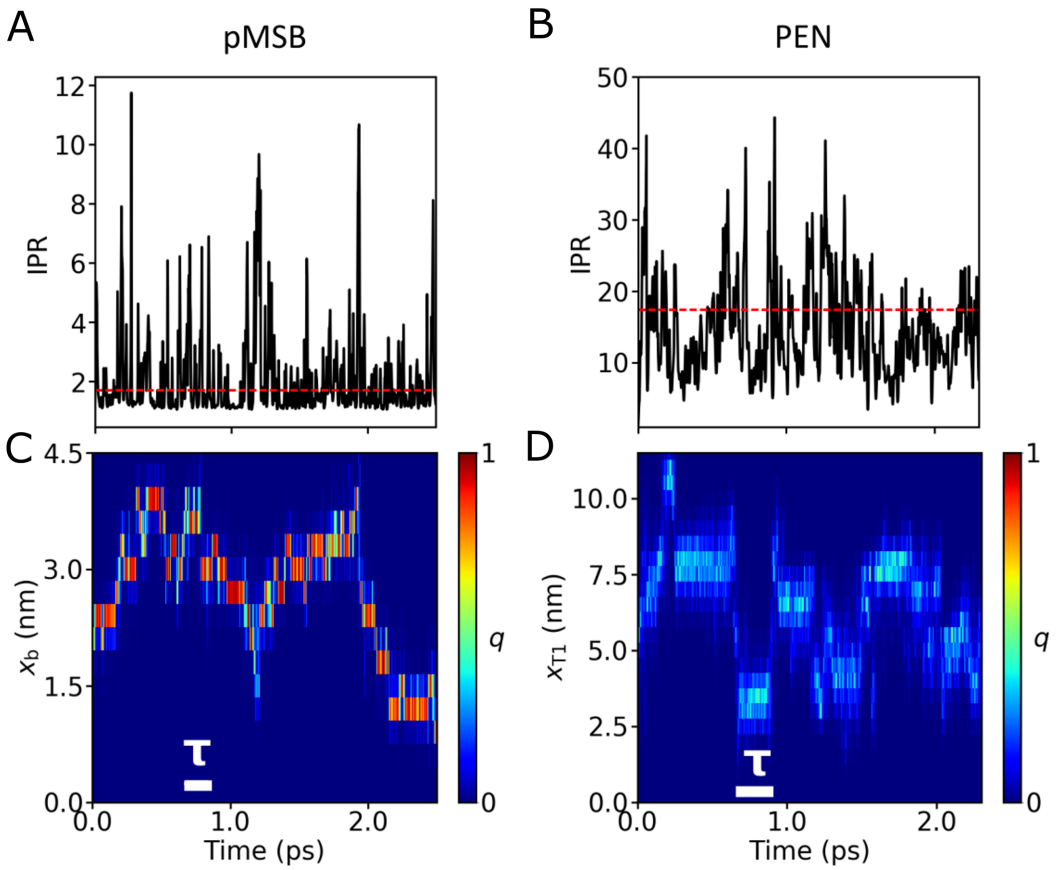

Figure 4.10: Time evolutions of IPR and carrier wavefunction on a picoseconds time scale. A single representative FOB-SH trajectory at $T = 300$ K in the herringbone layer of pMSB (A)-(C) and pentacene (B)-(D) is illustrated. In (A) and (B), the IPR is reported with black lines and the average IPR, given in Table 4.5, with dashed red lines. In (C) the quantum amplitudes of the molecules within the herringbone layer, $|u_i(t)|^2$, are projected on the b direction, $q(x_b,t) = \sum_{i,x_{b,i}=x_b}^{\text{molecules}} |u_i(t)|^2$, and in (D) the projection is on the T_1 direction, $q(x_{T1},t) = \sum_{i,x_{T1,i}=x_{T1}}^{\text{molecules}} |u_i(t)|^2$. The charge carrier is strongly localized in regions coloured in red and delocalized in regions coloured in light blue. The time scale characteristic for electronic coupling fluctuations, τ (see Table 4.5), is indicated by white bars. At $t = 0$, $\Psi(t)$ is fully localized on a single molecule ($q = 1$) in both materials. In pMSB small polaron hopping events (motion along x_b) and in pentacene large diffuse jumps of a delocalized polaron are observed (motion along x_{T1}).

diffusive jump motion from the perspective of the charge-nuclear dynamics in the valence or conduction band, as simulated by FOB-SH. In essence, I will show that short-lived thermal intra-band excitations to delocalized band states drive the dynamics of the charge. To this end I consider two other OSs, i.e. NAP and RUB, still respectively representing a poor and a good mobility semiconductor at room temperature.

At first I consider the potential energy, E_a, of the active valence band state, ψ_a, on which the nuclear dynamics is run in FOB-SH, (lines in red in Figure 4.11(A-B), top of valence band at 0 meV). We can observe frequent surface hopping events (dashed black

lines) that ensure approximate Boltzmann population of the active valence band state on the fast ps time scale of present simulations (see Section 3.3). The average electronic energy is $\langle E_a \rangle \approx -1.5\, k_B T$ ($T = 300$ K) and low-lying valence band states up to ≈ -200 meV below the top of the valence band are occupied for very short durations of time. Notably, there is a good correlation between energy and delocalization of the band states: the lower E_a the higher the IPR of the active state, IPR_a (blue lines). This is in accord with the analysis of the DOS (Figure 4.4) and the well known fact that the states in the middle of the valence band are more delocalized than at the top of the valence band.

The actual hole carrier wavefunction of RUB and NAP, $\Psi(t)$, closely tracks the active valence band state of the system, $\Psi(t) \approx \psi_a(t)$, due to the DC, except, of course, when the non-adiabatic couplings are large and two (or more) band states interact. Consequently, the IPR of $\Psi(t)$ (blue lines in the middle panels of Figure 4.11(A) and 4.11(B)) also closely follows IPR_a, though we can observe that the former is smoother and peaks with a certain delay compared to the latter due to the finite decoherence time.

Crucially, the IPR of $\Psi(t)$ correlates very well with the instantaneous rate of charge carrier displacement or classical drift velocity $v_{\mathrm{d}_a}(t)(v_{\mathrm{d}_b}(t))$ contributing to the MSD (green lines (see Eq. 4.3), subscript denoting displacement along the a-direction (b-direction) of RUB (NAP)). I have evaluated this quantity by defining first the center of charge (COC) of the carrier wavefunction as:

$$\langle \mathbf{r} \rangle(t) = \sum_{k}^{M} |u_k(t)|^2 \mathbf{r}_k \tag{4.2}$$

where the sum goes over the M site of the systems, $\mathbf{r}_k$ represent the center of mass of a given site. This quantity is projected along the a-direction (b-direction)) for RUB (NAP), $\langle x_{a(b)} \rangle(t) = \langle \mathbf{r} \rangle(t) \cdot \mathbf{e}_{a(b)}$, where $\mathbf{e}_{a(b)}$ is the unit vector in a or b direction. Finally the classical drift velocity can be calculated by taking the time derivative of the charge displacement:

$$v_{\mathrm{d}_{a(b)}}(t) = \frac{\mathrm{d}\langle x_{a(b)} \rangle(t)}{\mathrm{d}t} \tag{4.3}$$

The peaks in the IPR give rise to peaks in the instantaneous drift velocity in about 75% of cases - these are the productive resonances resulting in charge carrier displacement and mobility, as exemplified in Figure 4.11(C) and (E) at about 200 fs. There are also unproductive resonances where a peak in the IPR does not lead to a corresponding increase in drift velocity, e.g. at 160 fs and 260 fs in Figure 4.11(B) for NAP. This happens, e.g., when the

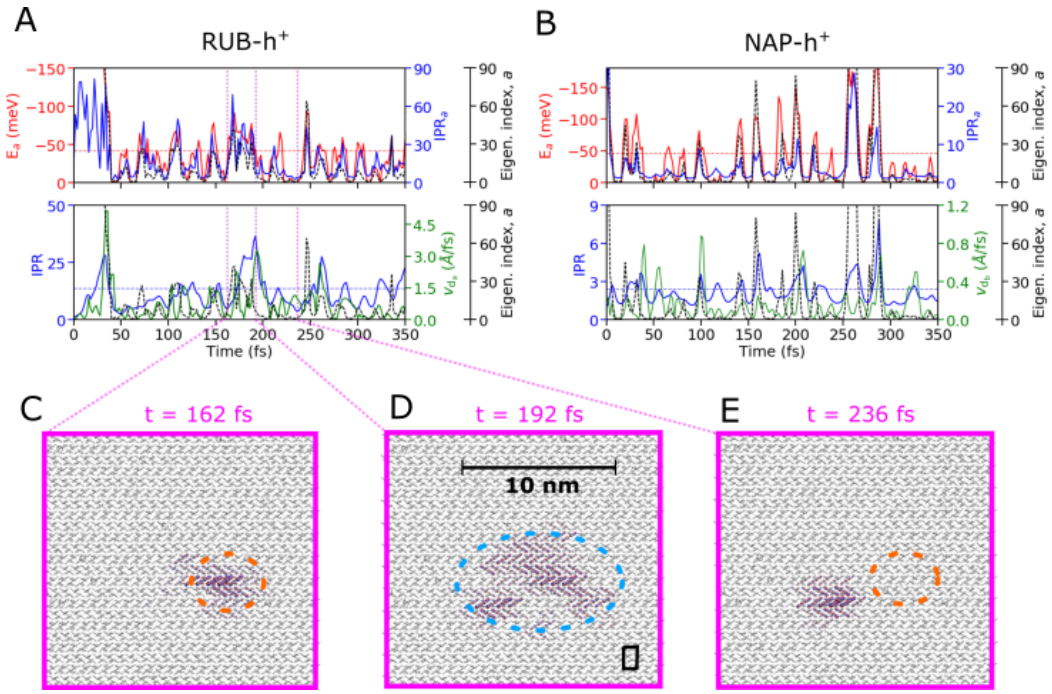

Figure 4.11: Diffusive jumps motion correlated with the delocalization of the adiabatic band states[a]. Panels (A) and (B) show time series along a single representative FOB-SH trajectory for rubrene (RUB) and naphtalene (NAP), respectively. Top panels: potential energy of the active valence band state on which the nuclear dynamics is run in FOB-SH simulations, E_a (red lines), time average of E_a (red dashed lines), IPR of the active valence band state, ψ_a, IPR$_a$ (blue lines) and eigenstate index of the active valence band state, a (dashed black lines, index $a=0$ corresponds to the hole ground state = top of valence band). Bottom panels: IPR of the charge carrier wavefunction, $\Psi(t)$ (blue lines), the classical drift velocity, v_d (green lines), calculated from the charge displacement along the highest mobility directions (direction a for RUB, v_{d_a}, and direction b for NAP, v_{d_b}), average IPR of $\Psi(t)$ over the swarm of FOB-SH trajectories (horizontal dashed blue lines) and eigenstate index (black lines, replicated from upper panel. Note the correlation between the intra-band excitations, i.e. eigenstate index a, the IPR of $\Psi(t)$ and the drift velocity. Panels (C)-(E) depict a representative "diffusive jump" of the charge carrier wavefunction $\Psi(t)$ resulting in drift velocity and charge mobility. Initially the polaron is of average size, about 5 nm (C); upon thermal excitation it extends to about 10 nm (D) and finally re-localizes at a position about 5 nm apart from the original position. For comparison, the unit cell of rubrene is schematically indicated in (D). Isosurfaces for $\Psi(t)$ are chosen as described in Figure 4.7.

[a]The charge transport animations for the full representative FOB-SH trajectories are provided at https://www.dropbox.com/sh/a9jtv83sand4er9/AACWW2M0MefPIg9Sm3TOZ7Wya?dl=0 and/or as supplementary material at https://onlinelibrary.wiley.com/doi/full/10.1002/adts.202000093

polaron undergoing an expansion returns to its original position or when the expansion is near symmetric around the original position so that the center of charge does not move.

4.4 Charge mobility limiting factors

As mentioned before in Section 4.2.2 and in agreement with other works [29, 189], the delocalization of the polaron and hence its mobility is limited by the detrimental effect

of diagonal and off-diagonal electronic disorder. While the diagonal disorder is due to intramolecular vibrations, the off-diagonal disorder is due to intermolecular vibrations and several attempts have been made to suppress them, e.g. by introduction of bulky side chains or by inducing strain to limit the amplitude of these fluctuations [53, 181, 190]. Moreover, Schweicher et al. recently reported that in one OS, C8-DNNT-C8, 75% of the off-diagonal disorder is due to a single "killer mode" associated with a long-axis sliding motion [191]. It is therefore pertinent to explore whether such "killer modes" also exist in the OSs presented in this thesis.

4.4.1 Filtering out off-diagonal electron-phonon couplings

In order to investigate the nature of the intermolecular modes that give rise to off-diagonal disorder limiting charge transport and the effect on carrier delocalization when these modes are suppressed, I calculated the Boltzmann and time averaged IPR of the band states, $\langle \mathrm{IPR} \rangle_\mathrm{B}$, as

$$\langle \mathrm{IPR} \rangle_\mathrm{B} = \frac{1}{T} \int_0^T \mathrm{d}t \frac{\sum_i \mathrm{IPR}_i(t) e^{-E_i(t)/k_B T}}{\sum_i e^{-E_i(t)/k_B T}} \tag{4.4}$$

in which i runs over the eigenstates of the system and the $\mathrm{IPR}_i(t)$ is calculated according to Eq. 2.39 for all the i band states.

The change in the $\langle \mathrm{IPR} \rangle_\mathrm{B}$ is then a proxy for the expected change in mobility, as the wavefunction delocalization is directly related to the extension of the band tail states as seen in Section 4.3.1 (and predicted by transient localization theory). In this analysis all off-diagonal thermal fluctuations larger than a given cutoff-frequency, ω_max, are removed (so-called "filtering analysis") to test their importance for the delocalization of the states. In brief this procedure works in this way: (i) MD trajectories (at least 10 ps) are run for converged supercell sizes and the complete Hamiltonians is computed every 2 fs along these trajectories. (ii) From these Hamiltonians the time series of the electronic couplings are calculated and subsequently Fourier transformed to obtain the frequency resolved spectra for each of the couplings. (iii) The Fourier components above a given frequency cut-off (ω_max in Figure 4.12) are set to zero, and the spectra transformed back to the time domain for reconstruction of the time-dependent Hamiltonians with the off-diagonal frequencies larger than ω_max missing. (iv) Finally, these Hamiltonians are diagonalized at each time step giving the frequency-filtered band energies $E_i(t)$ and the Boltzmann and time-averaged IPR according to Eq. 2.39.

These values have been reported in Figure 4.12 for pMSB, NAP, PEN and RUB as a

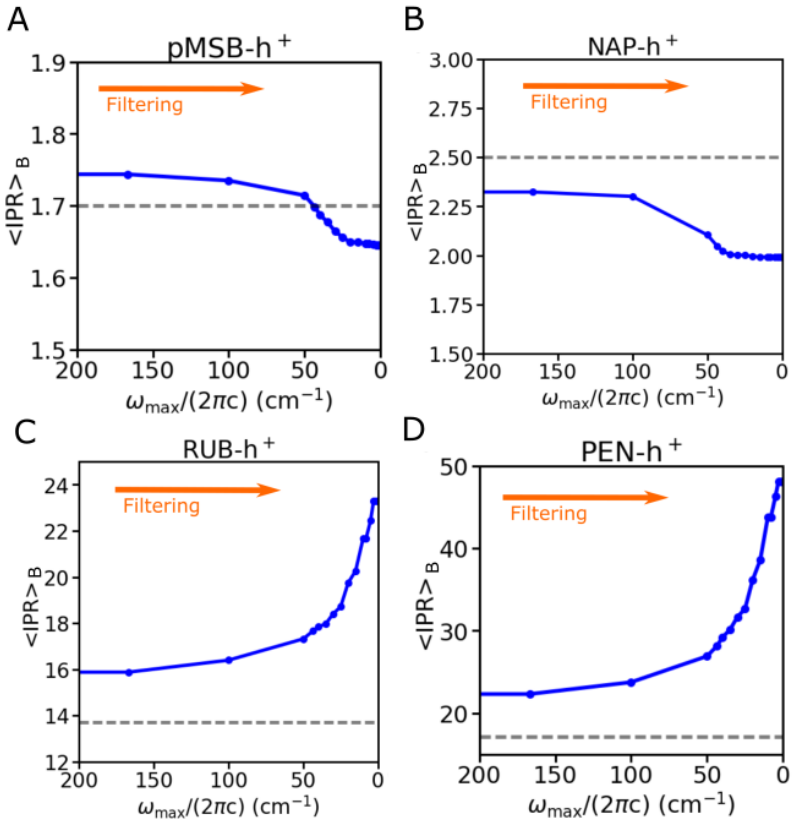

Figure 4.12: Influence of removal of off-diagonal electron-phonon couplings on polaron delocalization. The Boltzmann and time-averaged IPR of the valence band eigenstates, ψ_i, $\langle \mathrm{IPR} \rangle_\mathrm{B}$ (Eq 4.4, blue lines), is plotted against the angular cut-off frequency, ω_max, for low mobility OSs pMSB, NAP (A) and (B) and high-mobility OSs RUB and PEN (C) and (D). The data are obtained by removing ("filtering") all thermal fluctuations of all off-diagonal coupling matrix elements H_{kl} with an angular frequency $\omega > \omega_\mathrm{max}$. For comparison, the average IPR of the charge carrier wavefunction from FOB-SH trajectories, $\Psi(t)$, is shown in dashed grey lines. Notice the different trends for low and high-mobility OSs, see the text for an explanation.

function of ω_max (blue lines). For comparison, the average IPR of $\Psi(t)$, $\langle \mathrm{IPR} \rangle$, obtained from FOB-SH runs with all frequencies included is shown in dashed grey lines. For OSs with medium to high mobilities, such as PEN, and RUB, I found that $\langle \mathrm{IPR} \rangle_\mathrm{B}$ indeed strongly increases when coupling fluctuations slower than 50 cm^{-1} are removed, e.g. Figure 4.12(C) and (D). Hence, removing coupling fluctuations for these materials will increase the transport efficiency. Yet, the increase in $\langle \mathrm{IPR} \rangle_\mathrm{B}$ is smooth and appears to be a collective effect of many modes - it is not possible from this analysis to single out a small set of discrete phonon frequencies that would be particularly important in increasing the delocalization. I also note that even when all coupling fluctuations are filtered out ($\omega_\mathrm{max} = 0$) the charge remains localized over a finite number of molecules due to diagonal disorder.

The situation is qualitatively different for the low mobility OSs pMSB and NAP:

$\langle \mathrm{IPR} \rangle_\mathrm{B}$ now slightly decreases as the coupling fluctuations are removed, e.g. Figure 4.12(A) and (B). In these materials the magnitude of electronic coupling is small and the low frequency fluctuations increase, but only very slightly, the delocalization of these states (see also Figure 4.5) thereby favouring formation of resonances and facilitating charge transport [30]. If one applies Marcus theory for these OSs (with the above caveats), this trend becomes immediately obvious: the hopping rate is proportional to $\langle |H_{kl}|^2 \rangle = \langle H_{kl} \rangle^2 + \sigma^2$ and therefore increases with increasing off-diagonal thermal fluctuations σ^2. This analysis shows that the mobility of high-mobility OSs can be further increased by removing off-diagonal thermal disorder, but that low mobility OSs cannot be turned into high-mobility OSs via this strategy.

4.4.2 Discussion on design rules for high-mobility OSs

In the previous sections I have shown that key to high-mobility OSs is a high density of thermally accessible delocalized states at the top of the valence band (hole) or bottom of the conduction band (electron). For OSs this is only the case when several conditions are met (1) electronic couplings larger than half the reorganization energy, $V > \lambda/2$, where $V = \sqrt{\langle |H_{kl}|^2 \rangle}$ is the mean coupling, to avoid trapping and formation of small polarons, (2) small thermal fluctuations of electronic coupling (i.e. low off-diagonal disorder), $\sigma < V$. (3) For 2D and 3D conduction, isotropic couplings with specific sign combinations favouring low-energy delocalized electronic states. Importantly, I note that the same consensus on design rules has been reached before on the basis of transient localization theory [56].

The problem with most OSs is that one or more of these requirements are not fulfilled. While many OSs exist where (1) is fulfilled, it is still an open question how to best reduce off-diagonal disorder (2) without simultaneously diminishing the mean electronic coupling V. As mentioned before, reduction of thermal fluctuations has been attempted with various degree of success via core functionalization of organic molecules [53, 191] and by application of external crystal strain and pressure [181, 190, 192]. Even more challenging is the design of specific sign combinations of couplings due to the complicated nodal shape of the relevant frontier orbitals. Consequently, the thermally accessible states in most materials tend to be rather localized resulting in modest instantaneous drift velocities and mobilities, as illustrated for pMSB and NAP in Figure 4.12. Arguably, among all known molecular OSs, RUB fulfils these criteria best, though its mobility would be even greater if the couplings were more isotropic and the off-diagonal electronic disorder was smaller (see

Figure 4.5(C) for the extreme case of zero off-diagonal disorder). Nevertheless, the quantities appearing in rules (2)-(3) can be relatively straightforwardly calculated from DFT and used to refine high throughput screening studies that have previously focused on rule (1) [193, 194].

4.5 Conclusion

In conclusion in this Chapter, I have demonstrated that FOB-SH enables unprecedented insight into the elusive, intricate and long-debated nature and dynamics of charge carrier transport in crystalline OSs, based on rigorous physical principles. Computed values for polaron size and charge mobility are in excellent agreement with reliable experimental experimental estimates. I have also reported the full 2D charge mobility tensors for six organic crystals in their highly conductive planes and uncovered the real-time dynamics of the charge carriers. In contrast to traditional transport theories, FOB-SH provides a sound description of the notoriously challenging but practically important charge transport regime of room temperature high-mobility OS materials and correlates very well with the recently proposed transient localization theory. I found that the charge carrier wavefunction forms a flickering, highly dynamic polaron that is delocalized over many molecules in the most conductive crystals and of finite size due to thermal energetic disorder. Thermal intra-band excitations lead to short expansion ("diffusive jumps") of the polaron during which it travels several lattice spacings at a time in highly conductive crystals, followed by de-excitation and relocalization. It is these short bursts that drive charge carrier diffusion in these materials. Hence, from this dynamical perspective, it is more suitable to describe charge carrier transport in OSs as a transient delocalization (rather than transient localization) process. These findings are in agreement with the experimental evidence of a coexistence between delocalized and localized carriers in OSs.

Chapter 5

Temperature dependence of the mobility in organic semiconductors

In this Chapter*, I consider the trend of the charge carrier mobility as a function of temperature and study the crossover from hopping to band-like transport in organic semiconductors using the FOB-SH code. The relationship between the temperature dependence of the charge mobility and the underlying transport mechanism in organic semiconductors has been a widely visited and debated topic in the literature [4, 15, 58, 173]. The advantage of non-pertubative methodologies, like FOB-SH, thereby one solves explicitly the coupled charge-nuclear motion, is that the mechanism is directly observable from the simulation, without reference to its temperature dependence (see also Chapter 4). The latter, in fact, is often used to discern a hopping-like mechanism (commonly thermally activated) from a more delocalized transports (characterized by a negative power law).

The question I would like to answer in this Chapter is whether FOB-SH is able to recover the two extreme regimes and how the crossover between hopping transport at low electronic coupling to a power law band-like temperature dependence at high coupling takes place. I also investigate to what extent FOB-SH is able to capture the temperature dependence of the mobility measured for real OS materials.

5.1 Background on the mobility temperature dependence

An increase in mobility with decreasing temperature that obeys a power-law relation, $\mu \propto T^{-n}$ with $0.5 < n < 3$, has been often seen as a signature of band-like transport [12, 195] as found in high-quality single-crystal devices from time-of-flight [10, 98, 176], time-resolved terahertz pulse spectroscopy [196], and space-charge-limited current measurements [161]. The modelling of this kind of transport has usually been done by assuming that the electronic coupling is much larger compared to the reorganization energy (or local electron-phonon coupling), $V >> \lambda/2$, and therefore describing the adiabatic states of the

*The content of this Chapter related to Section 5.2 is published in Giannini, S., Carof, A. & Blumberger, J. Crossover from Hopping to Band-Like Charge Transport in an Organic Semiconductor Model: Atomistic Nonadiabatic Molecular Dynamics Simulation. *J. Phys. Chem. Lett.* 9, 31163123 (2018). The following figures and related equations have been derived by Dr. Antoine Carof: Figure 5.5 and Figure 5.6. The last part in Section 5.3 regarding the temperature dependence of the mobility in real OSs is currently unpublished work.

systems as delocalized Bloch states and treating the relaxation due to the interaction of the charges with the lattice vibrations as a small perturbation. On the other hand, a thermally activated mobility, described by an Arrhenius-like relation, is generally seen as a signature of hopping transport typical of disordered systems (polymeric and solution-processed semiconductors). In these materials, the charge is trapped in a localized state and it needs some thermal activation energy to be transferred to a neighbouring site. The trapping can originate, e.g., from a disordered morphology, giving rise to a broad distribution of site energies. In this case Marcus and related rate theories have been widely considered and it was assumed that $V << \lambda/2$.

However, both these interpretations are not always valid. In fact, as seen in the Introduction, it is now accepted that in OSs there is often a coexistence of localized and more delocalized states as seen by experiments [18]. Moreover, although the band-like transport proposed for high-mobility organic semiconductors has some common features with the classical band transport found in many inorganic semiconductors, as seen in Chapter 4, it is fundamentally different due to the fact that, in organic crystals, the charge carrier is delocalized only over a few molecules, since the states thermally accessible by the charge are localized tail states (see Figure 4.4). In addition, it is also known that for certain combinations of parameters characterizing OSs also the hopping mechanism can produce a negative slope [100].

5.2 Crossover from hopping to band-like charge transport

I will show in the following Section that non-adibatic molecular dynamics is a powerful tool to investigate the dichotomy between the hopping-like and the more delocalize band-like transports as a function of temperature and other important parameters (i.e. local and non-local electron-phonon couplings and related fluctuations). To this end, I have used an analogue OS model as the one adopted in Chapter 3, i.e. a chain of ethylene molecules. This model allows me to span a wide range of transport parameters (e.g. electronic couplings) without changing the actual characteristic of the system, thus making the investigation consistent across all different transport regimes.

5.2.1 Simulation details

FOB-SH calculations presented here are carried out for hole transport along linear 1D chains of ethylene-like molecules (ELMs). The set-up and parametrization of the organic semicon-

ductor model formed by of ELMs follows the description given in Section 3.1.1.

The reorganization free energy λ for hole transfer between two ELMs is fixed to 200 meV. FOB-SH simulations are carried out for three different coupling strengths, $C = 75.0$, 354.0, 1414.0 meV giving average coupling values $V = \langle |H_{kl}|^2 \rangle^{1/2} = 8$, 30, 120 meV, denoted in the following as "small", "medium" and "large" coupling. The required length of the chain, i.e. number of ELMs, depends on the coupling strength: 5, 30, 50 molecules are used for small, medium and large coupling, respectively, which were shown to give converged mobilities. The chains are placed in rectangular boxes of length 60, 160, 300 Å, lateral size 60×60 Å^2, and are embedded in 123, 505, 993 neon atoms, respectively. The neon atoms take the role of a heat bath facilitating energy exchange with the ELMs while running the FOB-SH simulation in the NVE ensemble. This way I avoid the introduction of artificial bias forces due to the thermostat.

For preparation of initial configurations with the hole localized on ELM 1, the system is equilibrated for 1 ns in the NVT ensemble on the diabatic potential energy surface H_{11}, where ELM 1 is described with the force field parameters for the charged state and all other ELMs with the ones for the neutral state. The last configuration is used to run a 1 ns NVE trajectory on the same diabatic surface to retrieve initial positions and velocities for the FOB-SH simulations. The hole carrier wavefunction is initially placed on ELM 1, $\Psi(0) = \phi_1(0)$. The MD time step is chosen to be 0.1 fs unless stated otherwise, which was shown to give converged mobilities (see Figure 5.3 below), and the electronic time step was set to 0.02 fs. The mean squared displacement of the charge MSD (Eq. 2.31) was averaged over 1000 trajectories of variable length that was chosen to reach the diffusive regime for each coupling strength and temperature. For large coupling, trajectories are run for 1 ps at all temperatures. For medium coupling, trajectories are run for 5 ps at all except the lower temperatures 100, 75, 50 K, where longer trajectories of lengths 10, 15 and 25 ps were required. For small coupling, I generated 5 ps trajectories for all except the lower temperatures 140, 124, 105, 87 K, where 15, 25, 25 and 80 ps were required. Error bars for mobility were estimated from blocks of 200 trajectories.

5.2.2 Impact of algorimitc improvements at various temperatures

First of all, I briefly consider again the role of the implemented algorithms, already extensively discussed in Chapter 3, namely the state tracking procedure, the DC method and spurious charge transfer correction (SCTC) in tackling the trivial crossings problem and re-

lated unphysical long-range charge transfers (see Section 3.3). Compared to Chapter 3, I go one step further here by considering the convergence of mobility, not only with system size, but also with time step, and more importantly I investigate the impact of the decoherence time on the mobility and wavefunction delocalization as a function of coupling strength and temperature.

I have previously pointed out that the DC is very important to keep the localization of the wavefuntion similar to that of the active state (i.e. the wavefunction should resemble the active state whenever it leaves the non-adiabatic coupling region as seen in Section 2.2.3). As mentioned before, different DC approaches are available in the literature and I have implemented some of them within our code. A very good consistency between the quantum probabilities and the fraction of trajectories in each state can be retrieved by using the damping algorithm (see benchmark in Section 3.2). Here, in Figure 5.1 I compare the mobility (blue bars) and the IPR (red bars) obtained with three decoherence times: the Heisenberg uncertainty principle-related decoherence time, Eq. 2.23 (termed PDDC in Chapter 3), the energy-based decoherence time with $C_0 = 0.1$ Ha [87], Eq. 2.22 (EDC) and and the force-based decoherence time, Eq. 2.24 (FORCE-BASED), with the result obtained without any DC. I performed this analysis for the two extreme temperatures (100 and 1000 K) and two coupling regimes (30 and 120 meV).

Importantly, I observe that, provided that the DC is included, the actual decoherence time in the damping procedure (Section 2.2.3) does not significantly influence the mobility or the IPR for this system (the variations are within the error bars). This means that, although the decoherence events are paramount to relocalize the wavefunction and recover an adiabatic state, the time with which this happens is not so relevant for mobility calculations, as long as the internal consistency is maintained (see also Figure 3.3). It is worth to point out that, in all temperature regimes, the polaron size (IPR) is strongly overestimated without DC. Indeed, in the absence of DC, when the wavefunction delocalizes after passing through the crossing region it cannot relocalize again and the higher lying electronic states (generally more delocalized as seen in Figure 4.4) remains occupied. That is, the temperature of the electronic subsystem becomes infinite, the problem of the original Ehrenfest and surface hopping methods. Interestingly, the difference between mobility results with and without DC is large at low temperature (factor 5-10 at 100 K) and much smaller at high temperature (factor 1.3-1.6 at 1000 K). A possible explanation is that in the high temperature regime

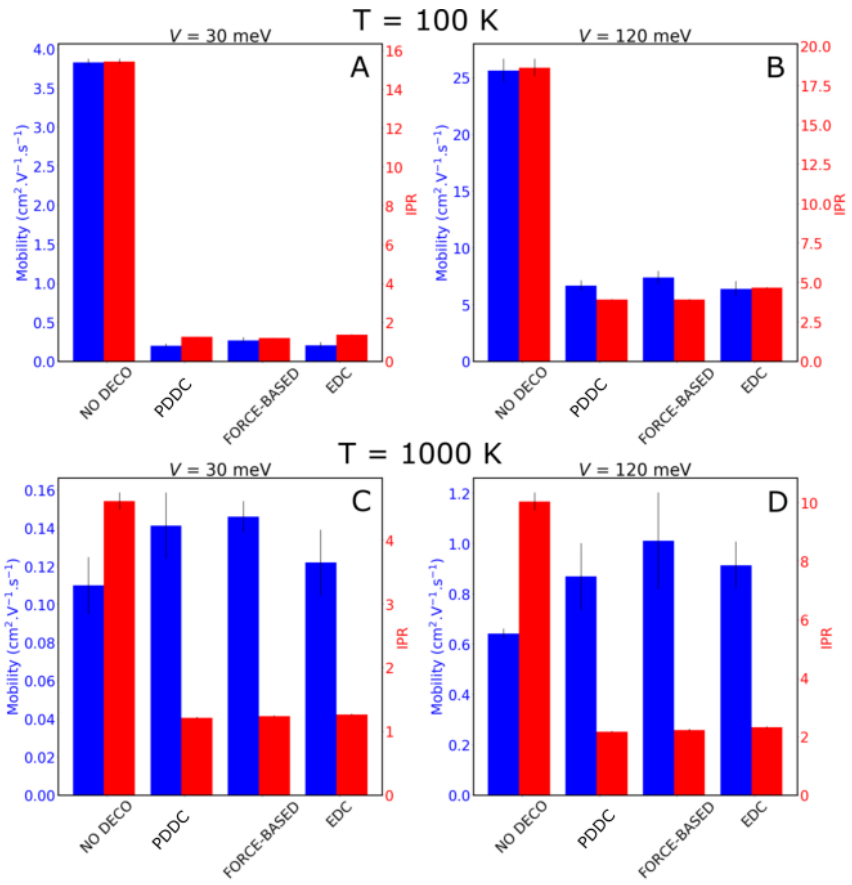

Figure 5.1: Decoherence as a function of electronic coupling and temperature. Hole mobility (blue bars) and IPR (red bars) using no DC, and three decoherence times as reported in Section 2.2.3: Eq. 2.23 (PDDC), Eq. 2.22 (EDC) and Eq. 2.24 (FORCE-BASED). These values are shown for medium and large coupling at 100 K in (A) and (B) respectively and at 1000 K in (C) and (D) respectively.

the wavepacket remains always coherent (due to the larger number of hops between states), thus the actual decoherence mechanism is less important and so it is the time with which it occurs.

Turning the attention to the trivial crossing problem, it is important to stress again, that even when the identity of states is properly tracked and the trivial crossing events are effectively corrected using both tracking algorithm and self consistence correction (SC-FSSH) (Section 2.2.4), the *ad-hoc* decoherence damping procedure itself could induce spurious long-range charge transfers. The reasons behind the decoherence-induced spurious charge transfer (DCICT) problem was extensively discussed in Section 2.2.5, alongside a useful correction to counteract this issue called spurious charge transfer correction (SCTC). Both these algorithms help to properly converge mobility results with time step as well as system size for different coupling regimes as explained below. In particular, I briefly investigate

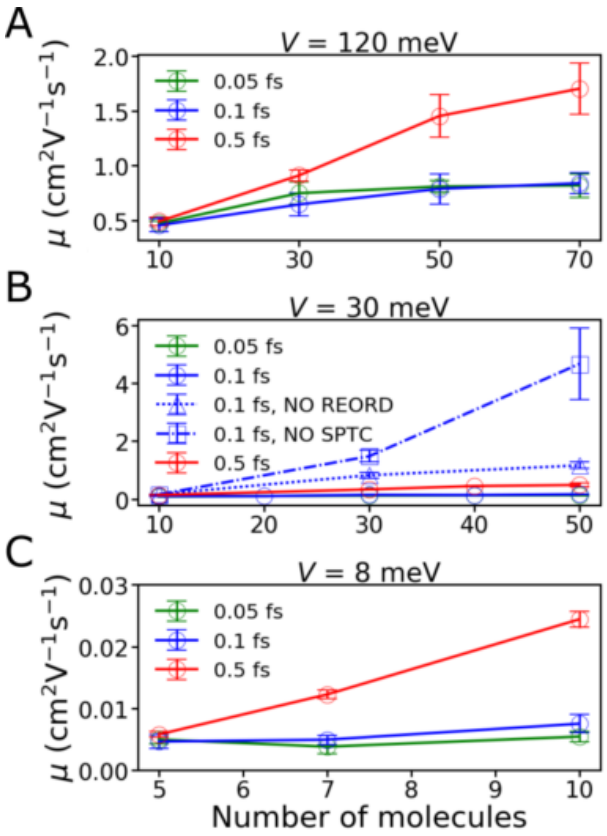

Figure 5.2: Convergence of hole mobility with respect to size and MD time step for a chain of ELM as a function of coupling strength. FOBSH simulations were carried out for (A) large, (B) medium and (C) small electronic coupling strengths V, with average values 120, 30, 8 meV, respectively, for 3 MD time steps (0.5, 0.1, 0.05 fs). $\lambda = 200$ meV and $T = 1000$ K in all simulations. In panel (B) I show results if reordering of states via the state tracking algorithm (NO REORD) or decoherence-induced spurious charge transfer correction is switched off (NO SCTC).

again here the convergence of mobility with chain length and MD time step for the the different electronic coupling strengths (i.e. low, medium and high coupling), the results are reported in Figure 5.2. I find that in all cases the mobility converges at a time step of 0.1 fs. The minimum chain length required for convergence increases with increasing coupling or mobility values from 5 ELMs for low coupling to 50 ELMs for high coupling strengths. The excellent convergence behaviour is due to the state tracking algorithm applied for detection of trivial crossings and the STCT algorithm applied to remove decoherence correction-induced artificial long-range charge transfers. When either one of the two is switched off the mobility steadily increases and diverges with chain length (dashed and dashed-dotted lines in Figure 5.2) for the reasons explained above. The two algorithms I employed here can deal with trivial crossings and spurious long-range transfers very effectively, in particular when considering that the results shown in Figure 5.2 are for very high temperatures (1000 K), which is the most challenging regime as nuclear motion is fast and the probability to miss a trivial crossing is high.

5.2.3 Mobility crossover from activated to band-like transport

I now come to the main result of this Chapter, the hole mobilty as a function of temperature, shown in Figure 5.3(A) for small, medium and large electronic coupling strength. For small and medium coupling values I observe thermally activated transport at low temperatures and band-like decay at higher temperatures. As the coupling strength is increased the activated regime gradually disappears. For the largest coupling strength investigated the mobility exhibits a band-like decrease for all temperatures according to a power law $\mu \propto T^{-1.2}$. These results, obtained here for a fully atomistic model with electronic structure detail, are similar to the ones reported in the model Hamiltonian studies by Wang and co-workers [72, 121] implying that the latter provides a realistic coarse-grained description for charge transport.

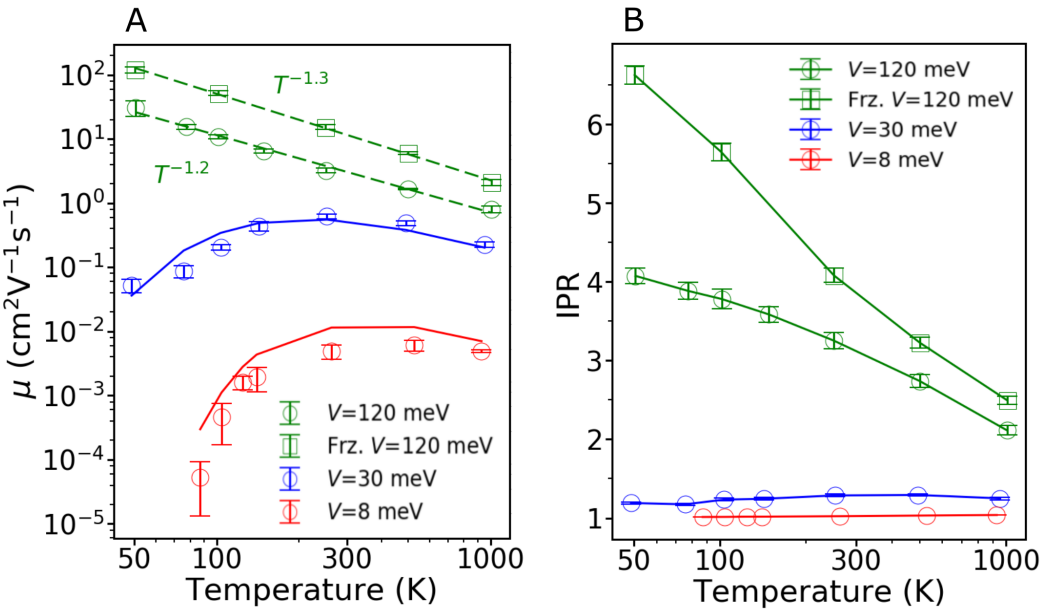

Figure 5.3: Temperature dependence of (A) hole mobility and (B) inverse participation ratio (IPR, Eq. 2.38) for small (red), medium (blue) and large (green) electronic coupling strengths V. The MD time step is 0.1 fs and $\lambda = 200$ meV in each case. FOB-SH mobilities are indicated by circles (◯ symbols), FOB-SH mobilities with off-diagonal elements H_{kl} frozen to V are indicated by squares ("Frz. V", □ symbols). Error bars are obtained from 5 blocks of 200 trajectories each. Hopping mobilities, obtained by solving a master equation with semiclassical ET rate constants, are indicated in solid lines for medium and low coupling strengths, see Appendix B.1 for details. Best fit to an inverse power law is indicated by dashed line for $V = 120$ meV.

To obtain some insight into the molecular mechanism of charge transport I characterize the localization length of the hole wavefunction by using the inverse participation ratio IPR(t) (Eq. 2.38). It converges rather quickly in these simulations, after 400 fs at high coupling and after 2 ps at medium and low coupling strengths. The converged values, in the

following simply denoted as IPR, are shown in Figure 5.3(B).

For small coupling, IPR= 1 for all temperatures, indicating that hopping of a fully localized hole is the charge transport mechanism in this regime (according to what assumed in Marcus theory). Hole hopping from one molecule to the next is driven by thermal fluctuations in the site energies. When the energy of the site carrying the hole (say, site 1, H_{11}) becomes resonant, i.e. within about H_{12} of the energy of the neighbouring site 2, H_{22}, the charge starts to oscillate between the two molecules and surface hops may take place. At the end of the lifetime of the resonance the hole may settle on site 2, followed by thermal relaxation to a lower site energy as determined by reorganisation energy λ. During this process the active adiabatic electronic state that drives the nuclear dynamics remains very localized and changes from a state close to diabatic state ϕ_1 to a state close to diabatic state ϕ_2. As seen before, the DC is paramount to achieve good internal consistency and localization of the hole wavefunction $\Psi(t) \approx \phi_2$ after the hopping event has taken place. If the DC is switched off $\Psi(t)$ spreads unphysically causing the IPR to diverge with time (see Figure 5.2).

The above observations suggest that charge transport in this regime may be well described by a simple hole hopping model,

$$\text{ELM1}^{+}\text{–ELM2–ELM3–} \underset{k_{12}}{\overset{k_{21}}{\rightleftharpoons}} \text{ELM1-ELM2}^{+}\text{–ELM3–} \underset{k_{23}}{\overset{k_{32}}{\rightleftharpoons}} \cdots$$

with ET rates k_{ji} obtained from electron transfer theory and evaluated for the same values of electronic coupling and reorganization energy that were used in the FOB-SH simulations. To this end, I have solved a chemical master equation for hole hopping to obtain the time-dependent hole population of each site and the corresponding hole hopping mobility (see Appendix B.1 for details on the algorithm that I have developed to solve the Master equation characterizing the hole hopping). The results are shown in Figure 5.3(A) for the two coupling strengths where hole hopping is observed (low and medium coupling, solid lines). The agreement with the FOB-SH mobilities is very good with deviations that are typically less than a factor of 3. The mobility saturation at around room temperature is because the ET activation free energy $\Delta A^{\ddagger}$ [197] becomes comparable to thermal energy at this point, $\Delta A^{\ddagger} = \lambda/4 - (V - V^2/\lambda) \approx 1 - 2k_{\mathrm{B}}T$ at $T = 300\,\mathrm{K}$ and $\lambda = 0.2\,\mathrm{eV}$ (see Eq. B.5). For higher temperatures the ET rate and diffusion coefficient become nearly temperature independent ($T^{-1/2}$ for non-adiabatic ET, T^0 for adiabatic ET) and the mobility decay is dominated by the T^{-1} dependence of mobility on the diffusion coefficient in the Einstein

equation (Eq. 2.31).

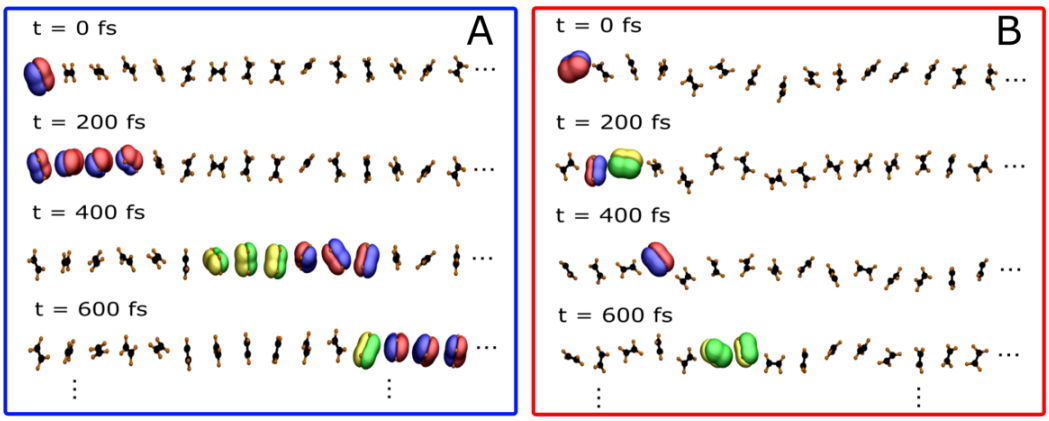

Figure 5.4: Snapshots of a FOB-SH simulation for a chain of 50 ELMs at large electronic coupling strength ($V = 120$ meV, $\lambda = 200$ meV) at (A) 50 K and (B) 1000 K. The real part of the charge carrier wavefunction $\Psi(t)$ Eq. 2.4 is shown in red and blue isosurfaces and the imaginary part in yellow and green isosurfaces. Note, the increased localization of the polaron at higher temperature (panel (B)).

The situation is strikingly different for large coupling strength where a finite activation barrier for hole transfer no longer exists ($V > \lambda/2$) [12, 16, 32]. At low temperatures the hole is delocalized over 4 ELMs on average and as the temperature is increased the IPR steadily decreases to 2. This decrease in IPR correlates remarkably well with the decrease in hole mobility.

In Figure 5.4, I show a few snapshots of the hole wavefunction $\Psi(t)$ along a randomly selected FOB-SH trajectory. At low temperature, the hole can quickly spread over several molecules to form a polaron that moves along the chain on the 100 fs time-scale. By contrast, at high temperature the hole wavefunction remains trapped over a smaller number of sites and cannot move as easily along the chain. What is perhaps surprising is that the extent of polaron delocalization is not very pronounced in this model, even at temperatures as low as 50 K. This is not an artefact of the finite size of the simulation system (all IPRs are well converged with respect to system size), but an indication that small thermal fluctuations are sufficient to prohibit the formation of extensively delocalized, band-like electronic states. Previously, localization of the polaron has been attributed to thermal fluctuations of electronic coupling (non-local electron-phonon coupling) [12, 56, 74] and site energy (local electron-phonon coupling) [72, 121]. To better understand the importance of these two contributions, I recomputed the mobility with the off-diagonal Hamiltonian matrix elements H_{kl} frozen to the thermal average V. The results are shown in Figure 5.3 (squared symbols in green). I find that the qualitative trends in mobility and IPR are already well reproduced

for frozen electronic couplings. Inclusion of coupling fluctuations enhances polaron localization and reduces mobility but does not change the qualitative picture. This means that the temperature-induced localization is strongly related to both site energy fluctuations and coupling oscillations.

5.2.4 A simple resonance model

In order to better understand the role of site energy fluctuations and temperature-induced localization of the wavefunction, I show in the following that the trends observed for an M-site chain, change in slope of mobility versus temperature at low couplings, and power-law decrease at high couplings, correlate well with the temperature-dependence of resonance in a simple two-site model. We can consider the standard ET model comprised of two parabolic free energy curves for donor and acceptor diabatic states, $A_1(\Delta E)$ and $A_2(\Delta E)$, respectively (see also Figure 1.2), as a function of the site energy difference $\Delta E = H_{22} - H_{11}$ and assume constant electronic coupling $V = H_{12}$. The free energy profile for the corresponding adiabatic electronic ground state can be written as [32]:

$$A(\Delta E) \approx \frac{A_1(\Delta E) + A_2(\Delta E)}{2} - \frac{1}{2}\sqrt{\Delta E^2 + 4V^2} \tag{5.1}$$

From the equation above, we can determine the corresponding probability of the site energies difference $P(\Delta E)$,

$$P(\Delta E) = \frac{\exp(-A(\Delta E)/k_B T)}{\int \exp(-A(\Delta E)/k_B T)\mathrm{d}\Delta E}. \tag{5.2}$$

Defining the ET resonance region (region of transition state and avoided crossing) as $-2V < \Delta E < 2V$, we can obtain the probability to be in resonance, P_{res}, by solving the integral

$$P_{\mathrm{res}} = \int_{-2V}^{2V} P(\Delta E)\mathrm{d}\Delta E. \tag{5.3}$$

The probability distributions Eq. 5.2 are shown in Figure 5.5 for small and large coupling strengths and for three different temperatures. The resonance probability Eq. 5.3 is indicated by the shaded areas in each case and P_{res}/T plotted on the secondary axes in Figure 5.6 (dotted lines).

For small coupling the peaks of the probability distribution are at $\pm\lambda$ for all temperatures, well outside the narrow resonance region explaining the low mobilities in the hopping

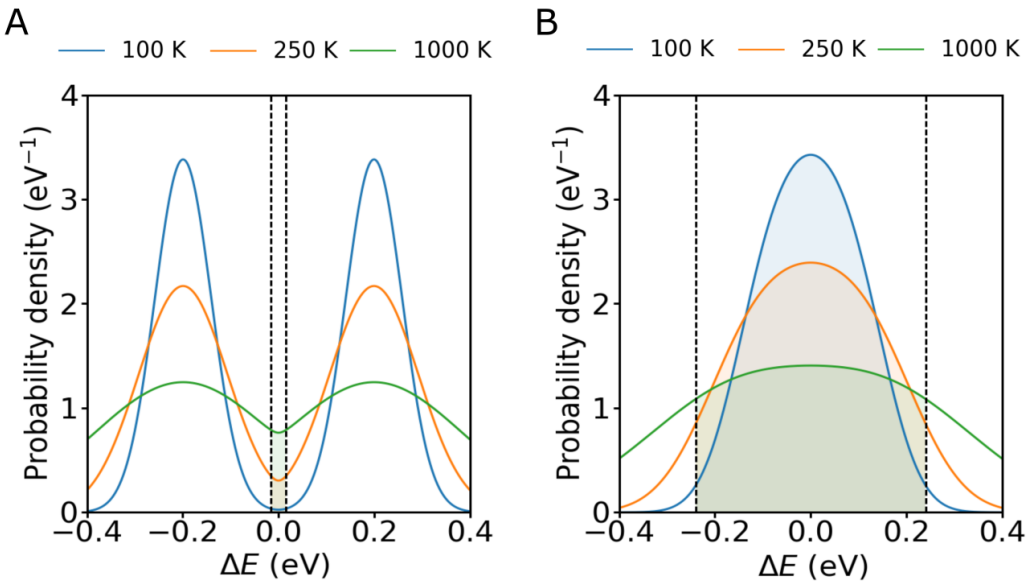

Figure 5.5: Probability density distributions Eq. 5.2 for the site energy difference $\Delta E = H_{22} - H_{11}$ of a 2-state model, $\lambda = 200$ meV. The resonance region for the charge transfer, $\pm 2V$ is indicated by black dashed vertical lines. (A) For small electronic coupling strength $V << \lambda/2$, temperature broadening of ΔE increases the resonance probability P_{res} (Eq. 5.3, shaded area under curves). (B) For large coupling strength $V \geq \lambda/2$ the temperature broadening reduces resonance probability. P_{res}/T correlates well with the computed mobilities for the ELM chain (dotted lines in Figure 5.6)

regime (Figure 5.5(A)). Increasing the temperature widens the energy gap distributions and increases the resonance probability and therefore the hopping mobility. However, this effect saturates at around room temperature causing the curve P_{res}/T to flatten and to crossover from a positive to a negative slope (Figure 5.6 (red and blue dotted lines)).

The situation is markedly different at high coupling, see Figure 5.5(B). In this case the barrier for ET no longer exists and the transition state at $\Delta E = 0$ becomes a minimum on the adiabatic free energy surface Eq. 5.1. Therefore the peak of $P(\Delta E)$ is centered at $\Delta E = 0$ for all temperatures, well within the resonance region. As the temperature is increased the distributions again broaden, but this leads now to a reduction in resonance probability. The downward slope that the model predicts is in excellent agreement with the results from FOB-SH simulations, see Figure 5.6 (green dotted lines). It is remarkable that this very simple two-state model can reproduce the trends in mobility for a M-site chain in all relevant mobility regimes bearing in mind that no dynamical effects are included, only equilibrium free energies. A natural extension of this model would be to include the possibility for M-site resonances (with $M > 2$) [32, 188] and to derive an expression for the average drift velocity as required for prediction of mobilities.

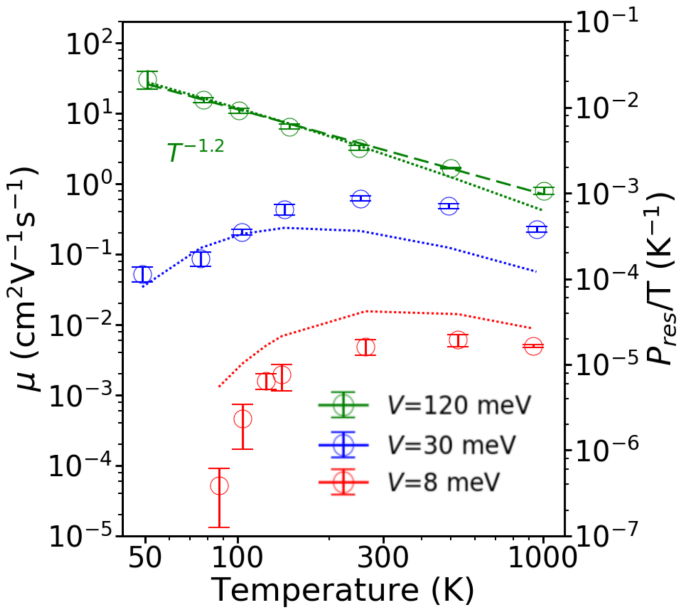

Figure 5.6: Probability resonance as a function of temperature. FOB-SH mobilities reported (from Figure 5.3) are compared with the probability resonance (dotted lines) divided by temperature (P_{res}/T) results obtained with the two states resonance model as explained in the text.

5.2.5 Discussion on the duality between hopping and band-like transport

Spanning four order of magnitude in the mobility and very different behaviours in the localization/delocalization of the charge with temperature going from hopping to band-like transport, the results obtained in this Section can provide an overall view regarding the underlying mechanisms leading the charge transport. When the coupling is small compared to reorganization energy FOB-SH recovers the activation regime characterizing small polaron theories often successfully applied to deal with structural disordered systems [12, 198]. The charge transport is mainly guided by disorder in the site energies created by the localized charges. The charge has to overcome the energetic barrier between diabatic surfaces in order to hop from one molecule to the other. Once this happens, the wavefunction is transferred to the nearby molecule along with its structural deformation.

The situation becomes quite different and possibly more interesting at high coupling, where there is a coexistence between delocalized and localized charges depending on the temperature. This is in agreement with the results obtained by Fratini and Ciuchi [52] where they employed Green's function to solve the Kubo formula and determined the carrier mobility in rubrene as a function of temperature. When $V > \lambda/2$, small polarons cannot be formed at any temperature preventing the existence of activation regime and the states are

more delocalized. In this regime off-diagonal fluctuations become detrimental for the transport and further localize the charge. In OSs such delocalization includes only a handful of molecules, in accordance with the findings of Wang and Beljonne in Ref. [72] where they used a modified surface hopping based on model Hamiltonians. Evidence from many experimental measurements have also pointed to the existence of finite size polarons typically localized on a few molecular sites [19–22].

5.3 Mobility temperature dependence in real OS crystals

I investigate at this point the temperature dependence of the mobility across the 2D herringbone layer of some of the OSs presented in Section 4.1 (i.e. naphthalene (NAP-h^+), anthracene (ANT-h^+), perylene (PER-e^-) and rubrene(RUB-h^+)). The objective is to explore the origin of the band-like dependence of the mobility as a function of temperature as found by experiments in these OSs [11, 98, 157, 160, 176, 199, 200]. In fact, it is now clear from the previous Chapters, that both band and hopping-like transport are hardly justified in explaining the temperature dependence in organic crystals (where the electronic coupling is commonly close to half the reorganization energy). I also would like to explore here whether FOB-SH can capture the experimental slope of the mobility versus temperature.

5.3.1 Simulation details

The systems set-up and parametrization are the same as detailed in Section 4.1.1 unless otherwise stated. Supercells were equilibrated at different temperatures in the range from 150 to 350 K for each system following the previously established protocol. The number of active molecules considered was 493 for NAP, 696 for ANT, 660 for PER and 1020 for RUB. Note that the active regions are larger then the ones reported at 300K in Table 4.2 in order to converge larger charge delocalization and mobility when lowering the temperature (see below). To counteract as much as possible the trivial crossing problem in these large cells the time step for FOB-SH was normally chosen as small as 0.05 fs. As a further note, the present simulations do not include the effect of lattice expansion/contraction as a function of temperature or the effect of possible polymorphisms that might be present in different conditions. These effects may change some of the parameters of the Hamiltonian (e.g. electronic couplings) in non-trivial ways. In particular, it was found that upon thermal expansion the phonon frequencies soften as the molecules move apart resulting in a shift toward lower frequencies [201, 202]. This may impact the amount of dynamic disorder

and ultimately the mobility. Some work, that may provide additional insights into this problem, is currently ongoing in our laboratory. The effect of compressive strain on off-diagonal disorder in a rubrene crystal is being scrutinized by using DFT-MD simulations (see Section 7.2) . In the present context, I was not interested in exploring these effects, but rather in investigating whether FOB-SH can recover to some extent the negative temperature dependence slope that is commonly observed in experiments.

5.3.2 Effect of thermal motion on the Hamiltonian

Before looking at the temperature dependence of the mobility, I focus here on the impact that thermal disorder has on key Hamiltonian parameters such as electronic coupling and site energy fluctuations. To this end, I have calculated average couplings and related standard deviations for two crystal pairs (P and T in Figure 4.1, except for PER where the pairs 6.1 Å and 8.1 Å apart with respect to each other, where considered). These averages were obtained by sampling the AOM couplings for all possible crystal $P(T)$ pairs in the crystal along 10 FOB-SH trajectories of length 1 ps at 200 and 350 K. At least 300 trajectories were used instead to calculate the variance $\sigma_{\Delta E}$ of the site energy difference $\Delta E_{kl} = H_{kk} - H_{ll}$ at the same two temperatures. The distributions are generally Gaussian to a good approximation so that the fluctuation of the couplings and site energies can be well characterised by their averages and standard deviations. All values are reported in Table 5.1.

Table 5.1: Temperature dependence of Hamiltonian parameters

			T pair			P pair		
System	Temp. (K)	$\sigma_{\Delta E}$ [a]	$\langle H_{kl} \rangle$ [b]	σ_H [b]	V [d]	$\langle H_{kl} \rangle$ [b]	σ_H [c]	V [d]
NAP	200	81.5	20.2	20.1	28.5	-29.6	14.4	33.7
	350	102.6	19.7	26.4	32.9	-29.4	18.8	33.4
ANT	200	73.3	-27.4	33.9	43.6	-49.0	22.7	51.6
	350	95.1	-24.7	43.4	50.0	-48.1	28.6	50.7
PER[e]	200	78.8	54.8	12.2	56.1	42.2	15.5	45.1
	350	100.4	52.9	15.2	55.0	40.8	19.2	43.8
RUB	200	71.9	-19.4	4.8	20.0	73.5	20.3	75.2
	350	93.1	-18.2	6.6	19.3	75.9	25.9	77.5

[a] Site energy fluctuations (meV), $\sigma_{\Delta E} = \sqrt{\langle \Delta E_{kl}^2 \rangle - \langle \Delta E_{kl} \rangle^2}$. [b] Average couplings (meV). [c] Coupling fluctuations (meV), $\sigma_H = \sqrt{\langle (H_{kl} - \langle H_{kl} \rangle)^2 \rangle}$. [d] $V = \sqrt{\langle |H_{kl}|^2 \rangle} = \sqrt{\langle H_{kl} \rangle^2 + \sigma_H^2}$. [e] For PER, T pair corresponds to 8.10 Å crystal pair, whereas P pair corresponds to 6.10 Å crystal pair.

I note that the standard deviation of the site energy difference $\sigma_{\Delta E}$ increases with increasing temperature. This is in agreement with Marcus linear response theory, where $\sigma_{\Delta E} = \sqrt{2K_B T\lambda}$. Notably, quantization of high frequency quantum modes is not captured by the present semiclassical (FOB-SH) dynamics and this may have some impacts on the mobility (see below for a discussion). The same trend characterises the coupling, σ_H, which modestly increases with increasing temperature, with $\sigma_H \propto \sqrt{T}$ consistently to what found in Ref. [57]. Whereas, the average coupling $\langle H_{kl} \rangle$, although slightly decreasing (in absolute value) with increasing temperature, remains essentially temperature independent for all the systems. These trends are in line with the findings of Troisi et. al in Refs. [203, 204]

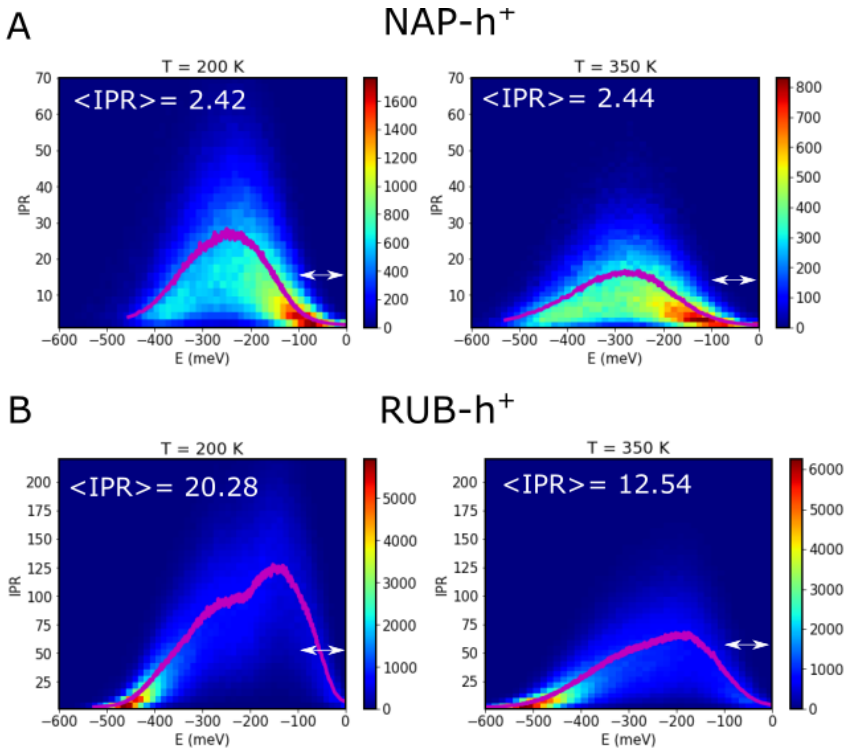

Figure 5.7: Valence band states delocalization at different temperatures for NAP (A) and RUB (B) depicted in a 2D histogram correlating IPR_i (Eq. 2.39) against energy of the band states, ψ_i. On the left panels the temperature is 200 K, while on the right panels is 350 K. The energy averaged IPR_i is shown in magenta lines. Notice that thermal disorder leads to (more strongly) localized thermally accessible states at the top of the valence band in RUB (see $\langle \text{IPR} \rangle_\text{B}$, Eq. 4.4), but the same effect is quite small in NAP. White arrows exemplify the thermally accessible states.

To quantify the effect that smaller site energy fluctuations and smaller coupling fluctuations have on the delocalization of the states at lower temperature, I have reported in Figure 5.7 the valence band states of two very distinct OSs: NAP, where the couplings are small compared to the reorganization energy, and RUB, where the couplings are comparable to the latter. In particular, I have considered 2D histograms correlating the IPR_i (Eq. 2.39) of

the eigenvectors of the FOB-SH Hamiltonian against their energy for two different temperatures (i.e. 200 K and 350 K). We can observe that the characteristic asymmetry in the DOS observed before in Figure 4.4 at 300 K is preserved at these two different temperatures. Importantly, at lower temperature the band states tend to become more delocalized especially in the middle of the valence band consistently with the fact that the thermal disorder is actually reduced (both site energies and couplings fluctuations decrease with decreasing temperature). This effect also causes the band tails to shrink, thus more delocalized states appear closer to the top of the valence band (or the bottom of conduction band if one would consider electron transport) [204]. In RUB this effect is quite pronounced as shown in Figure 5.7(B), whereas it is much weaker in NAP Figure 5.7(A). I have quantified this result by calculating the Boltzmann and time averaging IPR of the band states, $\langle \text{IPR} \rangle_{\text{B}}$ (Eq. 4.4, introduced in Chapter 4). The $\langle \text{IPR} \rangle_{\text{B}}$, gives a measure of the delocalization of the thermally accessible states at the top of the valence band for hole transport (bottom conduction band in the case of electron transport). In RUB, $\langle \text{IPR} \rangle_{\text{B}}$ is around 12.5 at 350 K and it increases to 20.2 upon lowering the temperature to 200 K. In contrast, in NAP the delocalization is quite modest for the thermally accessible state and the $\langle \text{IPR} \rangle_{\text{B}}$ remains quite independent with temperature ($\langle \text{IPR} \rangle_{\text{B}}$ about 2.4). The state in the middle of the band, despite being more delocalized, are not easily thermally accessed by the charge.

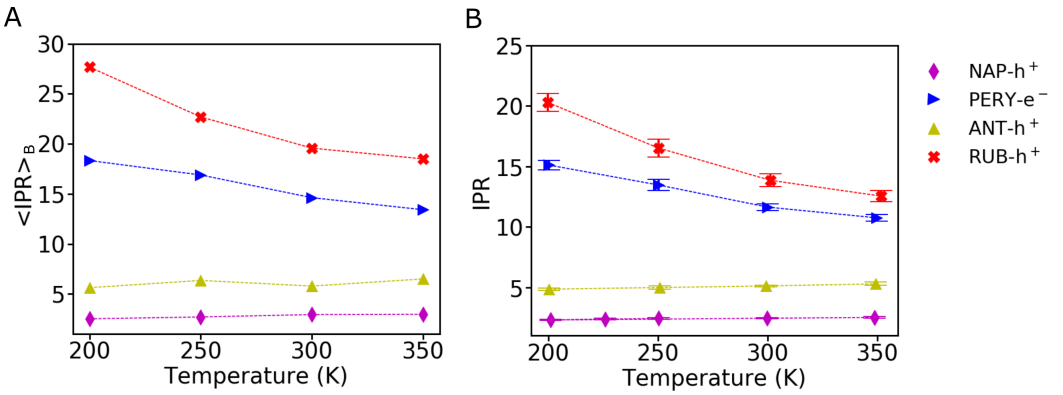

Figure 5.8: States and wavefunction delocalization versus temperature for the investigated OSs are reported in (A) and (B) respectively. $\langle \text{IPR} \rangle_{\text{B}}$ is calculated using Eq. 4.4, introduced in the previous Chapter, while IPR with Eq. 2.38.

As a further result on the effect of thermal disorder, for all the investigated OSs I compare in Figure 5.8 the influence of the temperature on the delocalization of the states thermally accessible by the charge $\langle \text{IPR} \rangle_{\text{B}}$ (Figure 5.8(A)) with the temperature dependence of the IPR of the carrier wavefunction, $\Psi(t)$ (Figure 5.8(B)). The latter IPR is an average

over 600 FOB-SH trajectories (with the exception of RUB where 300 trajectories were considered instead due to the higher computational cost). In the case of of PER and RUB, the extension of the wavefunction (IPR) decreases with increasing temperature, in line with the delocalization of the $\langle \mathrm{IPR} \rangle_{\mathrm{B}}$ of the band states. Notably, both PER and RUB have a favourable sign combination that guarantee a higher delocalization of the thermally accessible states at the bottom of the conduction band in case of PER and at the top of the valence band in case of RUB (see Figure 4.4). While the IPR of ANT and NAP is almost temperature independent (the states remain quite localize at top of the valence band for these two systems). This observation might be a reason for the weak temperature dependence of NAP as I will show in the next Section. In fact, as seen in Chapter 4, wavefunction delocalization correlates very well with mobility (Figure 4.5(B)). A higher delocalization is also a prerequisite for a larger mobility using the transient localization theory [56] in which the mobility is actually proportional to the square of the localization length of the charge (see Section 1.3.3).

5.3.3 2D Mobility tensor components versus temperature

FOB-SH mobilities (blue symbols) are compared with the best available experimental data (black symbols) as a function of temperature in Figure 5.9. When possible, I chose reference mobility data from TOF measurements performed by Karl and coworkers [98, 157, 176] which correspond more closely to FOB-SH simulation conditions (see Section 4.2.1 for a discussion). TOF mobilities show a characteristic power-law relation, $\mu \propto T^{-n}$ with n going from 2.50 in NAP to 1.22 in ANT. For RUB crystal, where TOF mobilities are not available, I report a series of FET measurements (with various colors) obtained by different groups [11, 160, 199, 200]. FOB-SH mobilities are shown along the same crystallographic direction used in the experiments (when this was given in the experimental reference).

Overall, I note that FOB-SH is able to capture the negative slope in the temperature dependence of the mobility often taken as a signature of band-like transport, although as shown in Figure 5.8 the IPR remains localize at most on 15-20 molecules in the highly conductive RUB crystal. In some cases (e.g. ANT along b), FOB-SH reproduces very well the experimental slope, but for other systems the agreement is less good (e.g. in NAP). A general feature for all the systems is the fact that the mobility temperature dependence obtained by FOB-SH is weaker and less steep then the corresponding experimental estimates. As mention before, there might be several reasons for this discrepancy. I discuss few of them

in the following.

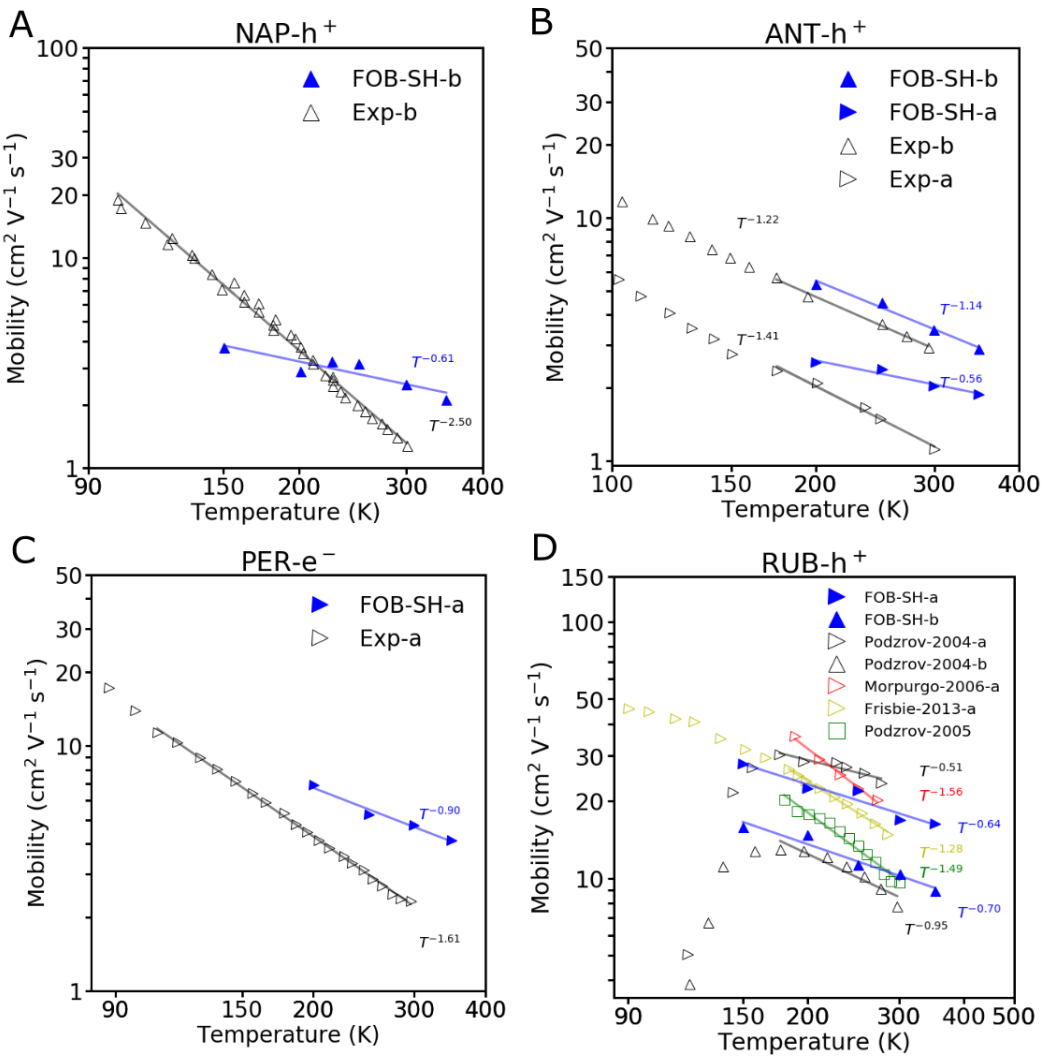

Figure 5.9: Mobility temperature dependence of relevant OSs. TOF measurements used for NAP, ANT and PER are taken from Ref. [98, 157, 176] and shown along the directions mentioned in the experimental works. For RUB, FET mobilities are given with different colors and taken from Ref. [11, 160, 199, 200]. FOB-SH charge mobilities are given with blue symbols. In all the plots, upper triangles are used for *b* crystallographic direction, while right pointing triangles are used for *a* direction. When the direction is not specified square symbols are used. The linear fitting is applied only to the points under the coloured solid line.

First of all, it is important to note that the power law coefficient n is quite dependent on the linear fitting and the number of points used. In this regard, the number of points should be quite high to minimize the uncertainty. When considering that FOB-SH simulations in extended 2D systems are computationally very challenging, n should be taken as indicative. On the one hand, the system dimensionality –on the order of thousands of molecules are required at low temperature to converge the mobility tensor– and the high density of states

stress the trivial crossing correction and the SCTC, due to the high number of state crossings. On the other hand, the computational burden of FOB-SH allows only a handful of mobility values to be calculated for the largest systems.

Secondly, as mentioned before the thermal expansion of the crystal upon increasing temperature has not been considered here. It is known that the lattice parameters in organic semiconductors may change to some extent with temperature, which is accompanied by changes in the electronic couplings (in the order of about 10 meV according to Ref. [205] for rubrene and pentacene). Obviously, such changes can also affect the behaviour of the mobility and its temperature dependence. However, I note that this reasonably small effect is unlikely to account, e.g., for the $n = 2.50$ slope going from low to high temperature in NAP crystal in experiment. So that, despite this effect might play a role when seeking quantitative agreement with experiments, it is not likely to be a determinant factor in the qualitative behaviour of the mobility temperature dependence.

A more relevant point, is the fact that nuclear quantum effects, such as nuclear tunnelling and zero point energy, are missing in the semiclassical FOB-SH description. These effects have been shown by Shuai and co-workers to be reasonably important in OSs especially at low temperatures [14, 177]. The authors also showed that the nuclear quantum effect can linearly increase with increasing reorganization energy [177]. This point might partially explain why the system whose temperature dependence is the least in agreement with experiments (from FOB-SH simulations) is NAP, for which the reorganization energy is the largest compared to the other investigated systems ($\lambda = 187$ meV). Additionally, for NAP the activation barrier for the transport is also the largest compared to the other OSs considered here, ≈ 19.3 meV (estimated using Eq. B.5). This means that in reality at low temperature the charge might partially tunnel through the barrier rather then going over it (this effect is not captured in FOB-SH). In other systems, like RUB, where there is no activation barrier for the charge transfer, the agreement between FOB-SH and experiments is actually better, despite the difficulties described above related to the dimensionality of RUB system and the additional uncertainties in the experimental FET measurements. In fact, these measurements yield quite different values for the power low n: from about 0.6 to 1.5, making difficult a quantitative comparison.

It is worth noting that many of the aforementioned results given by Shuai et. al were obtained by using quantized Marcus rate expressions (i.e. expressions analogue to Eq. 1.1,

but supplemented with quantum vibrational modes to account for nuclear quantum effects). For this reason, despite these perturbative rate-related results are helpful to give a reasonable qualitative picture of the importance of nuclear quantum effects in OSs, they still rely on the charge hopping from site to site assumption at any temperature. This is definitely not the case as shown in Figure 5.8 since the charge is delocalized over several molecules. Most importantly, rates theories do not capture correctly the asymmetry of the DOS as the rate depends on the absolute value of the electronic couplings but not on their relative signs (see Section 4.1.3 for a discussion).

By combining FOB-SH with path integral based simulations (using the framework of ring-polymer molecular dynamics), we have recently attempted to give more sensible picture on the importance of tunnelling and zero point energy effects on hole transfer rates in OSs [122]. It was shown by Ghosh et. al that the transfer rate between the two diabatic states of an ELM dimer (the usual OS model) is higher when nuclear quantum effects are included compared to the semiclassical case by more than an order of magnitude at low temperature. By contrast, at room temperature nuclear quantum effects have turned out to be quite modest. The importance of nuclear tunneling was supported by the fact that, for the ring polymer, the mean radius of gyration of all the atoms increases upon lowering the temperature [122]. I expect this conclusion obtained for a small OS model to be, to some extent, transferable to the real OSs investigated in the present Section. This might improve the agreement with experimental slopes in the mobility temperature dependence, since FOB-SH connected to ring-polymer molecular dynamics should be capable of accounting for two important effects at the same time: wavefunction delocalization and quantization of the nuclei. Work is currently on-going to extend and apply the FOB-SH code with quantum nuclei in this direction.

5.4 Conclusion

In conclusion, I have shown that FOB-SH is a powerful simulation tool that can be used for prediction of charge carrier mobilities as well as transport mechanisms in different regimes (i.e. localized, intermediate and delocalized transport regimes). Remarkably, FOB-SH can capture the crossover from slow activated hopping of a fully localized charge to fast diffusion of a polaron delocalized over several molecules as electronic coupling between the molecules exceeds the critical threshold $V > \lambda/2$.

I found that in the high coupling regime the mobility decreases with increasing tem-

perature. In this regime, the band-like temperature dependence of the mobility has been attributed to the presence of a dynamic disorder by both experiment [53] and theory [15]. Thermal motion and weak intermolecular interactions are often seen as the main source of dynamic localization for the charge carrier [15]. Some of the first theoretical evidence of the existence of this kind of disorder were given by Troisi and Orlandi [12, 74] and were ascribed to the increase of intermolecular coupling fluctuations and displacement between molecules as the temperature increases (in line with what found in this Chapter). I have shown here that, in these OSs, also the diagonal disorder (induced by site energies oscillations) is a leading process in the localization of the thermally accessible band states and thus of the charge carrier wavefunction [72, 135]. Increasing temperature increases the strength of such oscillations and decreases the probability of the charge to be in the favourable resonance region for the transfer, thus reducing the mobility (in the high coupling regime). Nevertheless, these fluctuations are usually related to high frequency intramolecular modes, which should be generally treated as quantum vibrations. This effect is missing in the present FOB-SH simulations and this is likely one of the reasons for the weaker temperature dependence of FOB-SH mobilities compared to experiments, especially in systems where there is an activation barrier for the transfer that the charge has to overcome. While a definitive answer to the question of why FOB-SH tends to underestimate the experimental slope in real OS crystals is not yet reached, I believe that this analysis has given several suggestions on why this might be the case and it has opened some avenues for further exploration and research.

Chapter 6

Exciton diffusion in molecular semiconducting crystals

In this Chapter*, I present the extension of the FOB-SH to effectively treat singlet exciton diffusion in molecular materials. The main motivation behind this work is the fact that long exciton diffusion lengths, along with efficacious free carrier transport and exciton separation processes at the donor acceptor heterojunction, constitute three of the most important requisites for technologically relevant organic photovoltaic (OPV) materials. In this regard, charge carrier transport in OSs has been investigated in previous Chapters, while the study of exciton separation processes occurring at the donor-acceptor interface is currently ongoing in our group and will be subject of future works.

The inability to systematically improve the power conversion efficiency of OPVs is a long-standing problem that hinders their development and use as efficient alternative to conventional solar panels. Similarly to the free carrier transport previously discussed, this problem partially originates from a lack of theoretical methods that can reliably predict the excited state dynamics of OS materials subjected to strong thermal disorder or irregular morphologies [88, 206]. Accurate modelling also requires the ability to study system large enough to fully accommodate delocalized excitons, and to account for effects arising from the interplay of thermal vibrations and electronic motion. If excitons delocalize over more than a few molecules, standard electronic structure methods, such as those based on (time dependent) density functional theory, are generally too computationally expensive to fully meet these requirements. On the other hand, it is possible to reconstruct, with reasonable accuracy, delocalized excitons from the properties of localized transitions. Here, I present an efficient way to use FOB-SH in combination with a site-based Hamiltonian, termed Frenkel exciton Hamiltonian. Within this model the excited state electronic structure of the system is described in a reduced basis of single molecule excitations, thus allowing the simulation of exciton diffusion in extended systems.

*The content of this chapter is currently unpublished. The diabatization program used for the excitonic coupling calculations was developed by Dr. Lorenzo Cupellini (University of Pisa).

6.1 Excitons in organic semiconductors

When an OS absorbs light, electrons can be excited from the valence to the conduction band forming Coulombically bound electron-hole pairs. Usually the optoelectronic properties of molecular semiconductors are dominated by low-lying electronic excitations (in the range of 2-3 eV) [1]. These excitations were described by Frenkel [207, 208] as energetic quasi-particles, that he named excitons. The microscopic properties of excitons, such as their spatial extension and energy are reflected in the macroscopic optoelectronic material properties. As seen in Chapter 4, OSs are characterized by a relatively small dielectric constant, thus the interaction between the bound electron-hole pair is quite strong and related excitations can be well-described by singlet excitations spatially confined on molecular sites of the aggregate (known as Frenkel excitons) [207, 208].

In an extended system such as a crystal or aggregate, the excitation energy can be shared between molecules or fragments, the interactions between different molecular sites lead to delocalization of the excitons and the excited state spectrum of the aggregate will differ from that of the isolated molecule. As I will explain below, the properties of delocalized excitons depend in particular on the strengths of electronic couplings (also termed excitonic couplings in this context) and how they fluctuate in time. The diffusion process of singlet excitons is driven by the excitonic couplings and the molecular relaxation upon excitation energy transfer (local exciton-phonon coupling or reorganization energy). I will present in Section 6.2 an approximate (yet very efficient) way of calculating these interactions based on transition electrostatic potential (TrESP) charges and parametrized force fields (in the same spirit of what was done in previous Chapters for charge transport) and I will discuss the accuracy of the model.

Notably, excitons generated by photo-absorption undergo different pathways (e.g. fluorescence, intersystem crossings, phosphorescence, non-radiative transitions etc.) depending on the energetics of the system and its interactions. In particular, along with singlet exciton diffusion, triplet exciton migration is another important process in many organic semiconductors. Triplet excitons cannot be directly generated following light absorption in these materials due to spin related selection rules and they are produced by intersystem crossing from the singlet to the triplet manifold of states. Triplets may have exciton lifetimes few order of magnitudes larger than the corresponding singlet lifetimes, potentially prompting to larger diffusion lengths [26]. At the current development stage, triplet states are not in-

cluded in the excitonic Hamiltonian that I will present in this Chapter and their formation neglected (see Section 6.1.1 for a more detailed discussion).

6.1.1 Frenkel Hamiltonian

The Frenkel Hamiltonian describes the excited electronic properties of a system with M molecules as:

$$\hat{H} = \sum_{k}^{M} \varepsilon_k(t)|\xi_k\rangle\langle\xi_k| + \sum_{k}^{M}\sum_{l\neq k}^{M} H_{kl}(t)|\xi_k\rangle\langle\xi_l| \tag{6.1}$$

where $|\xi_k\rangle$ represents a state with an exciton localized on molecule k, $\varepsilon_k(t)$ denotes the energy of that state and $H_{kl}(t)$ denotes the intermolecular excitonic coupling between states $|\xi_k\rangle$ and $|\xi_l\rangle$. The eigenstates of this Hamiltonian are the adiabatic excitonic states which can be delocalized over several molecules if the couplings between them are strong enough. Notably, this formalism is equivalent to the one used in Chapter 2 to describe charge transport and the Frenkel Hamiltonian is the analogue to the tight-binding Hamiltonian in Eq. 2.5.

As done before, the excitonic wavefunction can be written as a linear combination of Frenkel excitons, $\Psi(t) = \sum_{l=1}^{M} u_l(t)|\xi_l\rangle$. This allows one to use an equivalent electronic propagation to the one in Eq. 2.4 for charge transport. Obviously, the last term in Eq. 2.4, i.e. the non-adiabatic coupling between localized excitations $d_{kl} = \left\langle \xi_k|\dot{\xi}_l \right\rangle$ is again, to a very good approximation, negligible (see Section 2.1.7). In fact, for excitations on different molecules, this term is roughly proportional to the change in overlap of the two quasi-diabatic states and it is small since the overlap of states localized on different molecules is also very small, as discussed in Section 2.1.7. It is worth noticing that the phenomenological Frenkel Hamiltonian neglects by construction the interaction between different excited states of the same molecules (e.g., the first and the second excited state and/or other charge transfer states). These kind of non-adiabatic interactions can be important for some photophysical processes (e.g. internal conversion and intersystem crossing etc.) [75]. However, to account for non-adiabatic couplings between states of the same molecule, high-level quantum chemical methods would be required [90], defeating the purpose of using FOB-SH to study nano-scale systems. As an example, the inclusion of intersystem crossing to account for triplets formation requires the introduction of a spin-orbit coupling component inducing transitions between states with different multiplicities. The best way of doing this within the surface hopping approach is still an area of active research [90] and will not be discussed

in this work.

On the upside, using Frenkel-type Hamiltonians avoids the problem of describing for example charge transfer (CT) states, whereby excited electron and hole occupy different sites, by constructing supermolecular excitations from locally excited states of single molecules (e.g. the mixing between Frenkel exciton states and CT states are not included). The energies of these CT states are usually underestimated by TDDFT (unless adequate long-range corrected functionals are employed), giving a poor description of low-lying excitations, which are arguably the most important for long time diffusion processes (occurring after the initial ultrafast internal relaxation –following Kasha's rule). Neglecting CT states makes this model inappropriate for describing phenomena such as exciton dissociation along the dynamics. Nevertheless, extending the Frenkel Hamiltonian to include a potential dissociation pathway is possible [209], provided that an efficient way for computing the interaction between Frenkel excitons and charge separated states is found and the electron-hole interaction is considered. This extension, in the context of exciton dissociation at the donor-acceptor interface of organic photovoltaics, will be the subject of future work (see Section 7.2).

Assuming that all the molecules have the same excitation energy ε_k, one can parametrize the local exciton-phonon coupling (reorganization energy) upon excitation energy transfer using classical force fields to reproduce the TDDFT reorganization energy (analogously to what done in Section 2.1.3 for the charge transport). In an exciton transfer process, reorganization energy can be calculated using a four point scheme similar to the one already employed in Section 2.1.3 for the calculation of λ related to an electron transfer process [88, 210]. In particular, the following equation has been used:

$$\lambda = [E_{EX}(\mathbf{R}_N) + E_N(\mathbf{R}_{EX})] - [E_{EX}(\mathbf{R}_{EX}) + E_N(\mathbf{R}_N)]. \tag{6.2}$$

Firstly, one optimizes the geometry of the system and calculates the energy of the ground state ($E_N(\mathbf{R}_N)$) at the optimum geometry ($\mathbf{R}_N$). Then, using the optimized structure one can perform a (single point) TDDFT calculation to compute $E_{EX}(\mathbf{R}_N)$ and optimize the excited state geometry to find $E_{EX}(\mathbf{R}_{EX})$. Finally, the energy of the ground state corresponding to the optimum excited state geometry ($E_N(\mathbf{R}_{EX})$) is computed to complete the four points. The level of theory adopted for these calculations will be discussed in more details in Section 6.3.1. I note in passing that, for the usual anthracene molecule the reorganization energy

obtained from TDDFT (with a long-range corrected hybrid functional, i.e. ωB97xD [211]) gives an error of just about 5% compared to ab-initio SCS-CC2 method [210, 212], proving to be a much cheaper, yet accurate, calculation.

The exciton transport problem is, so far, essentially analogue to the charge transport discussed before in Chapter 2. The main difference is due to the evaluation of excitonic couplings and related gradients as I will explain in the following Section.

6.2 Theory of the excitonic coupling

The excitonic coupling H_{kl} (called V in the following for generality) between the (diabatic) states $|D^*A\rangle$ and $|DA^*\rangle$, where D and A are the donor (k) and acceptor (l) molecules of a given pair, can be generally written as,

$$V = V_{\text{Coulomb}} + V_{\text{Short}} \tag{6.3}$$

This is a sum of a long-range contribution, termed Coulomb coupling, because of its resemblance with the classical interaction between two density distributions (see below), and a short-range contribution that is dependent on the degree of overlap between donor and acceptor wavefunctions and decays exponentially with the distance [213, 214]. V_{Coulomb} is the main coupling ingredient of the Förster theory [215] for excitation energy transfer and it is generally by far the most important. On the other hand, the V_{Short} component is a quantum mechanical term and it was initially related by Dexter (some years after Förster) to an exchange mechanism between donor and acceptor wavefunctions (originated from the indistinguishably of the electrons) [216].

6.2.1 Coulomb contribution

The V_{Coulomb} is the usually the biggest contribution to the excitation energy transfer between singlet states. It can be written as the interaction between the transition densities of isolated donor and acceptor (singlet) states [213]:

$$V_{\text{Coulomb}} = \int \mathrm{d}\mathbf{r} \int \mathrm{d}\mathbf{r}' \rho_k^{T^*}(\mathbf{r}') \frac{1}{|\mathbf{r}-\mathbf{r}'|} \rho_l^T(\mathbf{r}) \tag{6.4}$$

where $\rho_{k(l)}^T$ is the diagonal part of the one-particle density matrix constructed from the ground and excited-state wave functions (i.e. many-body wavefunctions Ψ_i and Ψ_0, re-

spectively) [213],

$$\rho^T(\mathbf{r}) = N \int .. \int \Psi_i^*(\mathbf{r}, \mathbf{r}_2 .. \mathbf{r}_N) \Psi_0(\mathbf{r}, \mathbf{r}_2 .. \mathbf{r}_N) \mathrm{d}\mathbf{r}_2 \mathrm{d}\mathbf{r}_3 .. \mathrm{d}\mathbf{r}_N. \tag{6.5}$$

The transition densities of each molecule can be computed efficiently through an atomic orbital expansion in combination with configuration interaction singles (CIS), time-dependent density functional theory (TDDFT) and other electronic structure methods [214], as implemented, e.g., in Gaussian 16 software package [95, 217].

By definition, the total integrated transition density $\rho^T_{k(l)}$ is zero. As it is costume in Förster theory, at sufficiently large distances between sites (i.e. distance larger than the dimension of the interacting molecules), the transition densities of donor and acceptor can be approximated with the first non-zero term in a multipole expansion, i.e. the transition dipole moment. This approximation is referred to as point dipole approximation (PDA) and the related excitonic coupling, V_{PDA}, can be written as,

$$V_{\mathrm{PDA}} = \frac{\mu_k \cdot \mu_l}{r_{kl}^3} - \frac{3(\mu_k \cdot \mathbf{r}_{kl})(\mu_l \cdot \mathbf{r}_{kl})}{r_{kl}^5} \tag{6.6}$$

where $\mathbf{r}_{kl}$ is the vector distance between k and l molecules and μ_k and μ_l their respective transition dipole moments. The dipolar term in Eq. 6.6 yields the well known r^{-3} asymptotic dependence of the singlet electronic coupling. Importantly, while V_{PDA} has the clear advantage of only needing experimental data, i.e. the transition dipole moments and the distance between the molecular centers, this approximation breaks down at close molecular separations, when short-range effects and higher-multipole contributions become sizeable and the actual shape of the transition densities matters (see Section 6.4 below).

A more suitable approximate way of computing Eq. 6.4, without involving electronic structure calculations at run time, that has found widespread use, relies on the transition charge approximation. The transition densities are represented by a set of point charges located on the atoms of the donor and acceptor molecules, respectively. The Coulomb coupling is computed as the electrostatic interaction between these charges:

$$V_{\mathrm{TrESP}} = \sum_{A \in k}^{N} \sum_{B \in l}^{N} \frac{q_A q_B}{|\mathbf{r}_A - \mathbf{r}_B|} \tag{6.7}$$

where the indices A and B run over the atoms of k and l molecules, respectively. q_A and q_B

are the transition charges of atoms A and B, with positions $\mathbf{r}_A$ and $\mathbf{r}_B$, respectively. Herein, I use the transition charges obtained from the fitting of the electrostatic potential (ESP), the so-called TrESP charges. TrESP charges are obtained as proposed by Renger et al. [218], using the fitting of the electrostatic potential generated by the transition density, as it is typically done to parametrize point charge models in common force fields (see a detailed description of the procedure followed here in Section 6.4). Usually, TrESP charges are computed once, prior production run, and then used to compute couplings at different geometries. This scheme is computationally very efficient and the gradients, $\nabla_I H_{kl}$, necessary for computing adiabatic forces (Eq. 2.16) in FOB-SH are straightforward and analytic. As a downside, this approach neglects any possible dependence of the transition density on the geometry, which is generally a good approximation for rigid π-conjugated molecules forming OS crystals, but it may be less appropriate for more flexible molecules. In this case one would need to update transition charges along MD or use more refined interpolation schemes. I will discuss the accuracy of this approximation in Section 6.4.

6.2.2 Diabatization schemes

Short-range coupling terms, V_{Short}, (which, besides Dexter's exchange, include wavefunction overlap and polarization contributions as well [213]) are small especially when the donor acceptor distance is larger than 3-4 Å like in OSs [219] and there is no covalent bond between the sites. Nevertheless, these interactions become important when the transfer involves spin-forbidden transitions and the first Coulomb term is null (e.g. in triplet-triplet energy transfer) or when donor and acceptor moieties are bonded. In the latter case a through-bond interaction may enhance the short-range part [219]. Despite none of these factors is present in the investigated OS systems, it is worth exploring to what extent V_{Short} is negligible compared to the long-range part, so that $V \approx V_{\text{Coulomb}}$, thus allowing for an efficient computation of V_{Coulomb} as seen in Section 6.2.1.

An accurate strategy to evaluate the total coupling V, including both the Coulomb and short-range contributions, relies on a diabatization approach [213]. Starting from a supermolecule electronic structure calculation of the excited states in the donor-acceptor system, which are a combination of diabatic (i.e. charge- or excitation- localized) electronic states, the resulting electronic Hamiltonian is finally transformed into the diabatic basis to extract the coupling. Within this context, the main requirement is the definition of the diabatic states for the energy transfer process. Some of these diabatization strategies rely on constraints

imposed on the electron density, e.g., constrained density functional theory (CDFT) [220], while others use additional operators to define diabatic states [221, 222]. Although a detailed account of these approaches is beyond the scope of this thesis, I briefly describe here one of such a scheme, termed fragment excitation difference (FED) method [219, 221, 223], that I will employ herein to calculate the reference total coupling, V.

The FED scheme can recover the diabatic (localized) basis from delocalized excited states by using an additional operator Δx, which measures the difference in excitation number between the donor (k) and acceptor (l) molecules. The elements of the Δx matrix are given in terms of "excitation densities", defined as the sum of attachment (electron) and detachment (hole) densities [213]:

$$\Delta x_{ij} = \int_{\mathbf{r}\in k} \rho_{ij}^{\mathrm{ex}}(\mathbf{r})\mathrm{d}\mathbf{r} - \int_{\mathbf{r}\in l} \rho_{ij}^{\mathrm{ex}}(\mathbf{r})\mathrm{d}\mathbf{r} \tag{6.8}$$

where i and j are two adiabatic states and ρ_{ij}^{ex} is the excitation density, defined as,

$$\rho_{ij}^{\mathrm{ex}}(\mathbf{r}) = \rho_{ij}^{\mathrm{Att}}(\mathbf{r}) + \rho_{ij}^{\mathrm{Det}}(\mathbf{r}) \tag{6.9}$$

The quantity Δx has its extrema when the excitation is entirely localized on either the donor (k) or acceptor (l). Without loss of generality, assuming that the adiabatic states i and j are the combination of two diabatic states, $|D^*A\rangle$ localized on k, and $|DA^*\rangle$ localized on l, the eigenvectors of the 2×2 Δx matrix represent the transformation from the adiabatic to the diabatic basis ($\mathbb{U}$), and the eigenvalues are either 1 or -1 for $|D^*A\rangle$ and $|DA^*\rangle$ [219, 221, 223]. The diagonal matrix of adiabatic energies ($\mathbb{H}^{\mathrm{ad}}$) can be transformed into the diabatic basis of $|D^*A\rangle$ and $|DA^*\rangle$ by $\mathbb{U}^\dagger\mathbb{H}^{\mathrm{ad}}\mathbb{U} = \mathbb{H}$. The electronic coupling between these states is found as the off-diagonal element of $\mathbb{H}$.

In many cases, a 2 state adiabatic basis is not sufficient to retrieve completely localized states: in fact, an adiabatic state could be the combination of many diabatic states of both donor and acceptor. Moreover, charge-transfer states can mix with Frenkel exciton states, and viceversa [219, 224]. To overcome this difficulty and recover the coupling between completely de-mixed and localized (Frenkel) exciton states –which form the state space for the Frenkel Hamiltonian in Eq. 6.1– I employed in this thesis a multi-state variant of the FED approach which I will call herein multi-state FED (MFED). This approach is a generalization of the FED method described so far [219, 223, 224] and can make use

of multiple adiabatic eigenstates (of the donor-acceptor supermolecular system) to recover maximally localized and decoupled diabatic states. The code that I will use in the following was developed by Dr. Lorenzo Cupellini (University of Pisa). This strategy was previously successfully employed to recover excitonic couplings in light-harvesting and biological systems [214, 223] as well as bridged donor-acceptor moieties [219]. For a more detailed description of this approach I refer to Ref. [223, 224].

6.3 Investigated molecular crystals

The systems investigated in this Chapter are anthracene (ANT) [151], α-sexithiophene (OT6) [225], perylenetetracarboxylic diimides (PTCDI-H) [226] and dicyanovinyl-capped S,N-heteropentacene (DCVSN5) [227] in their crystalline form as depicted in Figure 6.1.

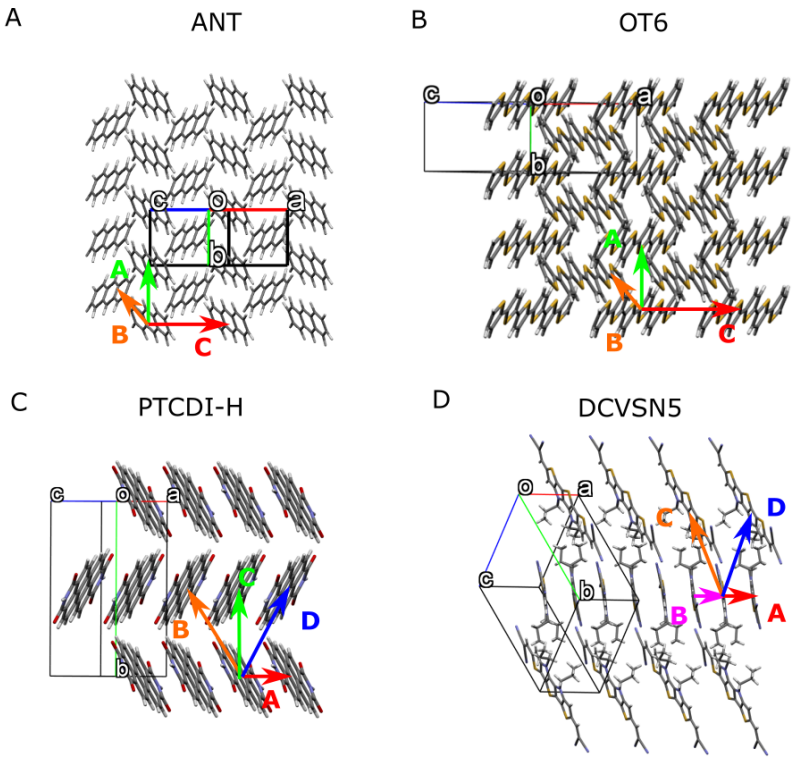

Figure 6.1: Crystal structures of investigated OSs. Few of the closest crystal coupling pairs (with the strongest excitonic coupling) are indicated with coloured arrows.

These systems are chosen in order to span a wide range of diffusion regimes (from incoherent to a coherent exciton transport) using the FOB-SH approach and for several reasons given below. ANT has been chosen primarily because its exciton transport properties were investigated experimentally before [228–230] and using both Marcus theories [88] as well as non-adiabatic molecular dynamics coupled to DFTB [231] electronic structure.

Therefore, ANT is ideal to test the approach and protocol developed here. OT6 is chosen because its optoelectronic properties are similar to those of polythiophene, making it a good prototype model system for studying thiophene-based polymeric semiconductors (e.g. P3HT), which are particularly important as electron donor system in organic photovoltaic heterojunctions. PTCDI-H is representative of another important class of organic semiconductors based on perylene-diimide (PDI) molecules [232]. The latter are arguably one of the most intensely studied class of semiconductors due to their high degree of chemical tunability and ability to form highly organized supramolecular assemblies via wet and dry processing methods [233]. PDI derivatives have recently found use in high-efficiency organic photovoltaic cells as replacements for fullerenes [25]. It is therefore important to study their electronic properties. Finally, DCVSN5 is technologically very interesting as it was found to give a remarkable power conversion efficiency of 6.5% when employed together with fullerene in bulk heterojuction solar cell. Additionally, this system was previously studied in Ref. [88] by Aragó et. al by means of Ehrenfest dynamics coupled to model Hamiltonians, thus providing a further comparison for FOB-SH dynamics.

6.3.1 Excitation energies

All quantum chemical calculations in the following Sections have been performed using the TDDFT implementation of Gaussian 16 software [95]. I computed the excitation energies of ANT, OT6, PTCDI-H and DCVSN5 single molecules with two different long range-separated hybrid functionals CAM-B3LYP [234] and ωB97xD [211]. These functionals are often required for organic molecules to get the correct asymptotic behaviour of the functional and because of their balanced description of locally excited and charge-transfer states. The basis-set was fixed to 6-31g(d,p) as commonly used in the literature for similar systems [88, 235, 236].

The vertical excitation energies as well as the adiabatic excitation energies for the lowest singlet excited state (S1) of ANT, OT6, PTCDI-H and DCVSN5 molecules are reported in Table 6.1. These data refer to optimized geometries of the single molecules in gas-phase. The reorganization energies (of the first excited state) obtained from the four-point scheme (Eq. 2.6), as described in Section 6.1.1, are reported in Table 6.1 as well.

The first important observation is the fact the two long-range corrected functionals give very similar values both for the energies and the oscillator strengths (f) of the lowest-energy excitation, pointing to a robust description of the transition density of this excitation. As

Table 6.1: Excitation and reorganization energies (eV) for the lowest-energy (singlet) state of ANT, OT6, PTCDI-H and DCVSN5.[a]

	Functional	S1 vert.	f [c]	S1 adiab.	S1 Exp. [d]	λ
ANT	CAM-B3LYP	3.70	0.086	3.41	3.3-3.4	0.572
	ωB97xD	3.71	0.089	3.43		0.561
OT6[b]	CAM-B3LYP	2.96	2.042	2.68	2.5	0.558
	ωB97xD	3.03	2.060	2.74		0.562
PTCDI-H	CAM-B3LYP	2.85	0.752	2.65	2.37	0.390
	ωB97xD	2.89	0.758	2.68		0.405
DCVSN5	CAM-B3LYP	2.79	2.049	2.64	2.13	0.294
	ωB97xD	2.86	2.061	2.69		0.320

[a] Basis set is fixed to 6-31g(d,p) as commonly used in the literature for similar systems [88, 235, 236]. [b] The geometry for OT6 was kept coplanar as done in Ref. [235] since oligothiophenes tend to crystallize in the solid state with coplanar thiophene units [235]. [c] The calculated oscillator strengths are reported in a.u. [d] Experimental values are taken for solution and gas-phase molecules from Ref. [237, 238] in the case of ANT, Ref. [239, 240] for OT6, Ref. [241] for a similar PTCDI derivative and Ref [227] for DCVSN5.

the following calculations are aimed at estimating correctly electronic couplings, as I will explain below, a good evaluation of the transition densities is the most important issue. It is also worth noting that the second lowest (singlet) excited state as found from both functionals is about 0.7-1.0 eV above S1. This means that the Frenkel approximation describing the excited state of the system as a combination of locally excited S1 states is likely to be a good approximation for these OSs. I further investigate this point by plotting the Natural Transition Orbitals (NTOs) [242] corresponding to the S1 excited state in Figure 6.2 for the investigated molecules. The NTOs offer a useful way of visualizing which orbitals give the largest contribution to a given single-particle excitation (the NTOs are obtained here by using the NTOBuilder tool [243]). For all systems we can see that the NTOs with the largest contributions are indeed essentially the same as the HOMO and LUMO orbitals of the single molecules. This rules out a possible mixing with other high-lying excited states (at least for the isolated molecule) and attests to the validity of the Frenkel Hamiltonian in describing the excitations of single sites as localized excited states.

As a final note, I observe that the reorganization energies in Table 6.1 for the excitation to S1 is much larger than the reorganization energies I have generally found for holes and electrons in Chapter 4 for similar OSs. Taking as an example the anthracene molecule, the hole reorganization energy is ≈ 140 meV while the relaxation of the exciton is about four times larger. This is due to the large charge redistribution occurring upon excitation. In

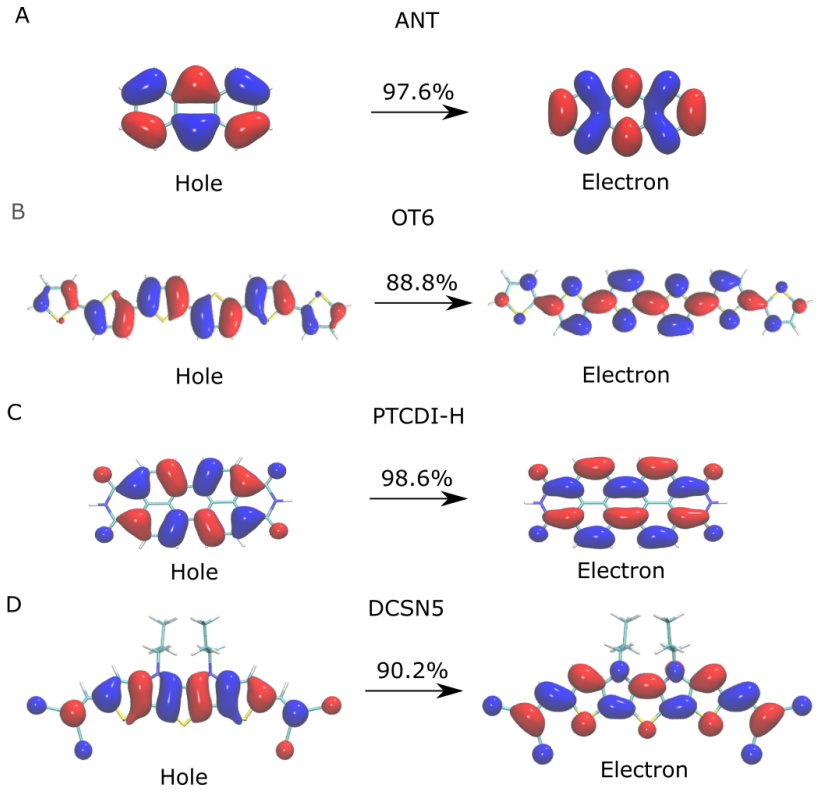

Figure 6.2: Natural transition orbitals for the first singlet excited state of ANT, OT6, PTCDI-H and DCVSN5. The contribution from the NTOs taking part to the main transition is also given. Notably these orbitals are essentially the same as the HOMO and LUMO of each molecule.

particular, just by looking at the NTOs, it is evident that almost every bonding interaction in the HOMO becomes an anti-bonding interaction in the LUMO and vice versa. This causes each bond to become stronger (in case of a bonding interaction) or weaker (for an anti-bonding one) changing the length of the actual bond and causing a large structural modification upon excitation (see also Figure 6.3). These sizeable reorganization energies, that in FOB-SH are used to re-parametrize the classical FF as explained in Section 2.1.3 and Section 6.1.1, are responsible for the strong exciton localization in these systems (see Section 6.5). Bond lengths displacement used for the parametrization of the force field of the excitonic state are reported in Figure 6.3.

6.4 Excitonic coupling results

I now turn to the excitonic coupling, which is one of the main ingredients of the Frenkel Hamiltonian. I evaluated excitonic couplings using the full Coulomb integral, V_{Coulomb}, in Eq. 6.4, the TrESP approach, V_{TrESP}, in Eq. 6.7 and the point-dipole approximation (PDA), V_{PDA}, in Eq. 6.6 for all the systems considered here. These values have been compared with

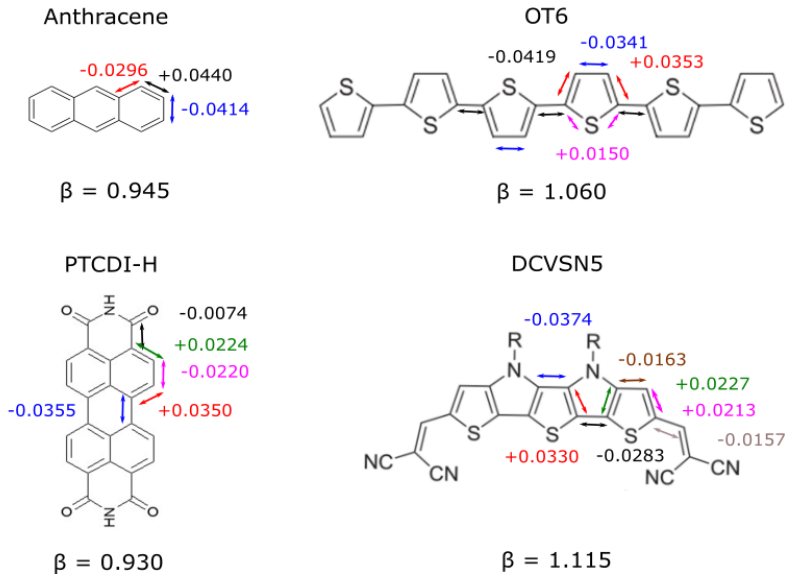

Figure 6.3: Force field parametrization singlet excitons. Changes in bond length upon change from neutral to excitonic state, as obtained from DFT calculations. Displaced bond distances in Å are reported with different colours according to the displaced bonds. The + and − signs indicate an increase and decrease in bond length going from the neutral to the excited system, respectively. The displacements are used to parametrize the force field for the molecules in their lowest energy singlet state. For clarity, displacements symmetric to the ones indicated are not shown. Scaling factor β for force field parametrization of reorganization energy, as described in Section 2.1.3, is also reported for each system.

the total excitonic coupling, V (Eq. 6.3), obtained using the multi-state fragment excitation difference approach (MFED) described in Section 6.2.2. This was done in order to assess the extent of the short-range coupling in these closely packed OS solids and the different levels of approximation of the long-range Coulomb interaction.

For the calculation of MFED couplings (V) and Coulomb contributions (V_{Coulomb}) I have used CAM-B3LYP [234] functional for OT6 and PTCDI-H (as suggested in Ref. [244]) and ωB97xD [211] for ANT and DCVSN5 (for a more consistent comparison with Ref [88]). As pointed out before, I found these two functionals to give very similar values for the Coulomb couplings of these systems (i.e. maximum discrepancies less than 5 meV in OT6). This is because the transition densities are described similarly by both functionals. The MFED diabatization procedure was carried out employing 20 excited states of the supermolecular donor-acceptor system to ensure a complete de-mixing between excitations of different nature (e.g. charge transfer and other excitonic states) and an optimal reconstruction of localized Frenkel exciton states and related couplings. The results are reported in Table 6.2 for three of the closest crystal pairs of the investigated OSs.

We can observe that V_{Coulomb} is generally very close to the total coupling V. The mean

relative unsigned error (MRUE) is about 6%. This small discrepancy can be attributed to the missing short-range part, V_{Short}. The observation that $V \approx V_{\text{Coulomb}}$ lays the groundwork for further approximations of the long-range Coulomb interaction (see Section 6.4.1). Notably, for ANT, the coupling found here from TDDFT compares very well with excitonic coupling found by using high-quality coupled cluster (SCS-CC2) methods (i.e. 26 meV for *A* pair [212]). Although such a good agreement might not be general for all systems, it is encouraging in this particular case.

6.4.1 Validation of approximate Coulomb interactions

The first order approximation of V_{Coulomb} is the point-dipole approximation (PDA). In Table 6.2, the V_{PDA} couplings are evaluated by using the transition dipoles obtained by the previous electronic structure calculations for the same crystal pairs (using the EXAT analysis tool [245]). We can see that PDA gives strongly overestimated couplings compared to the Coulomb interaction especially for OT6 and DCVSN5 molecules, where V_{PDA} couplings are factors 7 to 9 higher than the Coulomb integral. This means that considering the full transition density and not only the first order term in the multipole expansion is actually important to get a reliable coupling estimate. For this reason, despite being a very widely used and simple approach, the PDA should be used with great care, especially for closely packed solids, e.g. OS crystals. The reason for the overestimation of V_{PDA} compared to the V_{Coulomb} will be investigated in more detail further below.

In order to evaluate the Coulomb coupling using TrESP charges (V_{TrESP}, Eq. 6.7), an initial parametrization of the partial transition charges on each atom of the donor-acceptor pair is required (see Section 6.2.1). Similarly to what is commonly done for partial atomic ground state charges, I started by fitting the electrostatic potential (ESP) generated by the density distribution of the molecule. To this end, the same functionals employed so far and basis-sets have been used to get the charge density and the Merz-Singh-Kollman (MK) scheme has been adopted for the fitting. In case of excited state calculations though, the density distribution is actually a transition density related to the transition from the ground to the first excited state (Eq. 6.5), therefore the nuclear contribution to the ESP charges should be ignored [218]. Importantly, to check that the TrESP charges found from the ESP fitting procedure are meaningful, I have made sure that the sum of the TrESP charges is zero (as it would be the case if the full transition density were integrated over all space) and also that the dipole moments obtained directly from the charge densities, $\mu = \int d\mathbf{r}_I \rho^T(\mathbf{r}_I)\mathbf{r}_I$, are

Table 6.2: Excitonic couplings (meV)[a] for crystal structure pairs using the MFED diabatization scheme for the total excitonic coupling V, V_{Coulomb}, Eq. 6.4, V_{TrESP}, Eq. 6.7 and V_{PDA}, Eq. 6.6.

	Pairs	Dist. (Å)	$\lvert V\rvert$ [b]	$\lvert V_{\text{Coulomb}}\rvert$	$\lvert V_{\text{PDA}}\rvert$	$\lvert V_{\text{TrESP}}\rvert$ [c]
ANT	A	6.04	27.88	25.95	26.79	26.34
	B	5.24	6.40	4.53	1.75	4.47
	C	8.56	4.35	4.26	4.13	4.17
OT6	A	5.68	91.92	88.01	644.99	86.89
	B	5.38	101.15	96.14	256.15	95.45
	C	9.14	42.01	41.83	12.52	41.60
PTCDI-H	A	4.87	100.06	85.74	152.22	85.46
	B	9.47	31.97	31.88	43.85	31.84
	C	9.40	17.89	17.05	1.36	17.09
DCVSN5	A	3.64	137.65	135.61	1264.63	134.97
	B	4.46	151.93	141.59	258.12	142.04
	C	14.20	24.14	24.36	44.04	24.29
			MUE[d]	3.40	173.10	3.59
			MRUE[e]	6.38%	171.63%	6.71%

[a] Basis set is fixed to 6-31g(d,p) for the calculation of V and V_{Coulomb}, CAM-B3LYP is used for OT6 and PCTDI-H, whereas ωB97xD [211] is employed for ANT and DCVSN5 as done in Ref [88]. Notably since the dipole moment is quite robust with different functionals, the transition densities of the molecules and so the couplings are also very similar. [b] V couplings are evaluated using MFED diabatization approach (using the first 20 excited states for the diabatization procedure, see Section 6.2.2). [c] TrESP are parametrized using a single crystal structure (the same basis set and functionals reported above are employed). [d] Mean unsigned error (meV): MUE= $(\sum_n |y_{calc} - y_{ref}|)/n$. [e] Mean relative unsigned error (%): MRUE= $(\sum_n (|y_{calc} - y_{ref}|/y_{ref}))/n$.

identical with those calculated from the atomic TrESP charges, $\mu = \sum_I q_I \mathbf{r}_I$.

Remarkably, V_{TrESP} (Table 6.2) obtained by using the aforementioned charges are in very good agreement with V_{Coulomb} for all systems and crystal pairs. The notable difference is the fact that TrESP couplings are readily calculated without the need of repeating an electronic structure calculation when the charges have already been parametrized. This constitutes a huge advantage of using TrESP approach in combination with FOB-SH, as it permits to calculate many thousands of coupling elements (and related nuclear gradients) at each step along the MD, thus allowing the study of large nano-scale systems (see Section 6.5). Additionally, this approach permits to efficiently calculate both couplings and coupling fluctuations even beyond nearest neighbour pairs, thus allowing to account for all interactions when constructing the (Frankel) Hamiltonian of these systems. This approach can help going beyond model Hamiltonians where only (fixed) nearest neighbour excitonic couplings are commonly considered [88, 246].

6.4.2 Distance dependence of excitonic couplings

In order to explore the distance dependence of the excitonic couplings and how well the observations made before for the closest crystal pairs can be generalized to molecules further apart, I performed coupling calculations displacing the the two molecules forming the *A* pair at various distances. The results are reported in Figure 6.4 for all the present systems. This investigation will also allow to find a plausible threshold over which to set the long-range Coulomb coupling to zero to speed up the TrESP computation even further without loosing in accuracy.

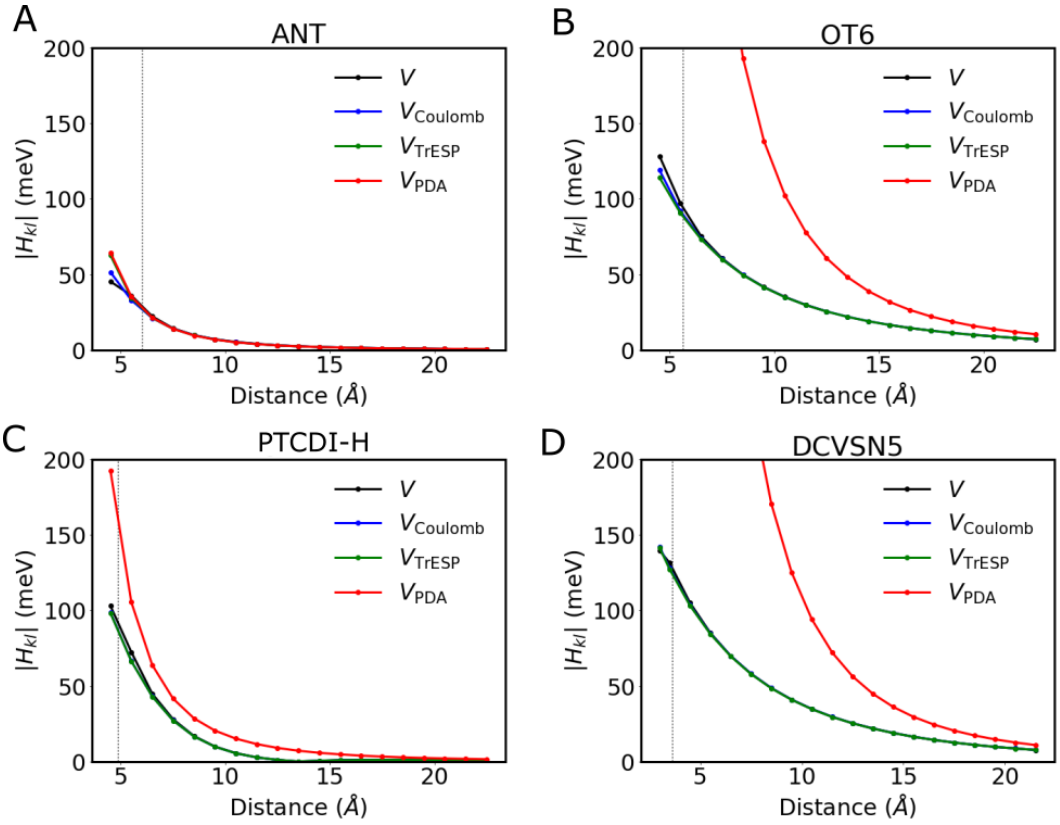

Figure 6.4: Excitonic couplings as a function of distance for the *A* pairs of ANT, OT6, PTCDI-H and DCSN5. Couplings are given in absolute values and have been evaluated using MFED diabatization approach (using the first 20 excited states for the diabatization procedure, see Section 6.2.2), V_{Coulomb}, Eq. 6.4, V_{TrESP}, Eq. 6.7 and V_{PDA}, Eq. 6.6. The PDA clearly fails to provide an accurate description of the excitonic coupling at short intermolecular distances.

As expected, V, V_{Coulomb}, V_{PDA} and V_{TrESP}, all perform very similarly at large distances, that is when the higher multiple terms of the transition densities can indeed be neglected. I also note that the total excitonic coupling V becomes very small beyond 20 Å in all systems. Therefore, a reasonable cut-off can be set at around 30 Å over which the excitonic interactions are effectively considered null. Notably, as the distance decreases, and the closest

distance between molecules in the crystal is approached (vertical dashed black line), the V_{PDA} approximation (red line) diverges from the other solid lines leading to strongly overestimated couplings for all the systems, but ANT. The reason is that the PCTDI-H molecule and, in particular, OT6 and DCVSN5 have spatially extended transition densities and, when the distance between the sites falls below the actual spatial extent of the electronic transition density, the PDA breaks down and it should no longer be used (i.e. the actual shape of the transition density needs to be taken into account). This suggests again caution in the application of the Förster theory when describing exciton dynamics for molecular semiconductors. On the opposite, the V_{TrESP} (green line) gives very good coupling estimates within the full distance regime, proving again to be a useful method. What remains to be investigated is how well fixed TrESP charges can capture the dynamics of the excitonic couplings in time and their fluctuations (see Section 6.4.3).

As a final observation, I note that, for all the systems investigated here, short range effects, V_{Short}, remain negligible even below the shortest crystal pair distance (dashed black vertical line), and the V_{Coulomb} is still a reasonably good approximation of the total V. Yet, short range effects might become important at even shorter distances when the overlap between donor acceptor wavefunctions becomes larger.

6.4.3 Excitonic coupling fluctuations

As mentioned before, the usefulness of the TrESP approach relies on the fact that the atomic transition charges can be calculated for a given structure and used for various different structures along an MD simulation. This scheme is computationally very efficient but it neglects any possible dependence of the transition density on the geometry. The time dependency of the excitonic coupling is solely related to the inverse distance dependence in Eq. 6.7. To assess to which extent this is a good approximation and the accuracy of the TrESP approach in capturing the fluctuations of the excitonic couplings, I computed both the Coulomb couplings and the TrESP couplings along 100 snapshots taken from an MD simulation the closest crystal pair (A). The results are reported in Figure 6.5 along with related coupling distributions. To slightly refine the TrESP charges and partially account for more "exotic" configurations during the parametrization, I repeated the fitting procedure for 50 different structures along an MD simulation for each system and then averaged the TrESP charges over all configurations (instead of using just a single molecular structure). A sign-tracking procedure was adopted to keep consistent the sign of the charges when doing the average.

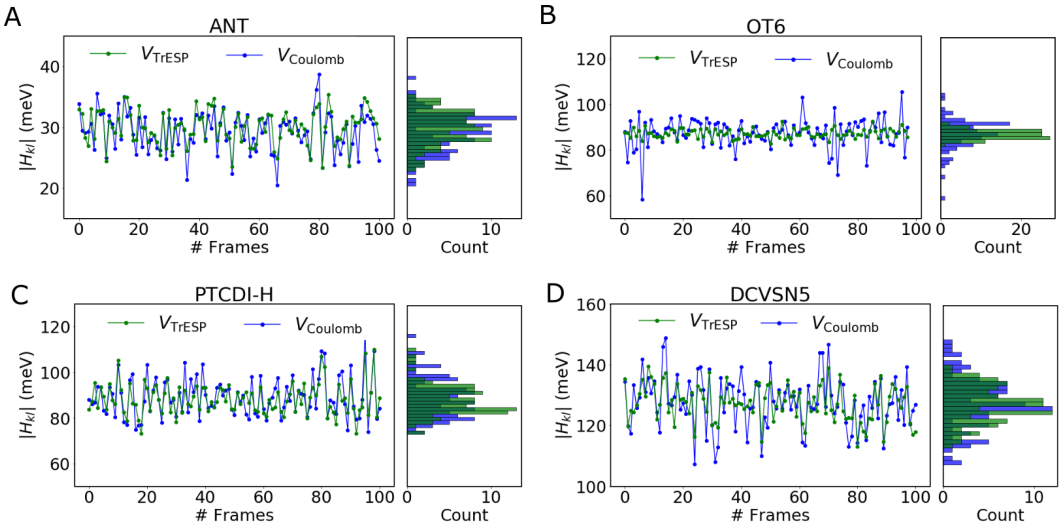

Figure 6.5: Excitonic coupling fluctuations for the investigated OSs. The couplings are evaluated (for the *A* pair) with V_{TrESP} and V_{Coulomb} for a series of 100 MD snapshots. The distribution of these couplings are shown as well.

As already found in the previous Section, we can observe that for all the systems TrESP approach is able to capture the mean value of the coupling extremely well. Interestingly, the coupling fluctuations and the structural dependence of the excitonic couplings are reasonably well capture for ANT, PTCDI-H and DCVSN5 as well. While, in OT6, the TrESP coupling fluctuations are somewhat underestimated compared to the V_{Coulomb}. The explanation for this behaviour is simply that for the first three molecules (ANT, PTCDI-H, DCVSN5) the rigidity of the aromatic structure and extended conjugation ensure that the transition density does not change significantly along the dynamics. Thus, TrESP charges provide a reasonable approximation for the latter. On the contrary, having a more flexible structure, OT6 presents larger structural variations along MD, and the TrESP approach does not capture as well the dependence of the transition density on the geometry.

I conclude by remarking that, despite the TrESP approximation inevitably leads to a loss of accuracy if compared with the rigorous Coulomb integral calculation especially for flexible molecules (e.g. polymers), it provides a very efficient scheme to evaluate a large number of coupling matrix elements along MD dynamics. It is also very accurate when it comes to mean couplings and fluctuations of rigid conjugated molecules that are of interest for this thesis. Importantly, updating the transition charges along MD using, for example, more sophisticated interpolation schemes (e.g. machine-learning techniques [247]), could help increasing further the accuracy of TrESP charges even for more

flexible molecules [247].

6.5 Exciton transport from non-adiabatic molecular dynamics

Having described an efficient way of evaluating the Frenkel Hamiltonian in combination with FOB-SH, I present here the results for exciton diffusion coefficient and diffusion length obtained using non-adiabatic molecular dynamics in the investigated semiconducting crystals. The diffusion length is an important observable characterizing the efficiency of the transport process and ultimately affecting the performance of photovoltaic devices (see Introduction). In fact, this quantity should be long enough in order for the exciton to reach the donor-acceptor interface and initiate the separation process. Similarly to what was done in the case of charge transport in Chapter 4, it is possible to evaluate the mean squared displacement (MSD) of the excitonic wavefunction along the different crystallographic directions according to Eq. 2.33. The diffusion tensor can then be calculated by taking the time derivative of the MSD in the long-time regime according to Eq. 2.32. From the diffusion tensor components, $D_{\alpha\beta}$ (with $\alpha(\beta)$, representing the Cartesian coordinates x,y,z), the diffusion length is defined as [26]:

$$L_{\alpha\beta} = \sqrt{2D_{\alpha\beta}\tau} \tag{6.10}$$

where τ is the particle lifetime, namely the time it takes for the exciton to relax to the ground state. This quantity can also be measured using photo-luminescence experiments.

In the following Sections, I calculate the MSD of the exciton as described in detail in Chapters 3 and 4 for charge transport. I use FOB-SH in combination with three important extensions of the original surface hopping method: decoherence correction (DC), removal of decoherence correction induced artificial long-range charge transfer and tracking of trivial surface crossings (see Section 2.2). The FOB-SH initialization procedure is analogue to the one established in Section 3.1.2 to initialize the charge transport. The exciton is initially chosen to be fully localized on a single molecule k, $\Psi(t=0) = \xi_k$ and propagated in time in the 2D $a-b$ planes of ANT, OT6 and PTCDI-H (activated to the exciton transport as done in Section 4.1.1 for charge transport). The DCVSN5 crystal presents a slightly different crystal structure compared to the other systems. In particular, π-stacked antiparallel columns, in this system, feature the largest excitonic couplings. DCVSN5 presents also intercolumnar interactions, where a molecule of the central column can interact with four

neighboring molecules via interactions between the cyano groups of one molecule and the vinylic/heteroaromatic hydrogens or sulfur atoms of the other molecules. The couplings for these lateral interactions are much smaller compared to *A* and *B* pair within the same column (see Table 6.2), albeit still present. Therefore, a reasonably good model to consider all the possible interactions consists of an active region composed by 5 columnar stacks along the *a* crystallographic direction. The portion of molecules activated to the transport counts more than 300 sites for all the systems (300 molecules for ANT, 392 for OT6, 336 for PCTDI-H and 395 for DCVSN5). The time steps used are 0.01 fs for ANT and 0.025 fs for OT6, PTCDI-H and DCVSN5. The following results are reasonably well converged in terms of system size and time step. On a final technical note, I remark that the sign consistency between excitonic couplings of different pairs is ensured by using the same set of TrESP charges (with the same phase) for all the sites.

6.5.1 Transport anisotropy and diffusion length

In Figure 6.6, I report the MSD of the excitonic wavefunction along *a* and *b* crystallographic directions over time for all the systems. The MSD is evaluated by averaging over 600 FOB-SH trajectories (1.5 ps long) and the diffusion coefficient estimated from the linear part of the MSD (dashed black lines).

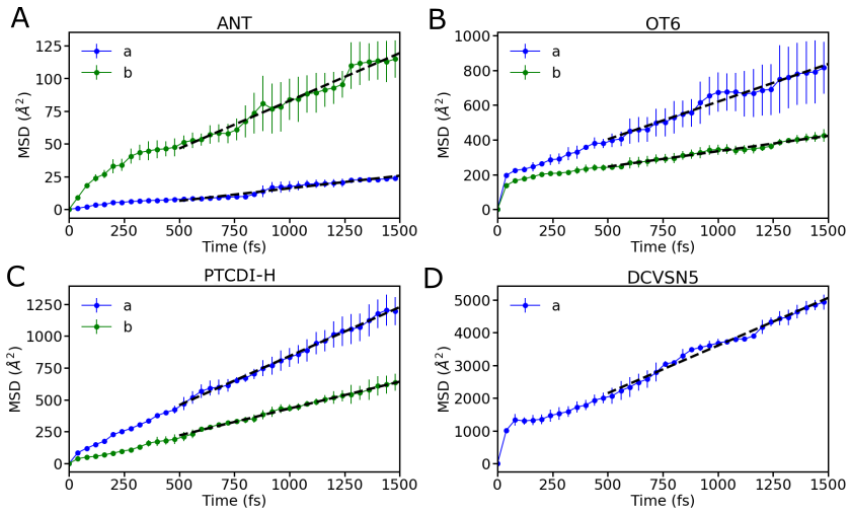

Figure 6.6: Mean squared displacement (MSD) of the excitonic wavefunction. MSD is obtained from 600 FOB-SH trajectories of the OS materials shown in Figure 6.1 along *a* and *b* crystallographic directions. Error bars are obtained by block-averaging over 3 blocks, 200 trajectories each. The diffusion coefficient is obtained from linear fits to the linear MSD portion (dashed black lines).

The diffusion coefficient is reported in Figure 6.7 against the IPR of the excitonic wavefunction (Eq. 2.38). The former quantity spans more than two order of magnitudes for

the chosen systems and the transport mechanism changes from a slow incoherent hopping in ANT crystal to a more coherent and faster transport in DCVSN5.

As expected the exciton tends to diffuse for longer distances along the crystallographic direction with the highest excitonic coupling and there is a good correlation between the efficiency of the diffusion process and the wavefunction delocalization (as already found for charge transport). The larger the excitonic delocalization, the higher the diffusion coefficient. However, due to the sizeable exciton-phonon coupling (exciton reorganization energy) the exciton remains localized over 1 to 2 molecules in all these systems. Yet, a larger delocalization is reached when higher-lying thermally excited states are populated during the transport process (see also Section 4.3).

Interestingly, by comparing ANT and OT6, that have a comparable exciton reorganization energy (see Table 6.1), one can see a much longer MSD in OT6 crystal compared to ANT and a factor of 6 larger diffusion in the former system when considering the high diffusion directions of both OSs (i.e. b direction for ANT, for which $D_b = 3.7 \times 10^{-3}$ cm^2 s^{-1}, and a direction for OT6 with $D_a = 2.2 \times 10^{-2}$ cm^2 s^{-1}). This is a direct consequence of the larger excitonic coupling in OT6 compared to ANT. Nonetheless, the diffusion length for ANT (Eq. 6.10) is about twice as large as the diffusion length in OT6 compared to ANT. In particular, L_b amounts to about 85 nm in ANT, while L_a in OT6 is between 21 and 42 nm. This is due to the longer exciton lifetime in ANT crystal, $\tau = 10$ ns according to Ref. [228], compared to the same quantity in OT6, which has been estimated to be between 100 and 400 ps by time-resolved photoluminescence spectroscopy [248]. However, it is fair to point out that τ for the OT6 system does not refer to the crystal structure (studied herein), but it is rather characteristics of a multilayer OT6 film deposited on silicon dioxide [248]. I also note in passing that the exciton diffusion length of a thin-film of OT6 molecules vacuum-deposited on quartz was reported to be about 60 nm by the quenching of the photoluminescence [249], in qualitative agreement with FOB-SH. However, different structures and morphologies of the sample make difficult a like-for-like comparison with these simulations and the latter should be taken just as indicative.

Notably, in contrast with OT6 and ANT, despite having a larger diffusion coefficient (from FOB-SH simulation) of about 0.04 cm^2 s^{-1}, PTCDI-H has a diffusion length of less then 1 nm due to the fast decay of the exciton to the ground state (of about 100 fs [232]). A negligible diffusion length was also found in Ref. [232] for a thin-film PDI derivative with

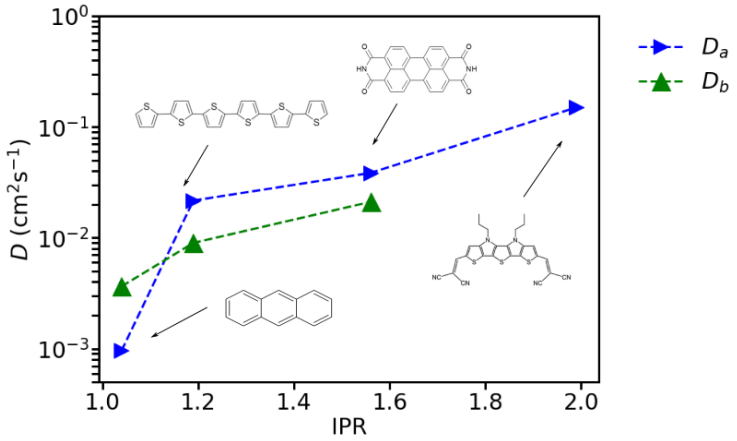

Figure 6.7: Diffusion coefficient against the IPR of the excitonic wavefunction for all the investigated systems. The diffusion coefficient (D) is reported in blue and green for a and b crystallographic directions, respectively. Notably D spans more than 2 order of magnitude going from ANT to DCVSN5 systems.

a linear butyl side-chain, although, once again the comparison can only be indicative.

Finally, I observe that, to the best of my knowledge, no experimental diffusion coefficient, nor diffusion length have been measured for DCVSN5 system. Nonetheless, Aragó et. al in Ref. [88] simulated the diffusion process in this crystal by using Ehrenfest dynamics coupled to a model Hamiltonian supplemented with effective local and non-local exciton-phonon coupling interactions. The authors found a diffusion coefficient of 1.9 cm^2 s^{-1}, which is an order of magnitude larger then what found here by using FOB-SH approach. This difference is most likely a consequence of the missing detailed balance and decoherence process in the Ehrenfest approach used in Ref. [88]. In fact, as seen in Chapter 3 and Chapter 4 of this thesis, when these two effects are missing the highly thermally excited states, that are more delocalized, tend to become strongly over-populated by the excitonic wavefunction. This causes a faster transport. I will point out in the next Section, that a far better comparison between FOB-SH and Erhenfest dynamics can be achieved when the latter non-adiabatic dynamics scheme includes a correction for the detailed balance (e.g. the so-called Boltzmann-corrected Ehrenfest dynamics [231]).

6.5.2 An assessment of different methods: the case of anthracene

Anthracene represents a useful system to carefully test the FOB-SH extension to exciton transport, since the diffusion coefficient and related diffusion length have been evaluated by other authors making use of Marcus-like rate expressions [88] as well as Boltzmann-corrected Ehrenfest dynamics [231]. Some experimental estimates are also available [228–

230] for the crystal structure of ANT and can be used as a suitable reference. As seen in Table 6.1, the reorganization energy of ANT is quite high compared to the excitonic coupling, supporting the formation of excitons mostly localized on a single molecule. The IPR calculated from FOB-SH simulations, Eq. 2.38, is indeed on average 1.04. This small IPR can be readily explained by considering that, the barrier for the exciton hopping between different molecules (estimated with Eq. B.5) is about 112 meV which is much higher than the largest coupling in the crystal of around 30 meV and the thermal energy at room temperature (25 meV). This observation has justified the use of perturbative rate theories [88] to study the transition mechanism for this system (see below). Notably, as shown in Figure 6.5 and already observed in the literature [88], the exciton couplings in anthracene exhibit sizeable thermal fluctuations compared to the mean coupling which provides a good motivation to explore direct dynamics methods (such as FOB-SH and Ehrenfest) as well.

To assess the quality of FOB-SH simulations I report in Table 6.3 a comparison between the diffusion coefficients and related diffusion lengths (estimated using an exciton lifetime of $\tau = 10$ ns as found by experiments [228]) with the same values obtained from other different computational methods and available experimental estimates. In particular, to calculate the diffusion coefficients, Elstner's group in Ref. [231] employed semi-empirical time-dependent density functional tight-binding (TD-DFTB) method in combination with Ehrenfest dynamics. The latter approach was opportunely corrected to approximately satisfy detailed balance (which is of utmost importance for an accurate dynamics as seen in Chapter 3). This approach is referred to as Boltzmann-corrected Ehrenfest method (BC-Ehrenfest). Using transition densities taken from the TD-DFTB, the authors obtained averaged Coulomb couplings along MD ($\sqrt{\langle |H_{kl}|^2 \rangle}$) of about 31 meV for A and 11 meV along B pairs. These values are very similar to what found in this work from the TrESP approach ($\sqrt{\langle |H_{kl}|^2 \rangle}$ about 30 meV and 7 meV for A and B pairs, respectively). Though a smaller reorganization energies of 302 meV was found in the former work, as a consequence of the approximate DFTB approach that relies on local functionals to describe the excited state geometry. This reorganization energy was employed to model the exciton-phonon coupling leading to a weaker exciton relaxation compared to FOB-SH, where the exciton reorganization energy is 561 meV. It also is worth to point out that the DFTB implementation is more expensive than the FOB-SH methodology coupled to an effective Hamiltonian proposed here. In fact, in Ref. [231], 1D chains were considered and, as shown in Chapter 4,

this reduced dimensionality could have an impact on electronic transport properties, such as wavefunction delocalization and diffusion coefficient of some systems (see Section 4.2.4).

Despite all these differences and the different underlying dynamics, FOB-SH and BC-Ehrenfest methods yield similar diffusion coefficients (see Table 6.3). The diffusion lengths from FOB-SH and BC-Ehrenfest are both slightly underestimated compared to the experiments. A possible reason is the absence of Frenkel exciton and charge transfer mixing (FE-CT) in these simulations, which is known to enhance singlet exciton diffusion as a consequence of the larger exciton dispersion [250]. This effect, however, is smaller in shorter acenes, such as ANT, than in bigger molecules, e.g. pentacene and fullerene, where the lowest-energy singlet state is a strong mixture of multi-electronic states of different nature. In the latter systems, this mixing would need to be included in the Hamiltonian for a more quantitative prediction of the diffusion.

Table 6.3: Couplings (meV) for $A(B)$ pair, diffusion coefficients and diffusion lengths from different computational methods and experiments.[a]

	FOB-SH[b]	BC-Ehrenfest[c]	MLJ-Rate[d]	Exp.[e]
$\sqrt{\langle\|H_{kl}\|^2\rangle}$ [f] (meV)	29.6 (6.8)	30.5 (11.4)	35.9 (17.7)	-
λ (meV)	561	302	589	-
D_a (cm^2 s^{-1})	9.60E-04	7.10E-04	2.90E-03	1.80E-03
D_b (cm^2 s^{-1})	3.65E-03	2.40E-03	8.20E-03	5.00E-03
L_a (nm)	43.82	37.68	76.16	60
L_b (nm)	85.44	69.28	128.06	100

[a] The diffusion length is estimated from Eq. 6.10 for all the different methodologies using an exciton lifetime $\tau = 10$ ns, as obtained by experiments [228]. [b] FOB-SH simulations are performed on 2D planes with 300 molecules and a nuclear time step of 0.01 fs as described in the text. [c] Boltzmann corrected Ehrenfest values are taken from Ref. [231]. The authors used reduced dimensionality 1D models along a and b crystallographic directions. [d] Perturbative rate theory result are taken from Ref. [88]. A rate expression very similar to the Marcus-Levich-Jortner rate for electron transfer was used by the authors by including an effective quantum mode coupled to the excitation energy transfer process. [e] Experimental estimated for the diffusion lengths are taken from Ref. [229, 230]. [f] Excitonic couplings, for FOB-SH, are averaged over 10 trajectories (1.5 ps long) considering all A and B pairs in the crystal (B given in brackets).

In Table 6.3 I compared both these numerical non-adiabatic propagation schemes with a perturbative rate theory used in Ref. [88] by Aragó et. al as well. The latter approach is reasonably well justified in this system by the high local exciton-phonon coupling and the incoherent hopping mechanism (observed by inspecting non-perturbative FOB-SH trajectories). The rate expression used by Aragó et. al [88] is very similar to the Marcus-Levich-Jortner

rate for electron transfer [32, 219]. It introduces an effective quantum high-frequency mode that is coupled to the exciton transfer process in order to effectively account for quantum-mechanical vibrations. In fact, in the common Marcus expression (see Section 1.3.1) all vibrational modes in the system are treated as classical harmonic oscillators. While such an approximation is generally good for treating low frequency motions of a general solvent, it is not completely accurate for intra-molecular modes of the molecules, since for these modes $\hbar\omega > k_B T$. The approach employed by Aragó et al. gives a diffusion coefficient in the same order of magnitude as FOB-SH and BC-Ehrenfest approaches and slightly longer diffusion length compared to both non-adiabatic propagation schemes. This can be explained with the fact that high frequency vibrations play a non-negligible role for the transport and, for systems with a reasonably high activation barrier (e.g. ANT), a classical treatment of modes might not be entirely justified (even at room temperature). Thus, providing an additional explanation for the lower diffusivity predicted by the FOB-SH and BC-Ehrenfest approaches, which treat all the modes with classical force fields, compared to both experiment and Marcus-Levich-Jortner like expression. On the other hand, the excitonic couplings computed by Aragó et al were found by using a diabatization scheme that includes only 2 adiabatic states [88], therefore the coupling between Frenkel exciton states, is and effective coupling still contaminated by mixing with charge-transfer states (see Section 6.2.2 for a discussion). For this reason, these couplings are larger compared with both TrESP and TDDFTB couplings (which by constructions do not include such a mixing with charge transfer states).

On the whole, considering the differences in simulation set-ups, parameters entering the various Hamiltonians or analytic expressions and the uncertainty commonly characterizing experimental measurements, I believe that the agreement between FOB-SH and other data is very encouraging.

6.6 Conclusion

In conclusion, in this Chapter I have devised and implemented a protocol to extend the FOB-SH approach for treating exciton transport in OSs. I have benchmarked this methodology against other computational methods and available experiments and addressed strengths and shortcomings in detail by applying this protocol to ANT, OT6, PTCDI-H and DCVSN5 systems. In particular, I have described how a phenomenological Frenkel type Hamiltonian can be used in combination with an efficient calculation of off-diagonal excitonic coupling

elements in order to study full atomistic OS systems.

This procedure is based on the calculation of transition electrostatic potential (TrESP) charges to effectively reproduce the transition density of the system at a given geometry. The excitonic coupling found using TrESP charges is in good agreement with the same quantity calculated using full transition densities and also with the total excitonic coupling obtained with a multi-state diabatization scheme. I found TrESP couplings to be more accurate than the point-dipole approximation commonly used in Förster theory to approximate the long-range interaction. Importantly, the short-range part of the excitonic coupling between fully localized (Frenkel) exciton states was found to be rather small compared to the Coulomb contribution in these OSs (at least for the molecular distances characterizing these crystals). The use of TrESP couplings in combination with FOB-SH has allowed me to evaluate the diffusion tensor and diffusion length for large systems and relatively long time scales and I found FOB-SH results in quite good agreement with other computational methods as well as experimental estimates.

In spite of its computational efficiency, the proposed model has some flaws and could be improved further. Firstly, only one excitonic state is considered for each site. Charge transfer states are not accounted for in the present form of the Hamiltonian. However, it would be possible to include them, provided that a fast approach to calculate the time-dependent coupling between Frenkel exciton and charge transfer states is developed. Additionally, triplet formation and dynamics are not included in the present implementation. I briefly mention here that in principle it would be possible to study triplet-exciton diffusion by using FOB-SH in combination with an Hamiltonian similar to the one given in Eq. 6.1. However, this would again require the development of an efficient on-the-fly scheme for the calculation of the short-range part (V_{Short}) in order to avoid any explicit electronic structure calculation analogously to what done for singlet excitons (e.g. a scheme based on orbital overlap [251]). Such a method could be, in turn, benchmarked with a fragment diabatization scheme (analogue to the FED presented in this work) that has been previously developed for the calculation of triplet-triplet energy transfer couplings [222]. Moreover, the TrESP approach used to compute excitonic couplings might not be able to capture large geometrical changes of more flexible molecules along the dynamics, preventing the utilization of FOB-SH, at least in the current form, to study for example polymeric molecules (more involved interpolation schemes could help improving this point). However, in the case of disordered

and amorphous systems, Marcus-like and related quantum expressions might be anyway more suitable and effective to simulate the incoherent transport mechanism. Finally, the classical description of quantum modes seems to be a source of error when the activation barrier for the exciton transfer process is much higher then excitonic coupling. Applying path-integral methods for the nuclear dynamics may address this issue [122], hopefully this will provide a solution in quantitative terms in future (in line with what discussed in Chapter 5).

The real strength of the FOB-SH used in combination with Frenkel Hamiltonian is its high efficiency, which enables direct exciton simulations in systems with experimentally relevant nano-scale sizes and the fact that it does not rely on prior assumptions of coherent or incoherent exciton transport, thus bridging all the intermediate regimes. After careful validation, I think that this Hamiltonian can be successfully combined with the tight-binding Hamiltonian used for charge transport processes in previous Chapter, and then extended in state-space in order to study all the relevant transport and exciton separation processes occurring in photovoltaics materials. The implementation of a more complete extended Hamiltonian that would enable us to effectively study fascinating photoinduced processes in real nano-scale heterojunction interface is under-way in our group.

Chapter 7

General conclusions and outlook

7.1 Conclusions

This work has focussed on electronic transport in organic semiconducting materials investigated from the perspective of a novel non-perturbative and fully atomistic non-adiabatic molecular dynamics approach termed fragment orbital-based surface hopping (FOB-SH). The method efficiently propagates the electron-nuclear motion in time without assuming prior transport mechanisms. It is thus free of limiting model assumptions (see Chapter 2). The goal of this thesis has been the optimization and further development of such a scheme in order to obtain accurate charge and exciton dynamics for experimentally relevant nanoscale system sizes and long time-scales.

I have shown, in Chapter 3, that some important improvements are necessary to make FOB-SH able to accurately fulfil total energy conservation, detailed balance and internal consistency. Importantly, I have found that a correction for missing electronic decoherence, detection of trivial crossings and removal of decoherence correction-induced spurious wavefunction transfers are crucial for a reliable and accurate dynamics. A well-founded set-up to run FOB-SH simulations of charge transport that converges wavefunction delocalization, diffusion coefficient and electronic mobility for different time steps and system sizes has been established and discussed.

These encouraging results set the stage for the application of FOB-SH to simulate charge and exciton transport in experimentally well-studied, application relevant organic crystals. This has been done in Chapter 4, where I tackled another major objective of this thesis, namely providing a better understanding about the interplay of thermal vibrations (particular important in weakly bonded OSs) and charge dynamics. In fact, this is one of the hottest and most actively studied topics in the field of organic electronics as it could ultimately help establish better design rules to drive the synthesis of new and more conducting OS materials. By applying FOB-SH and solving the time-dependent electronic Schrödinger equation coupled to nuclear motion in several OS crystals, I have found that the charge carriers form “flickering” polarons - highly dynamic quantum objects delocalized over many molecules but finite in size (in agreement with experimental evidence) due to thermal dis-

order. These polarons propagate through the crystal by diffusive jumps over several lattice spacings at a time. I have analysed in detail charge mobilities and other properties resulting from this mechanism, compared these quantities with existing analytic theories and validated FOB-SH results against the best available experiments. I have also investigated the temperature dependence of the mobility in Chapter 5 and provided a rationale –based on the relative magnitude of electronic coupling compared to reorganization energy– to explain the experimental evidence of a coexistence between localized and delocalized charge carriers in OSs. These two types of carriers exhibit a different temperature dependence behaviour (namely, a hopping-like transport when the carrier is localized by the disorder and a band-like transport for more delocalized carriers).

Going beyond free carriers dynamics, characterizing for example field effect transistor devices, I finally extended in Chapter 6 the FOB-SH formalism to study the diffusion of excitons (bound electron-hole pairs) in organic materials using a Frenkel-type Hamiltonian. This is an important primary process occurring in organic photovoltaic materials upon light absorption. This work represents a first step to the study of photoinduced processes occurring in organic solar cells from non-adiabatic molecular dynamics and it paves the way for an even more ambitious plan of using FOB-SH to study exciton dissociation and recombination occurring in OPV materials.

7.2 Outlook

Based on the findings of this thesis there are a number of avenues of further research that are currently being explored in our group and that will hopefully provide further advance in the field of nano-scale optoelectronic organic materials.

With regard to charge transport simulations, I believe that FOB-SH is now efficient and accurate enough to gain deeper insights about the structure-properties relationship of relevant organic field effect device morphologies. My efforts together with students and postdocs are now devoted to the understanding and the simulation of charge transport across different morphological domains (e.g. disordered and thin-films phases) of OS systems. In this regard, I have simulated charge transport across few-layer crystalline pentacene thin-films epitaxially crystallized on hexagonal boron nitride (hBN) [252].This system has been extremely well characterized by experiments [252] and it is very interesting as it shows different packing motifs and transport mechanisms across different semiconducting layers. Amorphous pentacene structures are also being generated as well by other students in the

group and, in the near future, we would like to study transport mechanism across ordered-disordered system interfaces. Here, the charge is expected to undergo delocalization-localization steps depending on the domain morphology and on the percolation coupling network. This project should provide a more realistic picture of the experimental conditions from which FET mobilities are extracted.

Another important goal currently being tackled in the group is the use of FOB-SH as a tool for the discovery of high-mobility OSs. On the one hand, it would be nice to use FOB-SH for treating more rigid covalent organic framework structure to reduce the thermal disorder and enhance the electronic coupling between covalently linked units [253]. Scaffolding and rigidity of conjugated molecules are expected to boost the mobility and efficiency for this class of OSs (as predicted in Chapter 4 by artificially freezing the thermal fluctuations of the electronic coupling). On the other hand, another important aspect characterizing OS materials is actually their flexibility, exploited, for example, in flexible organic light-emitting diodes for display applications. A recent experimental study of the strain-mobility relationship in a rubrene crystal suggested a strong, anisotropic enhancement of the mobility under compressive strain [254]. This might be regarded as a new alternative way of improving the efficiency of this material. Molecular simulations will play a key role in understanding the relationship between strain and mobility at an atomistic level. Such knowledge might open up ways to use the mechano-electric response as a new means of enhancing the mobility in organic materials.

Finally, regarding the field of exciton transport and exciton dissociation at the donor-acceptor interface of OPVs, myself and others are extending the FOB-SH formalism to increase the state space of the tight-binding site Hamiltonian to include charge separated states as well as singlet Frenkel excited states. The main goal in the future will be a thorough study of the photoinduced dynamics and electronic processes occurring in organic solar cells aiming at finding new design rules that may help optimising the power conversion efficiency (PCE) of these devices. This project will go far beyond the free-carriers and singlet-exciton transport studied in this thesis. The main challenges that we are currently addressing are the development of a strategy to efficiently and reliably calculate electronic couplings between charge separated states and locally excited states as well as an accurate evaluation of the Coulomb barrier between electron and hole at various separations.

Appendix A

FOB-SH: technical details

A.1 AOM parametrizations

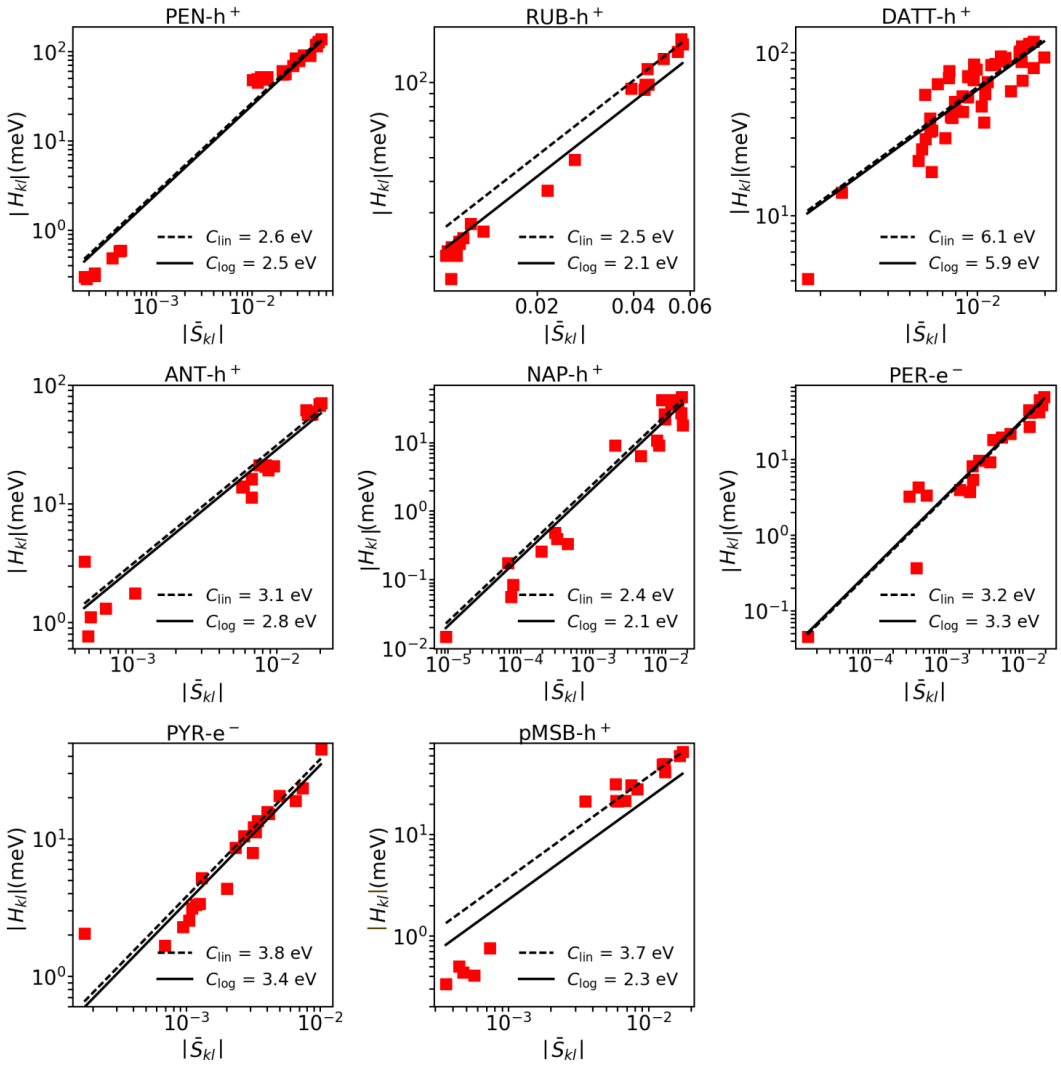

Figure A.1: Analytic overlap method (AOM) couplings parametrization. Electronic couplings H_{kl} between neighbouring molecules in the crystal structure and along MD trajectories were obtained from sFODFT [100–103] and plotted against the HOMO or LUMO overlap $\bar{S}_{kl}$. The constant of proportion C for the approximately linear relationship $|H_{kl}| = C|\bar{S}_{kl}|$ was obtained from linear (dashed) or logarithmic fitting (solid), giving $C = C_{\text{lin}}$ and $C = C_{\text{log}}$, respectively.

A.2 Electronic couplings and comparison with the literature

The scaled FODFT couplings are compared with other computational methods from the Literature.

Table A.1: Couplings comparison with literature.

crystal	dir.	dist. (Å)	$\|H_{kl}\|$ (lit.) (meV)	$\|H_{kl}\|$ (sFODFT) [r] (meV)
DATT-h$^+$ [a]	*P*	6.26	70[a], 66.8[o], 86.5[p]	94.9
RUB-h$^+$ [b]	*P*	7.18	81[i], 83[j], 107[k], 140[l], 95.7[m]	113.4
PEN-h$^+$ [c]	T_1	4.73	85[j], 81[k], 130.6[l], 96.7[n], 90.7[m]	116.7
ANT-h$^+$ [d]	*T*	5.24[q]	26[i], 23[j]	25.2
	P	6.04	40[i], 44[j]	57.0
NAP-h$^+$ [e]	*P*	5.95	43[i], 35[j],	46.2

[a] Ref [154]. [b] Ref [153]. [c] Ref [155]. [d] Ref [151]. [e] Ref [150]. [g] Ref [255]. [i] Ref [96]. [j] Ref [135]. [k] Ref [178]. [l] Ref [56]. [m] Ref [256]. [n] Ref [257]. [o] Ref [177]. [p] Ref [258]. [q] T-shaped molecular pair along the given direction. [r] Electronic couplings for crystal structure geometries obtained using scaled FODFT (sFODFT) as described in Section 2.1.4.

A.3 Accuracy of the multiple time step algorithm and neglect of d_{kl}

An efficient multiple time step (MTS) algorithm as well as a valuable optimization for the non-adiabatic coupling elements have been introduced in Section 2.1.7 in order to deal with large systems without losing the accuracy of the FOB-SH dynamics. Here I benchmark the quality of these two important algorithmic improvements on the ANT 2D crystal with 378 molecules forming the active plane. I ran 600 trajectories, 1 ps long with a 0.1 fs nuclear time step for different combinations with increasingly optimized FOB-SH (i.e. "d_{kl}" in which the diabatic NACEs in the orthogonal basis are calculated at each nuclear time step (as explained in the next section) and linearly interpolated when solving the electronic equation of motion, Eq 2.4 (the MTS algorithm is inactive); "no d_{kl}" in which these NACEs are neglected; "MTS+d_{kl}" in which the MTS algorithm is activated and the off-diagonal gradients are updated only every 100 MD time steps (namely, every 10 fs using a 0.1 fs MD time step), and "MTS+no d_{kl}", in which NACEs are not calculated and the MTS algorithm is activated).

Importantly in Figure A.2, I show that MSD both along a and b crystallographic directions, the number of (successful and rejected) hops, the mobilities along a and b and the IPR, all remain virtually unchanged (within statistical errors) when going from "d_{kl}" scheme to "MTS+no d_{kl}". As expected, upon activation of the MTS algorithm the energy conservation decreases from 2.1×10^{-8} to 6.0×10^{-7} Ha/ps/atoms (though remaining well below the typical energy conservation of $ab-initio$ MD of about 10^{-5} Ha/ps/atoms). Yet, I notice a significant speed-up in the time needed to complete a time step (almost factor of 3 when the system becomes larger than a thousand molecules). This makes the FOB-SH code capable of affording almost twice as large systems at the same computational cost without sacrificing accuracy of the actual dynamics (see Figure A.2(E)).

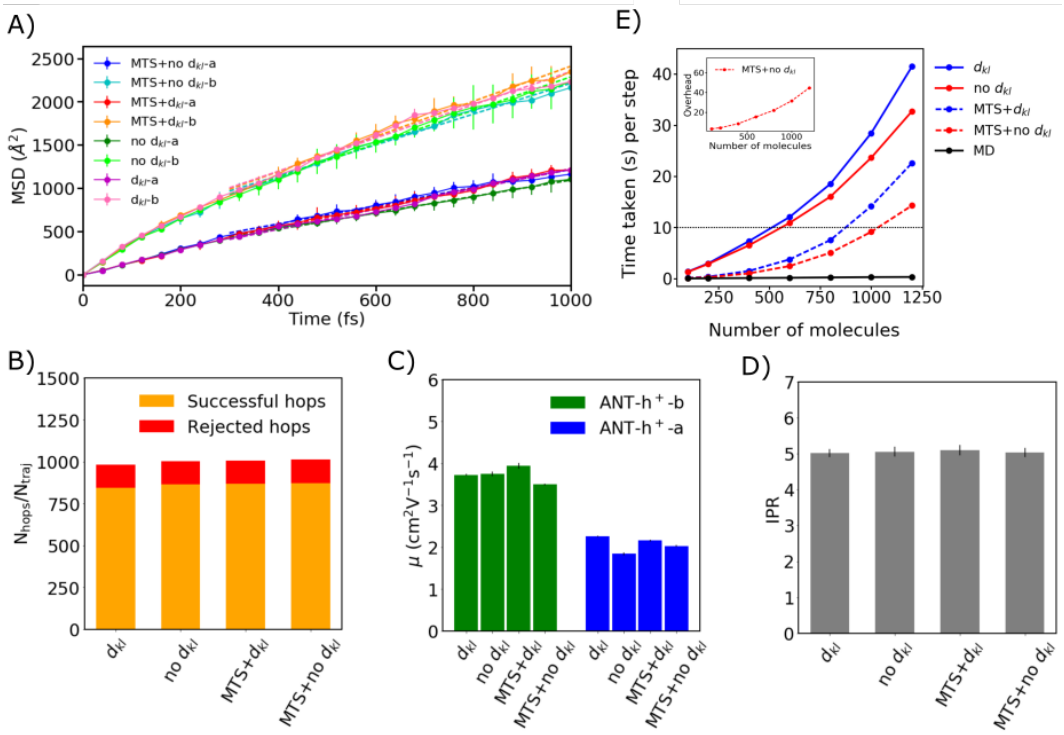

Figure A.2: Algorithmic optimization for code speed-up. The different algorithmic optimizations described in the text ("d_{kl}", "no d_{kl}", "MTS+d_{kl}" and "MTS+no d_{kl}") are compared for ANT crystal. (A) The mean squared displacement (MSD) of the charge carrier wavefunction is shown along the respective eigendirections of the MSD tensor. The diffusion coefficient is obtained from linear fits to the MSD after initial relaxation, as indicated by dashed lines. The MSD is obtained from 600 FOB-SH trajectories and the error bars are obtained by block-averaging over 3 blocks. (B) Average number of successful and rejected hops for 600 trajectories. (C) and (D) represent, respectively, the mobilities along the eigendirections as obtained from the MSD fitting in (A) and the IPR. (E) Time taken in (s) to complete a nuclear time step as a function of total number of molecules in the system on a single CPU core. The black line indicates the time for a classical MD on the same system size and the dashed black line indicates the time required for computing 1 ps (10,000 steps) per day. The inset shows the overhead of the 'MTS+no d_{kl}" compared to a standard MD run in CP2K. Processor used for the timing: Intel(R) Xeon(R) x86_64 CPU E5-2687W v4 3.00GHz

Appendix B

Alternative transport algorithms

B.1 Master equation and rate constants

In the regime of small electronic coupling strength ($V_{kl} = \langle |H_{kl}|^2 \rangle^{1/2} << \lambda/2$), the charge carrier wavefunction can be assumed to be localized on one molecule at all times and hopping from one site to the next. Thus, the actual dynamics can be well captured by a hopping model. To this end, by assuming to have only one carrier present in the system, I wrote and solved a chemical master equation for charge hopping along 1D chains as well as 2D lattices to obtain the time-dependent charge population of each site, k (see below). This quantity can then be used to evaluate the mean squared displacement (MSD) and the corresponding charge hopping mobility.

As an example, the hole transfer within a 1D chain can be illustrated by the following kinetic equation:

$$\mathrm{M}_k^+\text{–}\mathrm{M}_{k+1}\text{–}\mathrm{M}_{k+2}\text{–} \underset{k_{kk+1}}{\overset{k_{k+1k}}{\rightleftharpoons}} \mathrm{M}_k\text{-}\mathrm{M}_{k+1}^+\text{–}\mathrm{M}_{k+2}\text{–} \underset{k_{k+1k+2}}{\overset{k_{k+2k+1}}{\rightleftharpoons}} \cdots$$

where k_{kl} is the rate constants obtained from electron transfer (ET) theory between the various sites (note that the rate constant can be different for pairs at a different distance as seen for example for 2D lattices in Chapter 4). Few different rate expressions have been proposed in the literature [32] to deal with different ET regimes (namely, adiabatic and non-adiabatic ET regimes [32]). In this thesis for charge transfer reactions, I adopted the following semiclassical transition state theory formula valid in the non-adiabatic and adiabatic ET regime[16]

$$k_{kl} = \kappa_{\mathrm{el}} \nu_{\mathrm{eff}} \exp(-\beta \Delta A_{kl}^{\ddagger}), \tag{B.1}$$

where $\beta = 1/k_{\mathrm{B}}T$, κ_{el} is the electronic transmission coefficient,

$$\kappa_{\mathrm{el}} = \begin{cases} \dfrac{2P_{\mathrm{LZ}}}{1+P_{\mathrm{LZ}}} & \text{if} \quad \Delta A_{kl} \geq -\lambda \\ 2P_{\mathrm{LZ}}(1-P_{\mathrm{LZ}}) & \text{if} \quad \Delta A_{kl} < -\lambda \end{cases} \tag{B.2}$$

$$P_{\mathrm{LZ}} = 1 - \exp(-2\pi\gamma) \tag{B.3}$$

$$2\pi\gamma = \frac{\pi^{3/2} \langle |H_{\mathrm{kl}}|^2 \rangle_{\mathrm{TS}}}{h\nu_{\mathrm{eff}} \sqrt{\lambda k_{\mathrm{B}} T}}, \tag{B.4}$$

ν_{eff} is the effective nuclear frequency (in these systems, taken to be the stretching frequency of an aromatic carbon double bond: $1600\,\text{cm}^{-1}$) and $\Delta A_{kl}^{\ddagger}$ is the activation barrier. For vanishing driving force, $\Delta A_{kl}^{0} = 0$, as is the case here, $\Delta A_{kl}^{\ddagger}$ is given by[197],

$$\Delta A_{kl}^{\ddagger}(\Delta A_{kl}=0) = \frac{\lambda}{4} - (V_{kl} - \frac{V_{kl}^2}{\lambda}). \tag{B.5}$$

$\Delta A_{kl}^{\ddagger}$ and κ_{el} were evaluated for the same reorganization energy λ. Note that, the mean couplings $V_{kl}^2 = \langle |H_{kl}|^2 \rangle$ and it is obtained along MD simulations (see for example Table 4.3). I point out that $\langle |H_{kl}|^2 \rangle = \langle H_{kl} \rangle^2 + \sigma_V^2$, namely the square average of the couplings in the hopping rate takes into account the fluctuations of the coupling along the dynamics (these fluctuations help the charge going over the activation barrier in the low coupling regime).

The time evolution of the population for each site can be found solving the first order differential equation:

$$\frac{d\mathbf{P}(t)}{dt} = \mathbb{K}\mathbf{P}(t) \tag{B.6}$$

where $\mathbf{P}(t)$ is a vector containing site populations and $\mathbb{K}$ is the matrix of rate constants. The diagonals and off-diagonals of this kinetic matrix can be generally written as:

$$[\mathbb{K}]_{kk} = -\sum_{l \neq i} k_{kl} \quad \text{and} \quad [\mathbb{K}]_{kl} = k_{kl}. \tag{B.7}$$

In the particular 1D case (without including periodic boundaries and assuming equivalent sites) the kinetic matrix becomes:

$$\mathbb{K} = \begin{bmatrix} -k & k & 0 & 0 & \dots & 0 \\ k & -2k & k & 0 & \dots & 0 \\ 0 & k & -2k & k & \dots & 0 \\ 0 & 0 & k & -2k & \dots & 0 \\ \vdots & \vdots & \vdots & \vdots & \ddots & \vdots \\ 0 & 0 & 0 & \dots & k & -k \end{bmatrix}$$

The solution to Eq. B.7 is

$$\mathbf{P}(t) = \exp(\mathbb{K}t)\mathbf{P}(0) \tag{B.8}$$

where $\mathbf{P}(0)$ is the vector of initial populations, in this case the first component $P_k(0) = 1$ and all other components are zero. The MSD is then obtained through analogue Eqs. 2.31-2.33

in Section 2.3.2.

B.2 Transient localization theory

The mobility from transient localization theory (TLT), along a specific crystallographic direction (x), is written in the following form [15]:

$$\mu_x = \frac{e}{k_B T} \frac{L_x^2(\tau)}{2\tau} \tag{B.9}$$

$L_x^2(\tau)$ is referred to as localization length and it is a function of the fluctuation time (τ) given by typical intermolecular oscillation ($\tau = \frac{1}{\omega_0}$). According to this theory, the localization length can be expressed as [57]:

$$L_x^2(\tau) = \frac{1}{Z} \sum_n \sum_m e^{\zeta E_n/(k_B T)} |\langle n|[\hat{H}, \hat{x}]|m\rangle|^2 \frac{2}{(\frac{1}{\tau})^2 + (E_m - E_n)^2} \tag{B.10}$$

in which E_m, E_n are eigenvalues energies and $|n\rangle, |m\rangle$ the related eigenvectors of the Hamiltonian. $Z = \sum_n e^{\zeta E_n/(k_B T)}$ is the partition function, with $\zeta = +1$ for holes and $\zeta = -1$ for electrons [259]. Finally $\hat{x}$ is the position operator and [...] parenthesis indicate the commutator term. When $L_x^2(\tau)$ and $L_y^2(\tau)$ are calculated one can extract localization length as the average over the high mobility plane as:

$$L^2(\tau) = \frac{L_x^2(\tau) + L_y^2(\tau)}{2} \tag{B.11}$$

as well as the average mobilities μ.

The TLT mobilities were calculated by using the open source code provided in Ref. [57] and following the steps described above. In particular, the electronic Hamiltonian in Eq. 2.5 was sampled along FOB-SH trajectories and from it μ_{TLT} and μ^*_{TLT} were extracted from it, and reported in Figure 4.8. In the former case onsite energies were set to zero as done in Refs. [56, 57], whereas in the latter the complete Hamiltonian including diagonal thermal fluctuations was used. The intermolecular oscillation time $\tau = 1/\omega_0$ was taken from Ref. [85]. It is worth noticing that this oscillation time is not an essential parameters. It was found that dependence of the mobility on the molecular fluctuation time is weak and that τ does not change very much across different compounds [56].

Bibliography

[1] A. Köhler and H. Bässler, *Electronic processes in organic semiconductors: An introduction*. John Wiley & Sons, 2015.

[2] S. Fratini, M. Nikolka, A. Salleo, G. Schweicher, and H. Sirringhaus, "Charge transport in high-mobility conjugated polymers and molecular semiconductors," *Nat. Mater.*, vol. 19, no. 5, pp. 491–502, 2020.

[3] C. Wang, H. Dong, L. Jiang, and W. Hu, "Organic semiconductor crystals," *Chem. Soc. Rev.*, vol. 47, no. 2, pp. 422–500, 2018.

[4] G. Schweicher, G. Garbay, R. Jouclas, F. Vibert, F. Devaux, and Y. H. Geerts, "Molecular Semiconductors for Logic Operations: Dead-End or Bright Future?," *Adv. Mater.*, vol. 32, no. 10, 2020.

[5] B. Kippelen and J.-L. Bredas, "Organic photovoltaics," *Energy Environ. Sci.*, vol. 2, p. 251, 2009.

[6] K. Vandewal, S. Mertens, J. Benduhn, and Q. Liu, "The Cost of Converting Excitons into Free Charge Carriers in Organic Solar Cells," *J. Phys. Chem. Lett.*, vol. 11, no. 1, pp. 129–135, 2020.

[7] R. Friend, R. Gymer, A. Holmes, J. Burroughes, R. Marks, C. Taliani, D. Bradley, D. Dos Santos, J. Bredas, M. Lögdlund, *et al.*, "Electroluminescence in conjugated polymers," *Nature*, vol. 397, no. 6715, pp. 121–128, 1999.

[8] A. Tsumura, H. Koezuka, and T. Ando, "Macromolecular electronic device: Field-effect transistor with a polythiophene thin film," *Appl. Phys. Lett.*, vol. 49, no. 18, pp. 1210–1212, 1986.

[9] H. Jiang and W. Hu, "The Emergence of Organic SingleCrystal Electronics," *Angew. Chem. Int.*, vol. 59, no. 4, pp. 1408–1428, 2020.

[10] N. Karl, "Charge carrier transport in organic semiconductors," *Synth. met.*, vol. 133, pp. 649–657, 2003.

[11] V. Podzorov, E. Menard, J. A. Rogers, and M. E. Gershenson, "Hall effect in the accumulation layers on the surface of organic semiconductors," *Phys. Rev. Lett.*, vol. 95, p. 226601, 2005.

[12] A. Troisi, "Charge transport in high mobility molecular semiconductors: calssical models and new theories," *Chem. Soc. Rev.*, vol. 40, pp. 2347–2358, 2011.

[13] F. Ortmann, F. Bechstedt, and K. Hannewald, "Charge transport in organic crystals: Theory and modelling," *Phys. Status Solidi B*, vol. 248, pp. 511–525, 2011.

[14] Y. Jiang, H. Geng, W. Li, and Z. Shuai, "Understanding carrier transport in organic semiconductors: computation of charge mobility considering quantum nuclear tunneling and delocalization effects," *J. Chem. Theor. Comput.*, vol. 15, no. 3, pp. 1477–1491, 2019.

[15] S. Fratini, D. Mayou, and S. Ciuchi, "The transient localization scenario for charge transport in crystalline organic materials," *Adv. Funct. Mater.*, pp. 2292–2315, 2016.

[16] H. Oberhofer, K. Reuter, and J. Blumberger, "Charge transport in molecular materials: an assessment of computational methods," *Chem. Rev.*, vol. 117, pp. 10319–10357, 2017.

[17] V. Podzorov, "Organic single crystals: Addressing the fundamentals of organic electronics," *MRS Bull.*, vol. 38, no. 1, pp. 15–24, 2013.

[18] H. T. Yi, Y. N. Gartstein, and V. Podzorov, "Charge carrier coherence and Hall effect in organic semiconductors," *Sci. Rep.*, vol. 6, no. January, pp. 1–11, 2016.

[19] K. Marumoto, S. Kuroda, T. Takenobu, and Y. Iwasa, "Spatial extent of wave functions of gate-induced hole carriers in pentacene field-effect devices as investigated by electron spin resonance," *Phys. Rev. Lett.*, vol. 97, p. 256603, 2006.

[20] H. Matsui, A. S. Mishchenko, and T. Hasegawa, "Distribution of localized states from fine analysis of electron spin resonance spectra in organic transistors," *Phys. Rev. Lett.*, vol. 104, pp. 056602–4, 2010.

[21] J.-F. Chang, T. Sakanoue, Y. Olivier, T. Uemura, M.-B. Dufourg-Madec, S. G. Yeates, J. Cornil, J. Takeya, A. Troisi, and H. Sirringhaus, "Hall-effect measurements probing the degree of charge-carrier delocalization in solution-processed crystalline molecular semiconductors," *Phys. Rev. Lett.*, vol. 107, pp. 066601–4, 2011.

[22] T. Sakanoue and H. Sirringhaus, "Band-like temperature dependence of mobility in a solution-processed organic semiconductor," *Nat Mater.*, vol. 9, pp. 736–740, 2010.

[23] H. Sirringhaus, T. Sakanoue, and J.-F. Chang, "Charge-transport physics of high-mobility molecular semiconductors," *phys. status solidi (b)*, vol. 249, no. 9, pp. 1655–1676, 2012.

[24] V. Coropceanu, X.-K. Chen, T. Wang, Z. Zheng, and J.-L. Brédas, "Charge-transfer

electronic states in organic solar cells," *Nat. Rev. Mater.*, vol. 4, no. 11, pp. 689–707, 2019.

[25] J. Hou, O. Inganäs, R. H. Friend, and F. Gao, "Organic solar cells based on non-fullerene acceptors," *Nat. Mater.*, vol. 17, no. 2, pp. 119–128, 2018.

[26] O. V. Mikhnenko, P. W. M. Blom, and T.-Q. Nguyen, "Exciton diffusion in organic semiconductors," *Energy & Environmental Science*, vol. 8, no. 7, pp. 1867–1888, 2015.

[27] V. May and O. Kühn, *Charge and energy transfer dynamics in molecular systems*. John Wiley & Sons, 2008.

[28] V. Coropceanu, Y. Li, Y. Yi, L. Zhu, and J. L. Brédas, "Intrinsic charge transport in single crystals of organic molecular semiconductors: A theoretical perspective," *MRS Bull.*, vol. 38, no. 1, pp. 57–64, 2013.

[29] G. Schweicher, Y. Olivier, V. Lemaur, and Y. H. Geerts, "What currently limits charge carrier mobility in crystals of molecular semiconductors?," *Isr. J. Chem.*, vol. 54, no. 5-6, pp. 595–620, 2014.

[30] L. Wang, O. V. Prezhdo, and D. Beljonne, "Mixed quantum-classical dynamics for charge transport in organics," *Phys. Chem. Chem. Phys.*, vol. 17, pp. 12395–12406, 2015.

[31] T. Nematiaram and A. Troisi, "Modeling charge transport in high-mobility molecular semiconductors: Balancing electronic structure and quantum dynamics methods with the help of experiments," *J. Chem. Phys.*, vol. 152, no. 19, p. 190902, 2020.

[32] J. Blumberger, "Recent advances in the theory and molecular simulation of biological electron transfer reactions," *Chem. Rev.*, vol. 115, pp. 11191–11238, 2015.

[33] A. Ishizaki and G. R. Fleming, "On the adequacy of the Redfield equation and related approaches to the study of quantum dynamics in electronic energy transfer," *J. Chem. Phys.*, vol. 130, no. 23, p. 234110, 2009.

[34] A. V. Akimov and O. V. Prezhdo, "Large-Scale Computations in Chemistry: A Bird's Eye View of a Vibrant Field," *Chem. Rev.*, vol. 115, no. 12, pp. 5797–5890, 2015.

[35] J. C. Tully, *Nonadiabatic Dynamics*, pp. 34–71. World Scientific, 1998.

[36] J. C. Tully, *Mixed Quantum-Classical Dynamics*. Modern Methods for Multidimensional Dynamics Computations in Chemistry, World Scientific, 1998.

[37] J. Tully, "Mixed quantum–classical dynamics," *Faraday Discuss.*, vol. 110, pp. 407–419, 1998.

[38] J. C. Tully, "Perspective: Nonadiabatic dynamics theory," *J. Chem. Phys.*, vol. 137, pp. 22A301–7, 2012.

[39] L. Wang, A. Akimov, and O. V. Prezhdo, "Recent Progress in Surface Hopping: 2011-2015," *J. Phys. Chem. Lett.*, vol. 7, no. 11, pp. 2100–2112, 2016.

[40] L. Wang, J. Qiu, X. Bai, and J. Xu, "Surface hopping methods for nonadiabatic dynamics in extended systems," *WIREs Computational Molecular Science*, vol. 10, no. 2, p. e1435, 2020.

[41] B. Smith and A. V. Akimov, "Modeling nonadiabatic dynamics in condensed matter materials: some recent advances and applications," *J. Phys.: Condens. Matter*, vol. 32, no. 7, p. 073001, 2020.

[42] J. Spencer, F. Gajdos, and J. Blumberger, "Fob-sh: Fragment orbital-based surface hopping for charge carrier transport in organic and biological molecules and materials," *J. Chem. Phys.*, vol. 145, p. 064102, 2016.

[43] S. Giannini, A. Carof, M. Ellis, O. G. Ziogos, and J. Blumberger, *From atomic orbitals to nano-scale charge transport with mixed quantum/classical non-adiabatic dynamics: method, implementation and application*, ch. Chapter X. Ed. Dennis S. and Dongqing W. RSC book, submitted 2020.

[44] R. A. Marcus, "Electron transfer reactions in chemistry. theory and experiment," *Rev. Mod. Phys.*, vol. 65, pp. 599–610, 1993.

[45] T. Vehoff, B. Baumeier, A. Troisi, and D. Andrienko, "Charge Transport in Organic Crystals: Role of Disorder and Topological Connectivity," *J. Am. Chem. Soc.*, vol. 132, no. 33, pp. 11702–11708, 2010.

[46] L. Wang, Q. Li, Z. Shuai, L. Chen, and Q. Shi, "Multiscale study of charge mobility of organic semiconductor with dynamic disorders," *Phys. Chem. Chem. Phys*, vol. 12, no. 13, pp. 3309–3314, 2010.

[47] A. Troisi, "The speed limit for sequential charge hopping in molecular materials.," *Org. Electron.*, vol. 12, pp. 1988–1991, 2011.

[48] T. Holstein, "Studies of Polaron Motion .1. The Molecular-Crystal Model," *Annals of Physics*, vol. 8, no. 3, pp. 325–342, 1959.

[49] R. Munn and R. Silbey, "Theory of electronic transport in molecular crystals. ii. ze-

roth order states incorporating nonlocal linear electron–phonon coupling," *J. Chem. Phys.*, vol. 83, no. 4, pp. 1843–1853, 1985.

[50] F. Ortmann, F. Bechstedt, and K. Hannewald, "Theory of charge transport in organic crystals: Beyond holstein's small-polaron model," *Phys. Rev. B*, vol. 79, p. 235206, 2009.

[51] Y. Nakayama, Y. Mizuno, M. Hikasa, M. Yamamoto, M. Matsunami, S. Ideta, K. Tanaka, H. Ishii, and N. Ueno, "Single-crystal pentacene valence-band dispersion and its temperature dependence," *J. Phys. Chem. Lett.*, vol. 8, no. 6, pp. 1259–1264, 2017.

[52] S. Fratini and S. Ciuchi, "Bandlike motion and mobility saturation in organic molecular semiconductors," *Phys. Rev. Lett.*, vol. 103, p. 266601, 2009.

[53] S. Illig, A. S. Eggeman, A. Troisi, L. Jiang, C. Warwick, M. Nikolka, G. Schweicher, S. G. Yeates, Y. H. Geerts, J. E. Anthony, and H. Sirringhaus, "Reducing dynamic disorder in small-molecule organic semiconductors by suppressing large-amplitude thermal motions," *Nat. Comm.*, vol. 7, p. 10736, 2016.

[54] S. Ciuchi, S. Fratini, and D. Mayou, "Transient localization in crystalline organic semiconductors," *Phys. Rev. B*, vol. 83, p. 081202(R), 2011.

[55] S. Ciuchi and S. Fratini, "Electronic transport and quantum localization effects in organic semiconductors," *Phys. Rev. B*, vol. 86, no. 24, p. 245201, 2012.

[56] S. Fratini, S. Ciuchi, D. Mayou, G. T. d. Laissardiere, and A. Troisi, "A map of high-mobility molecular semiconductors," *Nat. Mater.*, vol. 16, pp. 998–1002, 2017.

[57] T. Nematiaram, S. Ciuchi, X. Xie, S. Fratini, and A. Troisi, "Practical Computation of the Charge Mobility in Molecular Semiconductors Using Transient Localization Theory," *J. Phys. Chem. C*, vol. 123, no. 12, pp. 6989–6997, 2019.

[58] S. Fratini and S. Ciuchi, "Dynamical localization corrections to band transport," *Phys. Rev. Research*, vol. 2, no. 1, p. 013001, 2020.

[59] D. Frenkel and B. Smit, *Understanding Molecular Simulation- From Algorithms to Applications*. San Diego: Academic Press, 1996.

[60] T. R. Nelson, A. J. White, J. A. Bjorgaard, A. E. Sifain, Y. Zhang, B. Nebgen, S. Fernandez-Alberti, D. Mozyrsky, A. E. Roitberg, and S. Tretiak, "Non-adiabatic Excited-State Molecular Dynamics: Theory and Applications for Modeling Photo-

physics in Extended Molecular Materials," *Chem. Rev.*, vol. 120, no. 4, pp. 2215–2287, 2020.

[61] S. Hammes-Schiffer and J. C. Tully, "Proton transfer in solution: Molecular dynamics with quantum transitions," *J. Chem. Phys.*, vol. 101, p. 4657, 1994.

[62] G. A. Worth, H.-D. Meyer, H. Koppel, L. S. Cederbaum, and I. Burghardt, "Using the mctdh wavepacket propagation method to describe multimode non-adiabatic dynamics," *Int. Rev. Phys. Chem.*, vol. 27, pp. 569–606, 2008.

[63] T. J. Martinez, M. Ben-Nun, and R. Levine, "Multi-electronic-state molecular dynamics: A wave function approach with applications," *J. Chem. Phys.*, vol. 100, no. 19, pp. 7884–7895, 1996.

[64] A. Abedi, N. T. Maitra, and E. K. U. Gross, "Correlated electron-nuclear dynamics: Exact factorization of the molecular wavefunction," *J. Chem. Phys.*, vol. 137, p. 22A530, 2012.

[65] F. Agostini, A. Abedi, and E. Gross, "Classical nuclear motion coupled to electronic non-adiabatic transitions," *J. Chem. Phys.*, vol. 141, no. 21, p. 214101, 2014.

[66] S. K. Min, F. Agostini, and E. K. Gross, "Coupled-trajectory quantum-classical approach to electronic decoherence in nonadiabatic processes," *Phys. Rev. letters*, vol. 115, no. 7, p. 073001, 2015.

[67] R. Kapral and G. Ciccotti, "Mixed quantum-classical dynamics," *J. Chem. Phys.*, vol. 110, no. 18, pp. 8919–8929, 1999.

[68] S. Nielsen, R. Kapral, and G. Ciccotti, "Mixed quantum-classical surface hopping dynamics," *J. Chem. Phys.*, vol. 112, no. 15, pp. 6543–6553, 2000.

[69] R. E. Wyatt, C. L. Lopreore, and G. Parlant, "Electronic transitions with quantum trajectories," *J. Chem. Phys.*, vol. 114, no. 12, pp. 5113–5116, 2001.

[70] J. E. Subotnik, A. Jain, B. Landry, A. Petit, W. Ouyang, and N. Bellonzi, "Understanding the Surface Hopping View of Electronic Transitions and Decoherence," *Annu. Rev. Phys. Chem.*, vol. 67, no. 1, pp. 387–417, 2016.

[71] M. Persico and G. Granucci, "An overview of nonadiabatic dynamics simulations methods, with focus on the direct approach versus the fitting of potential energy surfaces," *Theor. Chem. Acc.*, vol. 133, no. 9, pp. 1–28, 2014.

[72] L. Wang and D. Beljonne, "Flexible surface hopping approach to model the crossover

from hopping to band-like transport in organic crystals," *J. Phys. Chem. Lett.*, vol. 4, pp. 1888–1894, 2013.

[73] L. Wang and D. Beljonne, "Charge transport in organic semiconductors: Assessment of the mean field theory in the hopping regime," *J. Chem. Phys.*, vol. 139, pp. 064316–12, 2013.

[74] A. Troisi and G. Orlandi, "Charge-transport regime of crystalline organic semiconductors: Diffusion limited by thermal off-diagonal electronic disorder," *Phys. Rev. Lett.*, vol. 96, pp. 086601–4, 2006.

[75] A. V. Akimov and O. V. Prezhdo, "Nonadiabatic dynamics of charge transfer and singlet fission at the pentacene/C60 interface," *J. Am. Chem. Soc.*, vol. 136, no. 4, pp. 1599–1608, 2014.

[76] T. Nelson, S. Fernandez-Alberti, A. E. Roitberg, and S. Tretiak, "Nonadiabatic excited-state molecular dynamics: Modeling photophysics in organic conjugated materials," *Acc. Chem. Res.*, vol. 47, no. 4, pp. 1155–1164, 2014.

[77] W. Xie, D. Holub, T. Kuba, and M. Elstner, "Performance of Mixed Quantum-Classical Approaches on Modeling the Crossover from Hopping to Bandlike Charge Transport in Organic Semiconductors," *J. Chem. Theory Comput.*, vol. 16, no. 4, pp. 2071–2084, 2020.

[78] J. R. Schmidt, N. Shenvi, and J. C. Tully, "Mixed quantum-classical equilibrium: Surface hopping," *J. Chem. Phys.*, vol. 129, pp. 114110–6, 2008.

[79] V. Parandekar and J. C. Tully, "Mixed quantum-classical equilibrium," *J. Chem. Phys.*, vol. 122, p. 094102, 2005.

[80] A. E. Sifain, L. Wang, and O. V. Prezhdo, "Proper treatment of classically forbidden electronic transitions significantly improves detailed balance in surface hopping," *J. Chem. Phys.*, vol. 144, p. 211102, 2016.

[81] J. C. Tully, "Molecular dynamics with electronic transitions," *J. Chem. Phys.*, vol. 93, pp. 1061–1071, 1990.

[82] A. Carof, S. Giannini, and J. Blumberger, "Detailed balance, internal consistency and energy conservation in fragment orbital-based surface hopping," *J. Chem. Phys.*, vol. 147, p. 214113, 2017.

[83] A. Carof, S. Giannini, and J. Blumberger, "How to calculate charge mobility in molecular materials from surface hopping non-adiabatic molecular dynamics beyond

the hopping/band paradigm," *Phys. Chem. Chem. Phys.*, vol. 21, no. 48, pp. 26368–26386, 2019.

[84] S. Giannini, A. Carof, and J. Blumberger, "Crossover from hopping to band-like charge transport in an organic semiconductor model: Atomistic non-adiabatic molecular dynamics simulation," *J. Phys. Chem. Lett.*, vol. 9, pp. 3116–3123, 2018.

[85] S. Giannini, A. Carof, M. Ellis, H. Yang, O. G. Ziogos, S. Ghosh, and J. Blumberger, "Quantum localization and delocalization of charge carriers in organic semiconducting crystals," *Nat. Comm.*, vol. 10, no. 1, p. 3843, 2019.

[86] S. Giannini, O. G. Ziogos, A. Carof, M. Ellis, and J. Blumberger, "Flickering Polarons Extending over Ten Nanometres Mediate Charge Transport in High-Mobility Organic Crystals," *Adv. Theory Simul.*, vol. 3, p. 2000093, 2020.

[87] G. Granucci and M. Persico, "Critical appraisal of the fewest switches algorithm for surface hopping," *J. Chem. Phys.*, vol. 126, pp. 134114–11, 2007.

[88] J. Aragó and A. Troisi, "Regimes of exciton transport in molecular crystals in the presence of dynamic disorder," *Adv. Funct. Mater.*, vol. 26, no. 14, pp. 2316–2325, 2016.

[89] O. G. Ziogos, S. Giannini, M. Ellis, and J. Blumberger, "Identifying high-mobility tetracene derivatives using a non-adiabatic molecular dynamics approach," *J. Mater. Chem. C*, vol. 8, pp. 1054–1064, 2020.

[90] R. Crespo-Otero and M. Barbatti, "Recent advances and perspectives on nonadiabatic mixed quantum–classical dynamics," *Chem. Rev.*, vol. 118, no. 15, pp. 7026–7068, 2018.

[91] J. Hutter, M. Iannuzzi, F. Schiffmann, and J. VandeVondele, "cp2k: atomistic simulations of condensed matter systems," *Wiley Interdiscip. Rev.: Comput. Mol. Sci.*, vol. 4, no. 1, pp. 15–25, 2014.

[92] F. Gajdos, S. Valner, F. Hoffmann, J. Spencer, M. Breuer, A. Kubas, M. Dupuis, and J. Blumberger, "Ultrafast estimation of electronic couplings for electron transfer between pi-conjugated organic molecules," *J. Chem. Theory Comput.*, vol. 10, p. 4653, 2014.

[93] A. Warshel and R. M. Weiss, "An empirical valence bond approach for comparing reactions in solutions and in enzymes," *J. Am. Chem. Soc.*, vol. 102, no. 20, pp. 6218–6226, 1980.

[94] D. A. Case, T. Darden, T. Cheatham, III, C. Simmerling, J. Wang, R. Duke, R. Luo, M. Crowley, R. C. Walker, and W. Zhang, *et al.* AMBER 10, University of California, San Francisco, 2008.

[95] M. J. Frisch, *et al.* Gaussian 16, Revision C.01, Gaussian Inc., Wallingford, CT, 2016.

[96] I. Yavuz, B. N. Martin, J. Park, and K. N. Houk, "Theoretical study of the molecular ordering, paracrystallinity, and charge mobilities of oligomers in different crystalline phases," *J. Am. Chem. Soc.*, vol. 137, no. 8, pp. 2856–2866, 2015.

[97] H. Yang, F. Gajdos, and J. Blumberger, "Inter-molecular charge transfer parameters, electron-phonon couplings, and the validity of polaron hopping models in organic semiconducting crystals: rubrene, pentacene and c60," *J. Phys. Chem. C*, vol. 121, pp. 7689–7696, 2017.

[98] N. Karl and J. Marktanner, "Electron and hole mobilities in high purity anthracene single crystals," *Mol. Cryst. Liq. Cryst. Sci. Technol. Sect. A. Mol. Cryst. Liq. Cryst.*, vol. 355, no. 1, pp. 149–173, 2001.

[99] H. Oberhofer and J. Blumberger, "Insight into the mechanism of the ru^{2+}-ru^{3+} electron self-exchange reaction from quantitative rate calculations," *Angew. Chem. Int. Ed.*, vol. 49, pp. 3631–3634, 2010.

[100] H. Oberhofer and J. Blumberger, "Revisiting electronic couplings and incoherent hopping models for electron transport in crystalline c_{60} at ambient temperatures," *Phys. Chem. Chem. Phys.*, vol. 14, pp. 13846–13852, 2012.

[101] F. Gajdos, H. Oberhofer, M. Dupuis, and J. Blumberger, "On the inapplicability of electron-hopping models for the organic semiconductor phenyl-c61-butyric acid methyl ester (pcbm)," *J. Phys. Chem. Lett.*, vol. 4, pp. 1012–1017, 2013.

[102] A. Kubas, F. Hoffmann, A. Heck, H. Oberhofer, M. Elstner, and J. Blumberger, "Electronic couplings for molecular charge transfer: benchmarking cdft, fodft and fodftb against high-level ab initio calculations," *J. Chem. Phys.*, vol. 140, pp. 104105–21, 2014.

[103] A. Kubas, F. Gajdos, A. Heck, H. Oberhofer, M. Elstner, and J. Blumberger, "Electronic couplings for molecular charge transfer: benchmarking cdft, fodft and fodftb against high-level ab initio calculations. ii.," *Phys. Chem. Chem. Phys.*, vol. 17, pp. 14342–14354, 2015.

[104] R. S. Mulliken, C. A. Rieke, D. Orloff, and H. Orloff, "Formulas and numerical tables for overlap integrals," *J. Chem. Phys.*, vol. 17, p. 1248, 1949.

[105] "Cpmd version 4.1, the cpmd consortium, http://www.cpmd.org, mpi für festkörperforschung and the ibm zurich research laboratory, 2015.."

[106] P. Pechukas, "Time-dependent semiclassical scattering theory. ii. atomic collisions," *Phys. Rev.*, vol. 181, no. 1, p. 174, 1969.

[107] M. F. Herman, "Nonadiabatic semiclassical scattering. i. analysis of generalized surface hopping procedures," *J. Chem. Phys.*, vol. 81, no. 2, pp. 754–763, 1984.

[108] G. Granucci, M. Persico, and A. Toniolo, "Direct semiclassical simulation of photochemical processes with semiempirical wave functions," *J. Chem. Phys.*, vol. 114, no. 24, pp. 10608–10615, 2001.

[109] F. Plasser, G. Granucci, J. Pittner, M. Barbatti, M. Persico, and H. Lischka, "Surface hopping dynamics using a locally diabatic formalism: Charge transfer in the ethylene dimer cation and excited state dynamics in the 2-pyridone dimer," *J. Chem. Phys.*, vol. 137, pp. 22A514–13, 2012.

[110] B. R. Landry and J. E. Subotnik, "Standard surface hopping predicts incorrect scaling for marcus golden-rule rate: The decoherence problem cannot be ignored," *J. Chem. Phys.*, vol. 135, pp. 191101–4, 2011.

[111] E. R. Bittner and P. J. Rossky, "Quantum decoherence in mixed quantum-classical systems: Nonadiabatic processes," *J. Chem. Phys.*, vol. 103, no. 18, p. 8130, 1995.

[112] J. Y. Fang and S. Hammes-Schiffer, "Improvement of the internal consistency in trajectory surface hopping," *J. Phys. Chem. A*, vol. 103, pp. 9399–9407, 1999.

[113] C. Zhu, S. Nangia, A. W. Jasper, and D. G. Truhlar, "Coherent switching with decay of mixing: An improved treatment of electronic coherence for non-born-oppenheimer trajectories," *J. Chem. Phys.*, vol. 121, pp. 7658–7670, 2004.

[114] C. Zhu, A. W. Jasper, and D. G. Truhlar, "Non-born-oppenheimer liouville-von neumann dynamics. evolution of a subsystem controlled by linear and population-driven decay of mixing with decoherent and coherent switching," *J. Chem. Theory Comput.*, vol. 1, pp. 527–540, 2005.

[115] M. J. Bedard-Hearn, R. E. Larsen, and B. J. Schwartz, "Mean-field dynamics with stochastic decoherence (mf-sd): A new algorithm for nonadiabatic mixed quan-

tum/classical molecular-dynamics simulations with nuclear-induced decoherence," *J. Chem. Phys.*, vol. 123, p. 234106, 2005.

[116] J. E. Subotnik and N. Shenvi, "A new approach to decoherence and momentum rescaling in the surface hopping algorithm," *J. Chem. Phys.*, vol. 134, no. 2, 2011.

[117] T. Nelson, S. Fernandez-Alberti, A. E. Roitberg, and S. Tretiak, "Nonadiabatic excited-state molecular dynamics: Treatment of electronic decoherence," *J. Chem. Phys.*, vol. 138, p. 224111, 2013.

[118] S. Fernandez-Alberti, A. E. Roitberg, T. Nelson, and S. Tretiak, "Identification of unavoided crossings in nonadiabatic photoexcited dynamics involving multiple electronic states in polyatomic conjugated molecules," *J. Chem. Phys.*, vol. 137, no. 1, p. 014512, 2012.

[119] J. Qiu, X. Bai, and L. Wang, "Crossing Classified and Corrected Fewest Switches Surface Hopping," *J. Phys. Chem. Lett.*, pp. 4319–4325, 2018.

[120] J. Qiu, X. Bai, and L. Wang, "Subspace Surface Hopping with Size-Independent Dynamics," *J. Phys. Chem. Lett.*, pp. 637–644, 2019.

[121] X. Bai, J. Qiu, and L. Wang, "An efficient solution to the decoherence enhanced trivial crossing problem in surface hopping," *J. Chem. Phys.*, vol. 148, p. 104106, 2018.

[122] S. Ghosh, S. Giannini, K. Lively, and J. Blumberger, "Nonadiabatic dynamics with quantum nuclei: simulating charge transfer with ring polymer surface hopping," *Faraday Discuss.*, vol. 221, pp. 501–525, 2020.

[123] E. Fabiano, T. Keal, and W. Thiel, "Implementation of surface hopping molecular dynamics using semiempirical methods," *Chem. Phys.*, vol. 349, no. 1-3, pp. 334–347, 2008.

[124] O. V. Prezhdo and P. J. Rossky, "Evaluation of quantum transition rates from quantum-classical molecular dynamics simulations," *J. Chem. Phys.*, vol. 107, pp. 5863–5878, 1997.

[125] B. R. Landry and J. E. Subotnik, "How to recover marcus theory with fewest switches surface hopping: Add just a touch of decoherence," *J. Chem. Phys.*, vol. 137, pp. 22A513–13, 2012.

[126] A. Jain, E. Alguire, and J. E. Subotnik, "An Efficient, Augmented Surface Hopping

Algorithm That Includes Decoherence for Use in Large-Scale Simulations," *J. Chem. Theory Comput.*, vol. 12, no. 11, pp. 5256–5268, 2016.

[127] G. Granucci, M. Persico, and A. Zoccante, "Including quantum decoherence in surface hopping," *J. Chem. Phys.*, vol. 133, no. 13, p. 134111, 2010.

[128] J. E. Subotnik, W. Ouyang, and B. R. Landry, "Can we derive tully's surface-hopping algorithm from the semiclassical quantum liouville equation? almost, but only with decoherence," *J. Chem. Phys.*, vol. 139, pp. 214107–16, 2013.

[129] T. Nelson, S. Fernandez-Alberti, A. E. Roitberg, and S. Tretiak, "Artifacts due to trivial unavoided crossings in the modeling of photoinduced energy transfer dynamics in extended conjugated molecules," *Chem. Phys. Lett.*, vol. 590, pp. 208–213, 2013.

[130] G. A. Meek and B. G. Levine, "Evaluation of the Time-Derivative Coupling for Accurate Electronic State Transition Probabilities from Numerical Simulations," *J. Phys. Chem. Lett.*, vol. 5, no. 13, pp. 2351–2356, 2014.

[131] L. Wang and O. V. Prezhdo, "A simple solution to the trivial crossing problem in surface hopping," *J. Phys. Chem. Lett.*, vol. 5, pp. 713–719, 2014.

[132] B. R. Landry, M. J. Falk, and J. E. Subotnik, "The correct interpretation of surface hopping trajectories: How to calculate electronic properties," *J. Chem. Phys.*, vol. 139, pp. 211101–4, 2013.

[133] A. Heck, J. J. Kranz, T. Kubař, and M. Elstner, "Multi-scale approach to non-adiabatic charge transport in high-mobility organic semiconductors," *J. Chem. Theor. Comput.*, vol. 11, pp. 5068–5082, 2015.

[134] A. Heck, J. J. Kranz, and M. Elstner, "Simulation of temperature-dependent charge transport in organic semiconductors with various degrees of disorder," *J. Chem. Theory Comput.*, vol. 12, no. 7, pp. 3087–3096, 2016.

[135] V. Coropceanu, J. Cornil, D. A. da Silva, Y. Olivier, R. Silbey, and J.-L. Bredas, "Charge transport in organic semiconductors," *Chem. Rev.*, vol. 107, pp. 926–952, 2007.

[136] R. Seidel, M. Faubel, B. Winter, and J. Blumberger, "Single-ion reorganization free energy of aqueous ru(bpy)$_3^{2+/3+}$ and ru(h$_2$o)$_6^{2+/3+}$ from photoemission spectroscopy and density functional molecular dynamics simulation," *J. Am. Chem. Soc.*, vol. 131, pp. 16127–16137, 2009.

[137] J. Moens, R. Seidel, P. Geerlings, M. Faubel, B. Winter, and J. Blumberger, "Energy

levels and redox properties of aqueous $mn^{2+/3+}$ from photoemission spectroscopy and density functional molecular dynamics simulation," *J. Phys. Chem. B*, vol. 114, pp. 9173–9182, 2010.

[138] R. Seidel, S. Thurmer, J. Moens, P. Geerlings, J. Blumberger, and B. Winter, "Valence photoemission spectra of aqueous fe2+/3+ and [fe(cn)6]4-/3- and their interpretation by dft calculations," *J. Phys. Chem. B*, vol. 115, p. 11671, 2011.

[139] J. Blumberger and K. McKenna, "Constrained density functional theory applied to electron tunnelling between defects in mgo," *Phys. Chem. Chem. Phys.*, vol. 15, pp. 2184–2196, 2013.

[140] C. P. Herrero, "Isotope effects in structural and thermodynamic properties of solid neon," *Phys. Rev. B*, vol. 65, no. 1, 2001.

[141] S. Nosé, "A molecular dynamics method for simulations in the canonical ensemble," *Mol. Phys.*, vol. 52, no. 2, pp. 255–268, 1984.

[142] S. Nosé, "A unified formulation of the constant temperature molecular dynamics methods," *J. Chem. Phys.*, vol. 81, no. 1, pp. 511–519, 1984.

[143] A. Becke, "Density-functional thermochemistry. iii. the role of exact exchange," *J. Chem. Phys.*, vol. 98, p. 5648, 1993.

[144] J. P. Perdew, K. Burke, and M. Ernzerhof, "Generalized gradient approximation made simple," *Phys. Rev. Lett.*, vol. 77, p. 3865, 1996.

[145] M. D. Hack, A. W. Jasper, Y. L. Volobuev, D. W. Schwenke, and D. G. Truhlar, "Quantum Mechanical and Quasiclassical Trajectory Surface Hopping Studies of the Electronically Nonadiabatic Predissociation of the Ã State of NaH 2," *J. Phys. Chem. A*, vol. 103, no. 32, pp. 6309–6326, 1999.

[146] A. Jain and J. E. Subotnik, "Surface hopping, transition state theory, and decoherence. ii. thermal rate constants and detailed balance," *J. Chem. Phys.*, vol. 143, p. 134107, 2015.

[147] J. Nelson, J. J. Kwiatkowski, J. Kirkpatrick, and J. M. Frost, "Modeling charge transport in organic photovoltaic materials," *Acc. Chem. Res.*, vol. 42, p. 1768, 2009.

[148] I. Yavuz, "Dichotomy between the band and hopping transport in organic crystals: insights from experiments," *Phys. Chem. Chem. Phys.*, vol. 19, pp. 25819–25828, 2017.

[149] R. Kabe, H. Nakanotani, T. Sakanoue, M. Yahiro, and C. Adachi, "Effect of molecu-

lar morphology on amplified spontaneous emission of bis-styrylbenzene derivatives," *Adv. Mater.*, vol. 21, no. 40, pp. 4034–4038, 2009.

[150] V. Ponomarev, O. Filipenko, and L. Atovmyan, "Crystal and molecular-structure of naphthalene at-150degreesc," *Kristallografiya*, vol. 21, no. 2, pp. 392–394, 1976.

[151] R. Mason, "The crystallography of anthracene at 95 k and 290 k," *Acta Crystallogr.*, vol. 17, no. 5, pp. 547–555, 1964.

[152] A. Camerman , J. Trotter and J. M. Robertson, "The crystal and molecular structure of perylene," *Proc. R. Soc. London*, vol. 279, no. 1376, pp. 129–146, 1964.

[153] I. Bulgarovskaya, V. Vozzhennikov, and S. Aleksandrov, "V. bel skii, latv. psr zinat," *Akad. Vestis Kim. Ser*, vol. 4, p. 53, 1983.

[154] K. Niimi, S. Shinamura, I. Osaka, E. Miyazaki, and K. Takimiya, "Dianthra [2, 3-b: 2, 3-f] thieno [3, 2-b] thiophene (datt): synthesis, characterization, and fet characteristics of new π-extended heteroarene with eight fused aromatic rings," *J. Am. Chem. Soc.*, vol. 133, no. 22, pp. 8732–8739, 2011.

[155] D. Holmes, S. Kumaraswamy, A. J. Matzger, and K. P. C. Vollhardt, "On the nature of nonplanarity in the [n] phenylenes," *Chem. - Eur. J.*, vol. 5, no. 11, pp. 3399–3412, 1999.

[156] C. C. Mattheus, A. B. Dros, J. Baas, A. Meetsma, J. L. de Boer, and T. T. M. Palstra, "Polymorphism in pentacene," *Acta Crystallogr., Sect. C: Cryst. Struct. Commun.*, vol. 57, no. 8, pp. 939–941, 2001.

[157] N. Karl, *Landolt-Börnstein. Numerical data and functional relationships in science and technology (New Series) Group III: Crystal and Solid State Physics.*, vol. 17. Springer, Berlin, 1985, 1988.

[158] R. Farchioni and G. Grosso, "Organic Electronic Materials: Conjugated Polymers and Low 39 Molecular Weight Organic Solids.," 2003.

[159] C. Reese and Z. Bao, "High-Resolution Measurement of the Anisotropy of Charge Transport in Single Crystals," *Adv. Mater.*, vol. 19, no. 24, pp. 4535–4538, 2007.

[160] V. Podzorov, E. Menard, A. Borissov, V. Kiryukhin, J. A. Rogers, and M. E. Gershenson, "Intrinsic charge transport on the surface of organic semiconductors," *Phys. Rev. Lett.*, vol. 93, p. 086602, 2004.

[161] O. D. Jurchescu, J. Baas, and T. T. M. Palstra, "Effect of impurities on the mobility of single crystal pentacene," *Appl. Phys. Lett.*, vol. 84, p. 3061, 2004.

[162] C. C. Mattheus, G. A. De Wijs, R. A. De Groot, and T. T. Palstra, "Modeling the polymorphism of pentacene," *J. Am. Chem. Soc.*, vol. 125, no. 20, pp. 6323–6330, 2003.

[163] A. Landi, A. Troisi, and A. Peluso, "Explaining different experimental hole mobilities: influence of polymorphism on dynamic disorder in pentacene," *J. Mater. Chem. C*, pp. 9665–9670, 2019.

[164] J. Lee, S. Roth, and Y. Park, "Anisotropic field effect mobility in single crystal pentacene," *Appl. Phys. Lett*, vol. 88, pp. 252106–252106, 2006.

[165] D. P. McMahon and A. Troisi, "Evaluation of the external reorganization energy of polyacenes," *J. Phys. Chem. Lett.*, vol. 1, no. 6, pp. 941–946, 2010.

[166] A. Troisi, "Dynamic disorder in molecular semiconductors: Charge transport in two dimensions," *J. Chem. Phys.*, vol. 134, no. 3, p. 034702, 2011.

[167] J. P. Perdew, K. Burke, and M. Ernzerhof, "Generalized Gradient Approximation Made Simple," *Phys. Rev. Lett.*, vol. 77, no. 18, pp. 3865–3868, 1996.

[168] J. P. Perdew, M. Ernzerhof, and K. Burke, "Rationale for mixing exact exchange with density functional approximations," *The J. Chem. Phys.*, vol. 105, no. 22, pp. 9982–9985, 1996.

[169] A. M. Rappe, K. M. Rabe, E. Kaxiras, and J. D. Joannopoulos, "Optimized pseudopotentials," *Phys. Rev. B*, vol. 41, no. 2, pp. 1227–1230, 1990.

[170] P. E. Blöchl, O. Jepsen, and O. K. Andersen, "Improved tetrahedron," *Phys. Rev. B*, vol. 49, no. 23, pp. 16223–16233, 1994.

[171] P. Giannozzi and et. al, "QUANTUM ESPRESSO: a modular and open-source software project for quantum simulations of materials," *J. Phys.: Condens. Matter*, vol. 21, no. 39, p. 395502, 2009.

[172] P. W. Anderson, "Local moments and localized states," *Rev. Mod. Phys.*, vol. 50, no. 2, p. 191, 1978.

[173] V. Podzorov, "Organic single crystals: Addressing the fundamentals of organic electronics," *MRS Bulletin*, vol. 38, no. 1, pp. 15–24, 2013.

[174] H. H. Choi, K. Cho, C. D. Frisbie, H. Sirringhaus, and V. Podzorov, "Critical assessment of charge mobility extraction in fets," *Nat. Mater.*, vol. 17, no. 1, p. 2, 2017.

[175] W. Warta and N. Karl, "Hot holes in naphthalene: High, electric-field-dependent mobilities," *Phys. Rev. B*, vol. 32, no. 2, p. 1172, 1985.

[176] W. Warta, R. Stehle, and N. Karl, "Ultrapure, high mobility organic photoconductors," *Appl. Phys. A*, vol. 36, no. 3, pp. 163–170, 1985.

[177] Y. Jiang, X. Zhong, W. Shi, Q. Peng, H. Geng, Y. Zhao, and Z. Shuai, "Nuclear quantum tunnelling and carrier delocalization effects to bridge the gap between hopping and bandlike behaviors in organic semiconductors," *Nanoscale Horiz.*, vol. 1, no. 1, pp. 53–59, 2016.

[178] H. Kobayashi, N. Kobayashi, S. Hosoi, N. Koshitani, D. Murakami, R. Shirasawa, Y. Kudo, D. Hobara, Y. Tokita, and M. Itabashi, "Hopping and band mobilities of pentacene, rubrene, and 2,7-dioctyl[1]benzothieno[3,2-b][1]benzothiophene (c8-btbt) from first principle calculations.," *J. Chem. Phys.*, vol. 139, p. 014707, 2013.

[179] J. Xi, M. Long, L. Tang, D. Wang, and Z. Shuai, "First-principles prediction of charge mobility in carbon and organic nanomaterials," *Nanoscale*, vol. 4, no. 15, pp. 4348–4369, 2012.

[180] G. I. Livshits, A. Stern, D. Rotem, N. Borovok, G. Eidelshtein, A. Migliore, E. Penzo, S. J. Wind, R. Di Felice, S. S. Skourtis, J. C. Cuevas, L. Gurevich, A. B. Kotlyar, and D. Porath, "Long-range charge transport in single G-quadruplex DNA molecules," *Nat. Nanotech.*, vol. 9, no. 12, pp. 1040–1046, 2014.

[181] T. Kubo, R. Hausermann, J. Tsurumi, J. Soeda, Y. Okada, Y. Yamashita, N. Akamatsu, A. Shishido, C. Mitsui, T. Okamoto, S. Yanagisawa, H. Matsui, and J. Takeya, "Suppressing molecular vibrations in organic semiconductors by inducing strain," *Nature Comm.*, vol. 7, p. 11156, 2016.

[182] C. Schnedermann, J. Sung, R. Pandya, S. D. Verma, R. Y. Chen, N. Gauriot, H. M. Bretscher, P. Kukura, and A. Rao, "Ultrafast tracking of exciton and charge carrier transport in optoelectronic materials on the nanometer scale," *J. Phys. Chem. Lett.*, vol. 10, no. 21, pp. 6727–6733, 2019.

[183] H. Nakanotani, M. Saito, H. Nakamura, and C. Adachi, "Highly balanced ambipolar mobilities with intense electroluminescence in field-effect transistors based on organic single crystal oligo (p-phenylenevinylene) derivatives," *Appl. Phys. Lett.*, vol. 95, no. 3, p. 197, 2009.

[184] V. C. Sundar, J. Zaumseil, V. Podzorov, E. Menard, R. L. Willett, T. Someya, M. E.Gershenson, and J. A. Rogers, "Elastomeric transistor stamps: reversible probing of charge transport in organic crystals," *Science*, vol. 303, pp. 1644–1666, 2004.

[185] Y. Takeyama, S. Ono, and Y. Matsumoto, "Organic single crystal transistor characteristics of single-crystal phase pentacene grown by ionic liquid-assisted vacuum deposition," *Appl. Phys. Lett.*, vol. 101, no. 8, p. 083303, 2012.

[186] T. Nematiaram, D. Padula, A. Landi, and A. Troisi, "On the Largest Possible Mobility of Molecular Semiconductors and How to Achieve It," *Adv. Funct. Mater.*, vol. 30, no. 30, p. 2001906, 2020.

[187] S. A. Arabi, J. Dong, M. Mirza, P. Yu, L. Wang, J. He, and C. Jiang, "Nanoseed assisted PVT growth of ultrathin 2D pentacene molecular crystal directly onto SiO 2 substrate," *Cryst. Growth Des.*, vol. 16, no. 5, pp. 2624–2630, 2016.

[188] Y. Zhang, C. Liu, A. Balaeff, S. S. Skourtis, and D. N. Beratan, "Biological charge transfer via flickering resonance," *Proc. Nat. Acad. Sci. USA*, vol. 111, pp. 10049–10054, 2014.

[189] A. Troisi, "Prediction of the absolute charge mobility of molecular semiconductors: the case of rubrene," *Adv. Mater.*, vol. 19, p. 2000, 2007.

[190] H. H. Choi, H. T. Yi, J. Tsurumi, J. J. Kim, A. L. Briseno, S. Watanabe, J. Takeya, K. Cho, and V. Podzorov, "A Large Anisotropic Enhancement of the Charge Carrier Mobility of Flexible Organic Transistors with Strain: A Hall Effect and Raman Study," *Adv. Sci.*, vol. 1901824, p. 1901824, 2019.

[191] G. Schweicher, G. D'Avino, M. T. Ruggiero, D. J. Harkin, K. Broch, D. Venkateshvaran, G. Liu, A. Richard, C. Ruzié, J. Armstrong, A. R. Kennedy, K. Shankland, K. Takimiya, Y. H. Geerts, J. A. Zeitler, S. Fratini, and H. Sirringhaus, "Chasing the Killer Phonon Mode for the Rational Design of Low-Disorder, High-Mobility Molecular Semiconductors," *Adv. Mater.*, vol. 1902407, p. 1902407, 2019.

[192] K. Sakai, Y. Okada, T. Uemura, J. Tsurumi, R. Häusermann, H. Matsui, T. Fukami, H. Ishii, N. Kobayashi, K. Hirose, and J. Takeya, "The emergence of charge coherence in soft molecular organic semiconductors via the suppression of thermal fluctuations," *NPG Asia Materials*, vol. 8, no. 3, pp. e252–e252, 2016.

[193] C. Schober, K. Reuter, and H. Oberhofer, "Critical analysis of fragment-orbital dft schemes for the calculation of electronic coupling values," *J. Chem. Phys.*, vol. 144, p. 054103, 2016.

[194] C. Y. Cheng, J. E. Campbell, and G. M. Day, "Evolutionary chemical space ex-

ploration for functional materials: computational organic semiconductor discovery," *Chem. Sci.*, vol. 11, no. 19, pp. 4922–4933, 2020.

[195] F. Ortmann, F. Bechstedt, and K. Hannewald, "Charge transport in organic crystals: interplay of band transport, hopping and electron–phonon scattering," *New J. Phys.*, vol. 12, no. 2, p. 023011, 2010.

[196] O. Ostroverkhova, D. Cooke, F. Hegmann, J. Anthony, V. Podzorov, M. Gershenson, O. Jurchescu, and T. Palstra, "Ultrafast carrier dynamics in pentacene, functionalized pentacene, tetracene, and rubrene single crystals," *Appl. Phys. Lett.*, vol. 88, no. 16, p. 162101, 2006.

[197] J. Spencer, L. Scalfi, A. Carof, and J. Blumberger, "Confronting surface hopping molecular dynamics with marcus theory for a molecular donor-acceptor system," *Faraday Discuss.*, vol. 195, pp. 215–236, 2016.

[198] K. Hannewald, V. M. Stojanovic, J. M. T. Schellekens, P. A. Bobbert, G. Kresse, and J. Hafner, "Theory of polaron bandwidth narrowing in organic molecular crystals.," *Phys. Rev. B*, vol. 69, p. 075211, 2004.

[199] I. N. Hulea, S. Fratini, H. Xie, C. L. Mulder, N. N. Iossad, G. Rastelli, S. Ciuchi, and A. F. Morpurgo, "Tunable Fröhlich polarons in organic single-crystal transistors," *Nat. Mater.*, vol. 5, no. 12, pp. 982–986, 2006.

[200] W. Xie, K. A. McGarry, F. Liu, Y. Wu, P. P. Ruden, C. J. Douglas, and C. D. Frisbie, "High-mobility transistors based on single crystals of isotopically substituted rubrene-d 28," *J. Phys. Chem. C*, vol. 117, no. 22, pp. 11522–11529, 2013.

[201] J. Nyman and G. M. Day, "Modelling temperature-dependent properties of polymorphic organic molecular crystals," *Physical Chemistry Chemical Physics*, vol. 18, no. 45, pp. 31132–31143, 2016.

[202] P. A. Banks, J. Maul, M. T. Mancini, A. C. Whalley, A. Erba, and M. T. Ruggiero, "Thermoelasticity in organic semiconductors determined with terahertz spectroscopy and quantum quasi-harmonic simulations," *Journal of Materials Chemistry C*, vol. 8, no. 31, pp. 10917–10925, 2020.

[203] A. Troisi and G. Orlandi, "Dynamics of the intermolecular transfer integral in crystalline organic semiconductors," *J. Phys. Chem. A*, vol. 110, no. 11, pp. 4065–4070, 2006.

[204] J. P. Sleigh, D. P. McMahon, and A. Troisi, "Effect of the intermolecular thermal

motions on the tail of the electronic density of states in polyacene crystals," *Applied Physics A: Materials Science and Processing*, vol. 95, no. 1, pp. 147–152, 2009.

[205] Y. Li, V. Coropceanu, and J.-L. Brédas, "Thermal Narrowing of the Electronic Bandwidths in Organic Molecular Semiconductors: Impact of the Crystal Thermal Expansion," *J. Phys. Chem. Lett.*, vol. 3, no. 22, pp. 3325–3329, 2012.

[206] C. K. Lee and A. P. Willard, "Representing the Molecular Signatures of Disordered Molecular Semiconductors in Size-Extendable Models of Exciton Dynamics," *J. Phys. Chem. B*, vol. 124, no. 25, pp. 5238–5245, 2020.

[207] J. Frenkel, "On the transformation of light into heat in solids. ii," *Phys. Rev.*, vol. 37, no. 10, p. 1276, 1931.

[208] M. Pope and C. E. Swenberg, *Electronic processes in organic crystals and polymers*. Oxford University Press on Demand, 1999.

[209] T. Fujita, S. Atahan-Evrenk, N. P. Sawaya, and A. Aspuru-Guzik, "Coherent dynamics of mixed frenkel and charge-transfer excitons in dinaphtho [2, 3-b: 2 3-f] thieno [3, 2-b]-thiophene thin films: The importance of hole delocalization," *J. Phys. Chem. Lett.*, vol. 7, no. 7, pp. 1374–1380, 2016.

[210] V. Stehr, R. F. Fink, M. Tafipolski, C. Deibel, and B. Engels, "Comparison of different rate constant expressions for the prediction of charge and energy transport in oligoacenes," *Wiley Interdisciplinary Reviews: Computational Molecular Science*, vol. 6, no. 6, pp. 694–720, 2016.

[211] J.-D. Chai and M. Head-Gordon, "Long-range corrected hybrid density functionals with damped atom–atom dispersion corrections," *Phys. Chem. Chem. Phys*, vol. 10, no. 44, pp. 6615–6620, 2008.

[212] V. Stehr, R. F. Fink, B. Engels, J. Pflaum, and C. Deibel, "Singlet exciton diffusion in organic crystals based on marcus transfer rates," *J. Chem. Theory Comput.*, vol. 10, no. 3, pp. 1242–1255, 2014.

[213] Z.-Q. You and C.-P. Hsu, "Theory and calculation for the electronic coupling in excitation energy transfer," *Int. J. Quantum Chem*, vol. 114, no. 2, pp. 102–115, 2014.

[214] L. Cupellini, M. Corbella, B. Mennucci, and C. Curutchet, "Electronic energy transfer in biomacromolecules," *Wiley Interdiscip. Rev. Comput. Mol. Sci.*, vol. 9, no. 2, pp. 1–23, 2019.

[215] T. Förster, "Zwischenmolekulare energiewanderung und fluoreszenz," *Ann. Phys.*, vol. 437, no. 1-2, pp. 55–75, 1948.

[216] D. L. Dexter, "A theory of sensitized luminescence in solids," *J. Chem. Phys.*, vol. 21, no. 5, pp. 836–850, 1953.

[217] M. F. Iozzi, B. Mennucci, J. Tomasi, and R. Cammi, "Excitation energy transfer (eet) between molecules in condensed matter: A novel application of the polarizable continuum model (pcm)," *J. Chem. Phys.*, vol. 120, no. 15, pp. 7029–7040, 2004.

[218] M. Madjet, A. Abdurahman, and T. Renger, "Intermolecular coulomb couplings from ab initio electrostatic potentials: application to optical transitions of strongly coupled pigments in photosynthetic antennae and reaction centers," *J. Phys. Chem. B*, vol. 110, no. 34, pp. 17268–17281, 2006.

[219] L. Cupellini, S. Giannini, and B. Mennucci, "Electron and excitation energy transfers in covalently linked donoracceptor dyads: mechanisms and dynamics revealed using quantum chemistry," *Phys. Chem. Chem. Phys*, vol. 20, no. 1, pp. 395–403, 2018.

[220] S. Yeganeh and T. V. Voorhis, "Triplet excitation energy transfer with constrained density functional theory," *J. Phys. Chem. C*, vol. 114, no. 48, pp. 20756–20763, 2010.

[221] C.-P. Hsu, Z.-Q. You, and H.-C. Chen, "Characterization of the Short-Range Couplings in Excitation Energy Transfer," *J. Phys. Chem. C*, vol. 112, no. 4, pp. 1204–1212, 2008.

[222] C.-P. Hsu, "The Electronic Couplings in Electron Transfer and Excitation Energy Transfer," *Acc. Chem. Res.*, vol. 42, no. 4, pp. 509–518, 2009.

[223] M. Nottoli, S. Jurinovich, L. Cupellini, A. T. Gardiner, R. Cogdell, and B. Mennucci, "The role of charge-transfer states in the spectral tuning of antenna complexes of purple bacteria," *Photosynth. Res.*, vol. 137, no. 2, pp. 215–226, 2018.

[224] C.-H. Yang and C.-P. Hsu, "A multi-state fragment charge difference approach for diabatic states in electron transfer: Extension and automation," *J. Chem. Phys.*, vol. 139, no. 15, p. 154104, 2013.

[225] T. Siegrist, R. Fleming, R. Haddon, R. Laudise, A. Lovinger, H. Katz, P. Bridenbaugh, and D. Davis, "The crystal structure of the high-temperature polymorph of α–hexathienyl (α–6t/ht)," *Mater. Res.*, vol. 10, no. 9, pp. 2170–2173, 1995.

[226] K. Tojo and J. Mizuguchi, "Refinement of the crystal structure of 3, 4: 9, 10-

perylenebis (dicarboximide), c24h10n2o4, at 263 k," *Zeitschrift für Kristallographie-New Crystal Structures*, vol. 217, no. 1, pp. 45–46, 2002.

[227] A. Mishra, D. Popovic, A. Vogt, H. Kast, T. Leitner, K. Walzer, M. Pfeiffer, E. Mena-Osteritz, and P. Bäuerle, "A-D-A-type S , N -Heteropentacenes: Next-Generation Molecular Donor Materials for Efficient Vacuum-Processed Organic Solar Cells," *Adv. Mater.*, vol. 26, no. 42, pp. 7217–7223, 2014.

[228] R. C. Powell and Z. G. Soos, "Singlet exciton energy transfer in organic solids," *Journal of Luminescence*, vol. 11, no. 1-2, pp. 1–45, 1975.

[229] B. Mulder, "Anisotropy of light absorption and exciton diffusion in anthracene crystals determined from externally sensitized fluorescence," *Philips Res. Rep*, vol. 22, pp. 142–149, 1967.

[230] B. Mulder, "Symmetry of the fluorescence and absorption spectra of anthracene crystals," *J. Phys. Chem. Solids*, vol. 29, no. 1, pp. 182–184, 1968.

[231] J. J. Kranz and M. Elstner, "Simulation of Singlet Exciton Diffusion in Bulk Organic Materials," *J. Chem. Theory Comput.*, vol. 12, no. 9, pp. 4209–4221, 2016.

[232] R. Pandya, R. Y. S. Chen, Q. Gu, J. Gorman, F. Auras, J. Sung, R. Friend, P. Kukura, C. Schnedermann, and A. Rao, "Femtosecond Transient Absorption Microscopy of Singlet Exciton Motion in Side-Chain Engineered Perylene-Diimide Thin Films," vol. 124, no. 13, pp. 2721–2730, 2020.

[233] C. Li and H. Wonneberger, "Perylene imides for organic photovoltaics: Yesterday, today, and tomorrow," *Adv. Mater.*, vol. 24, no. 5, pp. 613–636, 2012.

[234] T. Yanai, D. P. Tew, and N. C. Handy, "A new hybrid exchange–correlation functional using the coulomb-attenuating method (cam-b3lyp)," *Chem. Phys. letters*, vol. 393, no. 1-3, pp. 51–57, 2004.

[235] Y. Yi, V. Coropceanu, and J.-L. Brédas, "A comparative theoretical study of exciton-dissociation and charge-recombination processes in oligothiophene/fullerene and oligothiophene/perylenediimide complexes for organic solar cells," *J. Mater. Chem*, vol. 21, no. 5, p. 1479, 2011.

[236] M. Carmen Ruiz Delgado, E. G. Kim, D. A. Da Silva Filho, and J. L. Bredas, "Tuning the charge-transport parameters of perylene diimide single crystals via end and/or core functionalization: A density functional theory investigation," *J. Am. Chem. Soc.*, vol. 132, no. 10, pp. 3375–3387, 2010.

[237] H. Klevens and J. Platt, "Spectral resemblances of cata-condensed hydrocarbons," *J. Chem. Phys.*, vol. 17, no. 5, pp. 470–481, 1949.

[238] W. Lambert, P. Felker, J. Syage, and A. Zewail, "Jet spectroscopy of anthracene and deuterated anthracenes," *J. Chem. Phys.*, vol. 81, no. 5, pp. 2195–2208, 1984.

[239] R. Janssen, L. Smilowitz, N. Sariciftci, and D. Moses, "Triplet-state photoexcitations of oligothiophene films and solutions," *J. Chem. Phys.*, vol. 101, no. 3, pp. 1787–1798, 1994.

[240] J. S. de Melo, L. M. Silva, L. G. Arnaut, and R. Becker, "Singlet and triplet energies of α-oligothiophenes: A spectroscopic, theoretical, and photoacoustic study: Extrapolation to polythiophene," *J. Chem. Phys.*, vol. 111, no. 12, pp. 5427–5433, 1999.

[241] T. Kircher and H.-G. Löhmannsröben, "Photoinduced charge recombination reactions of a perylene dye in acetonitrile," *Phys. Chem. Chem. Phys*, vol. 1, no. 17, pp. 3987–3992, 1999.

[242] R. L. Martin, "Natural transition orbitals," *J. Chem. Phys.*, vol. 118, no. 11, pp. 4775–4777, 2003.

[243] L. Cupellini, S. Caprasecca, C. A. Guido, and B. Mennucci, "NTOBuilder - A python tool to compute NTO orbitals and related metrics.," 2020.

[244] R. Improta, F. J. A. Ferrer, E. Stendardo, and F. Santoro, "Quantum-Classical Calculation of the Absorption and Emission Spectral Shapes of Oligothiophenes at Low and Room Temperature by First-Principle Calculations," *Chem. Phys. Chem.*, vol. 15, no. 15, pp. 3320–3333, 2014.

[245] S. Jurinovich, L. Cupellini, C. A. Guido, and B. Mennucci, "Exat: Excitonic analysis tool," *J. Comput. Chem*, vol. 39, no. 5, pp. 279–286, 2018.

[246] M. Huix-Rotllant, H. Tamura, and I. Burghardt, "Concurrent effects of delocalization and internal conversion tune charge separation at regioregular polythiophene-fullerene heterojunctions," *J. Phys. Chem. Lett.*, vol. 6, no. 9, pp. 1702–1708, 2015.

[247] A. Farahvash, C.-K. Lee, Q. Sun, L. Shi, and A. P. Willard, "Machine learning frenkel hamiltonian parameters to accelerate simulations of exciton dynamics," *J. Chem. Phys.*, vol. 153, no. 7, p. 074111, 2020.

[248] E. Da Como, M. A. Loi, M. Murgia, R. Zamboni, and M. Muccini, "J-aggregation in

α-sexithiophene submonolayer films on silicon dioxide," *J. Am. Chem. Soc.*, vol. 128, no. 13, pp. 4277–4281, 2006.

[249] A. Mani, J. Schoonman, and A. Goossens, "Photoluminescence study of sexithiophene thin films," *J. Phys. Chem. B*, vol. 109, no. 11, pp. 4829–4836, 2005.

[250] H. Yamagata, J. Norton, E. Hontz, Y. Olivier, D. Beljonne, J. L. Brédas, R. J. Silbey, and F. C. Spano, "The nature of singlet excitons in oligoacene molecular crystals," *The Journal of Chemical Physics*, vol. 134, no. 20, p. 204703, 2011.

[251] R. D. Harcourt, G. D. Scholes, and K. P. Ghiggino, "Rate expressions for excitation transfer. II. Electronic considerations of direct and throughconfiguration exciton resonance interactions," *The Journal of Chemical Physics*, vol. 101, no. 12, pp. 10521–10525, 1994.

[252] Y. Zhang, J. Qiao, S. Gao, F. Hu, D. He, B. Wu, Z. Yang, B. Xu, Y. Li, Y. Shi, W. Ji, P. Wang, X. Wang, M. Xiao, H. Xu, J.-B. Xu, and X. Wang, "Probing Carrier Transport and Structure-Property Relationship of Highly Ordered Organic Semiconductors at the Two-Dimensional Limit," *Phy. Rev. Lett.*, vol. 116, no. 1, p. 016602, 2016.

[253] O. G. Ziogos, I. Blanco, and J. Blumberger, "Ultrathin porphyrin and tetra-indole covalent organic frameworks for organic electronics applications," *J. Chem. Phys.*, vol. 153, no. 4, p. 044702, 2020.

[254] H. H. Choi, H. T. Yi, J. Tsurumi, J. J. Kim, A. L. Briseno, S. Watanabe, J. Takeya, K. Cho, and V. Podzorov, "A large anisotropic enhancement of the charge carrier mobility of flexible organic transistors with strain: A hall effect and raman study," *Adv. Science*, vol. 7, no. 1, p. 1901824, 2020.

[255] A. Camerman and J. Trotter, "The crystal and molecular structure of pyrene," *Acta Crystallogr.*, vol. 18, no. 4, pp. 636–643, 1965.

[256] V. Stehr, J. Pfister, R. Fink, B. Engels, and C. Deibel, "First-principles calculations of anisotropic charge-carrier mobilities in organic semiconductor crystals," *Phys. Rev. B*, vol. 83, no. 15, p. 155208, 2011.

[257] A. N. Sokolov, S. Atahan-Evrenk, R. Mondal, H. B. Akkerman, R. S. Sánchez-Carrera, S. Granados-Focil, J. Schrier, S. C. B. Mannsfeld, A. P. Zoombelt, Z. Bao, and A. Aspuru-Guzik, "From computational discovery to experimental characterization of a high hole mobility organic crystal," *Nat. Comm.*, vol. 2, no. 1, p. 437, 2011.

[258] G. Nan and Z. Li, "Influence of lattice dynamics on charge transport in the dianthra [2, 3-b: 2, 3-f]-thieno [3, 2-b] thiophene organic crystals from a theoretical study," *Phys. Chem. Chem. Phys.*, vol. 14, no. 26, pp. 9451–9459, 2012.

[259] M. T. Ruggiero, S. Ciuchi, S. Fratini, and G. D'Avino, "Electronic Structure, Electron-Phonon Coupling, and Charge Transport in Crystalline Rubrene Under Mechanical Strain," *J. Phys. Chem. C*, vol. 123, no. 26, pp. 15897–15907, 2019.